UNIVERSIDAD DE SANTIAGO DE COMPOSTELA
Facultad de Física
Departamento de Física de la Materia Condensada
Grupo de Física No Lineal

Lagrangian Coherent Structures: Application to Unsteady Oceanic and Laboratory Flows

Estructuras Coherentes Lagrangianas: Aplicación a Flujos en el Océano y en el Laboratorio.

Memoria presentada por Florian Huhn para optar al grado de Doctor en Ciencias Físicas

Santiago de Compostela, October 2012

Dr. Vicente Pérez-Muñuzuri y **Dr. Alberto Pérez-Muñuzuri**, profesores titulares de la Universidad de Santiago de Compostela, y **Dr. Pedro Montero**, investigador principal en el instituto oceanográfico INTECMAR, Vilagarcía de Arousa,

CERTIFICAN

que la presente memoria, titulada *Lagrangian Coherent Structures: Application to Unsteady Oceanic and Laboratory Flows*, fue realizada por **Florian Huhn** bajo su dirección y que concluye la tesis que presenta para optar al grado de Doctor en Ciencias Físicas.

Santiago de Compostela, Octubre de 2012

Vicente Pérez-Muñuzuri **Pedro Montero**

Alberto Pérez-Muñuzuri

Acknowledgments

The work of my PhD thesis would not have been possible without the support and dedication of many people. First of all, I want to express my deep gratitude to Vicente Pérez Muñuzuri who introduced me to the topic of my thesis and guided my research with excellent mentorship, many fruitful ideas and his never-ceasing interest in new scientific approaches. He always shared his broad physical knowledge and inspired me with his enthusiasm. He also introduced me to the scientific community and always supported and enabled my assistance to workshops and conferences, as well as the cooperation with other researchers, which was a great motivating experience. During the first part of my thesis, I enjoyed working with the team from INTECMAR. I especially want to thank Pedro Montero, who always offered me a warm welcome at his office in Vilagarcia de Arousa and taught me a lot about the circulation in the Rias Baixas. Pedro, Silvia, Garbi and Alberto coordinated the drifter experiments and without them I would miss some of my most impressive field experiment experiences on the Ria de Vigo and the Ria de Arousa. These experiments provided a valuable drifter data set with the indispensable help of the Gardacostas de Galicia and local fishermen. In 2011, I had the fantastic opportunity to work with Javier Beron-Vera and Josefina Olascoaga at the Rosenstiel School of Marine and Atmospheric Science in Miami. They are both experts in oceanic fluid transport and did not hesitate to invite me for a research stay with them. From the very beginning, they offered me great confidence, let me be part of their current research, and promoted my work with valuable advice. Thank you very much for this experience. At RSMAS, far from home, I had a great time also thanks to the friendship with Ricardo and Gustavo. I sincerely want to thank Alberto Pérez-Muñuzuri and Gonzalo Miguez Macho who keep running the Nonlinear Physics Group at the University of Santiago de Compostela, and who always have an open ear and a helping hand for the daily problems in academic life. Thank you, to all former and current group members, Dani, Alberto, Dario, Jorge, Thomas, Lisa, Carlos, Alexandre, Luci, Jacobo, Daniel, for sharing the hours in the lab with many happy moments and for your help in uncountable occasions, also towards the end of this thesis. Special thanks go to Anabela and Eva from the oceanography department of MeteoGalicia, who introduced me to the MOHID model and never hesitated to help me with my questions or to provide me some model data. I really appreciated the friendly reception of the MeteoGalicia team. I am deeply grateful to my wife Alexandra, who is at the same time my best co-worker. Thank you also for the long scientific discussions and for the great fluid experiments, but especially for

being a constant source of joy, motivation and inspiration for me, and for your unconditional love and support in all parts of life. I also want to thank my parents and my sister for always supporting me. During large parts of my PhD thesis I received funding from a FPU scholarship from the Spanish Ministry for Education (AP-2009-3550).

Contents

Acknowledgments **v**

Contents **vii**

Summary **xi**
Context of the Study xi
Objective of the Study xii
Summary xiii

Resumen **xvii**
Contexto del Trabajo xvii
Objetivo del Trabajo xix
Resumen xix

1 Introduction **1**
1.1 Transport and Mixing 1
1.1.1 Basic Mixing Process 2
1.1.2 Steady Two-Dimensional Flow 3
1.1.3 Unsteady Two-Dimensional Flow 3
1.2 Transport Processes 5
1.2.1 Diffusion 5
1.2.2 Advection 6
1.2.3 Advection and Diffusion 7
1.3 Advective Transport in the Ocean 8
1.4 Objective of the Study 10

2 Chaotic Transport and Coherent Structures **11**
2.1 Chaotic Advection 11
2.2 *Eulerian* coherent structures 13
2.2.1 Okubo-Weiss parameter 13
2.3 Lagrangian Coherent Structures (LCS) 14
2.3.1 Stable and Unstable Manifolds in a Steady Linear Strain Flow 14
2.3.2 LCS in Unsteady Flows 16
2.3.3 Finite-Time Lyapunov Exponent (FTLE) 16
2.3.4 Finite-size Lyapunov exponents (FSLE) 20

2.3.5 Other Approaches for LCS Detection . . . 21
2.4 Synoptic Lagrangian Maps (SLM) . . . 22

3 Two-dimensional Flow Data 25
3.1 Oceanic Mesoscale Flow from Altimetry Measurements . . . 25
3.1.1 Geostrophic Balance . . . 25
3.1.2 Satellite Altimetry . . . 28
3.2 Coastal Currents and High Frequency Radar . . . 28
3.3 Faraday Flow . . . 29
3.3.1 Particle Image Velocimetry (PIV) . . . 30

4 A Phytoplankton Patch under Unsteady Flow Conditions 31
4.1 Introduction . . . 31
4.2 Models . . . 33
4.2.1 The Flow Models . . . 33
Gaussian Correlated Flow . . . 34
Altimetry Flow . . . 34
4.2.2 NPZ Model . . . 35
4.2.3 Numerical Methods and Initial Conditions . . . 36
4.3 Results and Discussion . . . 37
4.3.1 Gaussian Flow - Optimal Time and Length Scales . . . 37
4.3.2 Altimetry Flow . . . 41
4.4 Conclusions . . . 46

5 Zonal jets in the Madagascar plankton bloom 49
5.1 Introduction . . . 49
5.1.1 Madagascar Plankton Bloom . . . 50
5.1.2 South Indian Ocean Countercurrent (SICC) . . . 52
5.1.3 Transport Barriers in Jets . . . 52
5.2 Data and Methods . . . 54
5.3 Results and Discussion . . . 55
5.3.1 Jet-like Lagrangian Coherent Structures . . . 55
5.3.2 Velocity of Plankton Front . . . 61
5.3.3 Temporal Variability of the SICC . . . 63
5.4 Conclusions and Outlook . . . 63

6 Flow Patterns in a Tidal Estuary - Ria de Vigo 67
6.1 Introduction . . . 67
6.1.1 The Ria de Vigo - A Tidal Estuary . . . 69
6.2 Data . . . 70
6.2.1 MOHID - The Hydrodynamic Model . . . 70
6.2.2 Drifter Experiments and Data Processing . . . 72
6.3 Methods - Lagrangian Coherent Structures from Model Velocity Field . . . 74
6.4 Results and Discussion . . . 76
6.4.1 Comparison of Trajectories: Drifters - Model . . . 76

6.4.2 LCS in the Ria de Vigo 79
6.4.3 LCS during North and South Wind Conditions 87
6.4.4 Synoptic Lagrangian Maps (SLM) 89
6.5 Conclusions and Outlook 95

7 LCS in the Faraday Flow **99**
7.1 Introduction 99
7.2 Results 101
7.2.1 Vortices and Faraday Waves 101
7.2.2 Lagrangian Coherent Structures 107
7.2.3 Simultaneous LCS and Chemical Front 111
7.3 Conclusions and Outlook 113

8 Conclusions **115**

Bibliography **119**

Appendices **135**

A Data **135**
A.1 Ocean Color Remote Sensing - SeaWiFS 135

B Numerical Schemes **137**
B.1 Extraction and Filtering of FTLE Ridges 137
B.2 Gradient of the Flow Map 137

C List of Publications **139**

Summary

Context of the Study

In the year 2010, people in Europe and America were confronted with two large scale catastrophic events, both being controlled by the process of chaotic advection in the large scale atmospheric and oceanic context. First, the eruption of the Icelandic volcano Eyjafjallajökull in April 2010 produced a cloud of volcanic ashes that spread over Europe and caused severe problems in air traffic. Since a high concentration of volcanic ashes is harmful to jet engines, hundreds of flights were canceled and thousands of passengers were affected. During a second disaster, which was man-made, an oil spill caused by an accident on the Deep Horizon oil rig in the Gulf of Mexico spread over huge areas of the sea surface. The oil spill had and still has a devastating impact on the marine wildlife, on the fishing industry and on tourism in the region. In both cases, transport simulations based on large scale atmospheric and oceanic flow models helped to estimate the current distribution of contaminants and to predict the future spreading. In animations of these simulations, one could see the typical irregular patterns in the spatial distribution of the contaminants that appear in chaotic flows. Filaments of high concentration are a common feature in these distributions. A very prominent filament in the Deep Horizon oil spill was known as the *tigertail* [150]. As a consequence of the filamentous distribution, geographically close regions can exhibit completely different concentrations. While one zone might not at all be affected by the plume, another nearby zone can be highly contaminated. It is the transport in the chaotic flow on short time scales that makes the difference.

Irregular tracer patterns are typical for time-dependent flows and are not limited to the large length scales in the examples. They also appear at scales of some kilometers in coastal flows, or at the centimeter scale in laboratory flows. These patterns are generated by coherent flow structures like vortices or jets that have a similar size as the tracer cloud. If there was no large scale structure in the flow, and instead movements would be limited to length scales much smaller than the patch of contamination, the tracer would spread isotropically in all directions. With increasing distance from the source, it would be diluted by mixing with uncontaminated fluid and the tracer concentration would be a simple function of the distance to the source. Mathematically, a simple diffusion approach could account for this kind of behaviour. However, in the considered examples, the patterns are highly intermittent, i.e., at two different points at the same distance from the source of the contamination, totally different concentrations can occur.

Concepts from dynamical systems theory have shown to be very useful to study the fluid transport in flows with coherent structures. Dynamical system theory deals with the analysis of all kind of systems that evolve in time. The state of a system can be represented in the phase space given by the dynamic variables of the system. For the two-dimensional flows that we analyze in this work, the phase space is equivalent to the two-dimensional real space, i.e., the dynamical variables are the spatial coordinates (x, y) denoting the position of a small fluid parcel in the flow. Hence, we follow the trajectories of small fluid parcels which corresponds to an analysis in the Lagrangian frame. We seek to characterize the transport in a time-dependent flow by identifying coherent structures in phase space, in particular, hyperbolic points and the associated unstable and stable manifolds, that control the motion of the fluid during certain time scales. The extracted flow structures are termed Lagrangian Coherent Structures (LCS). They act as transport barriers in the fluid motion and order the flow into different regions corresponding to different dynamical behavior of the trajectories. We are interested in the deterministic evolution of the flow on short time scales, where due to the intermittency of the transport process a statistical description is not meaningful.

In order to extract the geometry of the mixing patterns in a flow, we need the complete spatio-temporal velocity fields that define the flow as a dynamical system. In the oceanic context, measurement systems, such as high-frequency radars at the coast and satellite altimetry for global data, as well as numerical models, provide valuable velocity data for the Lagrangian transport analysis. In the laboratory, we can use Particle Image Velocimetry (PIV) to measure two-dimensional velocity fields at a high spatial and temporal resolution. Using these velocity fields, the extracted advective transport patterns are strictly only valid for a conservative passive tracer, i.e., a tracer without sinks and sources that does not alter the fluid flow. Hence, the purely advective transport patterns give valuable information about possible pathways of discrete objects and the locations where fluid separates and merges. Beyond that, we examine interesting applications to the evolution of fields of reactive tracers, that have sources and sinks due to chemical or biological reactions. By definition, the concentration fields of these reactive tracers are not solely modified by advection, but nevertheless, advection can be dominant in shaping the spatial distribution of the reactive tracer. If we extract the geometry of mixing due to pure advection, we can compare the mixing patterns to the real distribution of the reactive tracers. Here, we do this comparison for a plankton bloom in the Indian Ocean and for an excitable chemical reaction in a two-dimensional turbulent flow in the laboratory. It turns out that the advective transport patterns agree well with the borders of the reactive tracer concentration.

Objective of the Study

In this thesis we study several spatio-temporal transport problems in two-dimensional time-dependent velocity fields that generate chaotic advection. We aim to clarify

the role of advective transport for the dispersion of passive and also for reactive tracers. Therefore, we want to characterize transport in these flows in the very detail with Lagrangian coherent structures that reveal the geometry of the irregular fluid motion, and especially emphasize the lines of separation and merging of fluid patches. We further want to examine the relevance of LCS for reactive tracers.

Summary

The studies presented in this document all deal with transport in chaotic flows and seek to clarify the role of Lagrangian coherent structures in ordering and controlling the fluid motion, and consequently, also the spatio-temporal patterns in continuous tracer fields. The four chapters, 4 to 7, presenting the results, are connected by a similar setting of the problem, while time and length scales of the flows differ largely. We give a general introduction to the main concepts and methods used in all chapters, while more specific introductory information on the respective characteristics of each study is given at the beginning of each result chapter. Hence, the result chapters can be read as independent studies as well, unified by similar Lagrangian methods.

In Chapter 1, we give a short introduction to the concept of mixing. The fundamental property of a mixing process in a liquid is the fact that close parts are separated and distant parts are brought together. In a discrete mapping, this process is realized by consecutive cutting, reorientating, and merging of the material. In unsteady flows, hyperbolic points are crucial for the mixing process, as their stable and unstable manifolds are the lines where fluid is separated and merged. In the following part, we recall the two basic transport processes in fluids, diffusion and advection. While diffusion is generated by small scale random motion and can therefore be described by a statistic approach, advection is deterministic and given by a velocity field. Since molecular diffusive transport is most often a slow process, the transport in many flows is dominated by advection. For chaotic advection in time-dependent velocity fields, methods from dynamical systems theory have been successfully applied to extract Lagrangian Coherent Structures that control the mixing dynamics. We review some of the work using Lagrangian coherent structures in the oceanic context.

In Chapter 2, we introduce the methods used to localize Lagrangian coherent structures (LCS) in unsteady flows. In particular, we identify LCS as ridges in fields of the finite-time version of the Lyapunov exponent (FTLE) of tracer particles in the time-dependent flow. In forward (backward) time direction tracer particles separate most rapidly close to stable repelling (unstable attracting) manifolds of hyperbolic points. Since the FTLE is a finite-time average of the exponential separation rate of initially close particles, lines of high FTLE values (ridges) turn out to be good estimates of the location of the finite-time stable and unstable manifolds. The time scale on which the estimated LCS are relevant for mixing is given by the integration time that is chosen for the tracer particles. Several other Lagrangian methods have been proposed to extract LCS from unsteady flows. We

present them in a short paragraph. Finally, we use another Lagrangian method called Synoptic Lagrangian Maps (SLM) that is introduced at the end of this chapter. SLM visualize the origin and fate of trajectories that cross a limited flow domain, e.g., a coastal flow bounded by the coast and a mouth to the open ocean. Furthermore, residence times of trajectories in the flow domain can be directly derived from the SLM.

In Chapter 3, we shortly describe the measurement systems and principles used to obtain the unsteady two-dimensional velocity fields which are analyzed in the following chapters. First, we explain how oceanic mesoscale currents are derived from satellite based altimetry measurements. Under the assumption of geostrophic balance, i.e., a balance in the Navier-Stokes equation of the Coriolis force and the pressure gradient force due to the elevation of the sea surface, ocean currents at the scale of $\sim 100\,\mathrm{km}$ are proportional to the inclination of the sea surface. The elevation of the sea surface can be measured at a very high precision of $\sim 2\,\mathrm{cm}$ from satellite altimeters. Altimeters measure the time of flight of a radar signal between the satellite on a known orbit and the sea surface. Second, we describe the high-frequency radar system that provides the surface currents in the outer parts of the estuary Ria de Vigo in NW Spain. In this system, radial velocities of the surface flow are estimated from a Doppler shift of a radar signal, taking into account the propagation velocity of the surface waves that scatter the emitted radar wave via Bragg reflection. With two radar systems covering the same surface area, time-dependent fields of both velocity components can be obtained. Third, a turbulent quasi two-dimensional fluid flow induced by Faraday waves in the laboratory is measured by Particle Image Velocimetry (PIV). For that purpose, images of a large numbers of floating particles on the fluid surface are taken and the velocity field is derived from the finite position differences of particles in subsequent images.

In Chapter 4, we consider a numerical reaction-diffusion-advection plankton model that is able to represent simple dynamics of plankton blooms in the ocean. It consists of three concentrations, an anorganic nutrient N, the phytoplankton concentration P, and the zooplankton concentration Z. In this NPZ model a basic food chain with three trophic levels is represented by three coupled differential equations. We study the growth of a single plankton patch emerging around a localized nutrient source that is active for a limited period of time. Due to the advective flow in the model, the plankton patch is distorted and can spread into regions around the nutrient source. We are interested in the dependence of the growth on length and time scales of the advective flow. For the advection term, we use first, a Gaussian correlated flow, and second, a more realistic mesoscale flow from satellite altimetry measurements of the North Atlantic Ocean. We find that the growth of a locally initialized plankton patch depends on the time and length scales of the underlying advective flow. A resonance appears, when the flow has time scales similar to the typical time scales in the biological model, leading to maximum growth of the plankton patch. Additionally, we study a selected region in the altimetry flow, where in apparently similar eddies the developed plankton patch is significantly larger in one of the eddies. We argue that the different topology of the steady flow in the eddies accounts for this finding. In

particular, the hyperbolic points around the eddies define the pathways on which the plankton patch can spread. This chapter is a slightly extended version of the study published in [165].

In Chapter 5, we analyze a specific plankton bloom, the Madagascar plankton bloom, with respect to the transport by geostrophic ocean currents. The Madagascar plankton bloom is a large bloom event east of Madagascar that appears irregularly, i.e., in some years the event is very strong and in others it fails to appear. The bloom typically starts south of Madagascar and propagates rapidly into the Indian Ocean, reaching its largest zonal extent of up to $2000\,\mathrm{km}$ in February or March. Different mechanisms for the initiation of the bloom have been proposed, but due to the lack of extensive in-situ data, that would be needed to represent the variability of the bloom, a rigorous explanation for the bloom is still missing. We concentrate here on the impact of chaotic advection by ocean currents on the propagation of the plankton bloom. We derive the ocean currents from satellite altimetry data assuming geostrophic balance for the flow dynamics. The surface chlorophyll concentration is obtained from satellite measurements. In the mesoscale ocean currents we seek for flow structures that can be related to the strong eastward propagation of the bloom. We find that the recently discovered South Indian Ocean Countercurrent (SICC) is most probably responsable for the eastward propagation of the bloom. In earlier studies, an eastward directed flow has not been considered as an explanation for the large extent of the bloom, and thus is a novel approach. A passive continuous tracer, released at the south tip of Madagascar, is transported eastward by the SICC and covers a similar area as the Madagascar plankton bloom. This supports the hypothesis that the origin of the plankton bloom is located south of Madagascar where upwelling could deliver the necessary nutrients. However, it is important to note that the front of the plankton bloom propagates faster than the purely advective velocity, suggesting that the biological reaction also plays a crucial role. We characterize the temporal variability of the jet to check if it is correlated with the occurrence of the bloom. We find that this is not the case. The jet is neither especially strong in bloom years nor especially weak in non-bloom years. We also extract the locations of possible transport barriers in the chaotic flow from fields of finite-time Lyapunov exponents (FTLE), and find that they largely coincide with the boundaries of the plankton bloom. This indicates that the flow shapes the boundaries of the bloom while it develops. The chapter is an extended version of the study published in [91].

In Chapter 6, we apply methods from dynamical systems theory to the chaotic transport in the tidal estuary *Ria de Vigo* in Spain. In this estuary, the oscillating tidal flow interacts with the longterm flow on the shelf and with quickly changing flows induced by wind, giving rise to complex flow patterns. We determine these flow patterns at the surface by computing Lagrangian coherent structures (LCS) in the surface layer of a three-dimensional hydrodynamic model of the Ria de Vigo. Our results are validated by comparing the LCS to surface drifter trajectories from four field experiments in the Ria de Vigo. The drifter trajectories agree with the flow patterns found in the model. Moreover, LCS for typical wind conditions are extracted that can help to better predict the pathway of drifting objects or

contaminations in the estuary during stable weather conditions. The LCS visualize the dynamics of the water exchange between the bay and the shelf. Additionally, the method of Synoptic Lagrangian Maps (SLM) is applied to currents fields measured with a high-frequency (HF) radar system. In SLM, trajectories are classified by their origin and fate. We quantify the transport across a limited flow domain in the outer part of the Ria de Vigo and relate the appearing flow patterns to the wind conditions. Residence times of fluid parcels in the flow domain turn out to vary from one to ten days. Spatial patterns of the residence times show intermittent patterns, where close fluid patches exhibit significantly different residence times. An exemplary comparison between a SLM computed from the HF radar flow and another SLM computed from the model flow demonstrate that SLM are useful to compare different velocity data sets in terms of global transport patterns. This chapter is an extended version of the study published in [90].

In Chapter 7, we study transport in an experimental quasi two-dimensional turbulent laboratory flow induced by the Faraday experiment. A thin fluid layer is vibrated vertically and the capillary waves appearing on the surface generate a horizontal flow, which we measure with Particle Image Velocimetry (PIV). We first examine the patterns of the vortices in the horizontal flow and find that they are correlated with the pattern of the Faraday waves on the surface. If we increase the vibrational forcing of the flow, the autocorrelation time of the vorticity decreases with the decreasing autocorrelation time of the Faraday waves, i.e., the persistence time of the vortices is limited by the time during which the Faraday wave pattern remains stable. Again, we are interested in persisting Lagrangian flow structures, LCS, that control the chaotic mixing in the Faraday flow on small to intermediate time scales. Similarly as in the studies of patterns of biological reactions (plankton) in chapter 4 and 5, we analyze the patterns in excitable active media, namely the chemical Belousov-Zhabotinsky (BZ) reaction. For certain flow conditions we observe a traveling chemical front whose boundaries have an irregular filamentous shape. We can simultaneously measure the Faraday flow quantitatively and the concentration of the BZ reaction qualitatively. This allows for a direct comparison of the LCS with the filamentous front. The LCS that we extract from the measured velocity fields align with the chemical front and indicate that its shape is dominated by advection.

In Chapter 8, we summarize the results of the different chapters.

Resumen

Contexto del Trabajo

En el año 2010, el atento lector de las noticias diarias se enfrentó a dos grandes eventos catastróficos relacionados con la advección caótica a gran escala en la atmósfera y en el océano. Por un lado, la erupción del volcán islandés Eyjafjallajökull en abril de 2010 produjo una nube de cenizas volcánicas que se esparció por Europa, causando graves problemas en el tráfico aéreo. Dado que una alta concentración de cenizas volcánicas es peligrosa para los turborreactores de los aviones, cientos de vuelos fueron cancelados y miles de pasajeros se vieron afectados. En un segundo desastre, provocado por la actividad humana, un derrame de petróleo causado por un accidente en la plataforma petrolífera *Deep Horizon*, en el Golfo de México, se extendió por grandes áreas de la superficie del mar y tuvo un impacto devastador sobre la fauna marina, la industria pesquera y el turismo en la región. En ambos casos, la realización de simulaciones de transporte basadas en modelos de flujo atmosférico y oceánico a gran escala contribuyó a diagnosticar la distribución de dichos contaminantes y predecir su futura dispersión. Los medios de comunicación presentaron los patrones irregulares típicos en la distribución espacial de los contaminantes que aparecen en los flujos caóticos. Los filamentos de alta concentración son una característica típica de estas distribuciones. Un filamento famoso en el derrame de petróleo procedente del *Deep Horizon* era conocido como el *tigertail* [150]. Como consecuencia de la distribución filamentosa, regiones cercanas pueden exhibir concentraciones totalmente diferentes; así, mientras una zona no se ve afectada por la contaminación, otra área cercana puede estar altamente contaminada. El responsable de dichas diferencias es el transporte en el flujo caótico a escalas de tiempo cortas.

Los patrones irregulares de trazadores son típicos de flujos dependientes del tiempo y no se limitan a las grandes escalas de longitud de los ejemplos anteriores. Aparecen también a escalas de unos pocos kilómetros en los flujos costeros, o a escalas de centímetros en los flujos de laboratorio. Estos patrones son generados por estructuras de flujo coherentes, como vórtices o chorros (jets), que tienen un tamaño similar a la nube de trazador. Si no hubiese ninguna estructura de larga escala en el flujo y, en lugar de eso, los movimientos se limitasen a escalas de longitud mucho más pequeña que la mancha de contaminación, el trazador se extendería isotrópicamente en todas las direcciones. Al aumentar la distancia a la fuente, se diluiría en el líquido no contaminado y la concentración del trazador sería una simple función de la distancia a la fuente. Sin embargo, en los ejemplos

considerados, los patrones son notablemente intermitentes; esto es, en dos puntos diferentes situados a la misma distancia de la fuente de contaminación pueden registrarse concentraciones totalmente diferentes.

Los conceptos de teoría de los sistemas dinámicos han demostrado ser muy útiles para estudiar el transporte de fluidos en flujos con estructuras coherentes. La teoría de sistemas dinámicos aborda el análisis de todo tipo de sistemas que evolucionan en el tiempo. El estado de un sistema puede representarse en el espacio de fase, definido por las variables dinámicas del sistema. Para los flujos bidimensionales que se analizan en este trabajo, el espacio de fase es equivalente al espacio real bidimensional, pues las variables dinámicas coinciden con las coordenadas espaciales (x, y) que representan la posición de una pequeña parcela de fluido en el flujo. De este modo, se han seguido las trayectorias de las partículas del fluido, lo que se corresponde con un análisis de tipo lagrangiano. Se ha buscado caracterizar el transporte en un flujo dependiente del tiempo mediante la identificación de estructuras coherentes en su espacio de fase y, en particular, de los puntos hiperbólicos y las variedades estables e inestables asociadas que controlan el movimiento del fluido. Las estructuras de flujo extraídas se denominan Estructuras Coherentes Lagrangianas (LCS). Estas estructuras actúan como barreras de transporte en el movimiento del fluido y ordenan el flujo en diferentes regiones correspondientes al diferente comportamiento dinámico de las trayectorias en dichas regiones.

Estamos interesados en la evolución determinista del flujo a escalas de tiempo cortas, donde a causa de la intermitencia del proceso de transporte una descripción estadística no es significativa. Con el fin de extraer la geometría de los patrones de mezcla en un flujo, necesitamos los campos de velocidad espacio-temporales completos que definen el flujo como un sistema dinámico. En el contexto oceánico, sistemas de medición como los radares de alta frecuencia en la costa y la altimetría por satélite para datos globales, así como los modelos numéricos, proporcionan datos valiosos para el análisis de transporte. En el laboratorio, se puede utilizar la técnica denominada Particle Image Velocimetry (Velocimetría de Partículas por Imagen, PIV) para medir campos de velocidad bidimensionales con una alta resolución espacial y temporal. Usando estos campos de velocidad, los patrones de transporte advectivo extraídos son estrictamente solo válidos para un trazador conservativo pasivo; esto es, un trazador sin sumideros ni fuentes que no altera el flujo. Los propios patrones de transporte proporcionan información valiosa sobre las posibles trayectorias seguidas por objetos discretos en el flujo y sobre los puntos donde el fluido se separa y converge. Además, se han examinado algunas aplicaciones interesantes a la evolución de los campos de trazadores reactivos, que tienen fuentes y sumideros como consecuencia de reacciones químicas o biológicas. Por definición, la distribución espacial de la concentración de estos trazadores reactivos no está únicamente modificada por la advección; sin embargo, la advección puede ser el mecanismo dominante que determine la distribución espacial del trazador reactivo. Si se extrae la geometría de mezcla debida a advección pura, podemos comparar los patrones de mezcla con la distribución real de los trazadores reactivos. Aquí realizamos esta comparación para una floración de plancton en el Océano Índico y para una reacción química excitable en un flujo bidimensional

turbulento en el laboratorio, resultando que los patrones de transporte advectivo concuerdan bien con las fronteras de la concentración de trazador reactivo.

Objetivo del Trabajo

En esta Tesis, se han estudiado varios problemas espacio-temporales de transporte en campos de velocidad bidimensionales dependientes del tiempo que generan advección caótica. Nuestro objetivo es aclarar el papel del transporte advectivo en la dispersión de trazadores pasivos y también de trazadores reactivos. Así, queremos caracterizar el transporte de estos flujos con gran precisión mediante Estructuras Coherentes Lagrangianas, que revelan la geometría del movimiento irregular del fluido y, en particular, remarcan las líneas de separación y confluencia de los elementos del mismo. Además, queremos examinar la relevancia de las LCS para trazadores reactivos.

Resumen

Los estudios presentados en este trabajo se ocupan del transporte en flujos caóticos y tratan de aclarar el papel de las Estructuras Coherentes Lagrangianas en el ordenamiento y control del movimiento de los fluidos, y en consecuencia, también los patrones espacio-temporales en campos de trazadores continuos. Los capítulos 4 a 7, donde se presentan los resultados, están conectados por el uso de métodos similares, si bien las escalas de tiempo y longitud de los flujos difieren en gran medida. Presentamos una introducción general a los conceptos y métodos utilizados de forma general en los diferentes capítulos, dejándose aquellas informaciones introductorias más específicas, relacionadas con cada estudio, para el principio de cada capítulo. Por lo tanto, los capítulos de resultados son, en realidad, estudios independientes unificados por los similares métodos lagrangianos utilizados, antes que una serie consecutiva en la cual un capítulo está directamente basado en el anterior.

En el capítulo 1, presentamos una breve introducción al concepto de mezcla. La propiedad fundamental de un proceso de mezcla en un material es el hecho de que partes cercanas se separan y partes distantes se unen. En un mapeo discreto, este proceso se realiza cortando, reorientando y uniendo el material de forma consecutiva. En los flujos inestables, los puntos hiperbólicos son cruciales para el proceso de mezcla, ya que sus variedades estables e inestables son las líneas donde el fluido se separa y converge. En la siguiente parte, recordamos los dos procesos básicos de transporte de fluidos: la difusión y la advección. Mientras que la difusión es generada por un movimiento aleatorio a pequeña escala, y por lo tanto puede ser descrita mediante una aproximación estadística, la advección es determinista y viene dada por un campo de velocidades. Puesto que el transporte difusivo es un proceso lento, el transporte en muchos flujos está dominado por la advección. Para la advección caótica en campos de velocidades dependientes del tiempo, los métodos de la teoría de los sistemas dinámicos se han aplicado con

éxito para extraer Estructuras Coherentes Lagrangianas, que controlan la dinámica de mezcla. Reseñamos algunos de los trabajos en el contexto oceánico.

En el capítulo 2, introducimos los métodos utilizados para localizar Estructuras Coherentes Lagrangianas (LCS) en los flujos inestables. En particular, se identifican las LCS como crestas en los campos del exponente de Lyapunov a tiempo finito (FTLE) de partículas trazadoras en el flujo caótico. Hacia adelante (atrás) en el tiempo, las partículas trazadoras se separan más rápidamente en las proximidades de las variedades estables (inestables) de puntos hiperbólicos.

Puesto que el FTLE es un promedio de tiempo finito de la tasa de separación exponencial de partículas inicialmente cercanas, líneas con elevados valores de FTLE (crestas) resultan ser buenas estimaciones de la ubicación de las variedades estables e inestables de tiempo finito. La escala de tiempo en la cual las LCS estimadas son relevantes para la mezcla viene dada por el tiempo de integración que se elige para las partículas trazadoras. Otros métodos lagrangianos, que presentamos en un breve párrafo, se han propuesto para extraer LCS de flujos inestables. Por último, se utiliza un método lagrangiano adicional denominado Mapas Sinópticos Lagrangianos (SLM), que se introduce al final de este capítulo. Los SLM visualizan el origen y el destino de las trayectorias que cruzan un dominio de flujo limitado, como por ejemplo un flujo costero delimitado por la costa y una boca abierta al océano. Además, los tiempos de residencia de las trayectorias en el dominio de flujo pueden derivarse directamente a partir de los SLM.

En el capítulo 3, se describen brevemente los sistemas de medición y los principios utilizados para obtener los campos de velocidad bidimensionales que se analizan en los capítulos posteriores. En primer lugar, se explica cómo las corrientes oceánicas de mesoescala se derivan de mediciones basadas en altimetría desde satélite. Bajo la hipótesis de balance geostrófico, es decir, un equilibrio en la ecuación de Navier-Stokes entre la fuerza de Coriolis y la fuerza del gradiente de presión debida a la elevación de la superficie del mar, las corrientes oceánicas en la escala de $\sim 100\,\mathrm{km}$ son proporcionales a la inclinación de la superficie del mar. La elevación de la superficie del mar se puede medir con una precisión muy alta de $\sim 2\,\mathrm{cm}$ mediante altímetros que miden el tiempo de vuelo de una señal de radar entre el satélite en una órbita conocida y la superficie del mar. En segundo lugar, se describe el sistema de radar de alta frecuencia que proporciona las corrientes superficiales en la parte exterior de la Ría de Vigo, situada en el noroeste de España. En este sistema, las velocidades radiales del flujo superficial se calculan a partir del desplazamiento Doppler de la señal de radar, teniendo en cuenta la velocidad de propagación de las ondas superficiales, que reflejan la onda emitida mediante reflexión de Bragg. Con dos sistemas de radar que cubren la misma superficie, los campos dependientes del tiempo de las dos componentes de la velocidad pueden obtenerse.

En tercer lugar, en el laboratorio, el flujo turbulento cuasi bidimensional inducido por las ondas de Faraday se determina mediante Particle Image Velocimetry (PIV). Así, se toman las imágenes de un gran número de partículas flotantes en la superficie del fluido y se deriva el campo de velocidades a partir de las diferencias finitas de posición entre las partículas en imágenes consecutivas.

En el capítulo 4 consideramos un modelo numérico sencillo de reacción-difusión-

advección que representa la dinámica de las floraciones de plancton en el océano. Se compone de tres concentraciones: la concentración de nutrientes inorgánicos N, la concentración de fitoplancton P y la concentración de zooplancton Z. Este modelo NPZ representa una cadena alimentaria básica con tres niveles tróficos mediante tres ecuaciones diferenciales acopladas. Se estudia el crecimiento de una sola mancha de plancton surgiendo alrededor de una fuente de nutriente localizada que es activa durante un periodo limitado. Debido a un flujo advectivo en el modelo, la mancha del plancton se distorsiona y se puede propagar hacia regiones alrededor de la fuente de nutrientes. Estamos interesados en cómo el crecimiento depende de las escalas de longitud y tiempo del flujo advectivo. Para el término de advección se utiliza, en primer lugar, un flujo con correlaciones gaussianas y, en segundo lugar, un flujo de mesoescala más realista procedente de mediciones de altimetría en el Océano Atlántico Norte. El crecimiento de una mancha de plancton depende en gran medida de las escalas de tiempo y longitud del flujo advectivo subyacente. Una resonancia aparece entre las escalas de tiempo típicas en el modelo y en el flujo, lo que lleva a un crecimiento máximo de la mancha de plancton. En el flujo de altimetría, se estudia además una región de flujo seleccionada en la cual, para dos remolinos aparentemente similares, se observa que el crecimiento de la mancha de plancton es significativamente mayor en uno de ellos. Entendemos que la topología diferente del flujo estacionario en los dos casos es la responsable de este comportamiento. En particular, el número de puntos hiperbólicos alrededor de los remolinos define las trayectorias por las cuales la mancha de plancton se puede propagar. Este capítulo es una versión ligeramente ampliada del estudio publicado en [165].

En el capítulo 5 se analiza una floración de plancton específica -la floración de plancton de Madagascar- con respecto al transporte de las corrientes oceánicas geostróficas. La floración de plancton de Madagascar es un gran evento de floración al este de Madagascar que se produce irregularmente; así, en algunos años el evento es muy intenso mientras que en otros no se produce. La floración comienza típicamente al sur de Madagascar y se propaga rápidamente por el Océano Índico, alcanzando su mayor extensión zonal, de hasta $2000\,\mathrm{km}$, en febrero o marzo. Diferentes mecanismos para la iniciación de la floración han sido propuestos, pero debido a la falta de grandes conjuntos de datos in situ, que serían necesarios para representar la variabilidad de la floración, no existe todavía una explicación rigurosa para este fenómeno. Nos centraremos en el impacto de la advección caótica a través de las corrientes oceánicas en la propagación de la floración de plancton. Las corrientes se derivan a partir de datos de altimetría, suponiendo un balance geostrófico en la dinámica del flujo. La concentración de clorofila superficial se obtiene a partir de mediciones de satélite. En las corrientes oceánicas de mesoescala, investigamos las estructuras de flujo que pueden estar relacionadas con la intensa propagación de la floración hacia el este. Encontramos que la recientemente descubierta South Indian Ocean Countercurrent (Contracorriente del Océano ndico Sur, SICC) es con toda probabilidad la responsable de la propagación hacia el este de la floración; en cambio, en estudios anteriores, un flujo dirigido hacia el este no había sido considerado como una explicación de la gran extensión de la floración. Un trazador pasivo continuo soltado en la punta

sur de Madagascar es transportado hacia el este por la SICC, cubriendo un área similar a la floración de plancton de Madagascar. Esto apoya la hipótesis de que el origen de la floración de plancton se encuentra al sur de Madagascar, donde el afloramiento podría aportar los nutrientes necesarios. Sin embargo, es importante señalar que el frente de la floración de plancton se propaga más rápido que la velocidad pura advectiva, lo que sugiere que la reacción biológica también juega un papel crucial. Caracterizamos la variabilidad temporal de la SICC para comprobar si está correlacionada con la aparición de la floración. No es este el caso: el chorro no es ni especialmente fuerte en años de floración ni especialmente débil en años sin floración. También se ha extraído la ubicación de posibles barreras de transporte en el flujo caótico a partir de los campos de exponentes de Lyapunov a tiempo finito (FTLE), encontrándose que las barreras de transporte coinciden en gran medida con los bordes de la floración de plancton. Esto indica que el flujo da forma a los bordes de la floración mientras se desarrolla. Este capítulo es una versión ampliada del estudio publicado en [91].

En el capítulo 6, se aplican los métodos de la teoría de los sistemas dinámicos al transporte caótico en la Ría de Vigo. En este estuario, el flujo de la marea oscilante interactúa con el flujo a largo plazo en la plataforma continental y con los flujos inducidos por el viento, los cuales cambian rápidamente dando lugar a patrones de flujo complejos. Se determinan los patrones de flujo en la superficie calculando Estructuras Coherentes Lagrangianas (LCS) en la capa superficial de un modelo hidrodinámico tridimensional de la Ría de Vigo. Nuestros resultados son validados mediante la comparación de las LCS con trayectorias de boyas de deriva procedentes de cuatro experimentos de campo en la Ría de Vigo. Las trayectorias de las boyas de deriva coinciden con los patrones de flujo que se encuentran en el modelo. Por otra parte, se propone que las LCS para las condiciones de viento típicas pueden ayudar a predecir mejor la trayectoria de deriva de objetos o contaminantes en el estuario. Las LCS visualizan la dinámica del intercambio de agua entre la bahía y la plataforma continental. Además, se aplica el método de los Mapas Sinópticos Lagrangianos (SLM) a los campos de corrientes medidas con un sistema de radar de alta frecuencia (HF). Para obtener un SLM, las trayectorias se clasifican según su origen y su destino. Se cuantifica el transporte a través de un dominio de flujo limitado en la parte externa de la Ría de Vigo y se relacionan los patrones de flujo que aparecen con las condiciones del viento. Los tiempos de residencia de las parcelas de fluido en el dominio de flujo resultan variar entre uno y diez días. Los patrones espaciales de los tiempos de residencia muestran patrones intermitentes, donde elementos de fluido muy próximos entre sí exhiben tiempos de residencia significativamente diferentes. Una comparación entre un SLM calculado a partir del flujo de radar HF y otro SLM calculado a partir del modelo demuestra que los SLM son útiles para comparar los diferentes datos de velocidad en términos de los patrones generales de transporte. Este capítulo es una versión ampliada del estudio publicado en [90].

En el capítulo 7 se estudia el transporte en un flujo turbulento cuasi bidimensional inducido por el experimento de Faraday. Una capa delgada de fluido se hace vibrar verticalmente, de forma que las ondas capilares que aparecen en la superficie generan un flujo horizontal que se mide mediante Particle Image

Velocimetry (PIV). En primer lugar, examinamos los patrones de los vórtices en el flujo horizontal y encontramos que éstos parecen estar correlacionados con el patrón de las ondas de Faraday en la superficie. Si se aumenta el forzamiento del flujo, la auto-correlación temporal de la vorticidad disminuye con la auto-correlación temporal de las ondas de Faraday; esto es: el tiempo de persistencia de los vórtices está limitado por el tiempo en el que el patrón de ondas de Faraday se mantiene estable. Nuevamente, estamos interesados en estructuras de flujo persistentes, LCS, que controlan la mezcla caótica en el flujo de Faraday. Del mismo modo que en los estudios de los patrones de reacciones biológicas (plancton), en los capítulos 4 y 5, se analizan aquí los patrones en medios activos excitables y, en particular, la reacción química de Belousov-Zhabotinsky (BZ). Para ciertas condiciones de flujo se observa un frente químico desplazándose en el recipiente, y cuyas fronteras tienen una forma filamentosa irregular. Podemos medir, simultáneamente, el flujo de Faraday cuantitativamente y la concentración de la reacción BZ cualitativamente. Ello permite una comparación directa de las LCS con el frente filamentoso. Las LCS que extraemos de los campos de velocidad medidos se alinean con el frente químico e indican que su estructura está dominada por la advección.

En el capítulo 8 se resumen los resultados de los diferentes capítulos.

Chapter 1

Introduction

Abstract

In this chapter we motivate the importance of transport in fluids in many natural systems and introduce the fundamental mechanism of mixing. We recall the basic transport processes diffusion and advection, and give a short review of studies that apply dynamical systems methods to advection in an oceanic context. Finally, we formulate the objectives of this work.

1.1 Transport and Mixing

Fluid flows are ubiquitous in nature and technology on all length scales. In nature, atmospheric and oceanic flows, for example, play a key role on the global scale transporting heat from the tropics towards the poles. This determines the local climate in many regions of the world. In general, most transport processes in geoscience are linked to moving fluids, as e.g., the erosion of solid material by rain and rivers, the dispersion of dust, moisture, and volcanic ashes [84] in the atmosphere, or the transport of nutrients, marine wildlife, dissolved gases or contaminations [150] in the ocean. In life sciences, the blood flow in animals and humans is crucial to supply cells with all necessary substances, while a similar flow in plants transports water and nutrients from the ground into the leaves. In technology, the engineering industries develop solutions to the problems of propulsion through air and water by cars, planes and ships, that are largely affected by the surrounding flow. The development of motors also includes flows of combustion processes in engines. In the contrary approach, renewable energy is extracted from geophysical flows as wind, ocean currents or rivers. Flows in pipes and tubes transport reactive substances in the chemical industry, allow for a transport of gas and oil over large distances, and they provide whole cities with fresh water and dispose of the waste water.

Fluids tend to become unstable for increasing velocity. This fundamental property of fluid motion is responsable for most of the aforementioned flows being time-dependent. In contrast to steady flows, time-dependent flows efficiently mix the fluid, i.e., the properties of the fluid, as impurities, the concentration of a

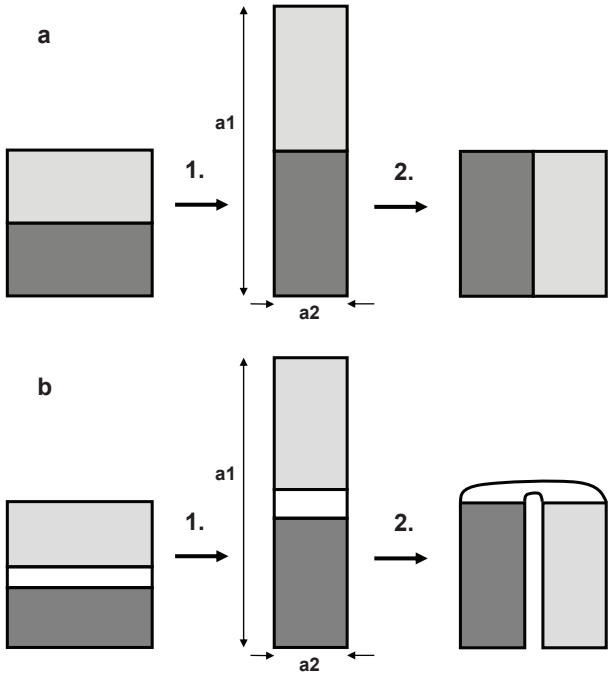

Figure 1.1: Sketch of the two steps of the (a) baker's map and the (b) horse shoe map, both being building blocks of mixing motion. Reproduced from [159].

physical or chemical quantity or also discrete solid particles, are transported by the fluid in a highly irregular way.

1.1.1 Basic Mixing Process

In order to understand mixing let us first consider a simple example of discrete mixing taken from [159]. The process of mixing is directly linked to a very basic condition that the mixing motion must fulfill. To mix a set of points or a continuous field, the motion has to separate close elements and displace them to distinct regions of the domain. At the same time, we expect that close elements originate from distinct regions, i.e., the motion has brought them together from a large distance. The most simple and intuitive example for such a motion is the baker's map in accordance to the natural mixing process, when a baker cuts and fuses dough [159]. Figure 1.1a shows the two discrete steps of the baker's map. Starting from a square domain of material, in the first step the domain is stretched by a factor $a_1 = 2$ in one direction. To conserve the area of the material, the domain is compressed in the orthogonal direction by a factor $a_2 = 1/2$, such that $a_1 a_2 = 1$. This condition defines a large class of maps, namely area-preserving maps. The corresponding condition for a two-dimensional continuous flow is the conservation of fluid, i.e., the velocity field is incompressible and satisfies $\nabla \cdot \mathbf{v} = 0$. In the second step, the stretched domain is cut, and the two parts are joined together to form a square again. The material deformed by successive application of the

baker's map is efficiently mixed in the following sense. Assume two regions A and B in the square domain, while only the material in A is transported by the baker's map to positions A' by multiple application of the map. Let N be a number of mappings such that for $n > N$ mappings some material of A is in region B, i.e., $A' \cap B \neq \emptyset$. If this is true for almost all regions A, B except some regions of measure zero, then the map is *strongly measure-theoretic* mixing the material [159].

In continuous deformation of material, or fluid in particular, no discrete cutting and joining is possible. If the second step of the baker's map is substituted by folding the two parts together, we obtain the famous horse shoe map, which is a building block of chaotic mixing (Fig. 1.1b). The horse shoe map looses material and other material entrains from the outside into the square domain, so it models an open flow. It is interesting to note that a invariant set of points never leaves the domain [158]. A typical characteristics of fluid mixing is that the constant stretching and folding of material leads to a fast reduction of length scales of any structure in the initial domain, as every initial region is stretched to a increasingly thin filament.

1.1.2 Steady Two-Dimensional Flow

As we have seen, mixing is basically an irregular rearrangement of material. We shortly argue here that mixing *does not* happen in a steady two-dimensional flow, following [142]. An incompressible two-dimensional velocity field $\mathbf{v}(\mathbf{x})$ can be written as derivatives of a scalar stream function $\Psi(x, y)$,

$$v_x(x, y) = -\frac{\partial \Psi}{\partial y} \qquad v_y(x, y) = \frac{\partial \Psi}{\partial x}, \tag{1.1}$$

such that the incompressibility condition is automatically satisfied. This formulation is equivalent to an autonomous dynamical system with one degree of freedom, where Ψ is the Hamiltonian. One can think of a mechanical system with a single point mass with constant energy. Such systems are integrable, and in such flows trajectories move along streamlines which are lines of constant level of the stream function. Trajectories cannot cross the streamlines that are either closed or end at two points on the border of the flow domain. Each streamline is a transport barrier and separates the flow domain into two regions which cannot exchange fluid. Therefore, no mixing can occur. In the elliptic regions, where trajectories move on closed orbits, a small perturbation of an initial condition grows linearly in time, and so does the length of a material line. In hyperbolic regions, close to saddle points of the stream function, a perturbation indeed grows exponentially fast, and fluid is separated and merged. However, this only happens at isolated points and does not lead to global mixing of the fluid [142].

1.1.3 Unsteady Two-Dimensional Flow

In the baker's map and in the horseshoe map in Sec. 1.1.1, we have seen that discrete stretching and folding generates an effective mixing process. The main

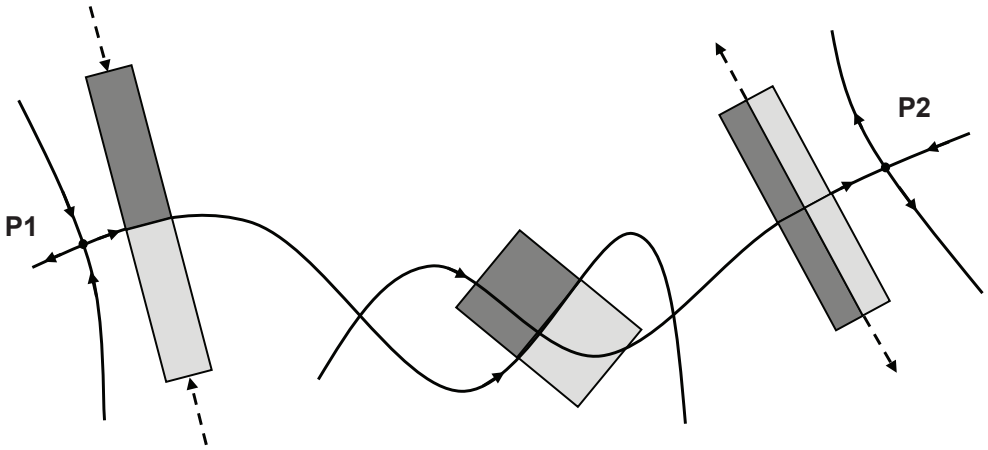

Figure 1.2: Sketch of a heteroclinic tangle of the stable and unstable manifolds of adjacent hyperbolic points $P1$ and $P2$ in a time-dependent flow. Modified from [226].

question is how this mechanism is realized in continuous flows. A time-dependent two-dimensional flow can still be written with a stream function as in (1.1), but instantaneous streamlines are not longer transport barriers. Now, instead, stable and unstable manifolds of hyperbolic points play a decisive role in organizing the fluid transport. Stable manifolds are the set of points that get infinitesimal close to a hyperbolic point in forward time $t \to \infty$, and unstable manifolds are the set of points that get infinitesimal close to a hyperbolic point in backward time $t \to -\infty$ [e.g., 8, 226]. These lines are transport barriers, since they consist of fluid particles that move with the flow. The stable and unstable manifolds of nearby hyperbolic points can intersect, forming a heteroclinic tangle, which is shown in Fig. 1.2. In this tangle between the two hyperbolic points the merging, stretching, folding and separating of fluid happens, that leads to efficient mixing. If we first look at point $P1$, two fluid patches on either sides of the unstable manifold merge. Due to the time dependence of the flow, the unstable manifold of $P1$ intersects with the stable manifold of $P2$ such that lobes are formed that enclose fluid. These lobes are crucial for the exchange of fluid between different regions in the time-dependent flow. Their dynamics is described by lobe dynamics theory [226]. Due to the lobes, the fluid coming from $P1$ finds its way to both sides of the stable manifold of $P2$ that defines the line of future separation at point $P2$. In other words, in the heteroclinic tangle, fluid that has merged at $P1$ is chopped in to different patches. These patches will separate at the next hyperbolic point $P2$. This basically is the process that merges initially distant parts of the fluid and separates initially close parts of the fluid. In the course of this work we will be especially interested in the location of the stable and unstable manifolds that can be estimated with methods presented in Chap. 2.

1.2 Transport Processes

In principle, the motion of a fluid could be described by the time-dependent velocities, or equally, by the trajectories of each individual molecule. However, this is not feasible and most fluid flows of interest are macroscopic and have length scales much larger than the molecular scale. Therefore, the fluid is described as a continuum. In this continuum, two conceptually different basic processes are practical to describe transport. In the following, we give a short definition of the basic two transport mechanisms, diffusion and advection. An overview over the topic of transport and mixing in fluids is given in the references [43, 142, 159, 224, 227].

1.2.1 Diffusion

Diffusion is a transport process that is induced by random motion, or more specifically, motion that can be described by statistical means. Molecular diffusion is the typical case, where the thermal Brownian motion of molecules or atoms is in principle deterministic, but due to the large number of collisions involved it can be described as a stochastic random walk. The direction and magnitude of displacements of molecules are then stochastic variables and obey certain probability distributions. In absence of a concentration gradient in the medium there is no net flux, as diffusive transport in one direction is exactly balanced by transport in the opposite direction. This changes if a concentration is not homogeneously distributed. The diffusive flux $\mathbf{J_D}$ from regions of high concentrations to low concentrations driven by random movements is described by Fick's first law

$$\mathbf{J_D} = -D\,\nabla C, \tag{1.2}$$

where ∇C is the concentration gradient and D is the molecular diffusion coefficient that depends linearly on temperature. Assuming a continuity equation for the concentration without source terms on the right hand side

$$\frac{\partial C}{\partial t} + \nabla \cdot \mathbf{J_D} = 0 \tag{1.3}$$

and a constant, isotropic, homogeneous diffusion coefficient D, we get Fick's second law, the diffusion equation

$$\frac{\partial C}{\partial t} = D\,\nabla^2 C. \tag{1.4}$$

It simply states that under a diffusive process the concentration increases at positive curvature of the concentration field (valleys) and decreases at negative curvature of the concentration field (mountains). Thus, the diffusion tends to equilibrate concentration differences and finally leads to a constant concentration, which is the most probable state of distribution. Transport by molecular diffusion is very slow for ambient temperature. The diffusion coefficient in water has a magnitude of $D \approx 10^{-9}\mathrm{m}^2\mathrm{s}^{-1}$, which means that diffusive transport over a length of $1\,\mathrm{mm}$ takes about $10^3\,\mathrm{s}$.

Diffusion is directly related to an uncorrelated random walk model, where subsequent steps of a particle are random in direction. As a consequence of the central limit theorem the variance of the displacement of a particle carrying out such a random walk grows as

$$\langle \mathbf{x}^2 \rangle \propto 2dDt \tag{1.5}$$

where d is the dimension of the random walk. When the variance grows linearly with time, these stochastic transport processes are referred to as normal diffusion. Anomalous diffusion is characterized by $\langle \mathbf{x}^2 \rangle \propto t^\gamma$, with $\gamma \neq 1$. Superdiffusion with $1 < \gamma < 2$ occurs in flows with long range correlations, e.g., jets and vortices, and subdiffusion with $\gamma < 1$ occurs in flows including regions where fluid can be trapped for very long times.

Instead of microscopic molecular Brownian motion, we can also think of macroscopic small scale irregular fluid motion that induces stochastic displacements of fluid parcels. These fluid parcels consist of a large number of fluid molecules. Although this motion is smooth and continuous in principle, it can be described by a random walk on time scales where the motion of fluid parcels become uncorrelated, $t \gg T_L$. Thus, for long times, the motion of a particle in a sufficiently irregular flow can be statistically described by the variance of the displacement satisfying

$$\langle \mathbf{x}^2 \rangle \simeq \langle v^2 \rangle T_L t. \tag{1.6}$$

$\langle v^2 \rangle$ is the variance of the velocity in the flow. This diffusive transport is named turbulent diffusion [70, 97, 205]. Fick's laws (Eq. 1.2, 1.4) can be applied, where the molecular diffusion coefficient D must be replaced by an effective turbulent diffusivity, D_t, that is typically many orders of magnitude higher than the molecular diffusion. As stated above, typical molecular diffusion coefficients are $D \approx 10^{-9}\,\mathrm{m^2 s^{-1}}$ whereas turbulent diffusion coefficients obtained from Lagrangian experiments in the ocean can be as high as $D_t \approx 10^{2}\,\mathrm{m^2 s^{-1}}$ at length scales of $100\,\mathrm{km}$ [149]. Turbulent diffusion is also referred to as eddy diffusion, corresponding to the image of turbulence as a conglomerate of interacting vortices or eddies that lead to random-walk-like trajectories in the fluid.

1.2.2 Advection

While diffusion is a statistical description of irregular motion, advection is the deterministic motion given by a velocity field. Let $C(\mathbf{x}, t)$ be the concentration field of a passive conservative tracer, i.e., a tracer which does not change the fluid flow (passive), does not have sinks nor sources, and does not react or decay (conservative). Then, the concentration field evolves under a flow as

$$\frac{\partial}{\partial t} C(\mathbf{x}, t) = -\mathbf{v} \nabla C(\mathbf{x}, t) \tag{1.7}$$

The motion of fluid can be described in two different reference systems: the Lagrangian frame and the Eulerian frame. In the Lagrangian frame we fix our coordinate system to the moving fluid parcels and evaluate the processes that act

on a infinitesimal fluid parcel to obtain differential equations for its behavior. The term *Lagrangian* is also often used more generally to refer to methods that are explicitly based on trajectories. In the Eulerian frame, we use a Cartesian coordinate system fixed in space, which is more convenient for the representation of fields. Differential equations in both frames are related by the material derivative

$$\frac{D}{Dt} = \frac{\partial}{\partial t} + \mathbf{v}\nabla. \tag{1.8}$$

It states that a rate of change of a property in the Lagrangian frame D/Dt translates to two terms in the Eulerian frame. At a fixed point in space, a field changes due to inherent rates of change $\partial/\partial t$, and because the field is advected over the fixed point, represented by the term $\mathbf{v}\nabla$. In the Lagrangian frame the advection equation (1.7) for a conserved tracer is simply

$$\frac{D}{Dt}C = 0 \tag{1.9}$$

expressing that the concentration in a fluid parcel is constant in time.

Flow measurements are possible in both, the Eulerian and Lagrangian frame. At first, the flow measurement at fixed points seems more natural, since measurement devices can be installed in one place and deliver velocity data at a well defined position (e.g., a mooring fixed at the seas floor with an Acoustic Doppler Current Profiler (ADCP), in the oceanographic context). However, this is often a very sparse sampling of the velocity field and only a good estimate of transport, if the flow is uniform over a large area or volume. If this is not the case, and instead the flow is highly irregular, Lagrangian measurements with drifting particles can give a much better insight into transport. Of course, Lagrangian measurements rely on an accurate positioning system for the Lagrangian particles. For this purpose, drifters on the sea surface can use the Global Positioning System (GPS). In the laboratory, the position of particles can be obtained using imaging techniques.

1.2.3 Advection and Diffusion

In all real fluid flows both processes, advection and diffusion, are present, and the interaction of both can lead to very efficient mixing. Eckart's [55] three phases of the homogenization of milk and coffee in a cup under stirring is a graphic example for this process [230]. In the first phase, only few circular patches of milk exist. The concentration gradient across the contact surface of milk and coffee is high, but the surface itself is small. In large parts of the fluid, the concentration is homogeneous and the gradient is zero. In the second phase, stirring by chaotic advection stretches and folds the initial patches of milk, which leads to an exponential increase of contact surface with very high gradients. Finally, in the third phase, molecular diffusion acts on the high gradients that are distributed over the whole fluid and homogenizes the mixture.

In the flows that we consider in this work, molecular diffusion plays a neglegible role for transport. This can be quantified by the Péclet number, the ratio of a diffusive time scale and an advective time scale of the flow on a length scale L.

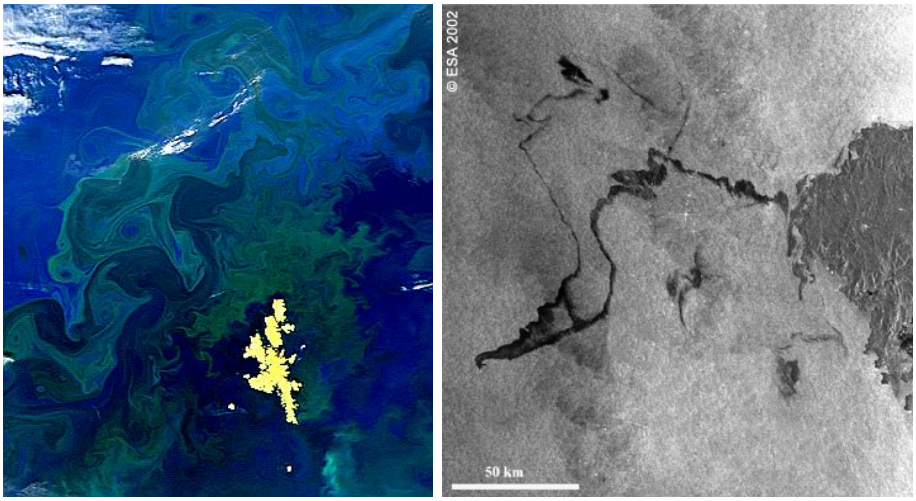

Figure 1.3: Lagrangian transport patterns. (left) Plankton bloom in the ocean off the Shetland Islands [2]. (right) Oil spill emerging from the oil tanker *Prestige* off the coast of Galicia, NW Spain, 2002 [1].

The Péclet number $Pe = UL/D$, with the velocity U and the diffusion constant D, is typically very large (remember: $D \sim 10^{-9}\,\mathrm{m^2 s^{-1}}$), indicating that diffusion at ambient temperature is a very slow process. However, turbulent diffusion can be an important contribution to transport.

For a continuous tracer, turbulent diffusion can be described with Eq. 1.4. However, for discrete particles, a different description is used. Lagrangian Stochastic Models (LSM) generate trajectories in a given advective flow, where the subgrid motion that is not resolved in the velocity field is modeled as a stochastic process. These models reproduce the statistical properties of real trajectories. LSM are widely used in the oceanographic community to study transport in ocean currents, and in particular to model drifter trajectories of ocean drifters [57, 75]. The particles are advected with a velocity that has a deterministic and a stochastic component. The simplest realization of such a model is a LSM of order 0, where the stochastic component is totally uncorrelated and no correlation time is involved [178]. A particle trajectory is then given by

$$\frac{d}{dt}\mathbf{x}(t) = \mathbf{v}(\mathbf{x}, t) + \sqrt{2D_t}\frac{\mathbf{dw}}{dt} \tag{1.10}$$

where $\mathbf{dw}$ is a random increment from a normal distribution with zero mean and a variance $2\,dt$. At each time step a random displacement is added to the position of the particle, such that the particles diffuse with a diffusion coefficient D_t.

1.3 Advective Transport in the Ocean

The description of dispersion of particles or continuous tracers, in terms of turbulent diffusion, as well as the Lagrangian stochastic models are statistical ap-

proaches that do not contain information about single specific trajectories. However, advection is deterministic and determines the motion of the fluid, and in many applications the specific trajectories do matter. In this work, we want to focus on the deterministic motion of water masses in the very detail, and ask how they separate and merge, how they are stretched and folded. Many practical transport problems of interest are affected by this chaotic motion of fluid and have short time scales of the order of some eddy turnover times. For example, in the case of an oil spill we are interested in its exact evolution for the following days and weeks rather than its overall mean advance as determined by the stochastic approach. If a container is lost from a ship, we want to know where it has drifted to over the last hours. Advection is the dominant process in these cases. It is therefore an appropriate approach to address the deterministic motion of objects or tracers in the ocean. Fig. 1.3 shows typical Lagrangian patterns in continuous tracers generated by advection in irregular ocean currents. The emerging patterns can be understood and predicted by analyzing the irregular advective transport as we will see in the following chapters.

Such studies have become more feasible nowadays, since numerical ocean models, satellite measurements, and high-frequency radar systems provide complete spatio-temporal velocity data sets that cover wide areas of the ocean. This allows for a detailed analysis of advective transport in these velocity fields. Even if the unresolved part of the flow is neglected, the obtained flow patterns are most relevant for transport. In particular, methods from dynamical systems theory have proved to be very useful to address finite time transport in such flows. In this approach the advective flow is regarded as a dynamical system, and transport is studied with tools that were originally developed to analyze the phase space of dynamical systems [227]. These methods are closely related to the notion of Lagrangian coherent structures (LCS), a term widely used in literature for those flow structures that control mixing [83]. We define LCS in the next chapter in more detail.

LCS have been used extensively to understand the Lagrangian transport in a variety of applications in geophysical flows ranging from the study of plankton dynamics to waste water treatment. We shortly review some of these studies, where LCS define the patterns of short time non-asymptotic mixing. The most direct way to verify the location of LCS derived from a modeled or measured flow field is to compare the LCS with trajectories of real surface drifters. Haza et al. [86] compute LCS from a model flow in the Adriatic Sea and demonstrate that drifters launched into a hyperbolic region are guided by the hyperbolic manifolds represented by the LCS. In a similar setting, but with flow data from a HF radar system, they also find a good agreement between the trajectories of surface drifters and the LCS in the flow [87]. Also Shadden et al. [191] perform drifter experiments in Monterey Bay, California, where surface drifter trajectories are in agreement with LCS from HF radar data.

A plankton bloom is an event where phytoplankton rapidly grows in limited regions of the ocean. The chlorophyll concentration is not strictly a passive tracer, since a biological reaction is involved (Chap. 4), but it turns out that advection often dominates the patterns appearing in these plankton blooms (cf. Fig.1.3).

Olascoaga et al. [153] hypothesized that a transport barrier on the West Florida Shelf, characterized as an LCS, provide favorable conditions for Harmful Algae Blooms (HAB) and they employ simulated LCS to trace back possible early locations of these blooms. Toner et al. [208] showed that plankton blooms in the Gulf of Mexico propagate in directions that agree with the LCS computed from a data-assimilating hydrodynamic model. Lehahn et al. [100] reported that patterns in plankton blooms in satellite sea color images are dominated by horizontal mesoscale stirring. They showed statistical evidence that LCS align with the contour lines of chlorophyll concentration. Coulliette et al. [41] and Lekien et al. [103] use LCS calculated from high-frequency radar velocity data in coastal areas to develop release strategies for waste water, in order to prevent damage to the sensitive coastal ecosystems. In this work we will extensively make use of the LCS approach to analyze transport in ocean currents on different scales.

1.4 Objective of the Study

In this thesis we study several spatio-temporal transport problems in two-dimensional time-dependent fluid flows that generate chaotic advection. We aim to clarify the role of advective transport for passive and also for reactive tracers. Therefore, we want to characterize transport in these flows in the very detail with the concept of Lagrangian coherent structures (LCS) that reveal the geometry of irregular fluid motion, and especially emphasize lines of separation and merging of fluid patches. We further want to examine the relevance of LCS to reactive tracers. The focus is set on the application of the LCS concept to several experimental or numerical flow fields where we unveil the geometry of fluid mixing to gain insight into dynamics of spatio-temporal tracer patterns.

Chapter 2

Chaotic Transport and Coherent Structures in Unsteady Flows

Abstract

The terms *chaotic advection* or *Lagrangian chaos* generally refer to the phenomenon that particle trajectories or tracer patterns being transported in an unsteady flow exhibit strong irregularities in time and space. In these flows, adjacent regions of the flow can have totally different fluid properties and the permanent separating and merging of different parts of the fluid leads to strong mixing. In this chapter, we introduce the phenomenon of chaotic advection and show methods from dynamical systems theory that allow to determine the geometry of mixing in chaotic flows, namely Lagrangian Coherent Structures (LCS) and Synoptic Lagrangian Maps (SLM).

2.1 Chaotic Advection

The term *chaotic advection* was introduced in a seminal paper by Aref [10] where he numerically studies the mixing of particles in a flow induced by two point vortices. The flow is very regular, as it consists solely of a rotational motion, and transport seems to be predictable. However, when the action of the vortices is alternately switched on and off (blinking vortex), particles in the flow undergo chaotic trajectories and mixing is significantly enhanced. Generally, *chaotic advection* refers to irregular motion of particle trajectories in a simple (even laminar) deterministic time-dependent flow that is given by an advective velocity field. In two dimensions, a simple time dependence can lead to chaotic mixing of the fluid. In three dimensions, even steady flows can be chaotic. Since the paper by Aref, a large number of studies has applied ideas from dynamical systems to the problem of mixing in fluids [11, 12, 159, 168]. Here, we are especially interested in the geometry of mixing, i.e., the spatial distribution of fluid volumes that are continuously merged and separated by the flow.

In order to unveil the geometry of mixing in time-dependent fluid flows we take the Lagrangian approach and analyze trajectories of infinitesimal fluid parcels. We represent these fluid parcels by point particles in the fluid. Their trajectories are

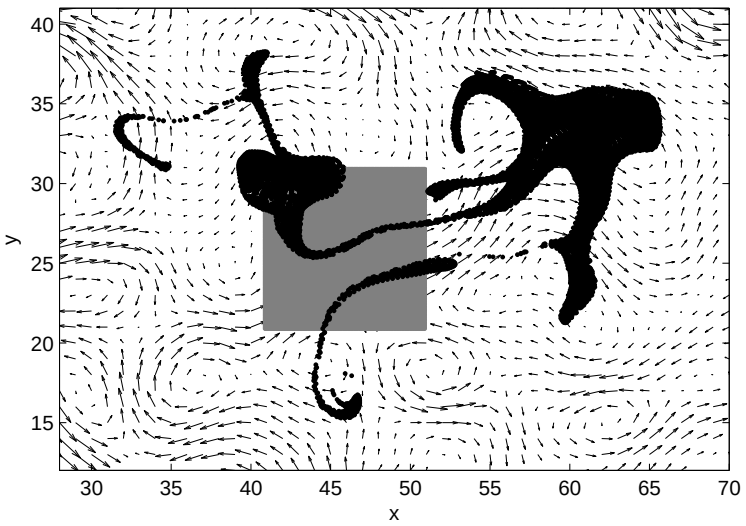

Figure 2.1: Typical pattern of a patch of fluid particles after advection in a chaotic flow for a finite time τ. Particle positions at a time $t = t_0 + \tau$ (black) depend critically on the initial position (gray) at $t = t_0$. The instantaneous velocity field $\mathbf{v}(\mathbf{x}, t = t_0)$ plotted in the background is given by geostrophic ocean currents in the South Indian Ocean.

solutions of the dynamical system

$$\dot{\mathbf{x}}(t) = \mathbf{v}(\mathbf{x}, t). \tag{2.1}$$

We assume that the velocity field $\mathbf{v}(\mathbf{x}, t)$ is known, obtained from experimental measurements, from a numerical hydrodynamic model solving the governing equations for fluid motion, or from an analytical kinematic model flow. Thus, the velocity field is given as a data set in a fixed Eulerian frame and we obtain particle trajectories by integrating Eq. (2.1). The dynamical system is numerically solved using a simple 4th order Runge-Kutta scheme and a cubic interpolation in time and space. A trajectory that starts from the initial condition $\mathbf{x}_0$ at time t_0 and evolves to its position at time t is denoted by $\mathbf{x}(\mathbf{x}_0, t_0, t)$. In this work, we focus on two-dimensional flows, although most concepts can equally be applied to three-dimensional flows.

In a chaotic flow the trajectories of fluid parcels depend highly on the initial conditions $(\mathbf{x}_0, t_0)$, i.e., the time and location where they are released. Therefore, initially close trajectories may rapidly diverge. Typically, the distance between both trajectories grows exponentially in chaotic flows and small patches of fluid are stretched to long filaments that are rolled up around vortices. Fig. 2.1 shows a typical pattern of a patch of particles in a chaotic time-dependent velocity field. We can observe that the positions of the particles at time $t = t_0 + \tau$ depend critically on the initial position of the trajectories.

The mixing patterns appearing in chaotic flows are solely determined by the dynamical system (2.1) that governs the advection. The patterns can be extracted from the trajectories that solve (2.1) by applying methods of dynamical systems

theory. In particular, dynamical system theory deals with the analysis of the phase space which is the space of the dynamic variables of the system. Here, the phase space is the real space in two dimensions (x, y). The topology of the phase space determines the dynamics of the trajectories, i.e., it controls in which direction fluid can flow. We seek to separate regions of different dynamics in the fluid by analyzing the portrait of the phase space of the flow.

In the following, we shortly mention the Okubo-Weiss parameter, a quantity often used to identify flow structures in Eulerian instantaneous velocity fields. Then, we choose a simple steady flow to introduce the basic dynamical systems concept of a hyperbolic fix point and its stable and unstable manifolds. We shortly present how these manifolds can be estimated also in unsteady flows for a finite time, and we give the definition of the finite-time Lyapunov exponent which is used throughout this work to extract the manifolds. We present the similar finite-size Lyapunov exponent in a short paragraph and give an outlook on the very recent development of a new theory to extract transport barriers from time-dependent flows. Finally, we introduce the Lagrangian method of Synoptic Lagrangian Maps (SLM).

2.2 Eulerian coherent structures

Looking at velocity data of a flow from measurements or a numeric simulation, it is tempting to draw quick conclusions about transport based on the instantaneous velocity field. In the best-case scenario, the time dependence of the flow is weak, and the topology of the velocity field is indicative of the geometry of transport. In this case, quantities derived from Eulerian velocity fields may give a rough sketch of how the fluid moves in space. However, in general, in particular for a strong time dependence of the flow, the conclusions drawn from the analysis of instantaneous velocity fields are incorrect and do not represent the trajectories of fluid parcels in the flow. For the sake of completeness, here we shortly present the Okubo-Weiss parameter, a quantity that is often used to separate rotational flow regions from flow regions where stretching dominates.

2.2.1 Okubo-Weiss parameter

The Okubo-Weiss parameter [24, 148, 223] is based on the gradient tensor of the velocity field

$$\nabla \mathbf{v}(\mathbf{x}) = \begin{pmatrix} \partial_x v_x & \partial_y v_x \\ \partial_x v_y & \partial_y v_y \end{pmatrix}. \tag{2.2}$$

with its eigenvalues

$$\lambda_{\pm} = \frac{1}{2}(\partial_x v_x + \partial_y v_y) \pm \left[\frac{1}{4}(\partial_x v_x - \partial_y v_y)^2 + (\partial_x v_y)(\partial_y v_x)\right]^{\frac{1}{2}}. \tag{2.3}$$

Introducing the differential properties of the velocity field

$$\begin{aligned}
&\text{divergence} && \nabla \cdot \mathbf{v} = \partial_x v_x + \partial_y v_y && (2.4)\\
&\text{normal strain rate} && s_n = \partial_x v_x - \partial_y v_y && (2.5)\\
&\text{shear strain rate} && s_s = \partial_x v_y + \partial_y v_x && (2.6)\\
&\text{vorticity} && \omega = \partial_x v_y - \partial_y v_x && (2.7)
\end{aligned}$$

the eigenvalues can be written as

$$2\lambda_{\pm} = \nabla \cdot \mathbf{v} \pm \left[s_n^2 + s_s^2 - \omega^2\right]^{\frac{1}{2}}. \tag{2.8}$$

For an incompressible flow, i.e. $\nabla \cdot \mathbf{v} = 0$, we get

$$2\lambda_{\pm} = \pm \left[s_n^2 + s_s^2 - \omega^2\right]^{\frac{1}{2}}. \tag{2.9}$$

The sign of the Okubo-Weiss parameter $OW = s_n^2 + s_s^2 - \omega^2$ determines whether the eigenvalues are real or imaginary. For $OW > 0$ we have real eigenvalues corresponding to exponential stretching in a hyperbolic region of the flow. For $OW < 0$ the eigenvalues are imaginary, corresponding to a rotational movement in an elliptic region of the flow. Although being only a vague indicator for structures in time-dependent flows, the Okubo-Weiss parameter is widely used in oceanography to separate strain-dominated regions from vorticity-dominated regions, in particular, to identify mesoscale eddies [20, 37].

2.3 Lagrangian Coherent Structures (LCS)

We seek to extract flow structures that order fluid trajectories in a time-dependent flow. In the (geophysical) fluid dynamics community these structures are referred to as Lagrangian coherent structures or LCS [163]. According to Haller [80], Lagrangian coherent structures are: (1) Organizing centers for Lagrangian patterns, (2) they are material lines, implying that they are transport barriers, and (3) they locally exhibit the strongest attraction, repulsion or shearing in the flow. LCS associated with hyperbolic trajectories are directly related to the concept of stable and unstable manifolds of hyperbolic fix points. We therefore introduce this concept and explain in the following, how LCS can be estimated from finite-time stretching fields of the fluid.

2.3.1 Stable and Unstable Manifolds in a Steady Linear Strain Flow

Here we illustrate the basic concept of hyperbolic fix points and stable and unstable manifolds and their role in structuring the phase space of a simple two-dimensional dynamical system [8, 115, 158, 225]. We consider a simple linear strain flow (Fig, 2.2) that defines a time-independent or autonomous dynamical system [28, 185]

$$\dot{\mathbf{x}}(t) = \mathbf{v}(\mathbf{x}) = a \begin{pmatrix} -x \\ y \end{pmatrix} \tag{2.10}$$

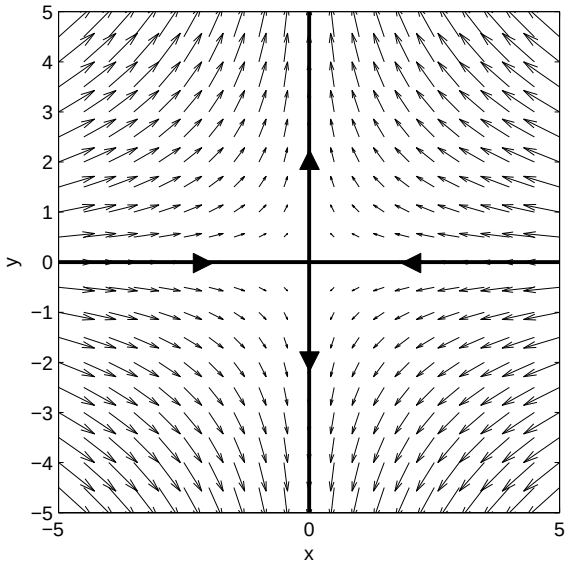

Figure 2.2: Linear strain flow defining a dynamical system with a hyperbolic fixed point $\mathbf{x_f} = (0,0)$. The x-axis and y-axis are the stable and unstable invariant manifolds of the hyperbolic fix point. Fluid parcels in each quadrant are confined to the respective quadrant by the hyperbolic manifolds.

where a is the strain amplitude. This flow field has a hyperbolic fix point $\mathbf{x_f} = (0,0)$ satisfying $\mathbf{v}(\mathbf{x_f}) = 0$. A small perturbation $\delta\mathbf{x}(t)$ to this fix point evolves as

$$\begin{aligned} \dot{\delta\mathbf{x}}(t) &= \mathbf{v}(\mathbf{x_f} + \delta\mathbf{x}) - \mathbf{v}(\mathbf{x_f}) && (2.11)\\ &\approx \mathbf{v}(\mathbf{x_f}) + \nabla\mathbf{v}(\mathbf{x_f})\delta\mathbf{x} - \mathbf{v}(\mathbf{x_f}) && (2.12)\\ &= \nabla\mathbf{v}(\mathbf{x_f})\delta\mathbf{x}. && (2.13) \end{aligned}$$

where the gradient matrix of the velocity field is

$$\nabla\mathbf{v}(\mathbf{x_f}) = \begin{pmatrix} \partial_x v_x & \partial_y v_x \\ \partial_x v_y & \partial_y v_y \end{pmatrix} = a \begin{pmatrix} -1 & 0 \\ 0 & 1 \end{pmatrix}. \quad (2.14)$$

Hence, the perturbation is stretched exponentially in time as given by the eigenvalues of $\nabla\mathbf{v}$ as

$$\begin{pmatrix} \delta x(t) \\ \delta y(t) \end{pmatrix} = \begin{pmatrix} e^{-at}\delta x_0 \\ e^{+at}\delta y_0 \end{pmatrix}. \quad (2.15)$$

The stable and unstable directions of the hyperbolic fix point are aligned with the x-direction and y-direction respectively. All points on the x-axis asymptotically converge to the fix point while they always stay on the x-axis. Therefore, the x-axis is the stable invariant manifold of the hyperbolic point $\mathbf{x_f}$. In contrast, all points on the y-axis asymptotically diverge away from the fix point while they

always stay on the y-axis. This characterizes the y-axis as the unstable invariant manifold. These stable and unstable manifolds separate regions in the phase space with different dynamics. As they are material lines, i.e., they consist of fluid particles, they cannot be crossed by fluid and act as transport barrier. In this case of an autonomous system, they completely separate the fluid into four regions that do not exchange fluid. However, we will see that in a time dependent flow, fluid exchange between separated regions is possible. The stable and unstable manifolds determine the geometry of this exchange and are therefore of high interest to obtain the geometry of mixing in the fluid.

2.3.2 LCS in Unsteady Flows

As seen in the previous section, stable and unstable manifolds of hyperbolic fix points are asymptotic concepts, i.e., they are defined for infinite time for a steady or a periodic flow. However, in many flows, e.g., in geophysical flows in the atmosphere or in the ocean, or in technical flows in chemical engineering, we are interested in chaotic transport on relatively short time scales, while the asymptotic mixing is irrelevant. Therefore, in the last two decades many theoretical and applied studies presented different definitions of stable and unstable manifolds for a finite time [83, 99, 115, 190, 227]. The analysis of finite-time stable and unstable manifolds is a powerful tool to extract mixing patterns in these flows.

It turns out that in many practical applications the manifolds can be estimated as lines of maximal stretching in the flow. Two trajectories on either side of a stable manifold separate much faster than two trajectories on the same side. If we compute the exponential separation rate of nearby trajectories in the flow we therefore expect the stable manifold to appear as a line of high stretching values. Similarly, on unstable manifolds, nearby trajectories separate exponentially fast if the flow is integrated backward in time. Hence, the stretching of a small fluid blob, or equally the separation rate of nearby trajectories, can be used to estimate the positions of stable and unstable manifolds in unsteady flows. Here, in order to quantify the stretching, we use a finite-time version of the Lyapunov exponent (FTLE) and identify Lagrangian coherent structures as ridges in the FTLE field, as in other studies [163, 189].

2.3.3 Finite-Time Lyapunov Exponent (FTLE)

The Lyapunov exponent is a classical measure to quantify the sensibility of a dynamical system to initial conditions [8, 16, 158]. A simple definition is

$$\lambda = \lim_{t\to\infty} \lim_{d(0)\to 0} \frac{1}{t} \ln \frac{d(t)}{d(0)}. \tag{2.16}$$

where $d(0)$ is the initial perturbation to a trajectory and $d(t)$ is the grown perturbation at time t. The orientation of the initial perturbation rapidly aligns with the direction of maximum stretching. In chaotic flows initially close trajectories separate exponentially fast, such that a positive Lyapunov exponent indicates chaotic behavior, while in regular flows the Lyapunov exponent is zero.

The Lyapunov exponent (2.16) is an asymptotic measure. In order to quantify the stretching of fluid parcels during a finite time, the Lyapunov exponent is modified to a finite-time version, the finite-time Lyapunov exponent (FTLE)

$$\lambda(t_0, \tau) = \frac{1}{\tau} \ln \frac{d(t_0 + \tau)}{d(t_0)}. \tag{2.17}$$

It measures the average exponential separation rate of trajectories with an initial distance $d(t_0)$ over a time period τ, assuming that the distance grows as

$$d(t) = d(t_0)\, e^{\lambda t} \tag{2.18}$$

Equation (2.17) is a rather intuitive definition of the FTLE, in the following paragraph we give a definition related to the deformation of the fluid which is useful to compute fields of the FTLE in a flow [189].

FTLE computation from flow map As the FTLE is sensitive to initial conditions, we integrate trajectories in a velocity field starting from a grid of initial positions $\mathbf{x_0}(t_0)$ at time t_0. After the finite-time τ the trajectories reach the positions $\mathbf{x}(t_0 + \tau)$. The initial positions $\mathbf{x_0}$ can be mapped to the final positions $\mathbf{x}(t + \tau)$ by the operator $\Phi_{t_0}^{t_0+\tau}$, called the flow map, such that

$$\mathbf{x}(t_0 + \tau) = \Phi_{t_0}^{t_0+\tau} \left(\mathbf{x_0}(t_0)\right). \tag{2.19}$$

In linear approximation, an infinitesimal perturbation vector $\delta\mathbf{x_0}(t)$ to a trajectory starting at $\mathbf{x_0}$ is deformed by the flow as

$$\begin{aligned} \delta\mathbf{x}(t_0 + \tau) &\approx \nabla \left[\Phi_{t_0}^{t_0+\tau} (\mathbf{x_0})\right] \delta\mathbf{x_0}(t_0) && (2.20)\\ &= \nabla \left[\mathbf{x}(t_0 + \tau)\right] \delta\mathbf{x_0}(t_0) && (2.21)\\ &= F(\mathbf{x_0})\, \delta\mathbf{x_0}(t_0) && (2.22) \end{aligned}$$

Hence, we have to differentiate the final positions $\mathbf{x}(t_0 + \tau)$ with respect to $\mathbf{x_0}$ to obtain the deformation tensor (see Sec. B.2 for a simple numerical scheme)

$$F(\mathbf{x_0}) = \nabla \Phi_{t_0}^{t_0+\tau}(\mathbf{x_0}) = \nabla \left[\mathbf{x}(t_0 + \tau)\right] = \begin{bmatrix} \frac{\partial x}{\partial x_0} & \frac{\partial x}{\partial y_0} \\ \frac{\partial y}{\partial x_0} & \frac{\partial y}{\partial y_0} \end{bmatrix} \tag{2.23}$$

We are interested in the stretching of the perturbation vector. Its norm is given by the inner product

$$\begin{aligned} \|\delta\mathbf{x}(t_0 + \tau)\| &= \left\langle \delta\mathbf{x_0}, F(\mathbf{x_0})^T F(\mathbf{x_0})\, \delta\mathbf{x_0} \right\rangle^{\frac{1}{2}} && (2.24)\\ &= \left\langle \delta\mathbf{x_0}, \mathbf{C}(\mathbf{x_0})\, \delta\mathbf{x_0} \right\rangle^{\frac{1}{2}} && (2.25) \end{aligned}$$

with the right Cauchy-Green deformation tensor $C(\mathbf{x_0})$. By definition $C(\mathbf{x_0})$ is a symmetric tensor and has real eigenvalues. The factor of maximal stretching $S(\mathbf{x_0})$ of the length of the perturbation $\delta\mathbf{x_0}(t)$ under the flow map $\Phi_{t_0}^{t_0+\tau}$ is given by

$$S(\mathbf{x_0}) = \left[\max_{i=1,N} \lambda_i(C(\mathbf{x_0}))\right]^{\frac{1}{2}} \tag{2.26}$$

where λ_i are the eigenvalues of $C(\mathbf{x_0})$. Finally, the field of finite-time Lyapunov exponents (FTLE) depending on initial conditions $(\mathbf{x_0}, t_0)$ and on the finite integration time τ is then

$$\Lambda(\mathbf{x_0}, t_0, \tau) = \frac{1}{\tau} \ln S(\mathbf{x_0}). \tag{2.27}$$

We obtain the forward FTLE field by taking $\tau > 0$ and integrating the velocity forward in time, while for the backward FTLE field the negative velocity field is integrated backward in time with $\tau < 0$. The backward FTLE field is denoted by $\Lambda^-(\mathbf{x_0}, t_0, \tau)$ and the forward FTLE field is denoted by $\Lambda^+(\mathbf{x_0}, t_0, \tau)$. The forward FTLE field reveals the strong stretching along stable hyperbolic manifolds and the backward FTLE field reveals the unstable manifolds, where fluid converges in forward time.

Choice of the Finite Integration Time For the computation of FTLE fields the integration time τ must be predefined. Basically, the time τ has to be long enough to allow trajectories to explore the Lagrangian coherent structures present in the flow (see also discussion in Sec. 6.3). A typical time scale in the flow is the eddy turnover time, defined as $\tau_\epsilon = L/v$. L is a typical length scale in the flow, e.g., the diameter of the dominant vortices, and v is a typical magnitude of the velocity, which can be estimated as the root-mean-square velocity $v_{rms} = \sqrt{|\mathbf{v}^2|}$ (cf. Sec. 7.2.2). If we use a multiple of the eddy turnover time as an integration time, clear linear structures should appear in the FTLE field. Generally, a small increase of the integration time above typical time scales in the flow would generate new detailed structures in the FTLE field, but nevertheless the main structures in the FTLE field remain the same (cf. Fig. 7.6). However, for very long integration times, the FTLE field completely looses its spatial structure.

LCS as Ridges in the FTLE Field We extract LCS as ridges of high values in the FTLE fields as proposed by Shadden [189]. We therefore use a criterion based on the gradient and the curvature of the FTLE field which is described in Sec. B.1. High FTLE values indicate a strong separation of initially close particles. These high values are ordered on linear structures being estimates of finite-time stable and unstable manifolds of hyperbolic points. Fig. 2.3 shows an exemplary FTLE field for an oceanic mesoscale flow. To present backward and forward FTLE field in one image, we plot the forward FTLE field as positive values and the backward FTLE field as negative values [51]. In Fig. 2.3 we numerically demonstrate the significance of the stable and unstable manifolds for transport by releasing particles on either side of a ridge in the FTLE field. The particles separate rapidly, in backward time direction at the unstable manifold (Fig. 2.3a) and in forward time direction at the stable manifold (Fig. 2.3b). This means that the unstable manifolds mark the lines where different fluid bodies merge in forward time. Therefore, we expect tracer patterns in the flow to be bounded by the unstable manifolds (compare the mixing pattern of the chlorophyll concentration with respect to backward FTLE ridges in Fig.5.7a and the pattern of the chemical concentration

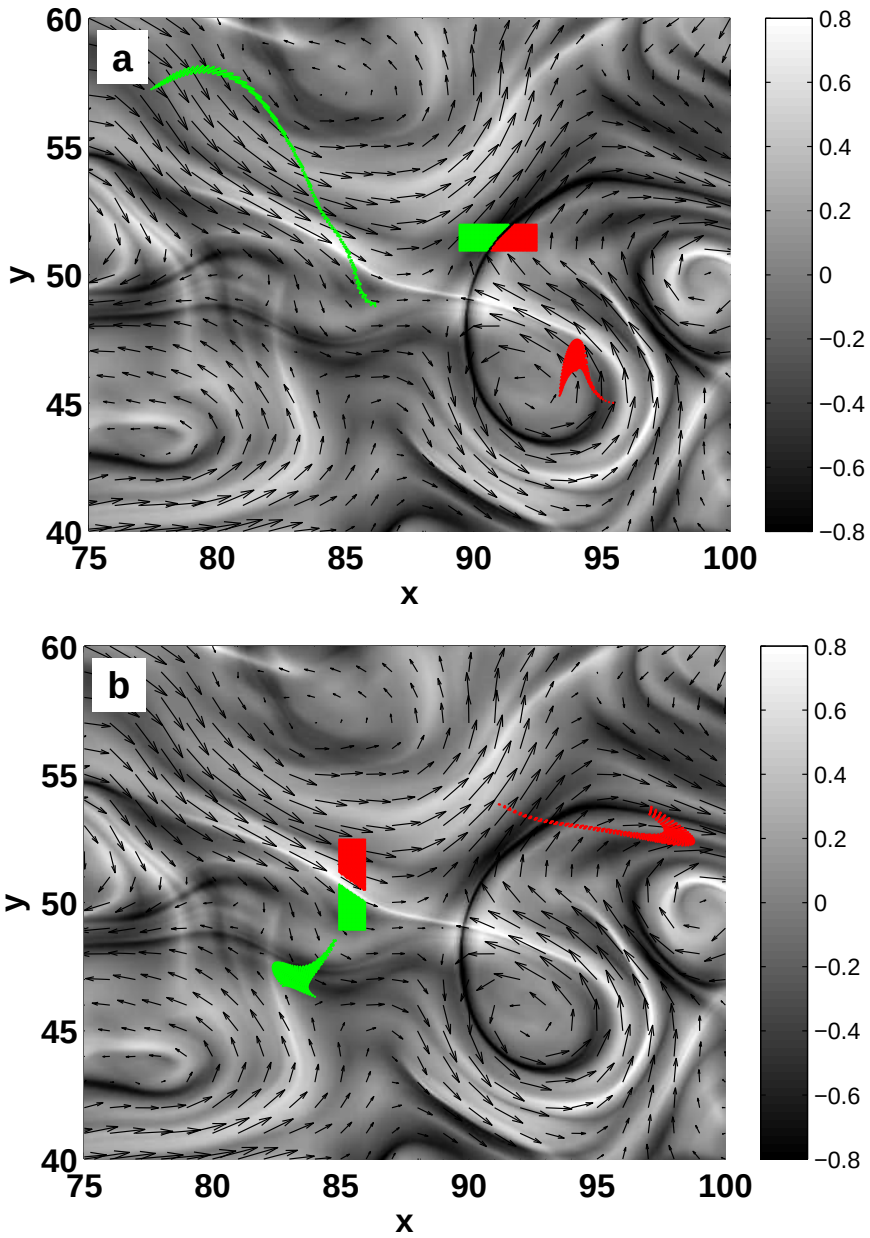

Figure 2.3: Flow region with finite-time hyperbolic point at about $(90, 50)$ and the instantaneous velocity field at $t = t_0$. The background field is the backward FTLE field subtracted from the forward FTLE field, $\Lambda^{\pm}(\mathbf{x_0}, t_o, \tau) = \Lambda^{+} - \Lambda^{-}$. (a) Ridges in dark tones mark the approximate position of unstable finite-time hyperbolic invariant manifolds in the flow. Particles positioned on different sides of a ridge at $t = t_0$ separate rapidly in backward time. Their final positions are plotted at $t = t_0 - \tau$. (b) Ridges in light tones approximate the stable finite-time hyperbolic invariant manifolds. Two groups of particles on either side of a ridge at $t = t_0$ separate in forward time. Their final positions are plotted at $t = t_0 + \tau$. The approximate stable and unstable manifolds intersect at the position of the finite-time hyperbolic point. Especially for the green particles in panel (b) it is evident that a prediction of transport based on the instantaneous velocity field is misleading.

in Fig. 7.10). The stable manifolds, instead, mark the lines where a compact fluid body is separated by the flow.

Limitations A critical question is if ridges of the FTLE field are material lines, i.e., if the flux across the ridge is zero. Shadden [189] derives an expression to quantify the flux and shows that it is small for many practical applications with a smooth flow. This means that FTLE ridges are almost *Lagrangian* and move with the flow very close to material lines, such that they are good estimates for transport barriers and fluid can barely cross them. However, it is important to note that this approach is only an approximation, and not an exact theory. There are simple analytic examples where either LCS cannot be identified as ridges in the FTLE field, or apparent ridges in the FTLE fields are not LCS or transport barriers [28, 79]. Indeed, the steady strain flow in Fig. 2.2 is an example for the first case. Obviously, there exist stable and unstable manifolds of the hyperbolic point, but the FTLE value is the same in the whole domain, such that the manifolds cannot be obtained from ridges in the FTLE field [28]. Furthermore, a common problem in FTLE fields are ridges induced by strong shear that are not manifolds associated to hyperbolic regions. Mathur et al. [123] propose a criterion to filter out these shear ridges.

2.3.4 Finite-size Lyapunov exponents (FSLE)

A similar definition of a non-asymptotic Lyapunov exponent is the finite-size Lyapunov exponent (FSLE). It is also used to extract mixing patterns in unsteady flows [14, 51, 87], but instead of fixing a finite time and evaluating the deformation of the fluid after that time, a finite length scale of typical flow structures d_f is predefined. In order to find LCS induced by mesoscale eddies, d'Ovidio et al. [51], for example, define $d_f = 110\,\text{km}$, the typical diameter of a mesoscale eddy. The trajectories in the velocity field are integrated, and when initially close trajectories have reached the predefined separation d_f, the time τ is measured. The FSLE is then computed as

$$\lambda(t_0, d_f) = \frac{1}{\tau} \ln\left(\frac{d_f}{d(t_0)}\right). \tag{2.28}$$

Typically, when the integration is stopped after a reasonable time, only a small part of the trajectory pairs have reached the predefined separation. The initial positions of the trajectories with the strongest separation rate are located on lines being estimates for the stable manifolds of the unsteady flow. The structure of these lines resembles the structure of ridges of the FTLE field. However, while for the FTLE a theory exists that measures the flux across the ridges and evaluates how close FTLE ridges are to material lines [189], such a theory is missing for the FSLE.

The FSLE was also proposed as a scale dependent dispersion measure [23]. The exponential separation rate λ of particle pairs in the flow is measured at the current length scale δ given by the actual distance between particles. The FSLE

is given by

$$\lambda(\delta) = \frac{1}{\langle \tau(\delta) \rangle} \ln r. \tag{2.29}$$

For the computation a small factor r close to unity is chosen, such that $\lambda(\delta)$ is independent of r. Although r is smaller than 2, it is often called the doubling factor. Many studies make the choice $r = \sqrt{2}$. For a particle pair with a distance δ the doubling time $\tau(\delta)$ is measured until the separation has grown by the factor r. Then, the average over a large number of particle pairs is taken. The slope of the function $\lambda(\delta)$ indicates different regimes of dispersion. If L is a typical correlation length of the flow, then

$$\lambda(\delta) = \begin{cases} \lambda & \delta \ll L \\ D\delta^{-2} & \delta \gg L \end{cases} \tag{2.30}$$

For very small separations the dispersion is exponential since the velocities of both particles are correlated, while for very large separations the velocities are not correlated and the dispersion is diffusive. Thus, the transition in the slope of $\lambda(\delta)$ tells us about the length scale of the largest structures in a flow. The FSLE is especially suitable to apply it to drifter data in the ocean to obtain information about the length scales present in the flow [97, 98, 169]. A particularly important question is if (small) submesoscale flow structures in the ocean significantly contribute to dispersion in the ocean [85] as suggested by measurements [110].

2.3.5 Other Approaches for LCS Detection

In order to characterize regions of different finite-time dynamics in a flow, several methods have been proposed that compute scalar quantities from properties of trajectories. The scalar fields change abruptly across stable or unstable manifolds which can be visualized by these methods. Rypina et al. [180] use two measures that quantify the complexity of trajectories, where the most complex trajectory is one that fills the whole domain, and the least complex trajectory is a stationary point. These measures are directly linked to the fractal dimension of the trajectory and are computed by a box-counting approach. Mendoza and Mancho [128] propose the arc length of finite-time trajectories as a scalar Lagrangian property that reveals the geometry of transport. In these fields, stable and unstable manifolds appear as thin lines of small values. Since this measure can be interpreted as the Lagrangian velocity averaged along the trajectory, it also serves to distinguish regions of fast trajectories (e.g., in jet cores) and slow trajectories (e.g., in eddy cores).

Very recently, Haller and Beron-Vera [81] published a new approach to find transport barriers in aperiodic two-dimensional flows. With this theory the transport barriers are obtained as tangential lines in a vector field derived from the Cauchy-Green deformation tensor (2.25). This is a big advantage over methods like the FTLE, where the approximate transport barriers have to be extracted as trenches or ridges in a scalar field. With the new theory it seems to be possible to extract very accurately hyperbolic transport barriers associated with hyperbolic

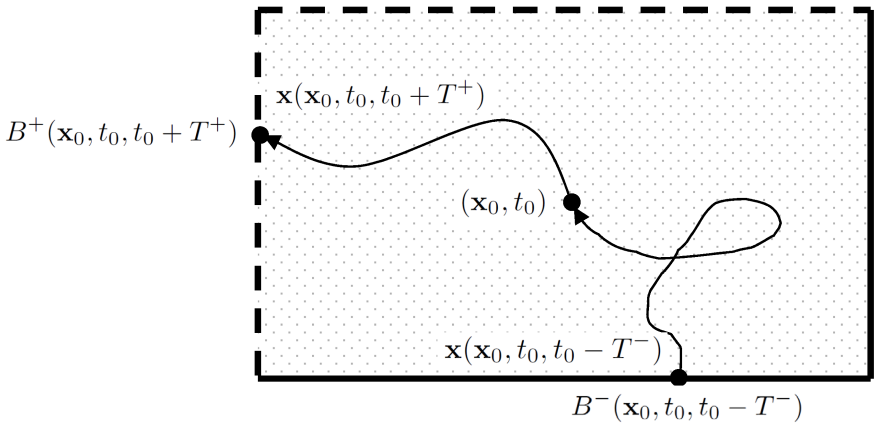

Figure 2.4: Synoptic Lagrangian Maps (SLM). Two different classes of boundaries (continuous and dashed line) define the rectangular flow domain. The entry time T^- and exit time T^+ is recorded for each trajectory with initial conditions $(\mathbf{x_0}, t_0)$ in the closed flow domain. B^- and B^+ denote the sections of the boundary where the trajectory enters and leaves the domain. The residence time is $T_R = T^+ + T^-$.

stable and unstable manifolds and elliptic transport barriers associated with lines of minimal stretching [82].

2.4 Synoptic Lagrangian Maps (SLM)

The approach of Synoptic Lagrangian Maps (SLM) was proposed by Lipphardt et al. [107]. It is closely related to the concept of exit times or escape times, that is widely used in the analysis of chaotic advection [142, 159]. SLM is a Lagrangian approach characterizing trajectories in chaotic coastal flows by their origin and fate, and by their residence time in a limited flow domain. The domain is predefined by a closed boundary line, which in parts typically corresponds to natural coastal boundaries. The boundaries can be open for the flow, e.g., at the mouth of an estuary to the shelf, or closed, e.g., at a beach, where fluid parcels simply run aground. Each trajectories has a point on the boundary where it enters the flow domain, and a point where it leaves the flow domain (Fig. 2.4). By dividing the boundary in a few meaningful classes, a trajectory can be associated to the class of border where it enters and leaves the domain. In the original paper, Lipphardt et al. [107] simply use the two boundary classes 'ocean' and 'coast' for their flow domain in Monterrey Bay, California.

The procedure to obtain a SLM is the following: The flow (2.1) is integrated forward and backward in time with initial conditions on a regular grid inside the flow domain. We chose a very long integration time until all particles have left the domain. For each trajectory two parameters are recorded: (1) the point on the boundary where the trajectory leaves the domain (these points are associated to a boundary class), and (2) the time period until the trajectory reaches the boundary. We allocate these values to the initial condition of the trajectory $\mathbf{x_0}$ and obtain

fields specifying the entry boundary $B^-(\mathbf{x}_0, t_0, t)$, the exit boundary $B^+(\mathbf{x}_0, t_0, t)$, the time since entry $T^-(\mathbf{x}_0, t_0, t)$, and the time until exit $T^+(\mathbf{x}_0, t_0, t)$ (see Fig. 2.4). The superscripts $+$ and $-$ correspond to forward and backward integration, respectively. We also denote these times as forward exit time and backward exit time. The residence time of fluid parcels is an important parameter for ecological studies, since it quantifies a typical time for water exchange. We obtain the residence time as $T_R(\mathbf{x}_0, t_0, t) = T^+(\mathbf{x}_0, t_0, t) + T^-(\mathbf{x}_0, t_0, t)$.

Chapter 3

Two-dimensional Flow Data

Abstract

The use of Lagrangian methods to analyze transport in a chaotic fluid flow requires the availability of the complete time-dependent velocity data of the flow. In this chapter, we recall and describe the methods and measurement techniques used to obtain the analyzed velocity fields. We consider geostrophic currents derived from satellite altimetry, a coastal tidal flow from high-frequency radar measurements, and a turbulent laboratory flow obtained by Particle Image Velocity (PIV) technique.

3.1 Oceanic Mesoscale Flow from Altimetry Measurements

Mesoscale currents in the ocean on length scales larger than $50\,\mathrm{km}$ and on time scales longer than a week are well represented by geostrophic currents. We can compute the velocity fields of these currents from altimetric satellite data under the assumption of geostrophic balance, i.e., the balance between the Coriolis force and the horizontal pressure force in the moving fluid. The pressure field is directly related to the elevation of the sea surface, which can be measured to a high precision with altimetry. Altimetry is a remote sensing technique that has developed rapidly in the last 15 years and has extensively been used to study mesoscale ocean currents [140]. Basically, the ocean surface forms a landscape of wide and very flat mountains and valleys. The surface elevation varies in the order of $1\,\mathrm{m}$ over a horizontal distance of several $100\,\mathrm{km}$ giving rise to geostrophic ocean currents of up to $1\,\mathrm{m/s}$. We use geostrophic currents derived from altimetry data as a valuable data set to investigate the transport and coherent structures in large scale ocean currents.

3.1.1 Geostrophic Balance

We recall here the assumptions for a flow in geostrophic balance and derive the geostrophic equations, following [201]. Therefore, we analyze the different terms

in the momentum equations to decide which terms are dominant. The momentum equation of a fluid parcel has the following form

$$\frac{\partial \mathbf{v}}{\partial t} + \mathbf{v} \cdot \nabla \mathbf{v} = -\frac{1}{\rho} \nabla p - 2\boldsymbol{\Omega} \times \mathbf{v} + \mathbf{g} + \mathbf{F}_r \tag{3.1}$$

with the fluid density ρ, the pressure p, the Earth's rotational frequency $\boldsymbol{\Omega}$, the gravitational acceleration $\mathbf{g}$ and the internal friction force $\mathbf{F}_r$. The first and second term on the right hand side are the pressure force and the Coriolis force. Separated into the three components we have

$$\begin{aligned}
\frac{\partial u}{\partial t} + u\frac{\partial u}{\partial x} + v\frac{\partial u}{\partial y} + w\frac{\partial u}{\partial z} &= -\frac{1}{\rho}\frac{\partial p}{\partial x} + 2\Omega v \sin\varphi + F_x && (3.2)\\
\frac{\partial v}{\partial t} + u\frac{\partial v}{\partial x} + v\frac{\partial v}{\partial y} + w\frac{\partial v}{\partial z} &= -\frac{1}{\rho}\frac{\partial p}{\partial y} + 2\Omega v \sin\varphi + F_y && (3.3)\\
\frac{\partial w}{\partial t} + u\frac{\partial w}{\partial x} + v\frac{\partial w}{\partial y} + w\frac{\partial u}{\partial z} &= -\frac{1}{\rho}\frac{\partial p}{\partial z} + 2\Omega v \cos\varphi + F_z - g && (3.4)
\end{aligned}$$

For large scale currents we estimate the typical magnitudes of the horizontal length scale L, depth H, horizontal velocity U, vertical velocity W, time T, Coriolis parameter $f = 2\Omega \sin\varphi$, gravity g, surface elevation S and density ρ as

$$\begin{aligned}
L &\approx 10^6\,\mathrm{m} && (3.5)\\
H &\approx 10^3\,\mathrm{m}\\
U &\approx 10^{-1}\,\mathrm{m/s}\\
W &\approx 10^{-4}\,\mathrm{m/s}\\
T &\approx 10^7\,\mathrm{s}\\
f &\approx 10^{-4}\,\mathrm{s}^{-1}\\
g &\approx 10\,\mathrm{m/s}^2\\
S &\approx 1\,\mathrm{m}\\
\rho &\approx 10^3\,\mathrm{kg/m}^3.
\end{aligned}$$

Using these values to estimate the magnitude of the different terms in the equation for vertical momentum (3.4), the equation reduces to the two dominant terms

$$\frac{\partial p}{\partial z} = -\rho g. \tag{3.6}$$

This is the hydrostatic equilibrium, i.e., gravity is balanced by the vertical pressure gradient and the vertical velocity is zero. With the same values and the horizontal pressure gradient $\partial p/\partial x = \partial p/\partial y = \rho g S/L$ in the horizontal momentum equations (3.2) and (3.3), all terms on the left hand side are small compared to the right hand side. Neglecting of the friction term leads to the geostrophic equations

$$\begin{aligned}
\frac{1}{\rho}\frac{\partial p}{\partial x} &= fv && (3.7)\\
\frac{1}{\rho}\frac{\partial p}{\partial y} &= -fu. && (3.8)
\end{aligned}$$

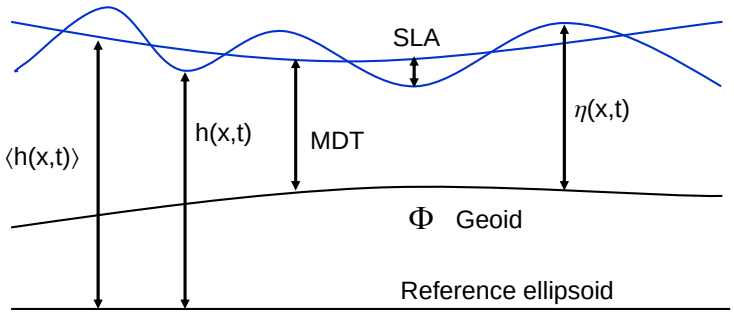

Figure 3.1: Quantities and reference surfaces involved in altimetry measurements of the sea surface. The altimeter measures the sea surface height $h(x, y, t)$ with respect to a reference ellipsoid. However, sea surface measurement have to be referenced to the geoid $\Phi(x, y)$, a surface of constant geopotential, and the geoid is not known at a sufficiently high resolution to resolve mesoscale features. Therefore, the mean dynamic topography (MDT), representing the steady ocean currents, is constructed from long-time current data sets from ship cruises, models and drifters. The time-dependent part of the measurement signal, the sea level anomaly SLA(x, y, t) (3.15) is added to the MDT to obtain the total dynamic topography of the ocean's surface.

Now, we define a reference surface of constant geopotential, the geoid $\Phi(x, y)$. One level surface of the geopotential is the ocean's surface when the whole ocean is at rest. Fluid moves along the surface $\Phi(x, y)$ without a change of potential energy. However, with respect to a reference ellipsoid the geoid is deformed due to an inhomogeneous gravity field [188]. Deformations can be as high as $50-100$ m. If we choose a geoid surface $\Phi(x, y)$ under the water surface, the water column over the geoid surface is

$$\eta(x, y, t) = h(x, y, t) - \Phi(x, y), \tag{3.9}$$

with the sea surface height $h(x, y, t)$, and the pressure is given by

$$p(x, y, z = \Phi) = \rho g\, \eta(x, y, t). \tag{3.10}$$

Finally, the geostrophic velocities are

$$u(x, y, t) = -\frac{1}{\rho f}\frac{\partial p}{\partial y} = -\frac{g}{f}\frac{\partial \eta(x, y, t)}{\partial y} \tag{3.11}$$

$$v(x, y, t) = \frac{1}{\rho f}\frac{\partial p}{\partial x} = \frac{g}{f}\frac{\partial \eta(x, y, t)}{\partial x}, \tag{3.12}$$

or in short form

$$\mathbf{v}(x, y, t) = \nabla \times \Psi(x, y, t), \tag{3.13}$$

$$\Psi(x, y, t) = -\left(0, 0, \frac{g}{f}\,\eta(x, y, t)\right) \tag{3.14}$$

where Ψ is the stream function. We see that the velocities are proportional to the inclination of the water surface with respect to the geoid and the flow is parallel to contour lines of the pressure field.

The surface elevation $\eta(x, y)$ that accounts for the subsurface pressure is defined relative to the geoid (3.9). However, the geoid of the Earth is only known at a coarse resolution, not sufficient to resolve mesoscale features [67, 201]. Therefore, the geoid cannot be used as a reference for altimetry measurements. Instead, the time dependent part of the measured sea surface height, the sea level anomaly (SLA)

$$\mathrm{SLA}(x, y, t) = h(x, y, t) - \langle h(x, y, t) \rangle \tag{3.15}$$

is determined from altimetry data and added to the constant mean dynamic topography (MDT). The MDT represents the steady ocean currents and is derived from huge long-time data sets of oceanographic currents including climatological data sets, model output or drifters. The currently used mean dynamic topography is the Rio05 MDT [176]. The sum gives the surface elevation

$$\eta(x, y, t) = \mathrm{MDT}(x, y) + \mathrm{SLA}(x, y, t) \tag{3.16}$$

from which the geostrophic velocities can be computed.

3.1.2 Satellite Altimetry

Altimeters use the simple measurement principle of time-of-flight of a microwave pulse. The microwave radiation is emitted from the satellite, is reflected by the sea surface, and the reflected part is registered by an antenna at the satellite. The time-of-flight Δt is recorded. In first order, the range from the satellite to the ground is simply [36]

$$r = \hat{r} - \sum_j \Delta r_j \tag{3.17}$$

where $\hat{r} = c\Delta t/2$ with the speed of light c. However, several corrections are necessary, denoted here with Δr_j, e.g., due to water vapor in the atmosphere that delays the signal. Finally, with all corrections the error of the distance measurement can be reduced to only a few centimeters. This accuracy is necessary, because if we assume, for example, a sea surface height variation of $5\,\mathrm{cm}$ over a horizontal distance of $100\,\mathrm{km}$ at a latitude of $\varphi = 30°$, this translates to a variation of the geostrophic velocity of roughly $\Delta v = 4\,\mathrm{cm/s}$, being an error of about 10% for typical ocean currents. Although based on a simple measurement principle, altimetry is a highly complex method of remote sensing. An excellent introduction and overview over satellite altimetry is given by Fu and Cazenave [66].

3.2 Coastal Currents and High Frequency Radar

High frequency radar systems have been used to measure surface submesoscale ocean currents for more than 30 years [18, 77]. The measurement principle is based on the Doppler shift of a radar signal that is backscattered by the rough sea surface. The Doppler shift is due to the relative motion of the dominant scattering gravity surface waves (Bragg scattering) with respect to the fixed radar station. This relative motion has two contributions: the velocity of the gravity

surface waves and the velocity of the underlying currents. As the wavelength of the dominant scattering surface waves is known from the Bragg condition and the radar frequency, the wave velocity can be obtained from the dispersion relation of gravity surface waves. Then, from the measured Doppler shift the current velocity in radial direction with respect to the radar station can be estimated. Since the radial velocities are one-dimensional, two radar stations are necessary to determine the two components of the horizontal surface velocity. Depending on the radar frequency the radar has a range of several hundreds of kilometers with a spatial resolution of the velocity field of some kilometers. For higher radar frequencies (very-high frequency radar VHF) the resolution can be increased to some hundreds of meters, while the range then decreases to about ten kilometers. Today, hundreds of HF radar systems have been installed worldwide and it has become a widely used measurement technique to study the ocean circulation near the coast [e.g., 35, 161, 177].

The VHF radar system installed at the Ria de Vigo and used in this study, is operated by the University of Vigo. In order to cover the whole region of the outer bay the two radar stations are located on either side of the bay (cf. Fig. 6.16). This results in a footprint on the water surface that reaches from the inner bay to the south mouth and the north mouth. A drawback of this configuration of the radar stations is the fact that on the baseline connecting the two stations both radial velocity components are parallel. Therefore, only unidirectional velocities can be measured and the second component has to be interpolated using Open boundary Modal Analysis (OMA) [102]. This can lead to high uncertainties in the zone along the baseline which might influence the results of our transport analysis. With a frequency of 46 MHz the VHF radar system at the Ria de Vigo has a spatial resolution of 375 m and a range of roughly 15 km. The radial velocity data of both stations is combined to a grid of 400 m. Velocity fields have a temporal resolution of 30 min and the data represent the velocity of a surface layer with the effective depth of ~ 25 cm [3]. Thus, the system provides a complete data set of time-dependent, two-dimensional horizontal velocity fields of the sea surface with a sufficient spatial and temporal resolution to study the complex flow in the Ria de Vigo on the submesoscale ($1 - 10$ km). Since the complete spatio-temporal velocity data is available, we can integrate the velocity fields and address transport by using Lagrangian techniques based on trajectories, as e.g., LCS and SLM (Sec. 6.4).

3.3 Faraday Flow

The Faraday instability on a vertically vibrated fluid surface is a well known phenomenon [59, 134]. Capillary waves form on the surface that can be ordered in a variety of patterns. Many experimental and numerical studies focus on these surface waves, their properties and their transitions [50, 166, 211, and references therein]. For this study, it is more important that the surface waves induce a horizontal flow in the fluid [130]. Only recently the flow has been measured in detail and characterized as turbulent [217]. We can vary the intensity of this horizontal

flow by increasing the acceleration amplitude of the vibrational forcing, while the frequency is left constant at $f = 50\,\text{Hz}$. For a Lagrangian analysis of transport in the Faraday flow the highly time-dependent two-dimensional velocity field is measured with Particle Image Velocimetry (PIV).

3.3.1 Particle Image Velocimetry (PIV)

Particle Image Velocimetry is an optical measurement technique primarily for two-dimensional, time-dependent velocity fields [see 7, and references therein]. Basically, the fluid is seeded with small tracer particles and the velocity information is gained from the finite position difference of the particles between two subsequent images. The tracers are chosen such that they follow the fluid motion as exactly as possible. Therefore, the particles have to be small and need to have a similar density as the fluid. The volume fraction of tracers in the fluid should generally be very low to not modify the fluid flow. In the classical PIV setup, the tracer particles are often illuminated by a light sheet that cuts a plane out of the 3D flow, while a camera looks perpendicular onto the light sheet to record the particle motion.

In our setup [218, supplementary data], we already have a two-dimensional setting. Hence, we use floating tracer particles on the free surface of the Faraday flow and a backlight for illumination. Using this shadowing technique, particles appear as dark spots in the image. Our images simultaneously show the particles and the chemical reaction (Fig. 7.1). Since the particles are very small and they have a high spatial wavelength, the smoother grayvalue variations in the image due to the chemical reaction can be filtered out by a high-pass spatial filter, such that the PIV velocity field represents only the motion of the particles. For the PIV analysis we employ the open source MPIV Matlab toolbox [139] with a minimum quadratic differences (MQD) method. Subsequent images with a time difference of $\Delta t = 1/50\,\text{s}$ are analyzed. In order to obtain a velocity vector at position (X_k, Y_l) of the image, a small window of width $2d + 1$ is taken from the first image I_1 and compared with windows of the same size in the second image I_2 that are shifted by a displacement $(\Delta x, \Delta y)$. The cost function

$$C_{kl}(\Delta x, \Delta y) = \sum_{i=-d}^{d} \sum_{j=-d}^{d} |I_1(X_{k+i}, Y_{l+j}) - I_2(X_{k+i} + \Delta x, Y_{l+j} + \Delta y)| \quad (3.18)$$

measures the difference in grayscale values between the shifted windows. Its minimum is determined and the shift $(\Delta x_{min}, \Delta y_{min})$ at the minimum is taken as an estimation for the displacement of the fluid between the two images. Hence, the velocity is estimated as

$$\mathbf{v}(X_k, Y_l) = \frac{1}{\Delta t} (\Delta x_{min}, \Delta y_{min}) \,. \quad (3.19)$$

Missing velocity vectors at positions where the cost function C_{kl} does not have a clear minimum are interpolated.

Chapter 4

A Phytoplankton Patch under Unsteady Flow Conditions

In collaboration with V. Pérez-Muñuzuri, published in Nonlin. Processes Geophys. 17, 177–186 (2010) [165].

Abstract

Fields of phytoplankton concentration in the oceans exhibit a high spatiotemporal variability, often referred to as plankton patchiness. This patchiness occurs when the biological dynamical system describing a plankton population is extended spatially and additionally stirred by a chaotic advective flow that generates highly irregular spatial patterns.

In this chapter, we consider the case of a single phytoplankton patch emerging from a localized nutrient source, and we study numerically how time and length scales of the advective flow affect the growth of the patch. To that end, we use a coupled reaction-diffusion-advection model, consisting of a standard three component ecological NPZ model and two different flow models able to mimic the mesoscale circulation observed in the ocean. We find optimal time and length scales in the flow models that favor the spreading of the plankton patch, and discuss the findings in terms of the time scale of the NPZ model and the interaction of the flow with the reaction front. Moreover, the spatial distribution of the patch is dominated by Lagrangian structures in the flow. We extract these structures and show that they reveal pathways where the plankton patch can spread, and transport barriers where the expansion of the patch is blocked.

4.1 Introduction

Spatial heterogeneity or "patchiness" in phytoplankton distributions is an old oceanographic observation that dates back to the 12th century [15, 76] and is still a field of current research. Phytoplankton forms the base of the food chain and is responsible for a large amount of the biological primary production in the oceans. Therefore it plays an important role for the entire marine ecosystem.

Furthermore, it acts on the ocean's CO_2 uptake, as a part of the carbon absorbed in phytoplankton by photosynthesis is transported to deep water, when dead organic matter sinks down. A striking feature associated with the dynamics of phytoplankton populations is the occurrence of rapid and extensive bloom formations after the injection of nutrients. Such events are characterized by a sharp rise in algae concentration of up to several orders of magnitude [19] followed by a sudden collapse, whereby the phytoplankton population returns to its original low level. An example for this behavior is the Madagascar plankton bloom that is discussed in chapter 5 of this work. Given the impact of phytoplankton blooms, it is of interest to understand the dynamics of plankton growth and the optimal conditions for a rapid and wide spread of a plankton patch.

A plankton population in the ocean can be seen as a biological system with predator-prey dynamics in a mobile environment that alters its spatial distribution. As the well-lit surface layer of the ocean is normally nutrient poor, a nutrient source is necessary to start a rise of the phytoplankton concentration above a low stationary level. Apart from occasional aeolian dust deposition [162], upwelling of nutrient rich water from deeper water layers or vertical mixing is assumed to be the main nutrient source [104, 113, 156]. A variety of hydrodynamical effects leading to vertical transport have been reported [104, 120], many of which may be highly localized in space. They represent an important cause for plankton patchiness. Pasquero et al. [162] showed that not only the mean value of the nutrient flux but especially its temporal and spatial variability influence the primary production, demonstrating the non-linear character of the system. Martin et al. [121] and Pasquero et al. [162] found a lower primary production for nutrient sources correlated with eddy cores than for uncorrelated source positions.

Assuming the presence of a nutrient source, horizontal transport in the time-dependent mesoscale and sub-mesoscale flow ($\sim 1-500$ km) modifies the patterns in the plankton distribution and influences the temporal evolution of plankton patches [5, 105, 119, 125]. Lehahn et al. [100] found that the gradients in chlorophyll concentration fields from satellite images align with unstable manifolds of the geostrophic velocity field, which suggests that horizontal transport controls the chlorophyll patterns. As the ocean is a multiscale system, a single plankton patch is advected and mixed by flow structures of very different time and length scales. The interaction of these scales with the parameters of the plankton system affects the spatio-temporal development of a plankton patch. One example for this interaction is the existence of a minimum width for phytoplankton filaments, which is determined by few parameters describing the flow and the growth of the plankton system [118, 126]. Another example are localized plankton blooms in vortices in the wake of an island. These appear when the long residence time of water masses in the vortices is comparable to the plankton growth time [186]. An extensive review of the topic can be found in [119].

Hence, we see that plankton patchiness emerges from non-linear interactions of the biological plankton system and the physical unsteady flow. In the following, we particularly focus on the interplay of length and time scales of a two-dimensional horizontal flow with the plankton dynamical system. We investigate the response of a plankton model to a well-defined hydrodynamical forcing and address the

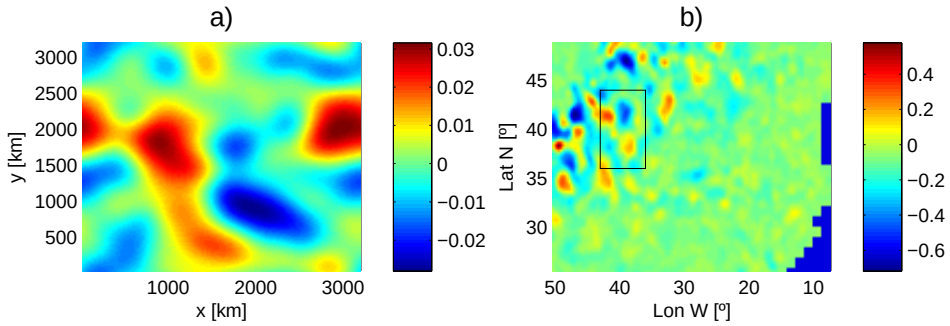

Figure 4.1: Stream function (a) for the Gaussian model and (b) for the altimetry data. Parameters: (a) time scale $\tau/T = 1$, length scale $\lambda/L = 10$, and domain size $N_x = N_y = 128$; (b) the area of simulation spans from $25^\circ\ N$ to $49^\circ\ N$, and from $7^\circ\ W$ to $50^\circ\ W$ ($N_x = 130, N_y = 90$). The marked area in the altimetry data is analyzed in detail later. The visible land structure in the lower right corner is the coast of Spain and Morocco.

question under which flow conditions a plankton patch, evolving from a single localized nutrient source, spreads optimally. We therefore choose a simple model flow defined by an autocorrelation length and time, and we analyze the final size of the plankton patch. The results are compared to a similar analysis of plankton patches in a multiscale altimetry flow. We include an example of two plankton patches, where the effect of different length and time scales can be seen. In the ocean, upwelling regions with a vertical flow are often linked to horizontal flow structures. In our model, we do not correlate nutrient upwelling regions to flow structures, since we investigate the response of the plankton system to basic spatio-temporal properties of a model flow.

4.2 Models

The role of mesoscale flow structures for the evolution of a phytoplankton patch is studied considering a two dimensional (2D) incompressible flow such that the velocity field is given by $\mathbf{V} = \mathbf{e_z} \times \nabla\psi$, where $\psi(x, y, t)$ is a time-dependent stream function. An ecological model, coupled to the flow, models the phytoplankton production.

4.2.1 The Flow Models

To study the effects of length and time scales of a flow on a phytoplankton patch, we use two flow models, an analytic and another more realistic one. Fig. 4.1 shows the two stream functions corresponding to the two depicted flows. The analytic Gaussian correlated flow is especially appropriate to investigate the influence of time and length scales on plankton production, because its time and spatial scales are independent and can be adjusted a priori. The obtained results for this artificial

flow are compared to a similar analysis for a flow derived from satellite altimetry measurements.

Gaussian Correlated Flow

The Gaussian correlated flow is defined in terms of a stream function whose dynamics is represented by a Gaussian spatiotemporal distributed noise. The noise has zero mean and the spatio-temporal autocorrelation function $G(\rho, s)$ is given by

$$\begin{aligned} \langle \psi(\mathbf{r}, t)\, \psi(\mathbf{r}', t') \rangle &= G\left(\left|\mathbf{r} - \mathbf{r}'\right|, \left|t - t'\right|\right) = \\ & \quad \Upsilon\left(\left|\mathbf{r} - \mathbf{r}'\right| / \lambda\right) \Theta\left(\left|t - t'\right| / \tau\right), \end{aligned} \tag{4.1}$$

with $\mathbf{r} = (x, y)$. The temporal correlation function, $\Theta(s/\tau)$, describes an Ornstein-Uhlenbeck (OU) process given by

$$\Theta(s/\tau) = \frac{1}{\tau} \exp\left(-s/\tau\right) \tag{4.2}$$

where τ corresponds to the correlation time for the OU process and $s = |t - t'|$. The spatial correlation is given by

$$\Upsilon\left(\rho/\lambda\right) = \frac{\sigma^2}{2\pi\lambda^2} \exp\left(-\rho^2/2\lambda^2\right), \tag{4.3}$$

where σ^2 is the noise intensity, λ is the correlation length and $\rho = |\mathbf{r} - \mathbf{r}'|$. In order to study the effects of noise, the noise dispersion $G(0, 0)$ is kept constant

$$G(0, 0) = \frac{\sigma^2}{2\pi\tau\lambda^2} = const \tag{4.4}$$

while varying τ or λ. Thus, an artificial flow is defined with specific typical length and times scales for the velocity. Details on the numerical generation of a spatiotemporal correlated noise, Eqs. (4.2-4.4), are given in Alonso et al. [9] and Sagués et al. [183].

Altimetry Flow

For the more realistic flow case, we consider geostrophic surface currents derived from satellite altimetry data (Sec. 3.1) provided by AVISO. The Ssalto/Duacs system processes data from all altimeter missions (Jason-1&2, TOPEX/Poseidon, Envisat, GFO, ERS-1&2 and Geosat) and merges data from all available satellites. We use global maps of Sea Level Anomaly (SLA). This is the time-dependent flow component of the mesoscale currents without the steady mean flow. It has a spatial resolution of $1/3^\circ$ on a Mercator grid and a temporal resolution of 1 day. For this data set geostrophic velocities are estimated as

$$V_x = -\frac{g}{f R_T} \frac{\partial \psi_{SLA}}{\partial \phi} \qquad V_y = \frac{g}{f R_T \cos\phi} \frac{\partial \psi_{SLA}}{\partial \ell} \tag{4.5}$$

where ψ_{SLA} is the SLA, g is the gravity, f the Coriolis parameter, R_T the Earth radius, ϕ the latitude and ℓ the longitude, and the derivatives were calculated with finite differences. The data analyzed here is from 12th November 2008. We chose the area to include a wide range of velocity absolute values and different local length scales, always keeping in mind that geostrophic velocities from altimetry data are only an estimate of the ocean currents and that altimetry data only resolves mesoscale structures.

4.2.2 NPZ Model

We use a well-established NPZ ocean ecosystem model representing the plankton dynamics [60, 65, 121, 157, 162]. It is a three component model describing the interaction of three species of the trophic chain: nutrients N, phytoplankton P, and zooplankton Z. Their concentrations evolve according to the following equations [162, 186, 187],

$$\begin{aligned} \dot{N} = F_N &= \Phi_N - f(N,P) \\ &\quad +\mu_N\left((1-\gamma)g(P,Z) + \mu_P P + \mu_Z Z^2\right) \\ \dot{P} = F_P &= f(N,P) - g(P,Z) - \mu_P P \\ \dot{Z} = F_Z &= \gamma g(P,Z) - \mu_Z Z^2 \end{aligned} \tag{4.6}$$

and

$$\begin{aligned} f(N,P) &= \beta\frac{N}{k_N+N}P \\ g(P,Z) &= \frac{\alpha\eta P^2}{\alpha+\eta P^2}Z. \end{aligned} \tag{4.7}$$

In this paragraph, we explain the single terms [157, 162]. The sinks and sources in the nutrient equation are expressed in three terms: the vertical nutrient flux into the nutrient-depleted surface layer Φ_N, the consumption of nutrient by phytoplankton $f(N,P)$, and the regeneration of nutrient from dead organic matter. The regeneration term includes excrements from zooplankton $(1-\gamma)g(P,Z)$, and fluxes from dead organic matter that equal the mortality rates of phytoplankton $\mu_P P$ and zooplankton $\mu_Z Z^2$. Only the fraction μ_N of dead organic matter is available for this process, while the fraction $(1-\mu_N)$ sinks down to deeper water and is lost. The phytoplankton equation contains the growth term $f(N,P)$ and sink terms $g(P,Z)$ and $\mu_P P$, where $g(P,Z)$ is the grazing of phytoplankton by zooplankton and $\mu_P P$ is the phytoplankton mortality. In the growth term, $f(N,P)$, nutrient uptake by phytoplankton is modeled with a Holling type II functional response $N/(k_N+N)$ [142, 195]. With this function the nutrient uptake first increases with increasing nutrient concentration and finally saturates at a constant value, which basically means that phytoplankton consumes "as much nutrient as it can". Zooplankton is modeled with the growth term $\gamma g(P,Z)$ and the mortality $\mu_Z Z^2$. γ represents the assimilation efficiency of the zooplankton, i.e. only the fraction γ of the consumed phytoplankton is transformed into zooplankton matter, while the excrements $(1-\gamma)$ enter into the nutrient regeneration. The

Table 4.1: List of parameters used in the NPZ model, Eqs. (4.6-4.8)

parameter	value	dimensionless value
β	0.66 d^{-1}	19.8
η	1 (mmol N m^{-3})$^{-2}$ d^{-1}	0.12288
γ	0.75	0.75
α	2 d^{-1}	60
S_l	0.00648 d^{-1}	0.1944
S_h	0.648 d^{-1}	19.44
k_N	0.5 mmol N m^{-3}	7.8125
μ_N	0.2	0.2
μ_P	0.03 d^{-1}	0.9
μ_Z	0.2 (mmol N m^{-3})$^{-1}$ d^{-1}	0.384
N_0	8 mmol N m^{-3}	125

Holling type III functional response of the phytoplankton uptake $\alpha\eta P^2/(\alpha+\eta P^2)$ accounts for an initially accelerating uptake and a final saturation, similar as for the Holling type II functional response.

Since we assume a two-dimensional flow, vertical mixing, which is a determinant factor for phytoplankton formation, must be parameterized. We consider a constant high nutrient concentration N_0 below the mixed layer [121, 162]. The upward nutrient flux then is

$$\Phi_N = S(x,y)(N_0 - N), \tag{4.8}$$

where the function $S(x,y)$ determines the strength of the upwelling by turbulent diffusion depending on the location in the flow. Eq. (4.8) can be seen as a formulation of Fick's second law (1.4), where $N_0 - N$ represents the concentration difference, and $S = D_v/L^2$ includes the vertical turbulent diffusivity D_v and a typical vertical length scale L [121]. $1/S(x,y)$ is the corresponding relaxation time. The parameters used are taken from [162, 186, 187] and are shown in Table 4.1. For this set of parameters the NPZ model has only one nontrivial stable fix point and exhibits stationary behavior in the long-term limit. To obtain dimensionless values, all quantities and parameters in the model are measured in units of length $L = 25$ km, time $T = 30$ days and nitrogen mass $M = 10^{12}$ mmol N following Sandulescu et al. [186].

4.2.3 Numerical Methods and Initial Conditions

The coupling of the hydrodynamic and NPZ models yields a reaction-diffusion-advection system described by the following set of partial differential equations:

$$\frac{\partial \mathbf{C}}{\partial t} + (\mathbf{V}\cdot\nabla)\,\mathbf{C} = \mathbf{F}(\mathbf{C}) + D\,\nabla^2\mathbf{C}. \tag{4.9}$$

Here, $\mathbf{C} = [N, P, Z]$ and $\mathbf{F} = [F_N, F_P, F_Z]$ is given by Eqs. (4.6-4.8). For 2D incompressible flows, the velocity $\mathbf{V} = [V_x, V_y]$ of an advected particle is given

by $\mathbf{V} = \mathbf{e_z} \times \nabla\psi$. The corresponding stream functions $\psi(x, y, t)$ for the different flows are described in subsection 4.2.1. Following [186] we use a constant value for the diffusion of all the biological fields $D = 10$ m^2/s which is given by the Okubo estimation [149]. The dimensionless value used was $D = 0.04147$. Nevertheless, for the scales considered here, diffusion of biological tracers plays a limited role and the dominant effect is the explicit spatial advection (see also Bracco et al. [26]). The reaction-diffusion-advection problem was integrated numerically on a $N_x \times N_y$ square lattice using a semi-Lagrangian algorithm [162, 186, 197, 199] with spatial step size $\Delta x = 1.0$ and time step $\Delta t = 10^{-3}$. The algorithm induces a numerical diffusion that is smaller than the real diffusion for the biological tracers [186] and the spatial advection.

As initial condition, all biological concentrations were set to their steady value, $N_0 = 0.185$, $P_0 = 0.355$ and $Z_0 = 0.444$ mmol N m^{-3} for a low nutrient flux with $S = S_l = 0.00648$ d^{-1}, simulating a nutrient poor domain ($P_{p_0} = 0.0633$ mmol N m^{-3} d^{-1}). In order to start the evolution of a plankton patch, we consider the effect of local upwelling and assume local strong vertical mixing leading to a nutrient rich spot in the mixed layer. This is numerically simulated by imposing a hundred times larger value of the nutrient transfer rate $S = S_h = 0.648$ d^{-1} on a small region of 3×3 grid points (75 km $\times$ 75 km). For each run the stream function for the flow is randomly chosen, so the position of the nutrient source, always in the middle of the domain, is uncorrelated with the flow. The upwelling is switched on for an active time T_f after which S is set to its low value again. Throughout this study we keep the active period of $T_f/T = 3$ ($T_f = 90$ days) constant. The influence of a periodic active time T_f on the primary production was analyzed by Pasquero et al. [162]. Periodic boundary conditions were imposed for the concentrations and velocity gradients for the Gaussian flow model. To quantify the phytoplankton population as a function of the time and length scales of the flow, we compute the plankton patch area B_s as the area, where the phytoplankton concentration P is clearly larger than the steady state concentration P_0

$$B_s = \int_{P>1.1P_0} dA \tag{4.10}$$

Maximal plankton concentrations in the patch are approximately $P/P_0 \approx 1.5$, so the criterion of $P > 1.1P_0$ is adequate to separate the patch from the background concentration.

4.3 Results and Discussion

4.3.1 Gaussian Flow - Optimal Time and Length Scales

The effect of how time and length scales of the flow act on the development of a phytoplankton patch is shown in Fig. 4.2 for the Gaussian flow model. The nutrient source with a high transfer rate $S = S_h$ and a size of 3×3 grid points was set at the center of the 128×128 domain and initiated the development of a plankton patch. The advective flow is obtained from the Gaussian correlated

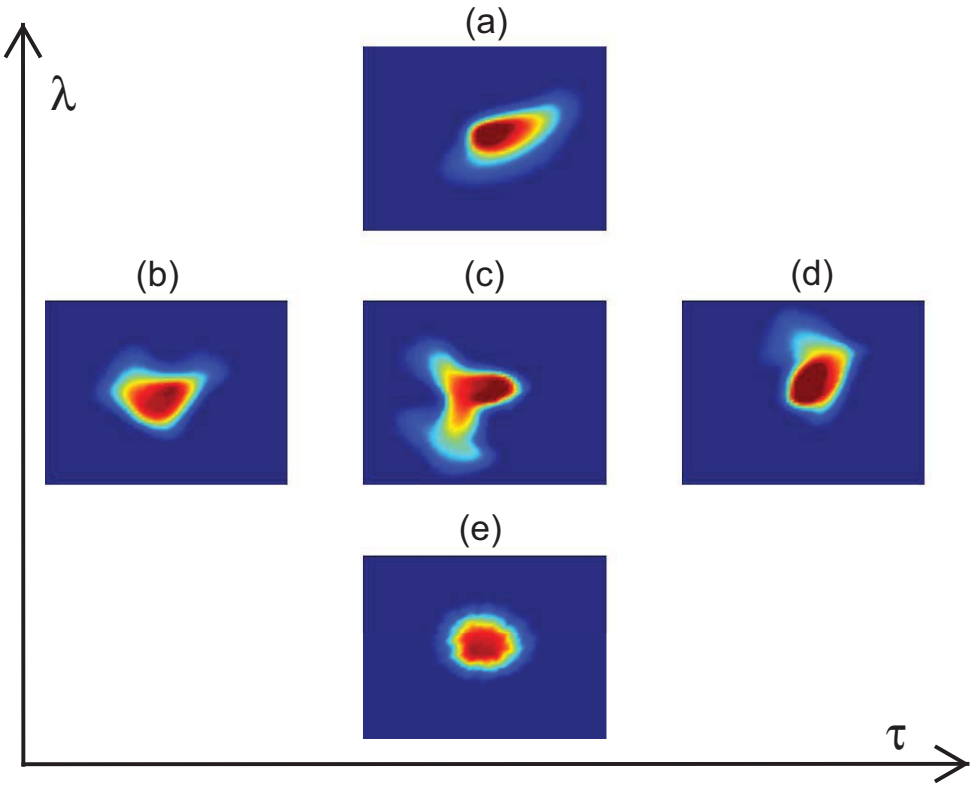

Figure 4.2: Phytoplankton patches observed for different pairs of time and length scales (τ, λ) for the Gaussian flow, Eqs. (4.2-4.4). Length scale increases from bottom to top, and the temporal correlation scale from left to right. Note the larger patch size for intermediate values of τ and λ. Set of parameters: $G(0,0) = 225$, $N_x = N_y = 128$. Length and time scales $(\log_{10}(\tau/T), \log_{10}(\lambda/L))$: (a) $(-0.5, 1.5)$, (b) $(-1.25, 1)$, (c) $(-0.5, 1)$, (d) $(1.5, 1)$, (e) $(-0.5, -0.5)$.

stream function defined by length scale λ and time scale τ. During the whole simulation of 30 days the nutrient source was switched on. Note that especially for intermediate values of the time and length scales (c) the advective velocity field interacts with the expanding reaction front which results in a folded structure of the front and a larger patch size than in the other cases. In the vertical triple of images with different length scales (a,c,e) it is apparent that for small length correlations (e) the patch grows mostly as a circular wave with small scale perturbations of the front, whereas for large length scales (a) the patch is just advected to the right. The horizontal triple of images with different time scales (b,c,d) shows that for intermediate values of the time correlation the patch is most deformed and has areas of still low but increasing plankton concentrations (green). This behavior indicates a resonant behavior between the flow time scale and the time scale of the NPZ model and will be analyzed in detail later.

In order to qualitatively understand, why optimal Eulerian time and length

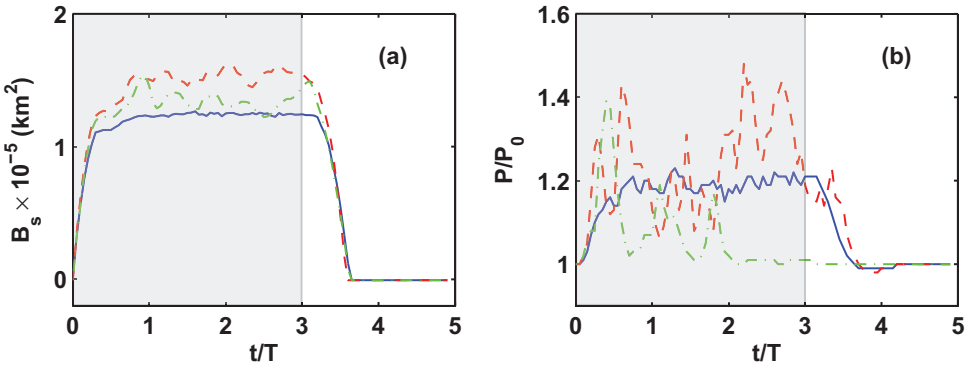

Figure 4.3: Time evolution of the phytoplankton patch size B_s (a) and the phytoplankton concentration 7 grid points apart from the upwelling region (b) for three pairs of Eulerian time and length scales (τ, λ) for the Gaussian flow, Eqs. (4.2-4.4). Blue solid line $(\log_{10}(\tau/T), \log_{10}(\lambda/L)) = (-0.5, -0.5)$, red dashed line $(-0.5, 1)$ and green dashed-dotted line $(-0.5, 1.5)$. Set of parameters: $G(0,0) = 225$, $N_x = N_y = 128$ and active upwelling time $T_f/T = 3$ (gray shade).

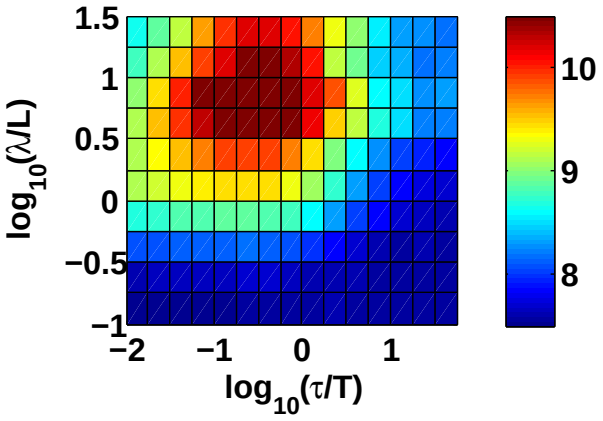

Figure 4.4: Mean phytoplankton patch size $\langle B_s \rangle \times 10^{-5}\,\mathrm{km}^2$ as a function of time and length scales (τ, λ) of the Gaussian flow, Eqs. (4.2-4.4). Optimal Eulerian time and length scales are approximately $(\log_{10}\tau_c, \log_{10}\lambda_c) = (-0.5, 0.875)$. Each data point shown in the figure has been calculated as an average over 30 different initial conditions for the flow. Set of parameters as in Fig. 4.3.

scales for the growth of the phytoplankton patch in the Gaussian flow can be expected, we consider the two limit cases of $\tau \to 0$ and $\tau \to \infty$ for a constant λ. For $\tau \to 0$ and finite dispersion, Eq. (4.4), the intensity of the flow σ^2 tends to zero and the stream function vanishes. In this case, the diffusive non-advective case is recovered. For $\tau \to \infty$ a steady unidirectional flow is obtained. In this case, relevant fluctuations of the flow are absent and their effects on the system are small [109, 183]. For a constant value of the time correlation τ, an analogous

reasoning as the previous one leads to the limit cases for λ. For $\lambda \to 0$ the totally uncorrelated diffusive case is reached and for $\lambda \to \infty$ the unidirectional flow cannot fold and distort the reaction front.

The temporal evolution of the phytoplankton patch size for different Eulerian time and length scales is shown in Fig. 4.3(a). Note that independently of τ and λ, a steady patch size is rapidly attained after an initial time $T_1 \approx 0.3T \approx 9$ days. It decays to zero after the nutrient source is switched off for times $t/T > T_f/T$. The size of the plankton patch is largest for intermediate values of τ and λ (red dashed line in panel (a)) as explained above. For an Eulerian flow time scale τ of the same order of magnitude as the initial time T_1, the patch size is maximal. This suggests a kind of resonant behavior between the flow and the plankton dynamical system. At an exemplary grid point close to the nutrient source, initially, the plankton concentration rapidly increases due to a high nutrient flux which is caused by the short relaxation time S_h^{-1} and the large nutrient difference $(N_0 - N)$ (Fig. 4.3(b)). During the active period T_f, flow fluctuations give rise to fluctuations in the phytoplankton concentration, when different fluid parcels are advected over the chosen grid point. Note that these fluctuations are larger and more frequent for intermediate values of τ and λ corresponding to a distorted reaction front that curls and folds continuously. Finally, the plankton concentration relaxes towards the stationary value as expected for the stable plankton dynamics.

The results for the Gaussian flow are summarized in Fig. 4.4, where the mean plankton patch size is represented as a function of Eulerian time and length scales of the flow, λ and τ. Both are varied independently over more than two orders of magnitude ($2.5\,\text{km} < \lambda < 790\,\text{km}$ and $0.3\,\text{days} < \tau < 950\,\text{days}$), exploring typical ocean mesoscales and beyond. For a fixed parameter pair (τ, λ), the mean patch size is calculated as the average of the value $\langle B_s \rangle_{T_1 < t < T_f}$ over 30 runs. A global maximum of the patch size is obtained for intermediate values of $\tau = \tau_c \approx 9 - 17\,\text{days}$ and $\lambda = \lambda_c \approx 140 - 250\,\text{km}$.

In order to study the influence of the mixing properties of the fluid flow on the phytoplankton growth, we measure the mixing efficiency $\varsigma(\tau, \lambda, t)$ in terms of finite-time Lyapunov exponents $\Lambda(\mathbf{r}, t)$ (FTLE, see Sec. 2.3.3). For a certain Gaussian flow with a constant time scale τ and length scale λ the mean mixing efficiency is defined as the mean of the FTLE values over the 3×3 area of the nutrient source

$$\varsigma(\tau, \lambda, t) = \langle \Lambda(\mathbf{r}, t) \rangle_{3\times 3}\,, \tag{4.11}$$

to quantify the relevant mixing for the plankton patch. Fig. 4.5 shows the mean mixing efficiency $\varsigma(t = 30\,\text{days})$ as a function of the parameters (τ, λ). The parameter space is the same as in Fig. 4.4. Note that the maximum value of the mixing efficiency $\varsigma(\tau, \lambda)$ is obtained for different values of (τ, λ) as the maximum patch size in Fig. 4.4. A flow with a maximum mixing efficiency provides optimal mixing for a passive tracer. A comparison between Fig. 4.4 and Fig. 4.5 suggests that reactive plankton does not spread optimally under the same conditions, as both maxima do not coincide.

The mixing efficiency calculated from FTLE values can also be interpreted as a Lagrangian time scale $1/\varsigma$ of the flow, representing the typical time for the tracer

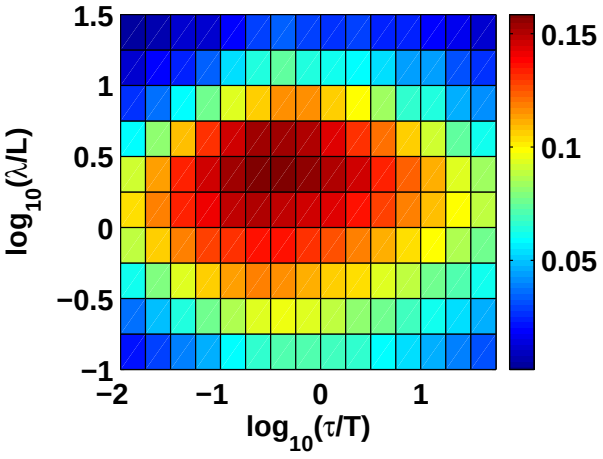

Figure 4.5: Mean mixing efficiency $\varsigma(\tau, \lambda)$ [days^{-1}] in terms of FTLE values at the nutrient source Eq. (4.11) as a function of Eulerian time and length scales (τ, λ) for the Gaussian flow, Eqs. (4.2-4.4). Set of parameters as in Fig. 4.3.

separation along a trajectory of the patch. It is obvious from Fig. 4.5 that for the Gaussian flow this Lagrangian time scale depends on both the Eulerian time and length scale. For optimal Eulerian values (τ_c, λ_c) concerning patch size, the Lagrangian time scale is $\tau_L = 1/\varsigma(\tau_c, \lambda_c) \approx 10$ days. This value is approximately the typical reaction time $T_1 \approx 9$ days the plankton needs to grow after the switch-on of the nutrient source. Faster mixing seems unfavorable for the spread of the plankton patch, because the patch is diluted before having grown, slower mixing reduces the patch size due to a lack of transport.

For the academic Gaussian flow model we found that there exist optimal time and length scales favoring phytoplankton growth in the NPZ model. For these optimal scales, the front becomes much more distorted than for other scales and the final patch area is maximized. Observations of the dynamics of the modeled phytoplankton patch show that flow regions of low velocity values (approximate constant stream function) trap and confine the plankton in "optimal conditions" while the bloom occurs. The surrounding filaments with larger velocity values tend to transport the plankton while not allowing it to grow laterally to the transport direction. This indicates that optimal time and length scales are needed to promote these optimal conditions.

4.3.2 Altimetry Flow

In this section we analyze the development of phytoplankton patches for a more realistic flow model derived from satellite altimetry data, Eq. (4.5). We choose a multiscale region of the North Atlantic, where eddies with different length scales are clearly visible (Fig. 4.1(b)). Although the real altimetry flow is time-dependent and changes over the integration time of 30 days, we use a simplified stationary flow. This allows for a better local definition of time and length scales and reveals

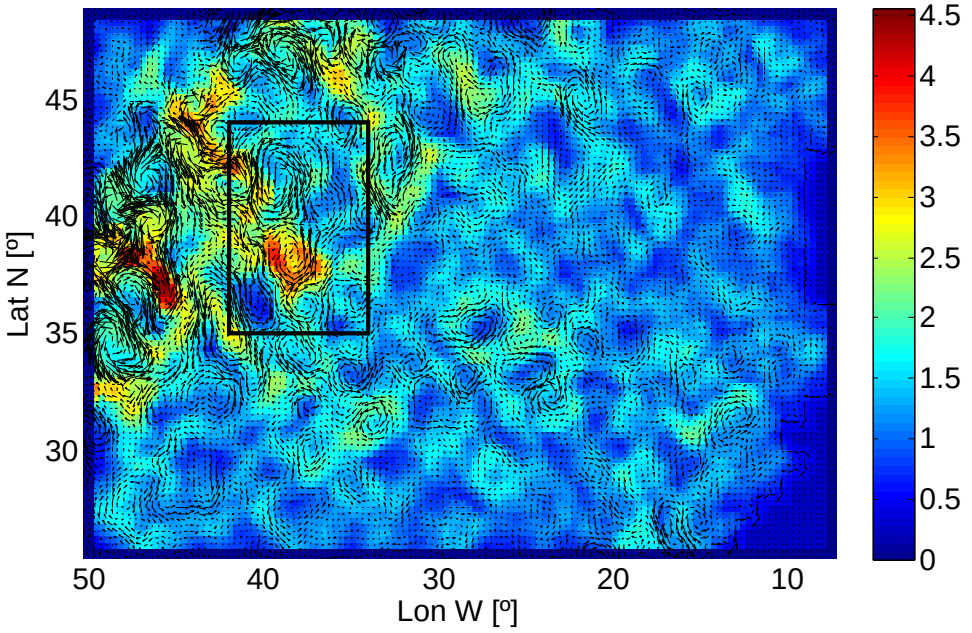

Figure 4.6: Phytoplankton patch size $B_s \times 10^{-5}$ km^2 after 30 days depending on the position of the nutrient source in the stationary altimetry flow. Especially in the black box (also marked in Fig. 4.1(b)) strong differences in patch size are obvious.

well-defined Lagrangian flow structures that dominate the plankton spreading. As in the Gaussian flow, a 3×3 constant nutrient source is set with its center positioned at each grid point of the 130×90 domain to initiate a plankton patch. Then the phytoplankton patch evolving from each of this nutrient sources is again modeled with the NPZ model. After 30 days, the final patch size B_s is calculated as in Eq. (4.10). Figure 4.6 shows the patch size as a function of the position of the nutrient source in the altimetry flow. It is obvious that the position of the nutrient source in the flow strongly affects the evolution and therefore the final size of the plankton bloom.

In order to compare the phytoplankton growth in the altimetry flow to that in the Gaussian flow, we compute time and length scales for each point in the constant altimetry velocity field. As Lagrangian time scale τ_L we use again the local reciprocal Finite-Time Lyapunov Exponent $\tau_L = 1/\Lambda$ at the nutrient source. The local length scale $\lambda(\mathbf{x})$ for the altimetry flow is derived from the autocorrelation function $\Phi(\mathbf{x}, r, \lambda)$ of the velocity field assuming an exponential decay,

$$\begin{aligned} \phi(\mathbf{x}, r) &= \left\langle \frac{\mathbf{v}(\mathbf{x})\mathbf{v}(\mathbf{x}+\mathbf{r})}{|\mathbf{v}(\mathbf{x})||\mathbf{v}(\mathbf{x}+\mathbf{r})|} \right\rangle_{r=|\mathbf{r}|=\text{const}} \\ &= \exp\left(-\frac{r}{\lambda(\mathbf{x})}\right). \end{aligned} \tag{4.12}$$

Although the spatial autocorrelation of the altimetry velocity field does not necessarily decay exponentially, we obtain a good estimate for the Eulerian length scale

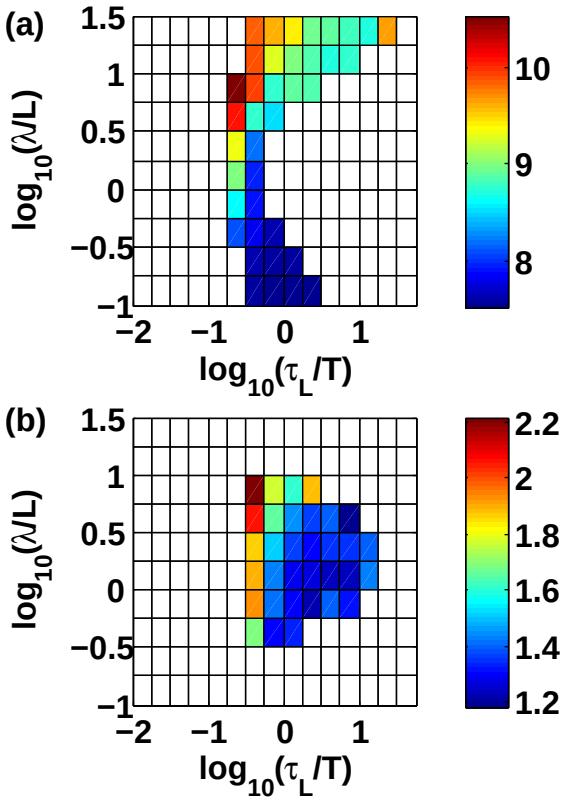

Figure 4.7: Phytoplankton patch size $B_s \times 10^{-5}\,\mathrm{km}^2$ as a function of Eulerian length scale (Eq. 4.12) and Lagrangian time scale $\tau_L = 1/\Lambda$ for the Gaussian flow (a) and the altimetry flow (b).

of the altimetry flow, similar to the a priori Eulerian length scale of the Gaussian flow model. The patch size data for both flow models is binned to these time and length scales, whereby we discarded data with few configurations for (τ_L, λ) values and therefore high errors. Fig. 4.7 shows the phytoplankton patch size as a function of Lagrangian time and Eulerian length scales for the Gaussian model flow (a) and the altimetry flow (b). In both figures, a clear maximum cannot be observed, as not the whole parameter space is covered by the altimetry flow. Nevertheless, both show a very similar dependence of the patch size on time and length scales. Fig. 4.7 suggests that for the covered parameters both flows provide optimal conditions for plankton spread at length scales $\lambda_c \approx 140 - 250$ km and $\tau_c \approx 5 - 15$ days.

Apart from the statistical analysis concerning time and length scales it is worthwhile to have a closer look on a selected region of the flow, to analyze the interplay of the different parameters on the plankton spreading. The selected region is marked in the stream function image (Fig. 4.1) and in the patch size image (Fig. 4.6). Note, that in the boxed area the overall patch size in the lower

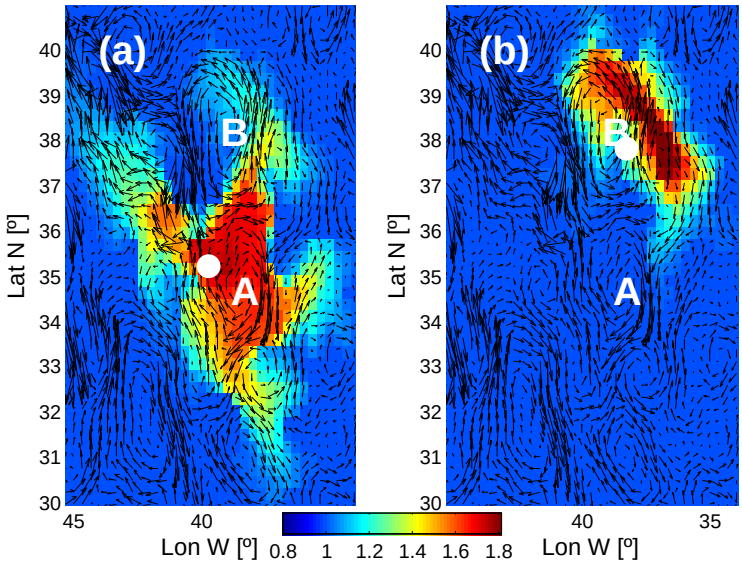

Figure 4.8: Phytoplankton concentration P/P_0 for two different patches in the North Atlantic ocean after 30 days of simulation initiated at the white dot. Letters A and B mark the centers of eddies of similar size.

eddy is significantly larger than in the upper one, although both eddies have similar velocities and diameters.

Fig. 4.8 shows a close-up of the region with two eddies, marked with letters A and B. In order to understand the different dynamics in both eddies that lead to the variation in plankton patch size, we exemplary choose two points, one in each eddy, with a strong difference in patch size. Both sources are positioned in the rotating eddy with a similar distance to the center. Figures 4.8(a,b) show the two phytoplankton distributions that developed from the chosen points after 30 days. For graph (a) the patch size is clearly larger than for graph (b). Fig. 4.9 serves to understand these differences. It shows the plankton patch size in the region of interest (panel a), the local Eulerian length scales (panel b), Lagrangian time scales (panel c), and the Lagrangian flow structure with hyperbolic points (panel d) obtained from an analysis of fields of the Finite-Time Lyapunov Exponent. The plankton patch in eddy A is advected around the eddy in optimal time and length scales while it passes successively four hyperbolic points that spread the plankton to neighboring regions with favorable conditions. Therefore, four filamentary arms are formed. In contrast to this, the patch initiated in eddy B is indeed also spread by one hyperbolic point, but into a western region of small length scales and into an eastern region with long time scales, so the patch development is hindered. As a result, we find here that not only the local time and length scales of the flow influence the growth of the plankton patch, but also the connectivity between regions with favorable conditions for plankton growth. In time-dependent flows the geometry of transport can only be seen in maps of Lagrangian quantities like the FTLE. Stable and unstable manifolds in the flow govern the transport of

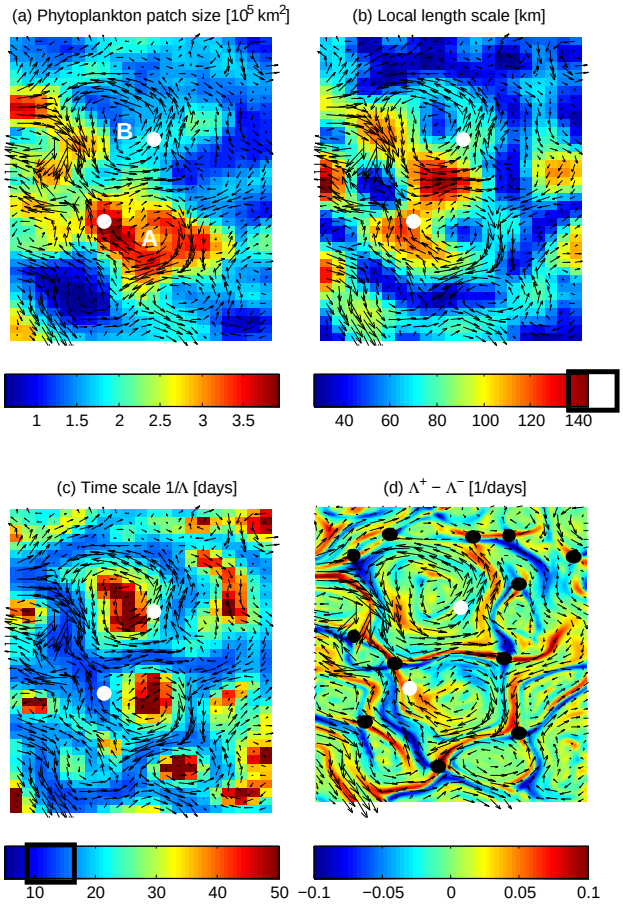

Figure 4.9: Discrepancy in plankton growth in two apparently similar eddies. (a) Size of plankton patch for a selected region in the North Atlantic Ocean after 30 days of simulation. For each grid point, color indicates the patch size $B_s \times 10^{-5}$ km^2 after a nutrient upwelling took place at that location. In eddy A plankton growth is favored. (b,c) The representations of Eulerian length scales and Lagrangian time of the flow show that both long length scales ($\lambda > 120\mathrm{km}$) and short time scales ($\tau_L < 15\mathrm{days}$) are necessary for a large plankton patch size. Black boxes at the color bars show the optimal time and length scales found for the Gaussian correlated flow. (d) Finite-Time Lyapunov Exponents calculated from forward (positive values) and backward (negative values) integration in time. The plotted field is $\Lambda^+ - |\Lambda^-|$. Mesoscale structures with jets and vortices can clearly be observed. The black dots indicate the hyperbolic points that are located at the intersections of the stable (red) and unstable (blue) manifolds. White dots correspond to the positions of the exemplary nutrient sources in Fig. 4.8

tracers [100], while hyperbolic points mark the positions where these manifolds cross and the direction of the velocity changes abruptly.

It is important to note here, that the pathways of transport could also be obtained from streamlines, i.e., lines tangent to the velocity field. In our case of a steady (time-independent) non-divergent flow the streamlines are closed and act as transport barriers (Fig. 4.10). Thus, they determine the directions of trans-

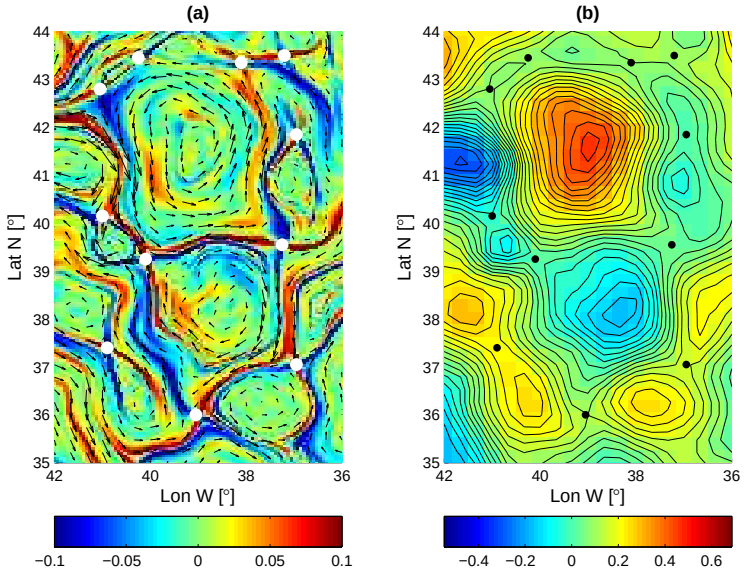

Figure 4.10: (a) Added forward and backward finite-time Lyapunov exponents [1/day] with estimated locations of hyperbolic points (white dots). (b) Contour lines of the streamfunction [m] from altimetry are identical with streamlines of the flow. The streamlines are closed and act as transport barrier to advective transport. The hyperbolic points (black dots) can be identified with saddle points of the stream function.

port of the plankton patch while transport across the barriers can only happen by diffusion. In the following chapters we will show that methods from dynamical systems theory, as for example the extraction of Lagrangian coherent structures from FTLE fields, are especially powerful for time-dependent flows, when instantaneous streamlines are not longer transport barriers.

4.4 Conclusions

We analyzed the effect of time scales and length scales, and the transport geometry of two different fluid flows on the growth of a single plankton patch.

- For both flow models we obtain that growth is enhanced for a critical time scale comparable to the one associated with the biological dynamical system, as it was also pointed out in previous studies [127, 186, 187]. We find an optimal Eulerian time scale for the Gaussian flow of $\tau_c \approx 9 - 17$ days and similar optimal Lagrangian time scales of $\tau_c \approx 5 - 15$ days for the Gaussian and the altimetry flow. The Lagrangian time scale is the more relevant time scale for the advected plankton system.

- We observe that for a critical Eulerian length scale of the order of $140 - 250$ km the patch size attains a clear maximum for the Gaussian flow. For this length scale the front becomes more distorted than for other scales and

the final patch area is the largest. A similar result is found for the altimetry flow.

- Spatial Lagrangian measures, as the FTLE field, allow to estimate stable and unstable manifolds that act as transport barriers and reveal the geometry of transport in the flow. A certain length scale between these barriers is needed to balance two unfavorable conditions: on the one hand, for shorter length scales, the flow rapidly mixes the plankton and does not allow transport over long distances, and on the other hand, for longer length scales, few hyperbolic points are present in the medium and due to the lack of separatrices (stable manifolds) the flow does not favor the spreading of the initial patch in different directions. Thus, length scales in the FTLE field of a flow can indicate regions where a large plankton bloom size can be expected.

- When these results are applied to real plankton systems the limitations of this study have to be considered. The model does not take into account many physical and biological processes that aditionally affect plankton growth, as vertical upwelling, sea temperature, or the depth of the mixed layer and it does not resolve explicitly 3-dimensional effects.

Chapter 5

Mesoscale transport and zonal jets in the Madagascar plankton bloom

In collaboration with A. von Kameke, V. Pérez-Muñuzuri, M.J. Olascoaga, and F.J. Beron-Vera, published in parts in Geophys. Res. Lett. 39, L06602 (2012) [91].

Abstract

The spatial distribution of many phytoplankton blooms is determined by horizontal stirring due to ocean currents on the mesoscale ($50 - 500$ km). In this chapter, we take a closer look at an especially pronounced bloom, the Madagascar plankton bloom, that occurs intermittently and exhibits an exceptionally fast propagation from the coast of Madagascar to the east. Although the entire bloom is a complex phenomenon including biogeochemical processes, passive advection of nutrients and plankton by mesoscale ocean currents might be a key process to explain its fast expansion. Therefore, we apply Lagrangian techniques and methods from dynamical systems theory to analyze the Lagrangian transport patterns in geostrophic ocean currents derived from altimetry data, and compare them to the patterns of the plankton bloom. We find that the recently discovered Southern Indian Ocean Countercurrent (SICC) can account for an important part of the eastward propagation of the plankton bloom. Additionally, meandering zonal jets act as transport barriers that shape the borders of the plankton bloom and limit its growth especially in northern direction.

5.1 Introduction

In this chapter, we focus on the role that advection by unsteady ocean currents may play in shaping the Madagascar plankton bloom. Chaotic advection is known to be a key process for shaping patterns observed in plankton bloom distributions, as it has been noted by many authors [53, 100, 119, 142, 153, 165, 208].

In particular, zonal jets, which have been observed in many parts of the world oceans [124, 174], can behave as meridional transport barriers [21, 22, 193] and thus contribute to the shaping of plankton bloom distributions. In the study region, the South Indian Ocean east of Madagascar, altimetry measurements and hydrographic data have revealed a narrow and shallow eastward propagating zonal jet, known as the Southern Indian Ocean Countercurrent (SICC) [141, 160, 194]. Eventhough it runs along $\sim$25°S, the latitude where the Madagascar plankton bloom typically develops, so far, to our knowledge, the SICC has not been linked to the Madagascar plankton bloom.

Here, we investigate the relation between the SICC and the remarkable eastward extension of the Madagascar plankton bloom of up to 2000 km. While many oceanographic studies analyze mesoscale transport by focusing on Eulerian aspects of the currents, we address transport using Lagrangian methods that take into account the temporal evolution of the flow. We present the first Lagrangian description of the SICC jet based on Lagrangian Coherent Structures (LCS) that determine the global mixing patterns in the flow. We show that the SICC generates a fast coherent eastward transport and acts as a weakly-deforming LCS that widely inhibits meridional transport, both processes that control the spreading of the plankton bloom.

5.1.1 Madagascar Plankton Bloom

The Madagascar plankton bloom is one of the largest dendroid blooms in the world oceans. It develops in summer at $\sim$25°S south east of Madagascar in zonal direction, reaching from the coast of Madagascar at $\sim$47°E up to $\sim$70°E into the South Indian Ocean. The largest extent is reached in February or March in most bloom years, but a strong interannual variability exists. For an overview over bloom years see [173] and [228, Fig. 10]. A complete sequence of the evolution of the Madagascar plankton bloom in 1999 can be seen in Fig. 5.1.

Several studies have addressed the mechanisms controlling the initiation and the propagation of the Madagascar plankton bloom. In the first description of the bloom, Longhurst [108] proposes mixed layer deepening as the nutrient providing process and finds some agreement between central (peripheral) upwelling in cyclonic (anticyclonic) eddies and the chlorophyll pattern in the bloom in 1999. Srokosz et al. [198] focus on the eastward propagation of the plankton bloom and report its assumedly direction against the mean flow, obtained by tracking Eulerian features in the Sea Surface Height (SSH) field. To justify the expansion of the bloom to the east despite a supposed lack of obvious eastward transport, Srokosz et al. [198] consider a simple reaction-diffusion-advection system as a model for the front propagation. According to their calculations, and assuming a high eddy diffusivity and the Fisher-Kolmogorov-Petrovskii-Piskunov (FKPP) relation for the biological plankton front [142], they find that a plankton wave could propagate fast enough to compensate the supposed western mean flow. Uz [215] contradicts the theory of Longhurst [108] that local upwelling is the main nutrient source, as the bloom occurs in a shallow and stably stratified surface layer. He introduces the hypothesis of remote nutrient supply by river runoff at the Madagascar coast.

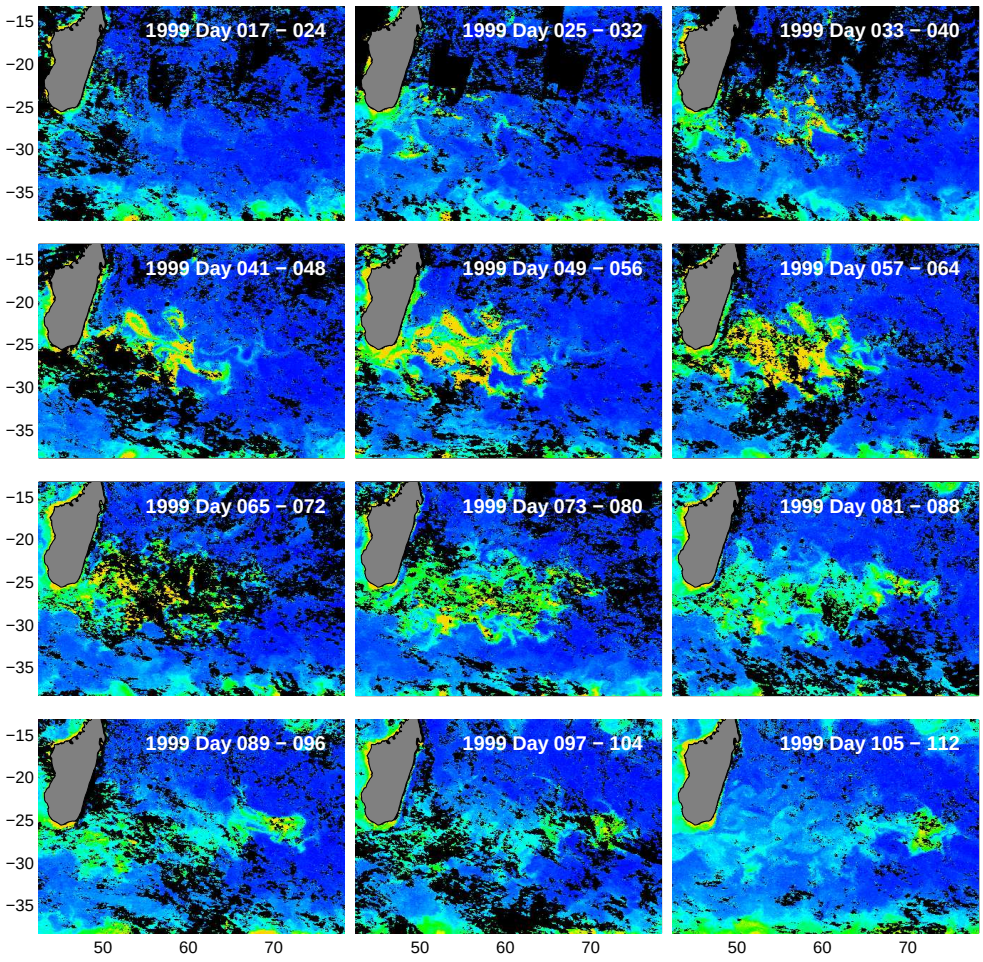

Figure 5.1: Temporal evolution of the Madagascar plankton bloom in austral summer from 17 January 1999 to 22 April 1999. The plankton bloom starts south-east of Madagascar and propagates eastward, more than 2000 km into the South Indian Ocean. Color indicates the chlorophyll concentration from $0\,\mathrm{mg/m^3}$ (blue) to $0.4\,\mathrm{mg/m^3}$ (yellow) on a linear scale as measured by the SeaWiFS sensor. Each frame shows a composite of the data of 8 days, provided by AVISO. In black regions no data is available due to cloud cover. Axes are Longitude East (horizontal) and Latitude South (vertical) in degrees.

Similarly, Lévy et al. [106] propose the upwelling of nutrients in a well-known upwelling region south of Madagascar [48, 89, 112] followed by eastward transport by a possible retroflection of the South East Madagascar Current [172] as an explanation for the bloom. However, the details of this transport mechanisms are not well understood. Raj et al. [173] explore a variety of longtime data sets and find upwelling along the south Madagascar coast, precipitation along east Madagascar, and mesoscale eddies as likely key factors influencing the bloom. All studies agree that the plankton bloom is somehow related to the high mesoscale eddy activity in the region. However, it remains unclear, how the currents act on the bloom, i.e., if they modify, favor or maybe even generate it.

5.1.2 South Indian Ocean Countercurrent (SICC)

The circulation in the South Indian Ocean near Madagascar is characterized by a complex network of strong interacting currents giving rise to a highly variable mesoscale eddy field. The East Madagascar Current (EMC), the most prominent current in the region, is considered a small western boundary current and flows polewards (south) along the eastern coast of Madagascar [172]. Its pathway and exact destination south of Madagascar is still an open question and a field of ongoing research [45, 111, 141, 172]. In this current system, a less pronounced current with special importance for this study is the South Indian Ocean Countercurrent (SICC). Only recently, it has been described in detail as a narrow and shallow eastward current, embedded in a planetary wave and eddy flow pattern [194]. It meanders eastward between $22°$S and $26°$S from the coast of Madagascar up to $80°$E and has a width of the order of 100 km. High velocities in the jet are limited to the upper 200 m, although the eastward currents partly reach down to 800m [194]. Since plankton blooms are confined to the upper 50–100 m due to light limitation in deeper water, especially the surface currents are relevant for our study. Several studies note that the SICC could be explained as a near-surface frontal jet along a meridional density front [141, 160, 194]. They also suggest that the upper layers of the EMC possibly retroflect and connect to the eastward flowing SICC, but more comprehensive observations and modeling studies are necessary to better understand the variability of these currents and their connection.

5.1.3 Transport Barriers in Jets

Jets in the ocean are fast directed currents that persist over a long time. Over certain finite times and depending strongly on the flow geometry, these jets can act as transport barriers such that fluid on both sides of the jet barely mix. A well-known example for a very large jet in the ocean is the Gulf Stream, the western boundary current of the North Atlantic. When the stream leaves the coast and flows into the open ocean it starts to meander, i.e. the jet begins to undulate around eddies that are generated next to it [185]. The propagation of meanders, their growth, and the possible pinch-off of eddies, is a complex fluid instability that can be due to barotropic and baroclinic instability [44]. It is a typical phenomenon for fast currents in rotating reference systems. Apart from the western boundary currents, many other currents meander, e.g. the different tropical countercurrents or the Antarctic Circumpolar Current. Moreover, zonal jets have been found all over the world's oceans [124, 174].

The spatio-temporal structure of the jet, in particular the dynamics of the meanders, determine the transport across the jet. In 1991 Bower [25] proposed a kinematic jet model for the Gulf stream. The study was motivated by observations with floats, and the model was used to investigate the main pathways of trajectories to be able to interpret the field experiments. This model consists of a stream function representing the basic geometry of a meandering jet and was extended with a time dependent term that accounts for periodic fluctuations of the meanders [184]. One example for this class of meandering jet flows is the following stream function (Fig. 5.2a) in a reference frame moving with the mean

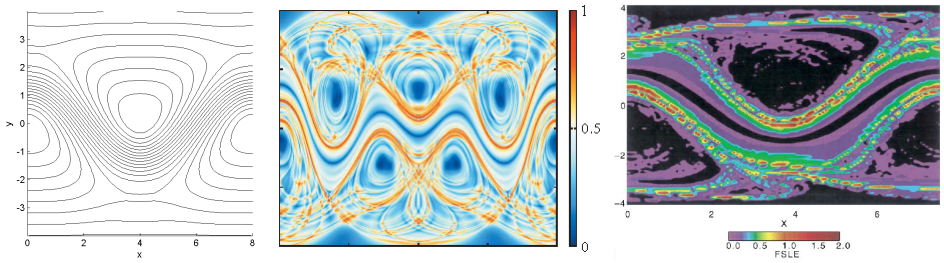

Figure 5.2: (a) Streamfunction of the meandering jet model, Eq. (5.2), with $B = 1.2$, $k = 2\pi/8$, $c = 0.2$. (b) FTLE field from a kinematic Bickley-jet model. The transport barrier at the core of the jet is characterized by small FTLE values in the added forward and backward FTLE field. From [22]. (c) FSLE field for the jet model, Eq. 5.2. The central black line can be identified as a transport barrier, where particles do not reach the finite-size separation. From [24]

velocity of the meanders [24]

$$\Psi(x,y,t) = -\tanh\left[\frac{y - B(t)\cos kx}{\sqrt{1 + k^2 B(t)^2 \sin^2 kx}}\right] + cy \tag{5.1}$$

$$B(t) = B_0 + \epsilon\cos(\omega t + \phi), \tag{5.2}$$

where $B(t)$ is the amplitude of the meanders, here periodically perturbed, k is the wave length of the meanders, and c is the uniform retrograde velocity far from the jet. It has been studied extensively, how transport and fluid exchange in this and similar jet models depend on the perturbation parameters ϵ, ω and ϕ [22, 29, 54, 184, 213, 219]. Without a temporal perturbation the flow is steady and the streamlines define three closed flow regimes: the core of the jet, the recirculation zones, and the exterior retrograde flow. Trajectories of floats or particles cannot leave these regimes and the borders of the regimes are impermeable transport barriers. Under temporal perturbation of the flow structure these borders break up, and different regions of the flow mix and exchange fluid.

Regarding the Madagascar plankton bloom, we are especially interested in the transport barrier property of the core of the jet. For a weak perturbation of the jet, this central barrier persists. Beron-Vera et al. [22] demonstrated that in the Bickley-jet model, that is similar to the model (5.2), a line of small FTLE values defines a weakly deforming Lagrangian coherent structure in the center of the jet that serves as a good estimate for a transport barrier (Fig. 5.2b). In numerical experiments, Lagrangian particles released on both sides of the jet do not cross this line, and thus, do not mix. Likewise, Boffetta et al. [24] find that particles barely separate close to the central transport barrier in the model flow described above, such that the barrier can be estimated from FSLE maps (Fig. 5.2c). In the following, we use these results from model flows to analyze the mesoscale currents in the region of the Madagascar plankton bloom and detect possible transport barriers that confine the transport of nutrients and plankton.

5.2 Data and Methods

Ocean Color We analyze the Madagascar plankton bloom based on standard global maps of chlorophyll concentration observed by the Sea-viewing Wide Field-of-view Sensor (SeaWiFS) and provided by NASA's ocean color data site (`http://oceancolor.gsfc.nasa.gov`). We use the 8-day composite level 3 product with a spatial resolution of $(1/12)^\circ \approx 9\,\mathrm{km}$ and temporal resolution of $8\,\mathrm{days}$. The measurement principles of the SeaWiFS sensor are shortly explained in Sec. A.1.

Geostrophic Velocities We consider advection by ocean currents derived geostrophically from altimetric SSH maps. AVISO provides weekly SSH anomalies at a spatial resolution of $(1/4)^\circ$ with respect to a 7-year (1993–1999) mean. These are added to the mean dynamic topography of the ocean surface based on altimetry, in-situ measurements, and a geoid model [176]. In a longitude–latitude spherical coordinate system (λ, θ) the position of a fluid particle on the ocean's surface is thus assumed to evolve according to

$$\dot{\lambda} = -\frac{g}{R^2 f(\theta)\cos\theta}\partial_\theta \eta(\lambda,\theta,t), \tag{5.3}$$

$$\dot{\theta} = +\frac{g}{R^2 f(\theta)\cos\theta}\partial_\lambda \eta(\lambda,\theta,t). \tag{5.4}$$

where $\eta(\lambda,\theta,t)$ is SSH, R the Earth's mean radius, g gravity and $f(\theta) := 2\Omega\sin\theta$ the Coriolis parameter with Ω the Earth's mean angular velocity. Here, particle trajectories are computed by integrating (5.3)–(5.4) using a Runge–Kutta scheme and a tricubic interpolation in time and space. A fine grid of particles with an initial separation of $(1/16)^\circ$ is advected to obtain fields of the Lagrangian quantities introduced below. The finite integration time is chosen to be $\tau = 12\,\mathrm{weeks}$, a typical time scale for the development of the bloom and the propagation of the jet.

Lagrangian Quantities: FTLE and FTZD Finite-Time Lyapunov Exponents (FTLE), a measure of stretching about fluid trajectories, are used here to estimate LCS as in many previous works [163, and references therein]. FTLE are computed in forward and backward time direction as suggested by Beron-Vera et al. [22]. Weakly deforming LCS, indicating meridional transport barriers, are unveiled by identifying regions where ridges of the forward and backward FTLE field do not excessively transversely intersect one another and FTLE values are relatively small [22, 24]. These weakly deforming LCS are associated with the cores of long meandering jets and thus will be referred to as jet-like LCS, in contrast to more entangled hyperbolic LCS, the locally strongest attracting or repelling material curves. Both types of LCS inhibit cross transport, so that a plankton bloom evolving on one side of such a LCS cannot be spread to the other side. More precisely, the strict barrier property of a jet-like LCS is limited by the coherence of the jet, i.e., the stability of its spatial structure under perturbations of the adjacent eddies. Real zonal jets are not always necessarily as coherent as ideal jets in model flows [22]. Thus, real zonal jets, while indeed providing a fast zonal

transport, might behave as strong though imperfect barriers with part of the water entraining and detraining along their path, leading to partial cross-mixing.

To further quantify the eastward transport, we introduce the Finite-Time Zonal Drift (FTZD) defined as the zonal distance between the final and initial position (λ_0, θ_0) of a backward advected particle

$$\delta^t_{t_0}(\lambda_0, \theta_0) := \lambda(t; t_0, \lambda_0, \theta_0) - \lambda_0 \tag{5.5}$$

with $t = t_0 + \tau$ and $\tau < 0$. It simply denotes the eastward directed zonal distance the particle has covered in the time τ.

5.3 Results and Discussion

5.3.1 Jet-like Lagrangian Coherent Structures

We search for Lagrangian coherent structures, especially jet-like LCS, in the mesoscale circulation east of Madagascar. The results of Beron-Vera et al. [21] suggest that these jet-like LCS at the center of coherent jets can be extracted from added fields of the forward and backward FTLE field. In Fig. 5.3 an exemplary forward and backward FTLE field on 31 March 1999 reveals a variety of Lagrangian structures with a typical size of $100\,\mathrm{km}$. These Lagrangian structures determine the geometry of mixing by unsteady ocean currents. Most of the dynamics is dominated by mesoscale eddies. The circular regions with very low FTLE values close to zero are associated to eddy cores with elliptic dynamics, where water circulates and neighbor water parcels stay close together, i.e. stretching is small. In contrast, the highest separation rates on the ridges of the FTLE field reach values of $1/2\,\mathrm{weeks}^{-1}$, corresponding to typical mixing time scales of $2\,$weeks or more. While we can already see a signature of the zonal SICC jet in the separated forward and backward FTLE fields, the added FTLE field in Fig, 5.4 reveals a much clearer meandering structure of small FTLE values bounded by parallel FTLE ridges along a latitude of $\sim 25°$S that mark the position of the SICC. This structure is a candidate for a jet-like LCS that acts as a barrier to meridional transport. It is important to note that the structure of the jet-like LCS in the flow given by real oceanic altimetry velocity fields is much less pronounced and more difficult to extract, if compared to the explicit numerical examples in Fig. 5.2. This is most probably due to the strong temporal variability of the SICC that considerably changes its position during the period of 24 weeks. Although it would be desirable to extract the jet-like LCS with an automatic procedure based on well-defined mathematical properties of the FTLE fields (c.f., Sec. B.1), we take here the simple approach to estimate the jet-like LCS by hand and compare its geometry to the Lagrangian patterns of the Madagascar plankton bloom.

In Figure 5.5 we exemplary choose a date during the extensive plankton bloom in 1999 to demonstrate the impact of the SICC on the spatial distribution of the chlorophyll concentration. Therefore, we extract the location of jet-like LCS and quantify the zonal transport of the SICC. We estimate two jet-like LCS (highlighted with a red line) on 17 February 1999 from the map of the added forward and backward FTLE fields (Fig. 5.5a). Along these potential transport barriers

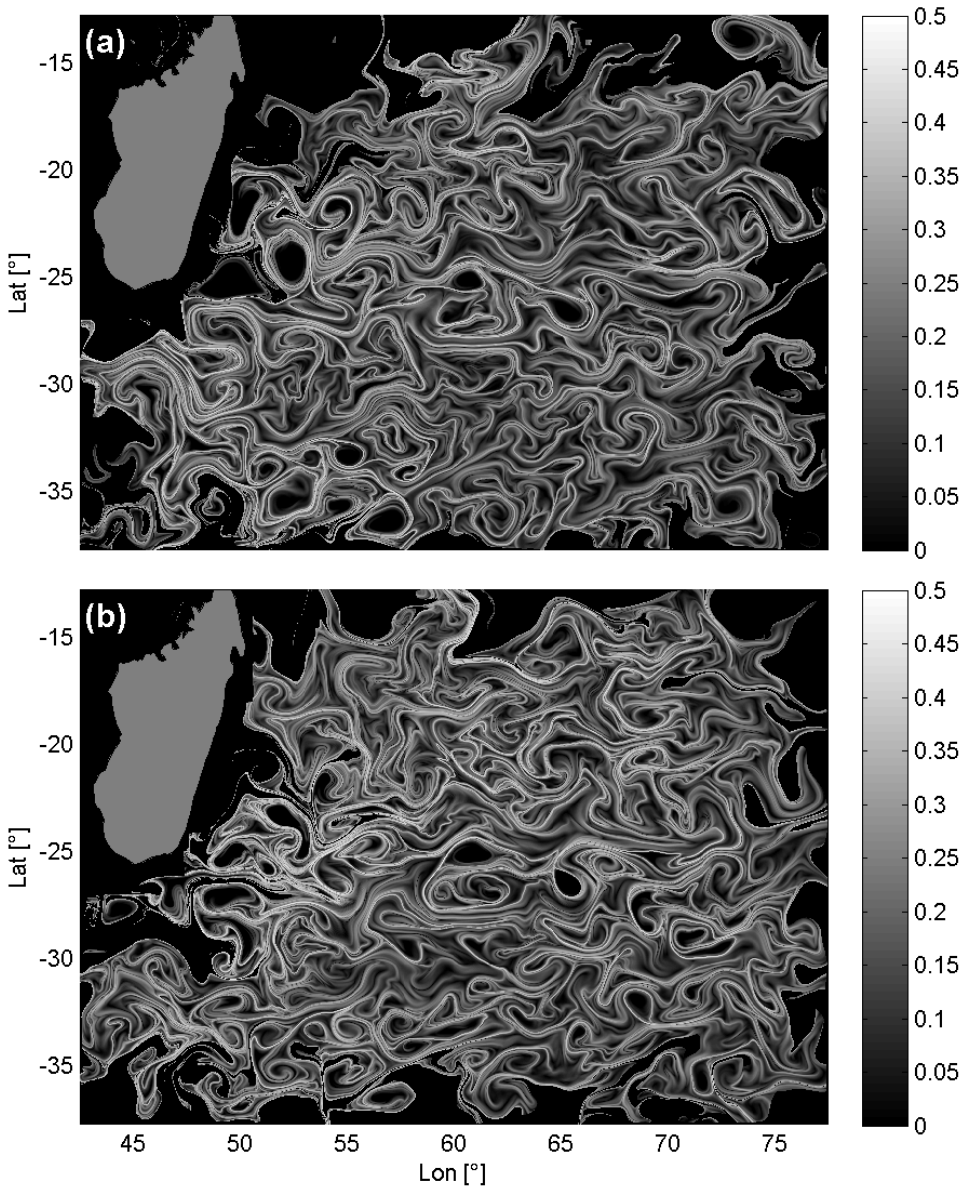

Figure 5.3: (a) Forward FTLE fields [1/weeks] on 31 March 1999. (b) Backward FTLE fields [1/weeks] on 31 March 1999. In both fields the ridges of high FTLE values mark a zonal meandering structure at $\sim 25°$S: the South Indian Ocean Countercurrent.

high gradients of tracers can be expected, and indeed, they coincide with large parts of the boundaries of the plankton bloom when compared to the spatial distribution of chlorophyll concentration in Fig. 5.5c. In some regions chlorophyll patches can be found across the jet-like LCS where the jets are leaking. This leakage can be identified with hyperbolic LCS of eddies adjacent to the jet (Fig. 5.5a), and thus can also be explained by advective transport. This is not further studied

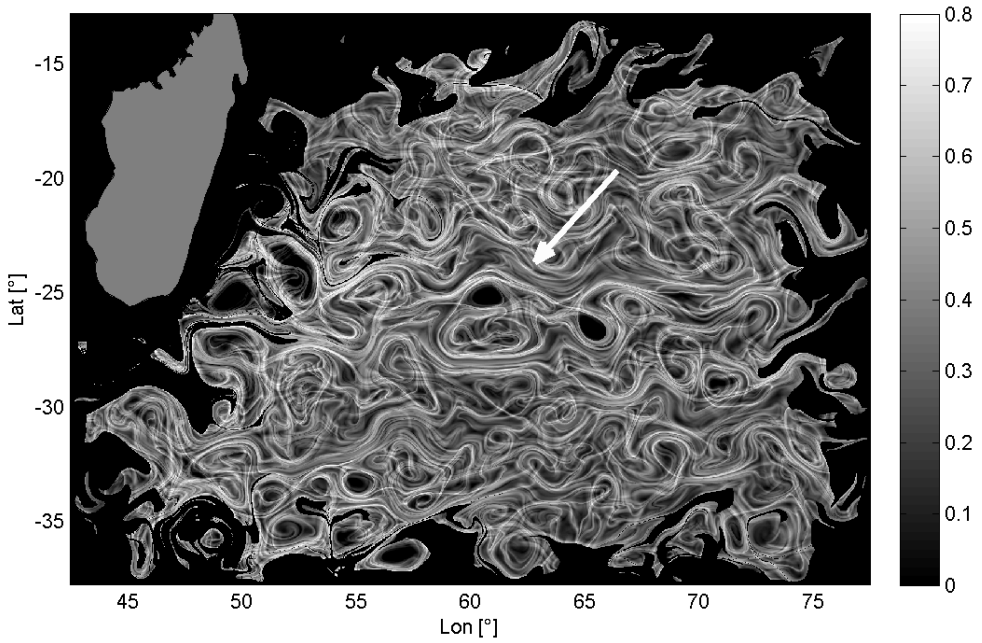

Figure 5.4: The sum of forward and backward FTLE fields [1/weeks] from Fig. 5.3. Along a meandering feature at $\sim 25^{\circ}$S (arrow) the values of both FTLE fields are small compared to adjacent regions, and ridges of high FTLE values are predominantly parallel and do barely intersect each other. This feature associated to the zonal SICC jet is a candidate for a jet-like LCS that acts as a transport barrier.

here.

Additionally to the geometric information of transport barriers revealed by the jet-like LCS, the new simple Lagrangian metric FTZD (5.5) in Fig. 5.5b allows for a spatially resolved quantification of the zonal transport east of Madagascar. This quantity is especially useful to address a possible mechanism for the fast eastward propagation of the Madagascar plankton bloom. As expected, the elongated regions (in red) with the highest eastward zonal transport match the jet's core lines represented by the jet-like LCS. Both bands of high zonal drift are bounded piecewise by backward FTLE ridges, indicating that the transport bands are well separated from adjacent water masses, and also revealing that the jets are composed of several parts rather than being one uninterrupted structure of 2000 km length. Eastward excursions of particles along these jets can be as long as $\sim$1200 km in 12 weeks, a distance comparable to a typical zonal extent of the Madagascar plankton bloom. With the underlying advection time of $12\,\mathrm{weeks}$ the jets are persistent transport bands at this time scale.

The origin of the eastward spreading Madagascar plankton bloom was proposed to be located south of Madagascar [106, 173, 215]. In order to demonstrate the ability of the SICC to transport water masses to the east from potential nutrient sources at the coast of Madagascar, we advect a passive continuous tracer concentration. The tracer is initialized as a Gaussian blob with a standard devi-

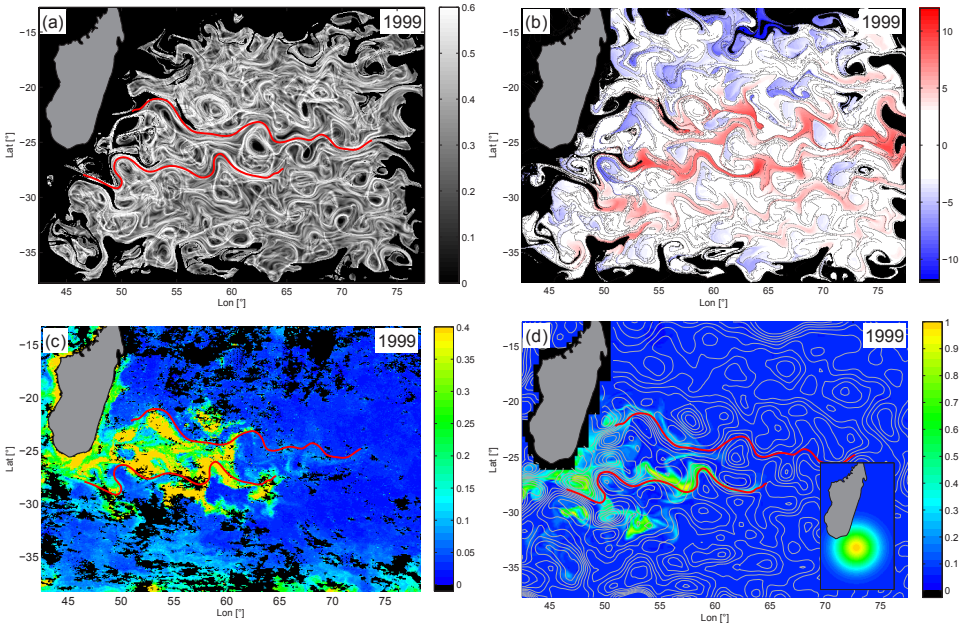

Figure 5.5: a) Instantaneous map on 17 February 1999 of added forward and backward FTLE [weeks^{-1}] with highlighted jet-like LCS inhibiting meridional transport. In black regions, tracers left the domain. b) Instantaneous map on the same date of FTZD (5.5) in units of $1^\circ\,\mathrm{Lon} \approx 100\,\mathrm{km}$. c) SeaWiFS chlorophyll concentration [$\mathrm{mg/m}^3$] with marked position of the jet-like LCS. The image corresponds to an 8-day composite centered around 21 February 1999. d) Distribution of a passive tracer [arb.u.] released as a Gaussian blob at the south tip of Madagascar. Instantaneous SSH contours are plotted in the background.

ation of ∼150 km at the south east tip of Madagascar where upwelling has been reported to take place [48, 89, 112] (Fig. 5.5d). A full sequence of the evolution of the continuous tracer can be seen in Fig. 5.6. With this numerical experiment we can verify if the ocean currents, in particular the SICC, are able to transport a passive tracer (simulating nutrient) to the east, and if the spatial distribution of passive tracer released at the south coast of Madagascar resembles the spatial distribution of the plankton bloom. This would be a clear hint that horizontal advection plays a major role for the spreading of the plankton bloom. In Fig. 5.5d two filaments of high tracer concentration extend to the east corresponding to the two present jets, while the associated jet-like LCS shape the boundaries of the passive tracer. In the background, contours of the instantaneous SSH field are plotted for comparison. Although eddies, defined as regions enclosed by SSH contours [38], drift westwards in this domain, the jets meander around them in eastward direction. This is clear evidence for a distinct eastward transport, supporting the above mentioned hypothesis that nutrient could be upwelled at the coast and be transported to the east. However, in order to obtain a maximum similarity in extent and form between the tracer pattern and the real widespread plankton bloom on 17 February 1999 (Fig. 5.7c), the tracer has to be released on

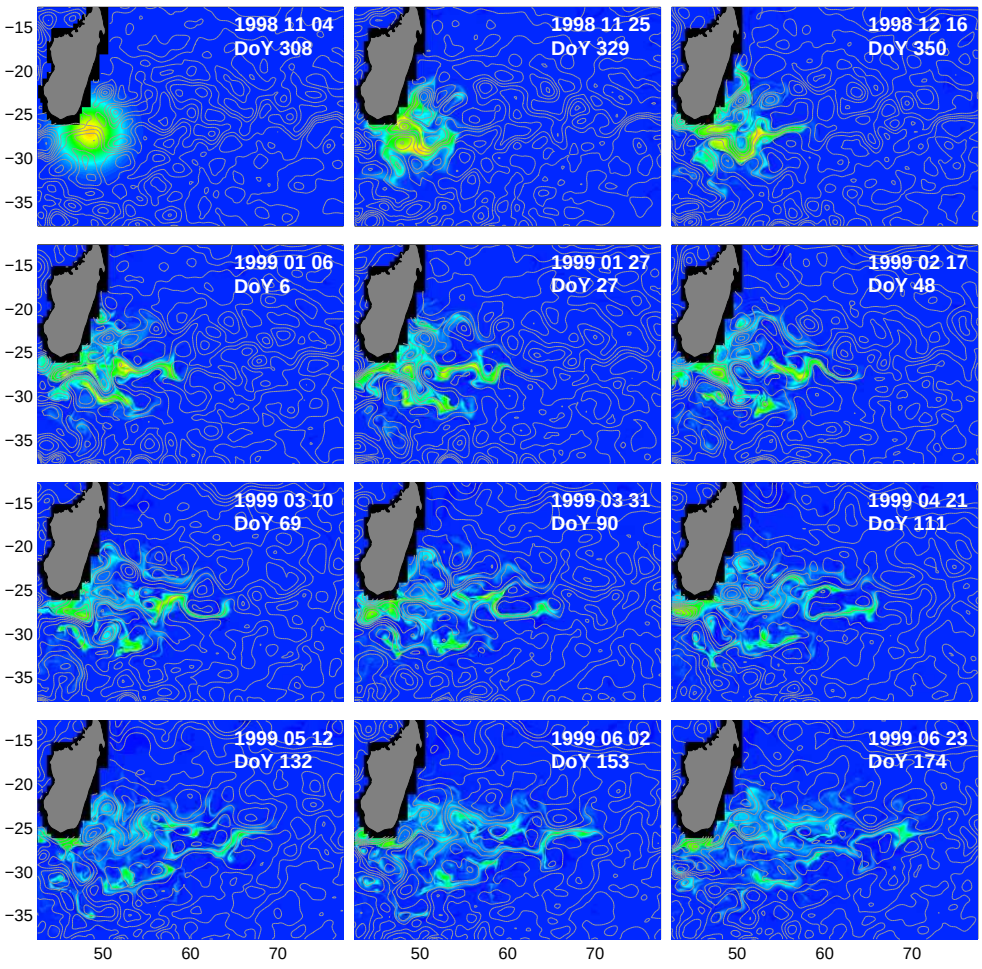

Figure 5.6: Temporal evolution of a passive tracer released as a Gaussian blob south-east of Madagascar on 11 November 1998. The tracer spreads progressively over the area that is typically covered by the Madagascar plankton bloom (cf. Fig. 5.1). Compared to the plankton bloom the pure advective eastward propagation of the passive tracer is slower. Color indicates the tracer concentration in arbitrary units, from low (blue) to high concentration (yellow). Axes are Longitude East (horizontal) and Latitude South (vertical) in degrees.

a date close to 4 November 1998, about two months before first traces of the bloom can be seen in the SeaWiFS data. On the one hand, this early release of the passive tracer may be justified with the seasonality of possible nutrient sources close to the release point, being river runoff at the beginning of the rain season or upwelling [173, 215]. On the other hand, the question arises if the velocity of the eastward transport is high enough to explain the fast eastward expansion of the plankton bloom. This question is addressed in Sec. 5.3.2.

As the first result, based on the above Lagrangian analysis of the flow conditions for the plankton bloom of 1999, we suggest two ways of impact of the zonal jets on the plankton bloom. First, a zonal jet represents a fast transport band that favors the eastward propagation of the plankton bloom. Second, a jet-like

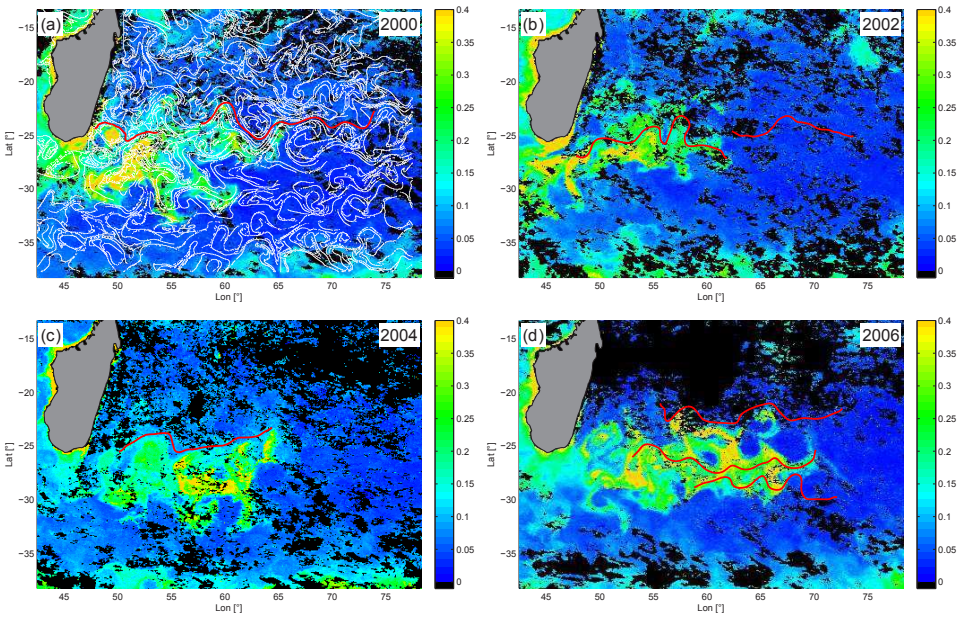

Figure 5.7: Spatial chlorophyll distributions in bloom years and jet-like LCS (red lines). a) 9 March 2000, the additionally plotted backward FTLE ridges (white lines), estimates for LCS, show that the bloom's boundaries are in large parts determined by horizontal transport. b) 10 April 2002, c) 18 April 2004, d) 13 February 2006.

LCS, sufficiently coherent over a long time, prevents meridional transport. In the following, we study both effects of a zonal jet in detail and for all bloom years.

In order to ensure that the impact of the SICC on the Madagascar plankton bloom in 1999 is not an individual case, we check other years with important plankton blooms for the same relation. Figure 5.7 shows the spatial chlorophyll distribution of the Madagascar plankton bloom with nearly maximal extent in the bloom years 2000, 2002, 2004 and 2006 respectively, overlaid with the jet-like LCS extracted as in Fig. 5.5a. In four out of five bloom years (1999, 2000, 2004, and 2006) persistent coherent jets are present along $\sim 25^{\circ}$S and the corresponding jet-like LCS largely mark the northern boundary of the plankton bloom. The jet-like LCS are embedded in a tangle of attracting hyperbolic LCS, estimated as ridges in the backward FTLE field (Fig. 5.7a). In 2002, an important part of the plankton bloom is located north of the jet-like LCS. As can be observed in sequences of the time-dependent flow, this is due to a strong perturbation of the jet at the time of the bloom, so that mixing across the jet occurs. In 2006, we observe the special case of a second jet-like LCS in the south, as also observed in 1999 (Fig. 5.5c). In both years, the jet-like LCS roughly coincides with the southern boundary of the chlorophyll data and likely represents an additional spatial confinement of the plankton bloom. Generally, in the other bloom years apart from 1999 and 2006, the southern boundaries of the plankton bloom are also shaped by LCS, but rather by more entangled attracting hyperbolic LCS (white lines in Fig. 5.7a)

	Velocity [m/s]
Plankton	~ 0.25
Particles	~ 0.14
Tracer	~ 0.14

Table 5.1: Mean propagation velocity of the chlorophyll front (plankton) estimated from SeaWiFS chlorophyll data in Fig. 5.8. Mean Lagrangian advective velocity of passive particles and the passive tracer in the SICC jet using the geostrophic flow derived from altimetry data.

than by jet-like LCS of the SICC.

5.3.2 Velocity of Plankton Front

As a result of numerical experiments with a passive tracer (Fig. 5.5d, Fig. 5.6), we found that the tracer must be released very early to resemble the spatial distribution of the plankton bloom, i.e., the plankton bloom seems to propagate faster. Therefore, in Fig. 5.8 we quantify the velocity of the eastward propagation of the plankton bloom and the velocity of the eastward transport of a passive tracer by plotting the corresponding space-time Hovmöller diagrams for several bloom years. SeaWiFS chlorophyll concentration data and the passive tracer are both averaged meridionally in the same narrow band along the principal axis of the bloom (box in inset in Fig. 5.8b) leading to a one-dimensional, time-dependent zonal concentration signal. In Fig. 5.8a, Hovmöller diagrams of the bloom in the years 1999, 2002, and 2004 show a clear eastward propagation with a similar front velocity of about $v_{pl} \approx 25^\circ/17\,\mathrm{weeks} \approx 2500\,\mathrm{km}/17\,\mathrm{weeks} \approx 0.25\,\mathrm{m/s}$, in contrast to the westward velocity of SSH features of typically $0.05\,\mathrm{m/s}$. Srokosz et al. [198] measure the front velocity of the bloom in 1999 as $\sim$0.12 m/s in a Hovmöller diagram, which we find underestimates the velocity by a factor of 2. In 2000 (not shown) the bloom expands similarly as in 2002. Only in 2006 a clear propagation of the bloom cannot be observed, as it appears rather instantaneously in the whole domain. The passive tracer (Fig. 5.8b) expands to the east along the jet in all years with a front velocity of about $v_{tr} \approx 0.14\,\mathrm{m/s}$. This is consistent with the integrated jet velocity of $v_{pa} \approx 10^\circ/12\,\mathrm{weeks} \approx 1000\,\mathrm{km}/12\,\mathrm{weeks} \approx 0.14\,\mathrm{m/s}$ estimated from the zonal transport of particles in Fig. 5.5b, as can be expected due to the same underlying geostrophic velocity data. Note the formation of tracer filaments along the jet in the insets of Fig. 5.8b that reveal a fast eastward expansion.

The analysis of the passive advected tracer in Fig. 5.8b shows that in all bloom years the jet provides a significant constant transport to the east, the direction of propagation of the Madagascar plankton bloom (Fig. 5.8a). However, we find that the magnitudes of the front velocities of the tracer and the bloom deviate (Tab. 5.1). This basically indicates that the spreading of the bloom cannot be understood as a purely passive advective process. We hypothesize that nutrients are most likely transported by the jet first, and then the biological reaction is triggered by another still unknown, possibly seasonal mechanism. Both processes are not necessarily well separated in time, i.e., the nutrient might be transported

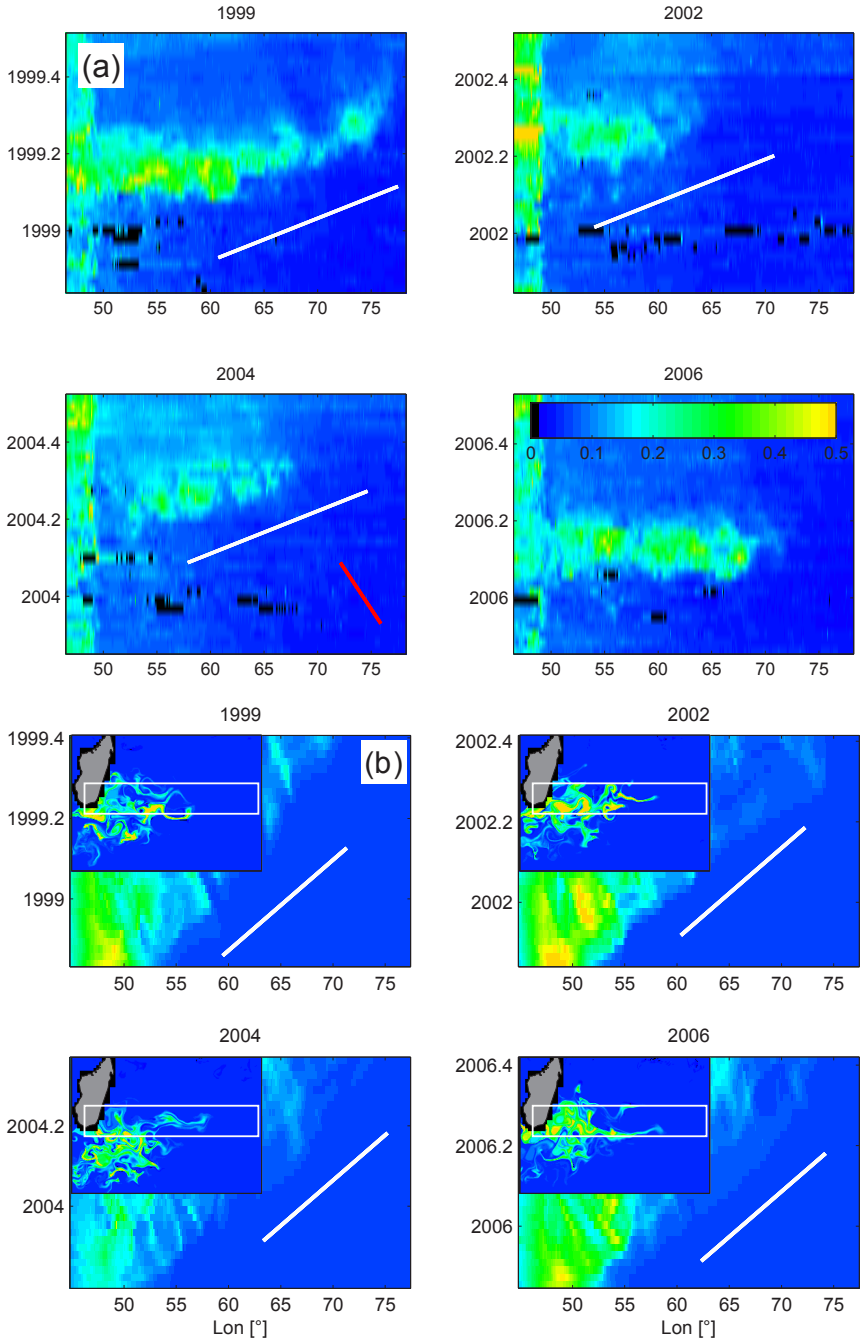

Figure 5.8: Hovmöller diagrams of plankton concentration and the passive tracer, averaged meridionally in the region shown in the insets (white rectangle). a) SeaWiFS chlorophyll data $[\mathrm{mg/m^3}]$ with a fast expansion of the bloom to the east with $\sim$0.25 m/s (white line). For comparison the westward velocity of SSH features is marked (red line). In 2006, the plankton bloom occurs at once in the whole domain, and no propagation can be observed. b) An advected passive tracer [arb.u.] expands eastwards along the jet with a velocity of $\sim$0.14 m/s (white line) in all bloom years.

while the trigger mechanism acts. It is also important to note that possible local vertical upwelling of nutrients along the jet [39] can also accelerate the front velocity and would further explain plankton growth in regions across the jet.

5.3.3 Temporal Variability of the SICC

Finally, we address the temporal variability of the eastward transport in the SICC. Since we have observed that a passive tracer is transported eastward by the jet in all bloom years, the following question arises: Is the interannual variability of the Madagascar plankton bloom related to the occurrence of the jet? It might be possible that a large intense plankton bloom preferentially coincides with a strong jet. In order to test this hypothesis, we quantify the ability of the SICC to transport water to the east using a simple measure. To this end, a large number of particles is released at time t_0 in a square region close to the coast of Madagascar and after $\tau = t - t_0 = 12\,\text{weeks}$ the easternmost final longitudinal position λ_{max} of the stretched filaments is recorded (Fig. 5.9, top)

$$\begin{aligned} \lambda_{max}(t_0) &= \max_{\lambda_0,\theta_0} \lambda(t; t_0, \lambda_0, \theta_0), \\ \lambda_0 &< 53^\circ\text{E}. \end{aligned} \tag{5.6}$$

For a fast coherent jet we expect the filament to reach far to the east, while for a weak or even absent jet no straight filaments would be observed and particles would stay closer to their origin. Figure 5.9 (middle, bottom) shows the time series of the easternmost position of the filament over ten years together with the time series of the chlorophyll concentration. No clear correlation between the intense bloom events at the beginning of years 1999, 2000, 2002, 2004 and 2006, and the eastward transport of the jet can be seen in this data. Although the length of the eastward filament fluctuates, the jet rather provides a relatively constant transport of about $8^\circ/12\,\text{weeks} \approx 800\,\text{km}/12\,\text{weeks}$ and never breaks down completely. In particular, the jet is also present and not especially weak at the beginning of no-bloom years when a bloom could be expected. These observations agree with the maps of FTZD. In these maps a band of high eastward transport, the footprint of the jet, is always present over the whole period of ten years. Hence, a strong SICC jet is most likely necessary, but not sufficient to cause an extensive plankton bloom in the region east of Madagascar.

5.4 Conclusions and Outlook

We studied the mesoscale circulation east of Madagascar based on geostrophic velocities derived from altimetry data, in order to investigate the impact of Lagrangian coherent structures in the flow on the shape and the evolution of the Madagascar plankton bloom. Two fundamental characteristics of the Madagascar plankton bloom, its eastward propagation from the south tip of Madagascar and its confinement within a narrow zonal band with low chlorophyll values in adjacent regions, can be linked to the presence of zonal jets in the South Indian Ocean Countercurrent (SICC). We focused here on the role of horizontal advection in

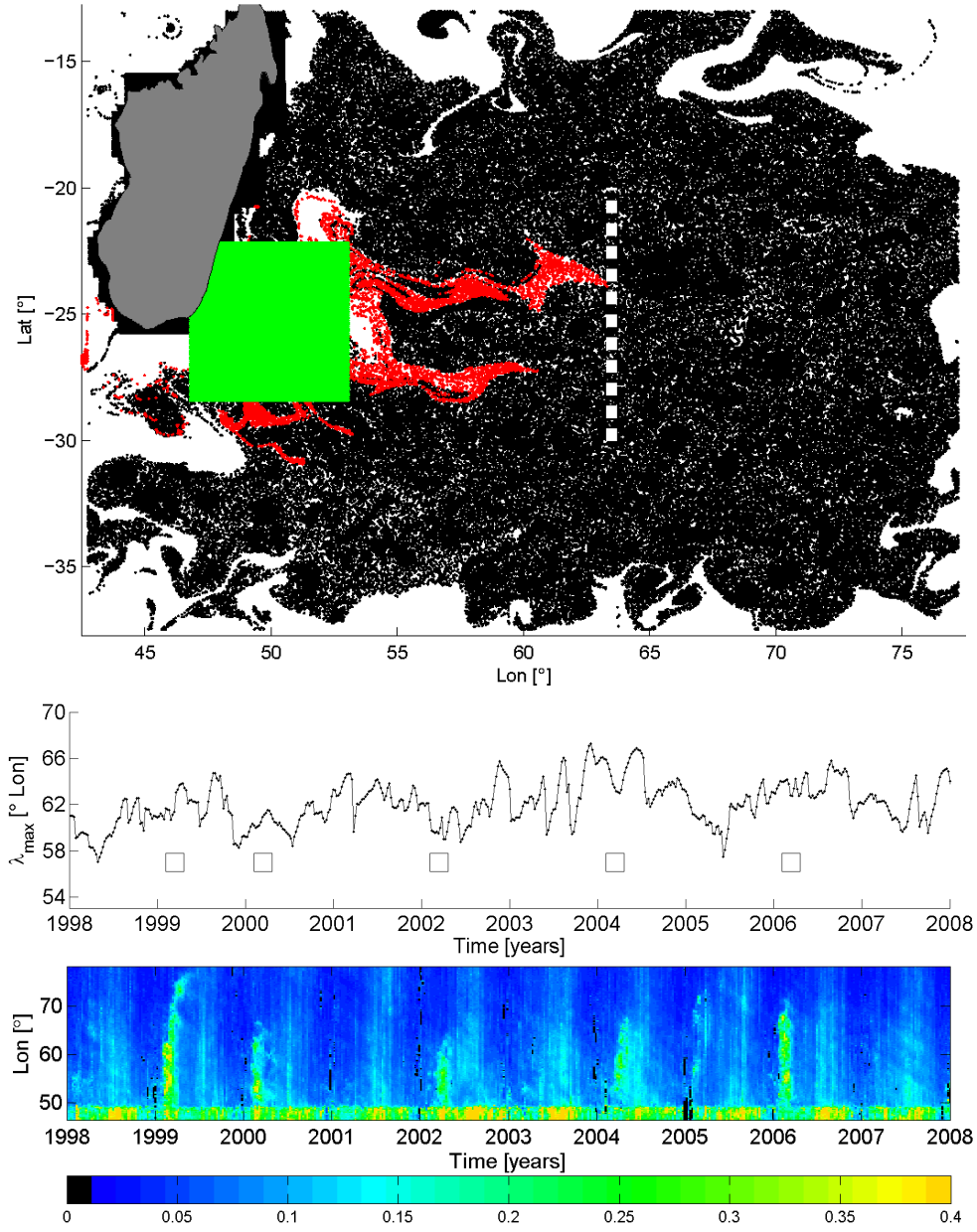

Figure 5.9: Variability of the eastward transport. (top) Particles start at the initial position (λ_0, θ_0) (green) on 31 March 1999 and are transported by the SICC jet to the final positions (λ, θ) 12 weeks later (red). The white dashed line marks the easternmost longitudinal position λ_{max} of particles belonging to the filament. (middle) Time series of easternmost longitudinal position λ_{max} of filamentous pattern. The occurrence of strong plankton blooms is marked (□). (bottom) Hovmöller diagram of chlorophyll concentration [mg m^{-3}] along a narrow longitudinal band in the main axis of the bloom. Bloom events in February/March of bloom years can clearly be seen.

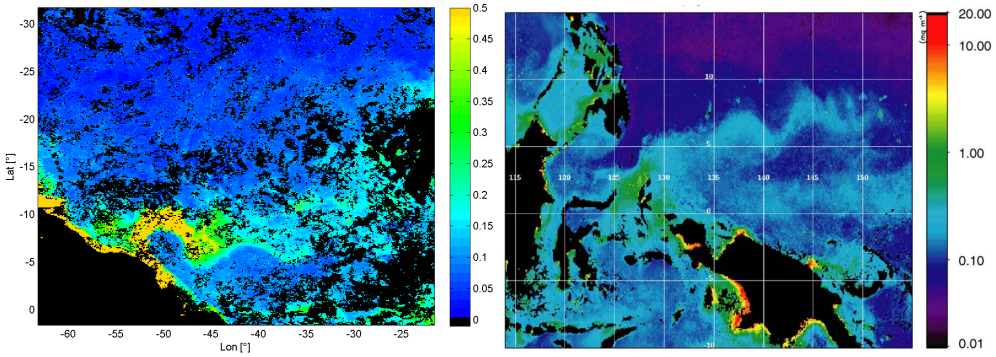

Figure 5.10: (a) Large bands of high chlorophyll concentration [mg m^{-3}] along the Atlantic North Equatorial Countercurrent off Brazil on 3 October 2000. Nutrients for the plankton bloom are provided by the Amazon plume [203]. To the south, the plankton bloom is limited by a sharp meandering boundary, most probably caused by a jet-like transport barrier. (b) Similar plankton bloom [mg m^{-3} chlorophyll] in the meanders of the Pacific North Equatorial Countercurrent on March 1998. From [39].

these jets, and, therefore, did not take into account any biochemical reaction dynamics nor diffusive subgrid motion. We suggest two basic mechanisms for the impact of the SICC jet on the Madagascar plankton bloom and draw the following conclusions:

- First, the jet provides a fast and persistent eastward transport that significantly contributes to the large extent of the plankton bloom.
- Second, zonal jet-like LCS associated with the SICC represent a transport barrier in meridional direction shaping the boundary of the bloom.
- We find that the jet alone cannot be the only reason for the plankton bloom, as the eastward jet persists throughout the years not matching the seasonality and interanual variability of the bloom.
- Additionally, we observe that the plankton front propagates with a higher velocity than the pure transport velocity of the jet.
- However, the resulting persistent eastward transport caused by the jet yield support for the hypothesis that the main nutrient source is located at the south tip of Madagascar and marks the origin of the plankton bloom [106, 173, 215].

Finally, we conclude that the recently discovered SICC causes a to date overlooked, significant rapid transport to the east at the exact location of the Madagascar plankton bloom and should not be ignored in future studies of this phenomenon. Similar plankton patterns with sharp zonal meandering boundaries can also be observed in ocean color data in the Atlantic North Equatorial Countercurrent off Brazil and in the Pacific North Equatorial Countercurrent off Indonesia

[39], see Fig. 5.10. This suggests that the results presented here may be important in other regions of the ocean where plankton blooms are stirred and possibly shaped by prominent zonal jets. It would be very interesting to apply the methods used for the Madagascar plankton bloom in those regions. However, the ocean currents for such a study could not be derived from altimetry data, since the both regions are too close to the equator, where the assumption of geostrophic balance does not hold.

Chapter 6

Flow Patterns in a Tidal Estuary - Ria de Vigo

In collaboration with A. von Kameke, S. Allen-Perkins, P. Montero, A. Venancio, and V. Pérez-Muñuzuri, published in parts in Cont. Shelf Res. 39-40, 1-13 (2012) [90].

Abstract

While in open ocean flows on the mesoscale ($50 - 500$ km) strong vortices, the mesoscale eddies, dominate the horizontal transport and mixing, in coastal flows on the submesoscale ($1 - 10$ km) coherent persistent vortices are rarely observed. Instead, the interaction of the oscillating tidal flow and intermittent wind-driven flows with the complex coastal boundary can lead to chaotic dynamics and pathways of drifting objects that are difficult to predict.

In this chapter, we study horizontal surface transport in the Ria de Vigo, an estuary in NW Spain with tidal and wind-driven dynamics. Experiments with surface drifters and the surface flow from a high-resolution 3-D hydrodynamic model are compared to each other. From the model velocity fields, we extract Lagrangian Coherent Structures (LCS) that are found to mark transport barriers for the drifters. The LCS computed for two typical meteorological situations reveal in detail the separation of the time-dependent in- and outflow at the surface of the estuary. Further, as a complimentary approach to separate the water masses flowing in and out of our region of interest, we use Synoptic Lagrangian Maps (SLM) based on high-frequency radar flow fields. SLM visualize the patches of fluid that are exchanged between different open boundaries of the flow domain.

6.1 Introduction

Chaotic horizontal transport in highly time-dependent aperiodic velocity fields occurs in many oceanic flows, e.g., in tidal-driven systems at the coast [175], or at much larger scales in the open ocean [6]. In order to analyze transport in these

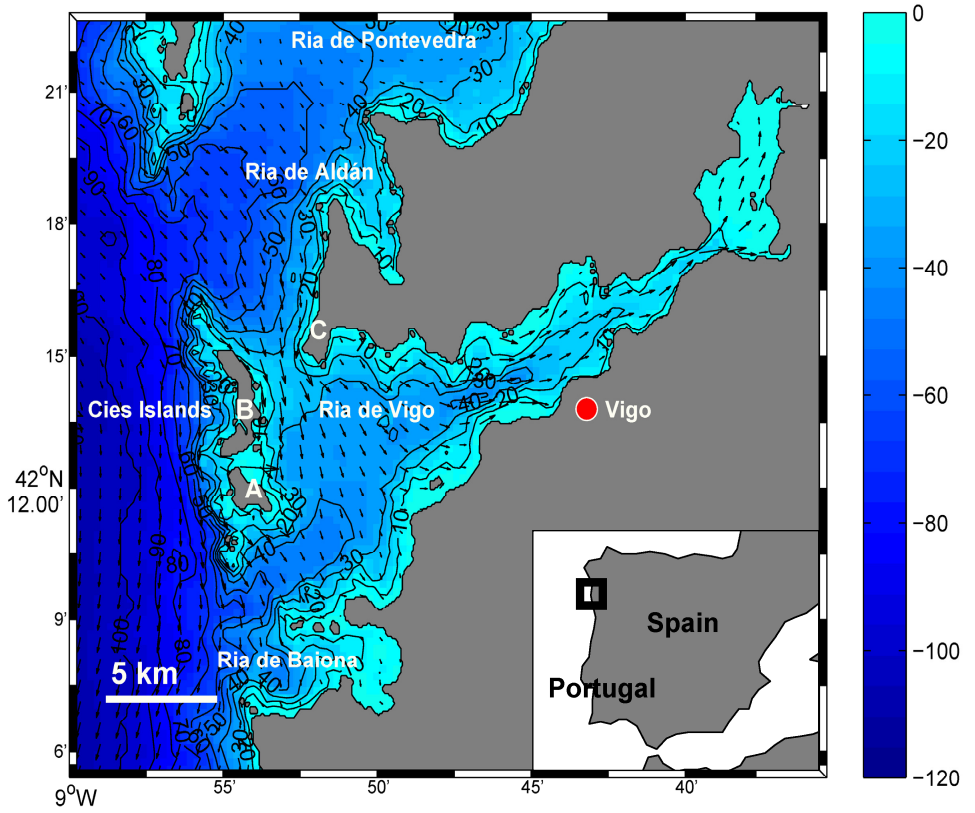

Figure 6.1: Study region: Ria de Vigo, NW Spain. An exemplary surface velocity field from the model is shown for incoming tide where each 3rd vector is plotted. Contour lines and colors correspond to the model bathymetry in meters [m]. Important topographic sites: San Martino Island (A), Monteagudo Island (B), and Cape 'Cabo Home' (C).

flows, concepts from dynamical systems theory have successfully been applied [227]. As in the previous chapter, we focus on Lagrangian Coherent Structures (LCS) here, geometrical structures that order transport in the flow [78, 93, 99], and use this Lagrangian method to examine the surface flow in the estuary Ría de Vigo in northwestern Spain. LCS are identified as the locally strongest repelling or attracting material lines and represent the core lines of Lagrangian patterns. Being material lines, i.e., a line of fluid particles, they cannot be crossed by ideal tracers. Therefore, they are transport barriers separating the flow into different water masses. As an integrated quantity, LCS are stable against errors in the velocity field [79, 88] and we demonstrate that they can still provide a sketch of the main circulation in a coastal region, when Lagrangian chaos impedes a meaningful direct comparison of single tracer trajectories. They reveal integrated Lagrangian information not directly obtainable from steady Eulerian velocity fields [24, 52, 69]. The applications of LCS to oceanic flows range from observations of the general ocean circulation [20, 51] to very specific exchange processes across jets [129] or fronts [116]. The LCS method has been used to understand the spreading of

plankton blooms (Chap. 5) [91, 100, 151, 152, 165] and to manage and predict the transport of contaminants and pollution in coastal waters [41, 103, 202], as well as to diagnose the mixing during oil spills [132].

LCS in Coastal Flows Only recently, coastal flows have been in the focus of studies using LCS. In the Gulf of Eilat, Israel, Gildor et al. [72] observe a clear temporary transport barrier between two water masses in high-frequency radar data. Two other studies are located in the Gulf of La Spezia, Italy [87], and in Monterey Bay, California, USA [191]. Both compare LCS from high-frequency radar velocity fields to surface drifters and find that the LCS determine the trajectories of the drifters. Coastal flows are especially challenging due to their complex 3-dimensional boundaries, a lack of isotropy of the underlying velocity fields, and a large variety of intermittent forcings and physical processes, such as unsteady wind influenced by the coastal topography. Yet, coastal regions are of great ecological and economical interest, they are often densely populated, and thus, the intensified investigation of transport in the coastal currents as a key process is necessary.

6.1.1 The Ria de Vigo - A Tidal Estuary

Our study region, the Ria de Vigo, is the southernmost of the four estuaries *Rias Baixas* in Galicia at the NW coast of Spain which is shown in Fig. 6.1. It has a typical V-shape and gradually deepens and widens towards its mouth. The Cies islands divide the mouth into a smaller northern mouth and a larger southern mouth [47, 73]. Being situated in the Iberian coastal upwelling system, the longterm circulation pattern with a time scale of several days to some weeks is determined by periods of northerly winds causing upwelling (typically in summer) and periods of southerly/westerly winds causing downwelling (typically in winter) [62, 145, 229]. The circulation and the resulting transport have been studied experimentally (deCastro et al. [47], Piedracoba et al. [167] and references therein) and by means of models [71, 73, 133, 138, 196, 204, 209]. In case of upwelling, the cold, nutrient-rich upwelled water generates a high biological production and gives rise to an intense human use of the estuary in terms of aquiculture of fish and shellfish [61]. However, contaminations and harmful algae blooms can threaten the productivity and the balance of the ecological system [64, 206]. Therefore, a better knowledge of transport patterns in the Ria de Vigo is desirable.

In this study, we concentrate on the outer region of the estuary, where the interaction of the tidal flow with the wind-driven longterm flow along the coast leads to interesting chaotic dynamics. We investigate the horizontal surface transport at the submesoscale ($1 - 10\,\mathrm{km}$) based on the high resolution hydrodynamic model MOHID and experiments with surface drifters. In particular, we compare experimental Lagrangian drifter data to the transport predicted by this hydrodynamic model. For our artificial tracers we concentrate here on the most important forcing: the water current. This might lead to discrepancies to the real drifters, which are subject to further forcings, such as wind. Indeed, the accuracy of modeled drifter trajectories can be improved by taking into account a variety

of proposed forcings, e.g., wind, waves or parametrized diffusion-like small scale transport [4, 56, 68, 144, 146, 147, 171]. We show that LCS in velocity fields from a coastal model are an extremely useful way to interpret the predicted transport. Coastal hydrodynamic models might not be as accurate as direct measurements of the surface currents via High Frequency (HF) Radar [87, 137, 191, 214], but they can be available in coastal regions where HF Radar systems have not (yet) been installed and provide the possibility of a prediction of several days. While classical numerical tracer particle studies of contaminants, sediments or biological tracers are common, e.g. [32, 33, 42, 49, 138], only recently, flows of coastal models have been analyzed using the LCS concept [27, 86]. We stress that we concentrate on the surface flow here, while decisive dynamics at the coast also involve the vertical dimension.

6.2 Data

6.2.1 MOHID - The Hydrodynamic Model

For our analysis we use the hourly output of the high resolution, 3-dimensional baroclinic hydrodynamic model MOHID (www.mohid.com) that is run operationally by MeteoGalicia (www.meteogalicia.es), the official Galician meteorological service. The MOHID model was developed at MARETEC at the Technical University of Lisbon and has shown its ability to simulate complex coastal and estuarine flows [40, 122]. It solves the three-dimensional incompressible primitive equations assuming hydrostatic equilibrium and the Boussinesq approximation [136]. The turbulent vertical mixing coefficient is determined using the General Ocean Turbulence Model (GOTM) [30].

Implementation and Boundary Conditions The model is implemented with three nested grids of increasing resolution. The largest grid has an extend of about $330 \times 390\,\mathrm{km}^2$ covering the entire Galician coast and parts of the Portuguese and Cantabrian coast with a resolution of $0.06^\circ \approx 6.7\,\mathrm{km}$. It receives boundary conditions from the POLCOMS model of the Spanish Operational Oceanographic System (www.eseoo.org). The POLCOMS model itself is forced by data of UK Met Office's data assimilating FOAM oceanographic model and the Spanish AEMET's HIRLAM atmospheric model. Tidal data enters from Aviso's data assimilating FES2004 product via a barotropic grid of Western Iberia. Atmospherical forcing is provided by a WRF (Weather Research and Forecasting) Model at 12 km resolution with boundary conditions from NOAA's GFS (Global Forecast System) model. The second grid has a resolution of $0.02^\circ \approx 2.2\,\mathrm{km}$ and comprises the four estuaries Rias Baixas, the southernmost of which is the Ria de Vigo. The finest model grid for the Ria de Vigo that we use in this study (Fig. 6.1) has a resolution of 300 m (156×153 grid points) and is integrated with a time step of $30\,\mathrm{s}$. It receives boundary conditions from the second grid and is forced by WRF wind data at a resolution of 4 km. The operative scheme is composed by a preliminary spin-up of five days hindcast followed by a three day forecast. For the next prediction the new initial condition is generated by running the previous day,

Table 6.1: Drifter experiments

#	Date dd/mm/yyyy	Drifter type	Drogue shape	Drogue length [m]	Number of drifters	Duration [h]
1	15/06/2009	Marexi TRBUOY	nylon tube	1	2	27
2	14/07/2009	Albatros MD02	nylon cone	1	2	25
3	04/08/2010	Albatros MD02	nylon cone	2	3	24
4	14/09/2010	Albatros MD02	nylon cone	2	4	24

starting with the hindcast output and using assimilated local meteorological data during the integration. Freshwater river outflow into the Ria de Vigo is predicted by the SWAT (Soil and Water Assessment Tool, http://swatmodel.tamu.edu). An accurate bathymetry is crucial for the model. Here, it was constructed based on data from the Spanish Hydrographic Institute. The bathymetry is widely reliable, however it must be mentioned that even at the high resolution of $300\,\mathrm{m}$ the accuracy might be limited at some extreme locations, e.g. details of the flow in the channel between the Cies Islands cannot be resolved.

Vertical Structure The vertical dimension of the model grid is structured in 16 Cartesian z-level layers with an increasing resolution towards the surface boundary layer. We use the uppermost surface layer of the 3D velocity output of the model to advect artificial tracers in two-dimensional space. The depth of this layer varies between $1\,\mathrm{m}$ and $3\,\mathrm{m}$ as the tidal elevation adds to this layer, but generally corresponds to the typical length of the drogues of the drifters. For the artificial tracers we assume that the vertical velocities close to the surface are negligible compared to the horizontal velocities, since the water surface imposes a boundary condition of zero vertical flow [27]. This is especially justified for floating tracers. We tested the positions of the resulting LCS computed from the upper three layers and obtained only small differences. For these reasons, in the following we choose the uppermost water layer only. For the further Lagrangian analysis the hourly velocity fields from the model are used.

The model was designed as an operational model that captures the general circulation in the Ria de Vigo, i.e., the propagation of the tidal wave in the complex bathymetry and the response of the flow to changing wind forcing, which drives the important longterm flow on the shelf with typical time scales of days to weeks [167]. Due to its hydrostatic approximation that neglects the vertical acceleration of fluid parcels [117] it might not accurately represent some physical processes as e.g. non-linear internal waves, Kelvin-Helmholtz instabilities under a fast spreading freshwater plume [192] or upwelling filaments [34]. However, these processes do not dominate the dynamics in the Ria de Vigo and hardly influence the drift of surface drifters. Internal waves have been reported to form on the shelf [63], but there is no clear evidence that they enter the Ria de Vigo and alter the horizontal circulation.

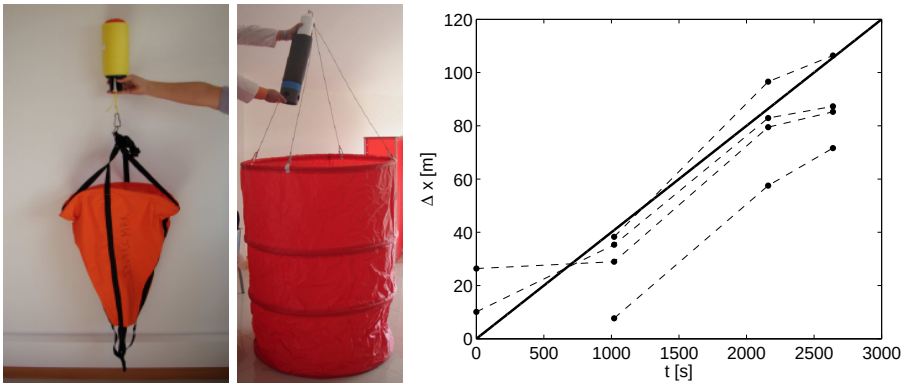

Figure 6.2: (left) Albatros MD02 drifter with a cone-shaped nylon drogue at $1\,\mathrm{m}$ depth. (middle) Marexi TRBUOY drifter with tube-shaped nylon drogue at $1\,\mathrm{m}$ depth. (right) Estimated wind slip of the MD02 drifter drogued with a nylon cone at $1\,\mathrm{m}$ depth at a wind speed of $\sim 2\,\mathrm{m/s}$. Dashed lines show the distance Δx [m] between four drifters and a dye patch in the water that served as a reference point. The wind slip velocity can be estimated as $\sim 4\,\mathrm{cm/s}$ as indicated by the black line.

6.2.2 Drifter Experiments and Data Processing

Drifter experiments in the Ria de Vigo were carried out by the Technological Institute for the Monitoring of the Maritime Environment (INTECMAR) in Vilagarcía de Arousa, Galicia, Spain, in the framework of the AMPERA funded DRIFTER project 'HNS, oil and inert pollution: Trajectory modeling and monitoring'. Data were collected for the project during 17 experiments over a period of 22 months from December 2008 till September 2010 in two Galician estuaries, the Ria de Arousa and the Ria de Vigo. The subset of data in the Ria de Vigo comprises 55 drifter trajectories. Drifters were deployed in clusters inside the Ria de Vigo, left in the water over night, and recovered the following day. Therefore, the mean duration of the trajectories is $19\,\mathrm{h}$ with a duration of $4\,\mathrm{h}$ for the shortest and $32\,\mathrm{h}$ for the longest drifter run. The total drifter time is 1077 drifter hours.

Characteristics of Drifters The original experiments were designed to compare different types of drifters and drogues for the management of contaminations and oil spills. For our study, we selected four drifter runs out of the entire data set fulfilling two criteria (Tab. 6.1): the drifters must have sufficient current following properties (equipped with an effective drogue) and trajectories must be in the vicinity of LCS computed from the model flow. In Tab. 6.1 we show the four selected drifter runs with two types of drifters fulfilling these requirements (Fig. 6.2): the MD02 drifter of Albatros Marine Technologies in three drifter launches, and the TRBUOY drifter of Marexi Marine Technology in one drifter launch. The MD02 drifter is a small coastal drifter that is robust due to its foam protection and therefore suitable for applications close to rocky coasts. Both drifters transmit their GPS position by sending SMS via the GSM system to a modem connected to a PC. GSM net coverage is limited to coastal areas impeeding offshore use of

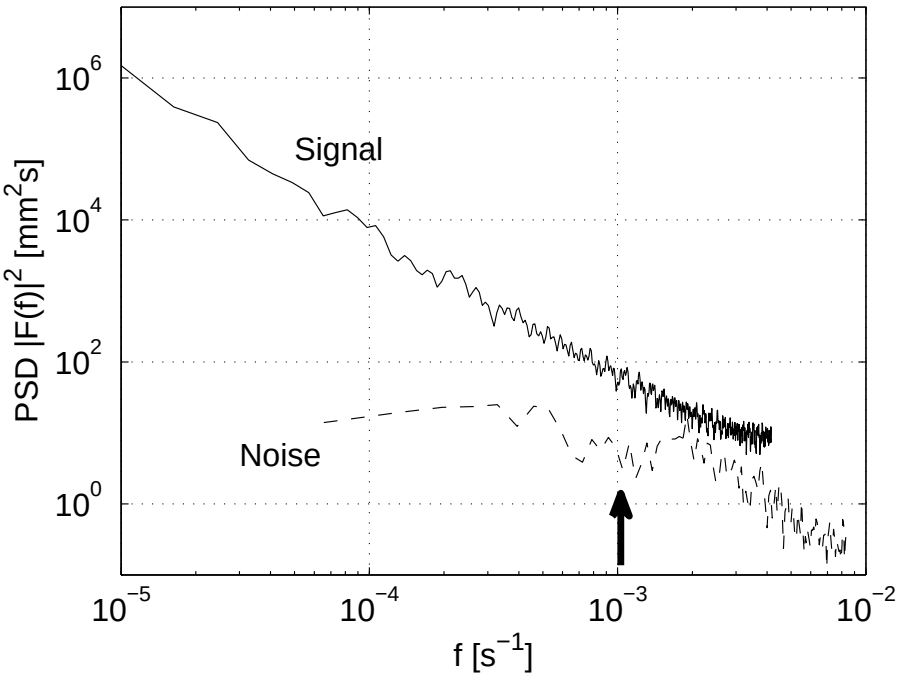

Figure 6.3: Signal to noise ratio of drifter trajectories from Experiment 4. The signal of the drifter position (solid line) is compared to the noise signal (dashed line) of a stationary positioning test. For frequencies $f < 10^{-3}s^{-1} \approx 1/16\,\mathrm{min}^{-1}$ the signal to noise ratio is larger than 10, i.e. the signal represents real drifter displacements. In contrast, above this frequency, the signal of the drifter position is of the same order as the noise due to uncertainties of the GPS position. Hence, the high-frequency signal is dominated by noise and is therefore filtered out.

these drifters. Wind slip could be estimated from a single experiment with moderate wind of $\sim 2\,\mathrm{m/s}$ where a dye patch was present as a reference point [171]. It turned out to be less than $4\,\mathrm{cm/s}$ for the MD02 drifter analyzed here (Fig. 6.2). For the MD02 drifter the standard deviation of the GPS position was estimated to be approximately $13\,\mathrm{m}$ by means of an experiment where 3 drifters were fixed at a constant position for $3\,\mathrm{h}$. This error is in the upper range of typical values reported by other studies [146, 200]. For the TRBUOY drifters the characteristics are expected to be likewise due to a similar construction as the MD02 drifter, although no systematic analysis of the uncertainties was made.

Processing of Drifter Data Drifter position data were recorded at a period of 10-15 min for most experiments and the period was decreased to 5 min for the last two experiments. All data were interpolated linearly to a time series with a $2\,\mathrm{min}$ time step and then lowpass filtered with a cutoff frequency of $1/15\,\mathrm{min}^{-1}$. Johnson and Pattiaratchi [94] give a valuable criterion for the cutoff frequency. They compare the frequency power spectrum of drifter trajectories to the spectrum of a stationary test (noise) and filter out high frequencies with a signal to noise

ratio smaller than 10. For our data, the frequency spectra of the drifter trajectories and of the noise due to GPS uncertainties are plotted in Fig. 6.3. The frequency threshold below which the signal to noise ratio is larger than 10 is around $f = 1/16\,\mathrm{min}^{-1}$ corresponding to the cutoff frequency of the filter used. In order to compare the velocity of the drifters to the velocity from the model, a further low pass filtering of the drifter trajectories up to the Nyquist frequency of the model of $1/2\,\mathrm{h}^{-1}$ would be appropriate. However, this does not change the drifter trajectories significantly. Drifter positions at full hours and Lagrangian velocities, derived by finite differencing, are then compared to the FTLE fields and Eulerian velocities obtained from the hydrodynamic model.

6.3 Methods - Lagrangian Coherent Structures from Model Velocity Field

In order to extract Lagrangian Coherent Structures we compute fields of the Finite-Time Lyapunov Exponent (FTLE) from the discrete hourly velocity data set of the hydrodynamic model as described in Sec. 2.3.3. Artificial tracers have an initial separation of $60\,\mathrm{m}$ corresponding to 5×5 tracer particles per model grid cell $(300\,\mathrm{m})$. Tracers are advected forward and backward in time in order to obtain estimates of repelling (stable, divergent) and attracting (unstable, convergent) hyperbolic manifolds. We present the combined FTLE fields $\Lambda^{\pm}(\mathbf{x}, t, \tau)$ computed as [51]

$$\Lambda^{\pm}(\mathbf{x_0}, t_0, \tau) = \Lambda^{+}(\mathbf{x_0}, t_0, \tau) - \Lambda^{-}(\mathbf{x_0}, t_0, \tau) \tag{6.1}$$

where $\Lambda^{+}(\mathbf{x}, t, \tau)$ is the forward FTLE field with $\tau > 0$ and $\Lambda^{-}(\mathbf{x}, t, \tau)$ is the backward FTLE field with $\tau < 0$.

Generally, the resolution of the FTLE fields is significantly higher than the velocity fields from the model due to the 5×5 tracer particles per model grid cell. The subgrid information in the FTLE field is contained in the time-dependent velocity field and can be considered real [88]. It stems from the integration of the velocity field along the trajectories of artificial tracers that have a length much longer than a grid cell. Moreover, subgrid flow structures can be contained in the temporal dependence of the velocity field.

Integration time In order to obtain meaningful FTLE fields, the finite advection time τ has to be chosen carefully. It defines the time scale of the Lagrangian processes that will be mapped in the FTLE fields. For small times τ, the probability distribution function (pdf) of the FTLE values is dominated by the distribution of the local instantaneous strain rate [6] and spatial FTLE fields do not show linear structures. For large times τ, the pdf converges very slowly to its asymptotic form, which in the case of a delta function denotes a uniform FTLE field without any spatial information. Figure 6.4 shows this evolution for the pdfs of FTLE fields in the Ria de Vigo. We use the pdfs of FTLE values here to investigate the influence of the tidal flow. Obviously, in Fig. 6.4b the curves of the pdf's mean and standard deviation carry the imprint of the tidal semi-diurnal (and quarter-diurnal) frequency. This reflects that the separation of tracers in the flow does not evolve

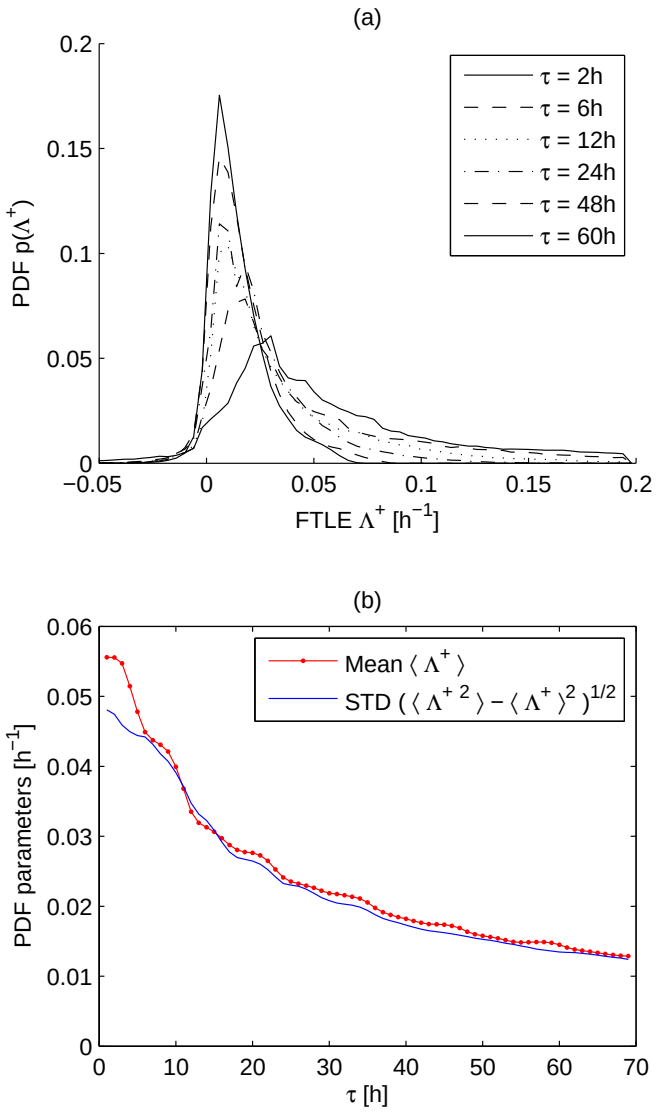

Figure 6.4: Tidal influence on particle separation. a) Typical probability distribution functions of a coastal FTLE field $\Lambda^+(\tau, \mathbf{x})$. Distributions become narrower and more peaked for increasing advection time τ. b) The evolution of the pdfs with increasing advection time τ shows an imprint of the tidal time scales, i.e. the pdf parameters *mean* and *standard deviation* show semi-diurnal and quarter-diurnal periods.

gradually, but intermittently with the tidal oscillations in the flow. Similarly, Orre et al. [155] reports that relative and absolute dispersion in a tidal model in a Norwegian fjord depend strongly on the tidal cycles and mixing predominantly happens during times of high velocities between high and low tide. However, the evolution of the pdfs in Fig. 6.4 does not indicate a strong oscillating behavior. Meaningful LCS can thus be obtained with τ close to a typical time scale of the flow. We choose $\tau = 24\,\mathrm{h}$ for the FTLE fields shown. This time can be extended

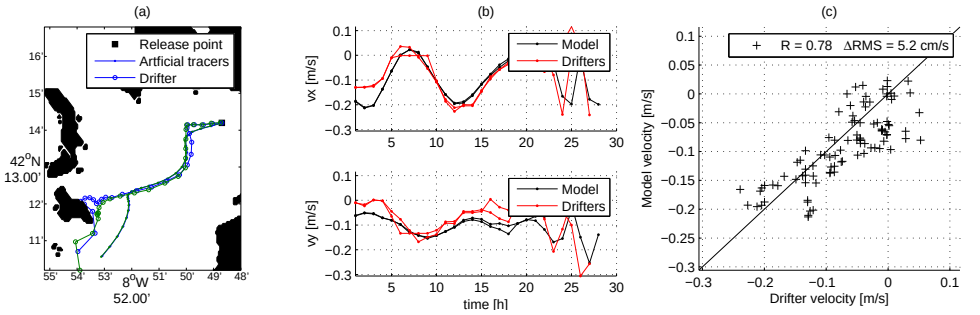

Figure 6.5: Experiment 1. a) Trajectories of drifters and artificial tracers. b) Comparison of the Lagrangian velocity of the drifters with the Eulerian velocity of the model interpolated to hourly drifter positions. c) Scatter plot of Eulerian model velocity and Lagrangian drifter velocity components shown in b) revealing the degree of correlation between both.

for calm meteorological situations, when the mean flow in the Ria de Vigo is small and sharp FTLE ridges do not appear until τ reaches several days. Finally, it must be mentioned that the studied coastal flow can be subject to several transitions, especially coupled with the wind forcing, so the choice of the advection time remains a subtle task [28]. Once reliable FTLE fields are obtained, estimates of the manifolds, representing the LCS, are extracted as ridges in the forward and backward FTLE field separately [181, 190] as described in Sec. B.1.

6.4 Results and Discussion

6.4.1 Comparison of Trajectories: Drifters - Model

We compare trajectories of the real drifters to trajectories of artificial tracers that are advected with the model velocity data. Apart from the wind forcing entering the hydrodynamic model, we do not use any additional direct wind forcing on the artificial tracers. We are aware that the drifters could be modeled in a more sophisticated way, taking into account its vertical extension at the boundary of the wind and water flow. Possible effects are drifter displacement due to wind, wave-induced Stokes drift and sub-scale dynamics not resolved by the hydrodynamic model. Including these additional forcings can lead to a better agreement between the trajectories of modeled tracers and real drifters when appropriate data of the forcings are available [68, 171]. Such a detailed model of drifting objects is especially desirable for search and rescue missions or for operational pollution management. Here however, the objective is to study the surface transport as predicted by the operational model and therefore we use the same ideal point-like tracers for the direct comparison of trajectories as for computing the FTLE fields. The uppermost layer of model velocity data is the most appropriate to compare to our Lagrangian data of real drifters. In the following, the term 'tracer' is used shortly for 'artificial tracer' in contrast to 'drifter' for the real drifters.

Figures 6.5 to 6.8 show the four drifter experiments considered due to the

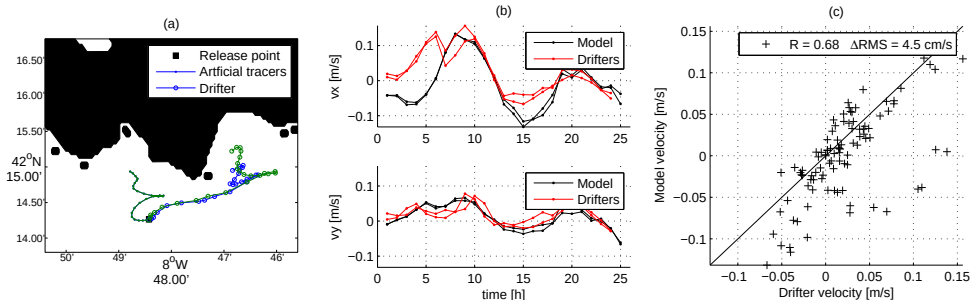

Figure 6.6: Experiment 2. Corresponding diagrams as in Fig. 6.5.

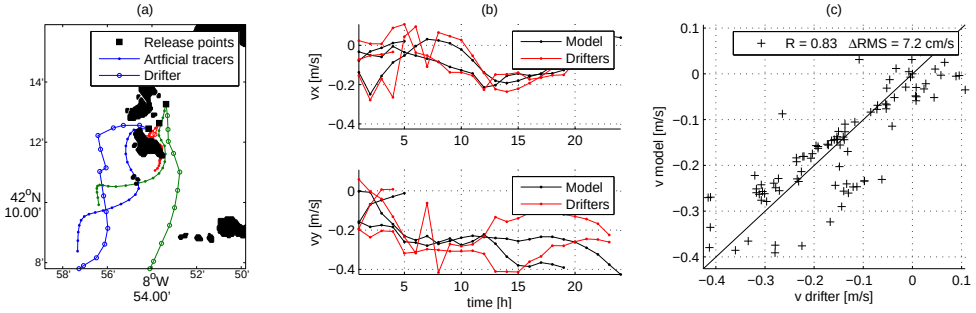

Figure 6.7: Experiment 3. Corresponding diagrams as in Fig. 6.5.

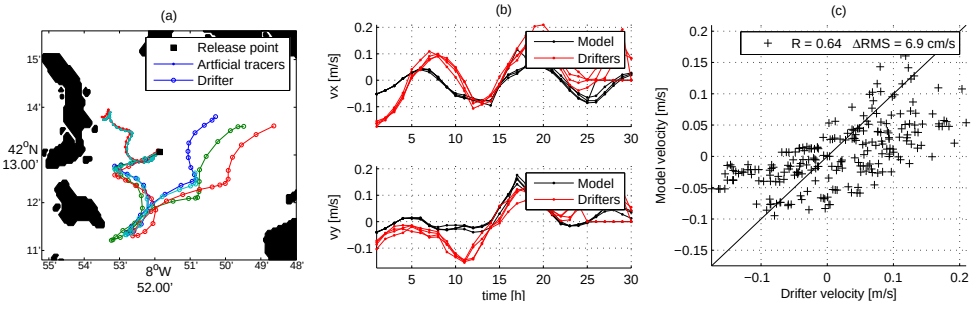

Figure 6.8: Experiment 4. Corresponding diagrams as in Fig. 6.5.

presence of LCS that interact with the drifter trajectories. The first panel (a) respectively shows the trajectories of real drifters and artificial tracers starting at the same release point. The other two panels (b) and (c) compare the Lagrangian velocity of the drifters with the Eulerian velocities of the model interpolated at the actual drifter position, in order to interpret the separation of trajectories. Drifter velocities are estimated from finite differencing of the hourly position data and the Eulerian velocity of the model is a linear interpolation of the two-dimensional model velocity field at the surface to the drifter position. Note that the latter is not

Table 6.2: Comparison of real drifters with artificial tracers.

#	d/D	Separation rate [km/h]	Form of trajectories	RMS(Δv) [cm/s]	R_{corr}
1	0.3	4/12	directional	5.2	0.78
2	1.0	3/24	oscillating	4.5	0.68
3	0.5	5/12	directional	7.2	0.83
4	1.0	3/24	oscillating	6.9	0.64

the Lagrangian velocity of the artificial tracers, but velocities are compared along the trajectories of the real drifters. Panels (b) show that the modeled velocities are in a reasonable agreement with the measured drifter velocities. A strong tidal signal with a semi-diurnal period can always be seen in both data sets that identifies the tide as the main forcing for both. In panels (c) correlation coefficients R_{corr} are around 0.8 for experiments 1 and 3, while in experiments 2 and 4 the agreement is lower with correlation coefficients of 0.68 and 0.64 respectively. An overview can be found in Tab. 6.2. We also quantify the deviation between drifter and model velocity components as $\Delta v_i = v_i^{drifter} - v_i^{model},\ i = x, y$. The root-mean-square deviation $\mathrm{RMS}(\Delta v) = \langle \Delta v^2 \rangle^{1/2}$ is a measure of the typical deviation between model and drifter velocities. It is in the order of $5\,\mathrm{cm/s}$ for our experiments (Tab. 6.2), similar to other studies where coastal drifters are compared to current data from High Frequency (HF) Radar [137, 147].

Despite the reasonable agreement of the velocity data, the real and artificial trajectories in experiments 2 and 4 separate drastically. The drifter trajectories of these two experiments show how slight velocity differences between the artificial and real tracers at the beginning of the experiment (here mainly in the x-direction, Fig. 6.6b and 6.7b) lead to strongly diverging trajectories in the following 24 hours. This divergence is partly due to the inherent behavior of Lagrangian chaos where small initial separations grow exponentially in time.

In order to quantify the accuracy of trajectory prediction (with velocity data from High Frequency (HF) Radar), Molcard et al. [137] and Ullman et al. [214] set the separation of drifters and artificial tracers

$$d(t) = \langle |\mathbf{r}(t)_{drifter} - \mathbf{r}(t)_{tracer}| \rangle \tag{6.2}$$

in relation to the total traveled distance of the drifters

$$D(t) = \langle |\mathbf{r}(t)_{drifter} - \mathbf{r}(0)_{drifter}| \rangle. \tag{6.3}$$

The ratio $d(t)/D(t)$ denotes a relative error of the trajectory prediction and for identical trajectories it is zero. Similar Lagrangian error metrics have also been introduced by Toner et al. [207].

We use this measure to further distinguish qualitatively the flows in experiments 1 and 3 from those in experiments 2 and 4 (Tab. 6.2). For experiments 2 and 4 the ratio $d(t)/D(t)$ has relatively high values of the order of one, as the drifters are located in an oscillating chaotic tidal flow with several return points

in the trajectories resulting in a small traveled distance $D(t)$. In contrast, in the unidirectional (wind-driven) less chaotic flow in experiments 1 and 3 the traveled distance of the drifters $D(t)$ is large, leading to small ratios $d(t)/D(t)$ of 0.3 and 0.5. The total separation rate between modeled and real trajectories is almost a factor 2 higher for the directional flows with $4\,\mathrm{km}/12\,\mathrm{h}$ compared to the oscillating flows with $3\,\mathrm{km}/24\,\mathrm{h}$, but is overcompensated in the ratio $d(t)/D(t)$ by the large traveled distance $D(t)$. Our separation rates are at the lower part of the typical range of $4-25\,\mathrm{km/day}$ found in open ocean studies as reported in Huntley et al. [92]. Velocities and especially velocity gradients in our strong tidal flow can be expected to be as high as or higher than in the open ocean, so it is meaningful to compare our results to separation rates in the open ocean. An important difference, however, is the presence of the strong constraint that the coastline imposes on our model flow and the well-defined forcing of the tides that in large parts determine the coastal model flow. This probably leads to the relatively low separation rates between drifters and modeled tracers that we find.

Based on the above comparison of drifter and model velocity data, we can consider a basic validation of the model and assume that the hydrodynamic model serves to approximately represent the flow in the Ria de Vigo. However, especially in two out of four experiments, we see that the flow is highly irregular and not unidirectional, so a small initial deviation between the drifter velocity and the model velocity can lead to a strong separation of the artificial tracers from the drifters. This strong dependence on initial conditions is an inherent property of chaotical systems. Therefore, instead of directly comparing trajectories, we concentrate on LCS as a more suitable approach to compare the drifter data set to the hydrodynamic model.

6.4.2 LCS in the Ria de Vigo

As described in Sec. 6.3, LCS are obtained from tracers advected with the Eulerian velocity field given by the hydrodynamic model. Fig. 6.1 shows an example of the model surface velocity field with a relatively unidirectional tidal in and outflow, that interacts in the outer parts of the estuary with the north-south flow on the shelf and with the Cies Islands off the coast. Fully developed eddies are absent, but some rotational structures appear as recirculations behind sharp capes. These have very short lifetimes of few hours, mostly less than a turnover time. Thus, in the investigated flow hyperbolic separation points are predominantly situated at the coast and are rarely found in the calmer center of the bay. Artificial tracers mostly separate due to a drift towards a coastal boundary or an island. Therefore, most LCS are connected to the coast with one end and extend a distance into the flow that depends on the advection time τ [101, 103, 191].

Figure 6.9 shows a case of pronounced repelling LCS in the Ria de Vigo with the above mentioned characteristics for a long advection time of $\tau = 60\,\mathrm{h}$. Such long advection times are feasible for a slow mean flow when artificial tracers stay inside the area of interest. We plot a square of artificial tracers at their initial positions consisting of three regimes separated by repelling LCS that mark three different water bodies. The distinct final positions of the three tracer regimes demonstrate

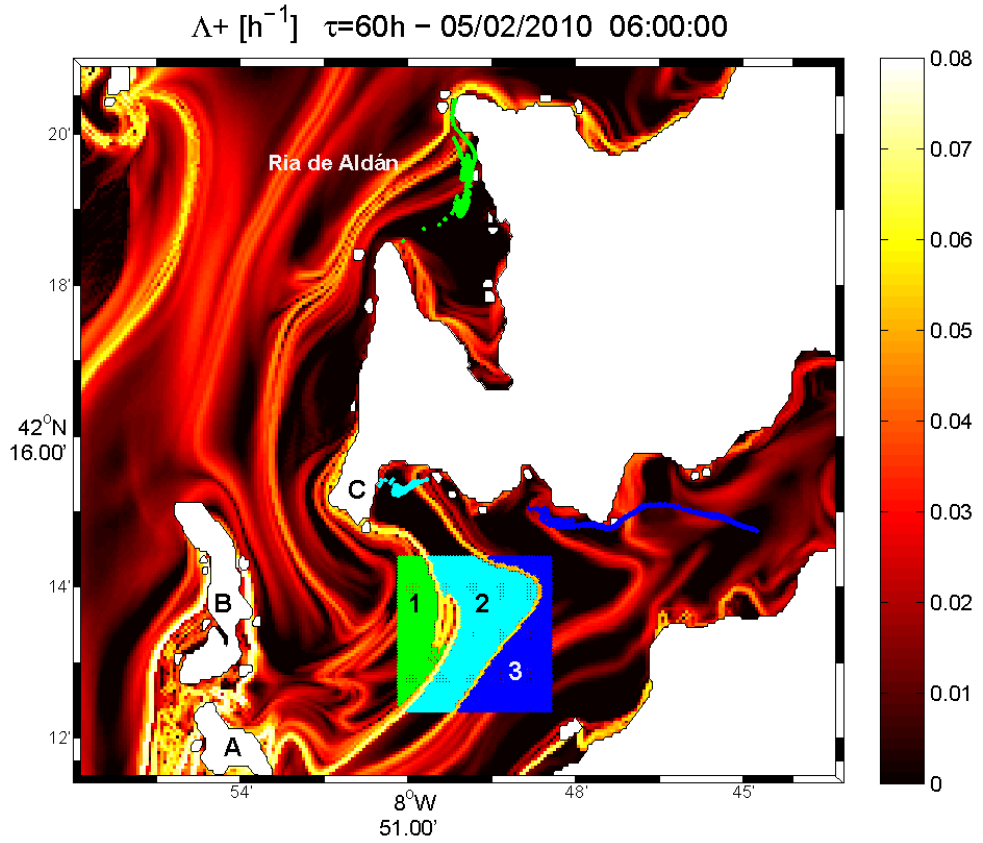

Figure 6.9: Prominent transport barriers in the Ria de Vigo during a period with south wind, 05/02/2010. The FTLE field from forward advected tracers $\Lambda^+(\mathbf{x})$ shows sharp ridges connected to capes and islands that are identified with LCS. The Cies Islands (A,B) and the Cape 'Cabo Home' (C) are decisive coastal boundaries for directing the flow and are attaching points for repelling LCS. Three regimes of colored artificial tracers released in a square (1,2,3) demonstrate the distinct final positions of the tracers after the advection time $\tau = 60$h.

the predicting character of the LCS: the green tracer regime (1) leaves the estuary northwards and enters the Ria de Aldan Bay, while the cyan regime (2) is caught at the north coast of the Ria de Vigo close to Cape 'Cabo Home', and the blue regime (3) is drifted eastwards into the estuary. Note the lobe defined by a strong ridge that encloses the water body that will be exchanged through the north mouth. These semi-circular structures in context with the exchange of water through a narrow channel have also been observed in FTLE fields of a tidal flow in a Norwegian fjord [155] and are probably due to strong shear. The enclosed area might even serve to estimate the exchange flux. Maximal FTLE values are around $0.08\,\mathrm{h}^{-1}$ corresponding to an exponential separation at a time scale of $12\,\mathrm{h}$, i.e., one tidal period.

In the following we perform a detailed comparison of the drifter trajectories to ridges in the FTLE field on the basis of Figures 6.11 to 6.14. The LCS are estimates of transport barriers for the model flow and we expect those LCS to be

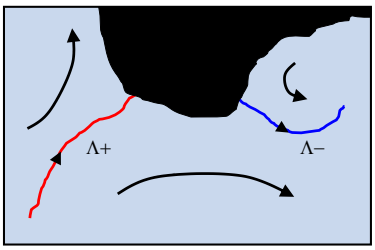

Figure 6.10: Idealized sketch of typical obtained LCS patterns. The flow separates and converges due to coastal boundaries (black area), hence LCS are tied to the coast. Repelling (stable/red) LCS are extracted from the forward FTLE field Λ^+ and attracting (unstable/blue) LCS are extracted from the backward FTLE field Λ^-. The principal directions of transport are indicated with arrows.

relevant for the trajectories of the real drifters as well, in the sense that drifters do not cross the LCS and follow the water bodies that are defined by the LCS. In Fig. 6.10 an idealized sketch of LCS observed in the model flow is completed with the principal transport directions in order to help to interpret the following maps of extracted LCS.

Experiment 1 The main feature in Figure 6.11 is an attracting (unstable/blue) LCS (L1) connected to Cape 'Cabo Home' (C) that marks the line of convergence between water entering the north mouth and water from inside the Ria de Vigo. Both drifters deployed inside the Ria de Vigo stay essentially east of this LCS along the entire experiment while being advected to the south. The drifter trajectories are also consistent with another attracting (unstable/blue) LCS (L2) emerging from the eastern most cape at the north coast. This LCS marks the abrupt movement in the drifter trajectories $4\,\mathrm{h}$ after the release stemming from the change of direction of the tidal flow at low tide, see Fig. 6.11a. The repelling (stable/red) LCS (L3) connected to San Martino Island (A) separating the outflow through the south mouth from the flow towards the island is crossed by one drifter. The crossing suggests a slight shift between the location of this LCS in the model and in the real flow. The other drifter follows the prediction by the model.

Experiment 2 Figure 6.12 shows experiment 2 at the north coast of the Ria de Vigo. LCS appear due to recirculations behind capes, but are less pronounced, since the tidal flow is basically oscillating parallel to the coastal boundary. Drifters stay between an attracting (blue/unstable) LCS (L1) and a repelling (red/stable) LCS (L2). The observed LCS turn out to be typical for tidal dynamics in the inner parts of the Ria de Vigo.

Experiment 3 Figure 6.13 shows experiment 3, a closeup of the separation of drifters in the tidal channel between San Martino Island (A) and Monteagudo Island (B). Wind and flow direction are similar to experiment 1 (Fig. 6.11). Drifters were deployed in the channel during falling tide in order to check the LCS of the

outflow. We want to highlight that even at the small scale of the order of $1\,\mathrm{km}$ the initial LCS are principally consistent with drifter trajectories. This agreement might be explained by the well defined flow in the small zone of interest due to a strong constraint imposed by the surrounding coastal boundaries. The repelling LCS (L1 and L2) between the initial positions of the drifters correctly predict that one drifter passes the channel, the second runs aground on San Martino Island (A) and the third drifts south, passing the island on the eastern side. Only later, the westernmost drifter crosses an attracting (unstable/blue) LCS (L3) twice, indicating a deviation of the model flow from the real flow.

Experiment 4 Figure 6.14 shows experiment 4 in calm conditions, i.e., without a directed longterm flow on the shelf outside the estuary. Mixing of neighboring water bodies and the resulting LCS are mainly due to an oscillating tidal flow around the Cies Islands. Drifter trajectories are consistent with a repelling (red/stable) LCS (L1) separating water inside the Ria de Vigo from water that moves westwards around the eastern cape of San Martino Island. In the second half of the experiment, drifters move to the center of the basin without the influence of any further pronounced FTLE ridges.

We compared drifter trajectories of four experiments to estimated transport barriers (LCS) from the model flow, and we find that overall LCS serve to predict and visualize the transport at the surface in the real flow in a global way. The used methods to estimate transport barriers (LCS) from FTLE fields turn out to be appropriate for the analyzed flow. Uncertainties of the positions of the transport barriers can be observed in at least two cases when a drifter crosses a pronounced transport barrier. Shadden et al. [191] estimates an error for the position of the transport barrier based on crossing events. Here, the error would be in the order of $1\,\mathrm{km}$, corresponding to approximately 3 grid cells of the model flow. In general, the model cannot be expected to represent the real flow exactly, as the bathymetry is complex and the wind forcing included in the hydrodynamic model does not respect local effects like shadowing of the mountains with a height up to $500\,\mathrm{m}$ surrounding the estuary. However, temporal sequences of drifter positions plotted over the LCS positions allow for a visual comparison of drifter trajectories to integral geometrical structures of the model flow. As a principal result, the subdivision of the flow into dynamically different water bodies can be roughly predicted by the model. In contrast, the direct comparison of trajectories of drifters to simple artificial tracers reveals high discrepancies, as velocity differences between model and real flow accumulate in the integration.

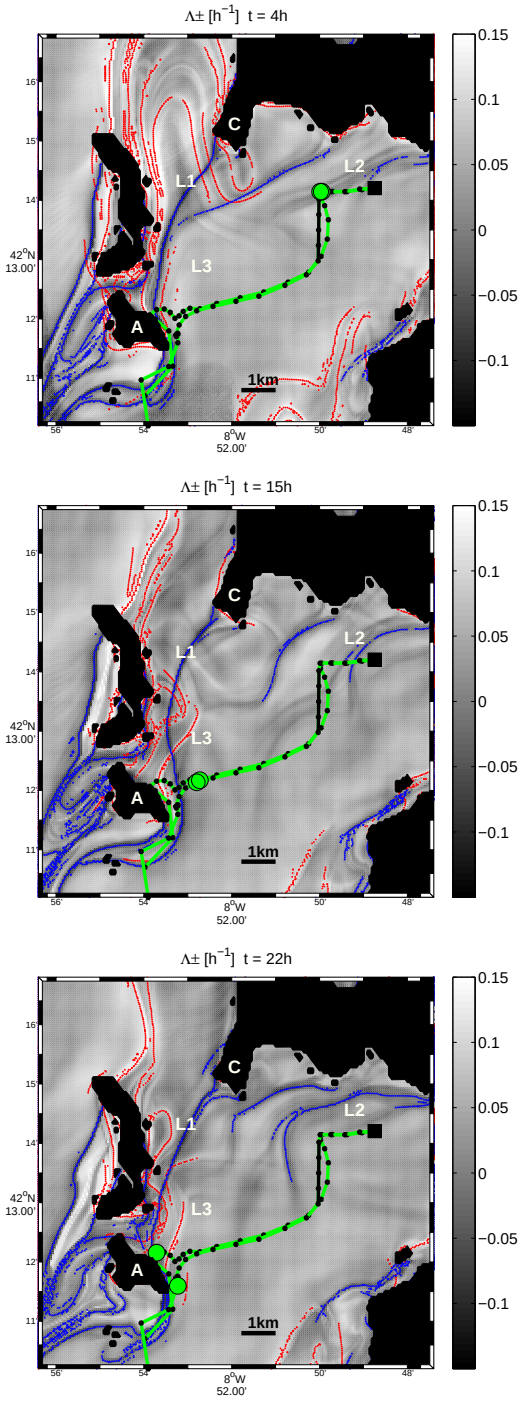

Figure 6.11: Drifters and LCS in experiment 1. Current positions of the two drifters are shown as green circles, starting at the release point (black square) and moving along the trajectories with hourly resolution (green line with black dots). The background field is the combined FTLE field $\Lambda^{\pm}(\mathbf{x}, t, \tau)$ in units $1/\mathrm{h}$. Advection time is $\tau = 24\,\mathrm{h}$. Extracted repelling (attracting) FTLE ridges are drawn in red (blue). The failure of one of the drifters for some hours is indicated by a black line.

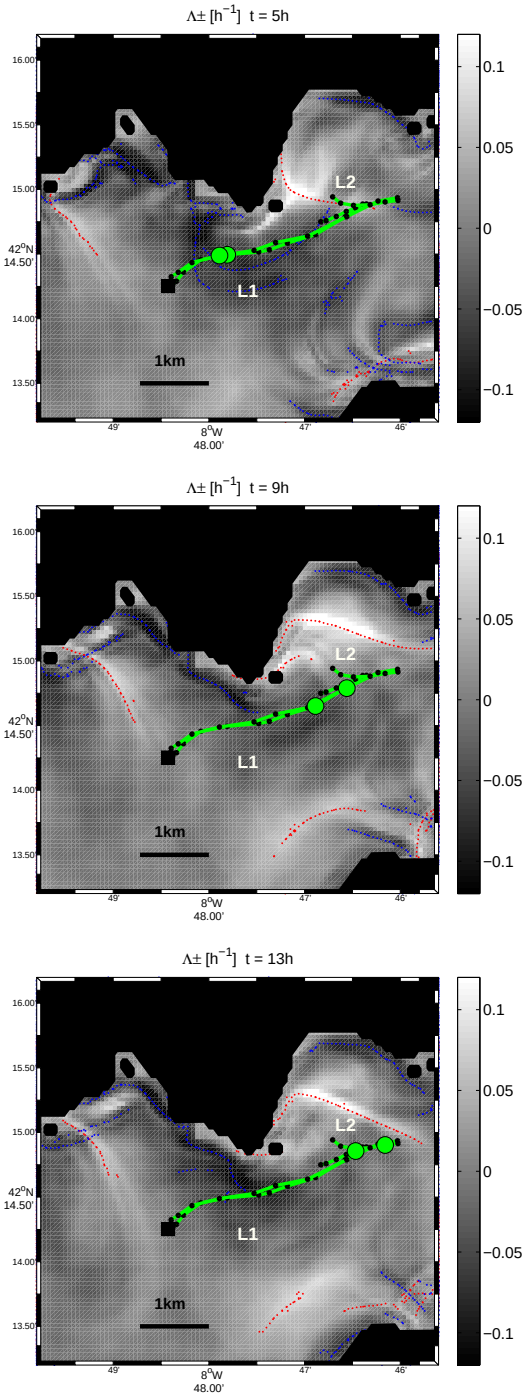

Figure 6.12: Drifters and LCS in experiment 2. Legend as in Fig. 6.11. Drifters move in a zone with small dispersion between two FTLE ridges that are connected to a cape at the north coast.

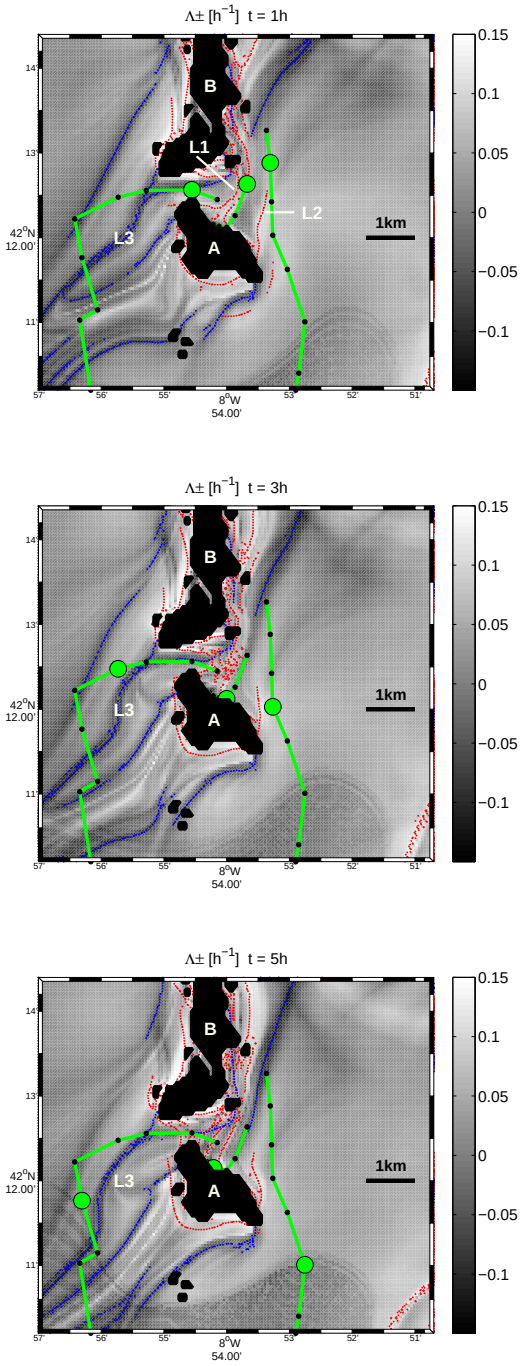

Figure 6.13: Drifters and LCS in experiment 3. Legend as in Fig. 6.11. Initial LCS correctly indicate that one drifter goes offshore through the channel, the second runs aground at San Martino Island (A) and the third is drifted south around the eastern cape of San Martino Island. Later, the westernmost drifter crosses an attracting (unstable/blue) LCS twice. The noisy structure at the bottom of the FTLE field appears because forward advected tracers leave the region of available velocity data.

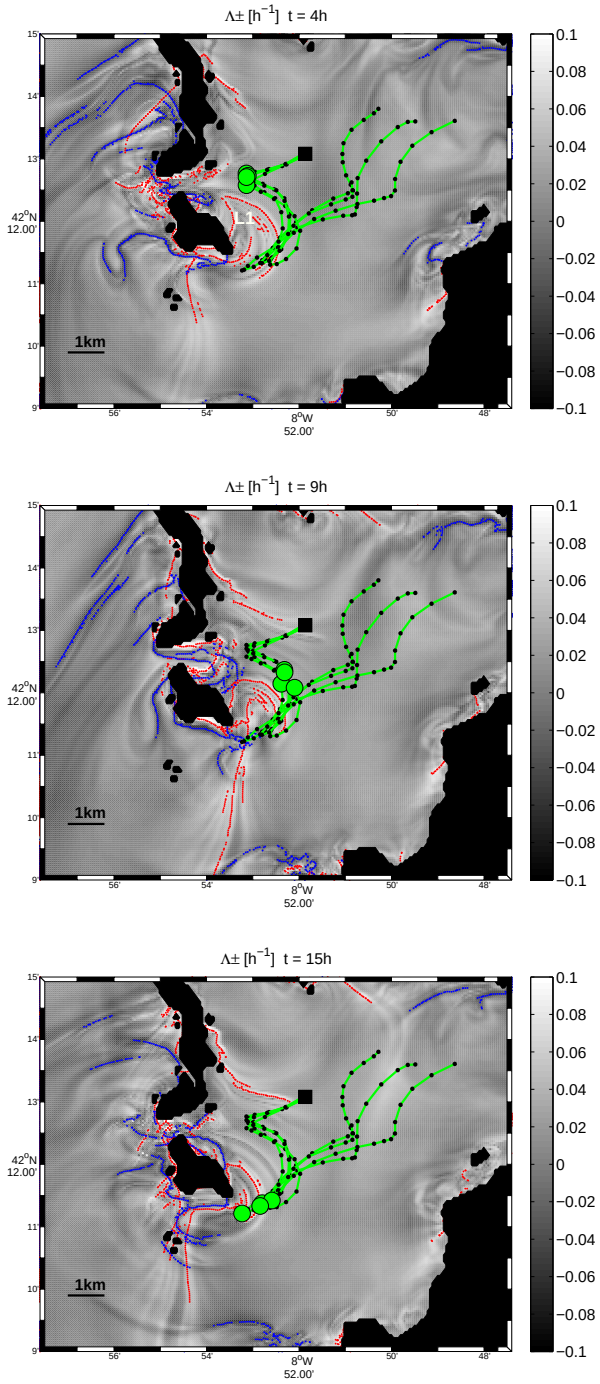

Figure 6.14: Drifters and LCS in experiment 4. Legend as in Fig. 6.11. Even though the trajectories of drifters and artificial tracers deviate strongly in this experiment (Fig. 6.8), the repelling (stable/red) LCS close to San Martino Island computed from the model is consistent with the drifter trajectories.

6.4.3 LCS during North and South Wind Conditions

The results demonstrate the relevance of the extracted LCS for the real flow. However, LCS are highly dynamic and intermittent, especially in transient meteorological conditions [28]. It is thus desirable to obtain more general information about the Lagrangian transport at the surface beyond the special cases of the four experiments. Wind forcing and the induced flow on the shelf play an important role for the circulation in the outer parts of the Galician Rias [46]. At the western Galicia coast, two wind directions are dominant that can also be related to upwelling and downwelling processes: northerly winds (often during summer) and southerly/westerly winds (often during winter). Here we extract LCS in these two meteorological conditions and show a Lagrangian sketch of the short-time surface circulation in the Ria de Vigo. Figure 6.15 shows LCS of the two typical flow patterns selected as examples for its pronounced north-south mean flow on the shelf indicated by white arrows. The LCS are time dependent and oscillate with the tide but they are computed for a time $\tau = 24\,\mathrm{h}$, twice the tidal period, and can be considered to represent the Lagrangian pattern of the short-time residual flow. Their persistence time is in the order of days, comparable to the persistence time of the flow pattern due to the wind forcing. In contrast to Eulerian measures, the LCS reveal the spatial information where surface water masses from the shelf and from the estuary converge or separate. The Cies Islands (A and B, Fig. 6.1) and Cape 'Cabo Home' (C, Fig. 6.1) play a key role for this circulation, since pronounced LCS are attached to these coastal boundaries. The inner and outer parts of the Ria de Vigo are not strictly separated, but surface water enters (leaves) the inner parts of the estuary during south wind (north wind).

South wind During south wind conditions (Fig. 6.15a), the most important repelling (stable/red) LCS mark the flow separation at the Cies Islands (L1) and at Cape 'Cabo Home' (L2). Only the water body in-between the LCS (L1) and the coast enters the Ria de Vigo at the south and most of the water leaves the estuary through the north mouth again. Attracting (unstable/blue) LCS connected to the Cies Islands in the north (L3) show that the outflow stays attached to the coast, drifting north into the Ria de Pontevedra.

North wind During north wind conditions (Fig. 6.15b), the flow is almost inverse to the flow during south wind conditions. A prominent attracting (unstable/blue) LCS (L4) impedes surface water to enter into the inner estuary from the north. The water body between Cies Islands and Cape 'Cabo Home' passes on both sides of San Martino Island and is drifted offshore.

Under both wind conditions, a transport barrier extending in north-south direction and connected to the Cies Islands clearly separates the flow that interacts with the inner part of the Ria de Vigo from the flow that passes by on the shelf. Note the two bays Ria de Aldán and Ria de Baiona which are almost cut off from the rest of the surface water exchange by LCS in both cases. These zones of retention can be of special importance for ecological studies as high concentrations of contaminants or biological tracers can persist in these areas. Even though

the discussed LCS under north wind and south wind conditions are subject to a certain variability, they correspond to typical flow patterns in the model appearing under similar meteorological conditions. Their relevance for the trajectories of real surface drifters has been demonstrated for the four experiments (Sec. 6.4.2).

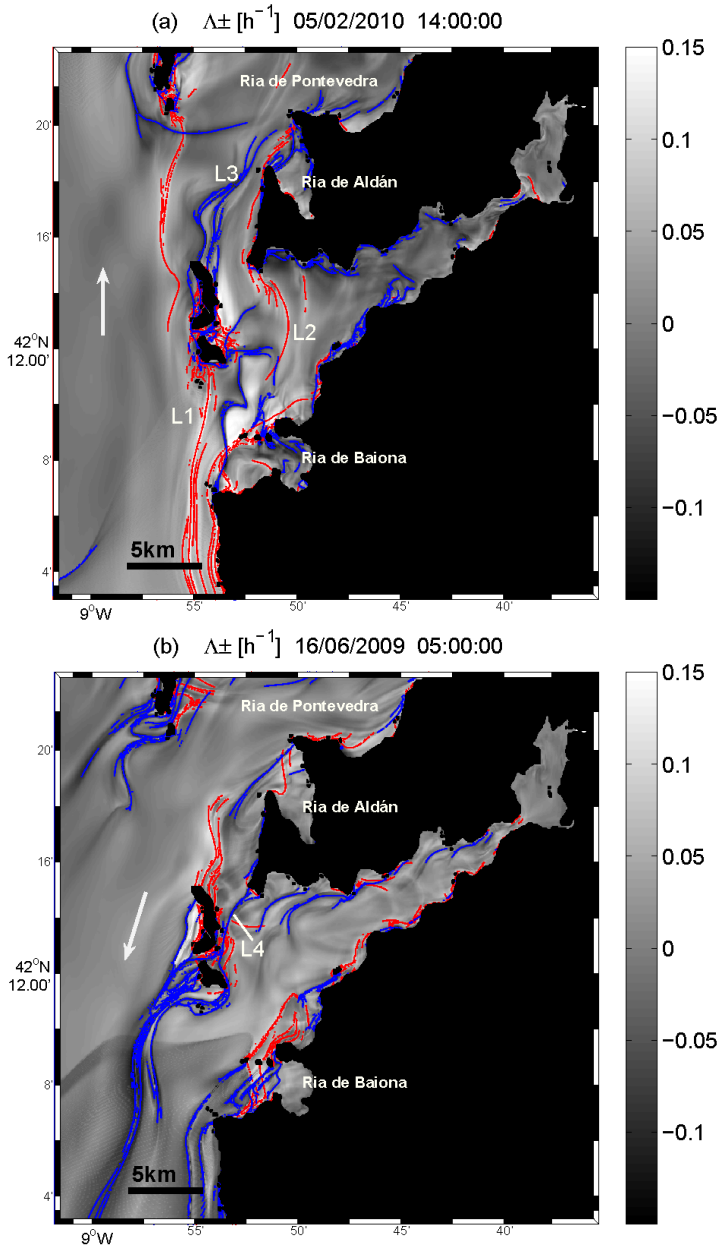

Figure 6.15: Examples of LCS in the Ria de Vigo for two typical meteorological situations: a) south wind in winter and b) north wind in summer. White arrows denote the approximate direction of the mean flow on the shelf. LCS (denoted L1 to L4) allow to distinguish the water entering, leaving and passing by the Ria de Vigo.

6.4.4 Synoptic Lagrangian Maps (SLM)

In the previous part we have seen that the surface currents in the Ria de Vigo generate chaotic trajectories. The geometry of transport is dominated by the complex coastal boundaries as revealed by hyperbolic LCS attached to capes and islands. We apply here the method of Synoptic Lagrangian Maps (SLM) (see also Sec. 2.4), another Lagrangian method, to analyze surface flow data of the same region obtained from HF radar measurements (Sec. 3.2).

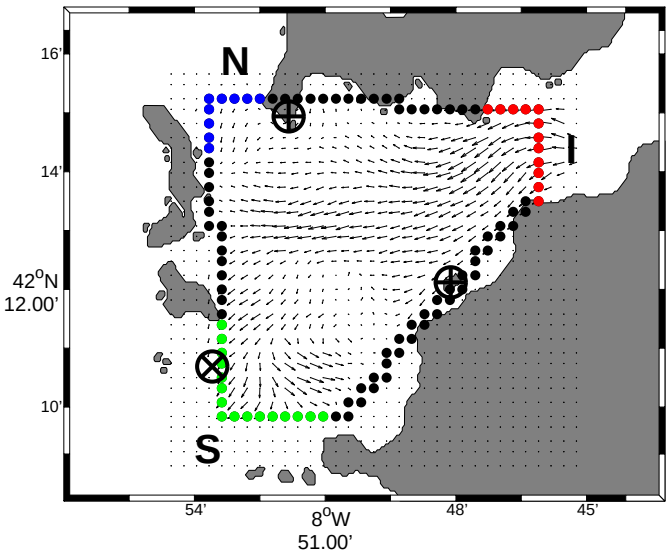

Figure 6.16: Boundaries of the flow domain in the Ria de Vigo that is covered by the HF radar. The open boundary sections marked by colored lines are the north mouth (N, blue), the south mouth (S, green) and the inner Ria (I, red). The position of the two HF radar stations is indicated as $\oplus$, as well as the oceanographic buoy close to the Cies Islands ($\otimes$) that measures the wind speed and direction.

We first define the boundaries of the flow domain as shown in Fig. 6.16. The two radar stations are located on either side of the bay to cover the basin in the outer part of the Ria de Vigo, which is bounded towards the open sea by the Cies Islands. Hence, the covered area naturally defines a flow domain with six boundary sections: Starting in the lower left corner, the first section defines the open boundary at the south mouth (green), followed by a closed section at the Cies Islands, where the possible flow through the channel between both islands is neglected. Further sections are the open section at the north mouth (blue), a closed section at the north coast, the open section towards the inner bay (red), and finally the closed south coast section. These boundaries coincide largely with the boundary definition for the Open boundary Modal Analysis (OMA) [102] used to decompose the measured velocity fields for an interpolation of missing or erroneous values.

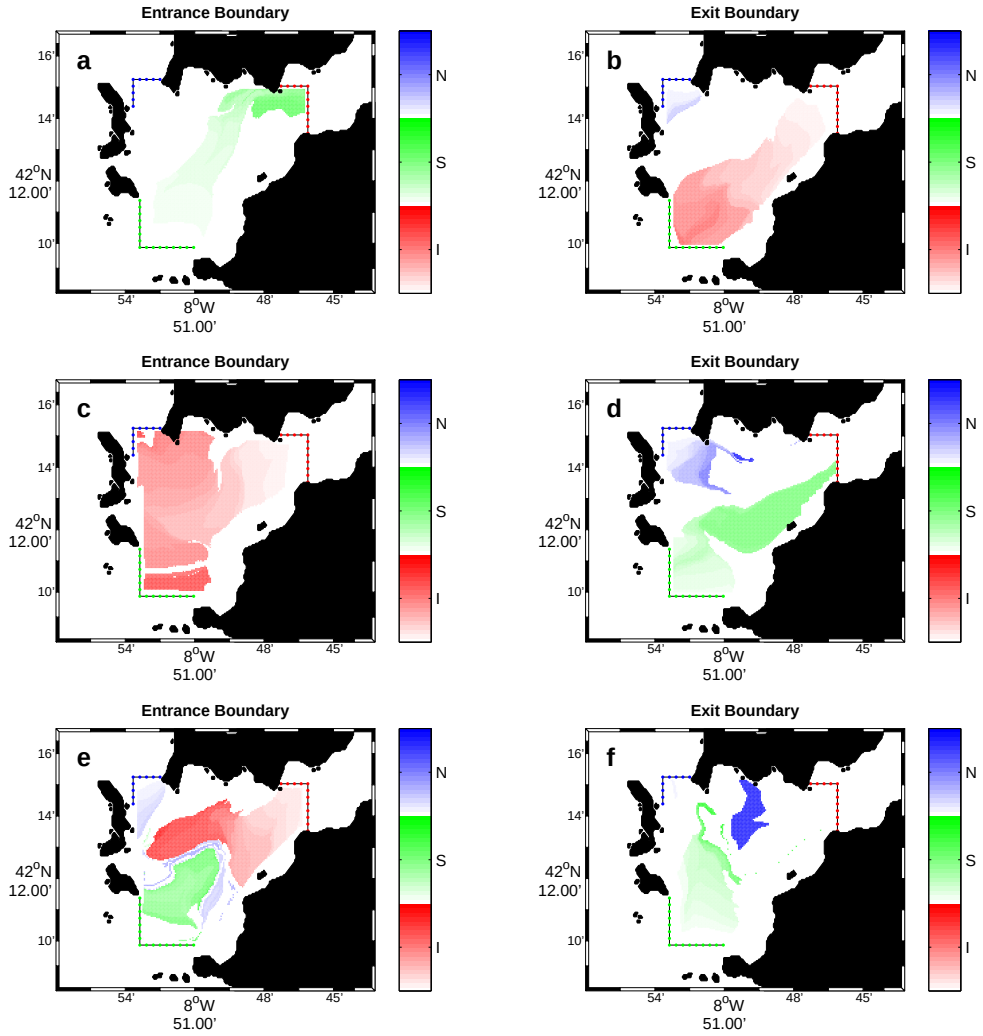

Figure 6.17: SLMs showing the fluid entering (left column) and leaving (right column) the domain through open boundaries. Trajectories are integrated forward and backward in time for $\tau = 6$ days. Colors indicate that particles passed through one of the open boundaries: North mouth (N), South mouth (S), and Inner bay (I). The time since entrance (until exit) is coded with the color intensity. (a,b) SLM on 13 December 2011, 9:00h. South-westerly winds induce a coherent directed surface transport north-eastwards into the bay. Water enters through the south mouth, leaving the domain towards the inner bay or though the north mouth. (c,d) SLM on 20 December 2011, 6:00h. North-easterly winds induce surface transport that is reversed if compared to (a,b). (e,f) SLM on 29 December 2011, 6:00h, without a directed flow. Instead, particles that entered through different boundaries mix and reveal typical irregular patterns of chaotic fluid advection.

However, it is important to note that the chosen boundaries in the Ria de Vigo are not only of practical concern for the modal analysis, but they naturally mark the entrances and exits of the bay which are of high importance for the exchange of water with the shelf. We are especially interested in this fluid exchange with the shelf, since possible biological or chemical contaminations, as e.g., harmful algae blooms or oil spills, would enter into the bay through the north mouth or through the south mouth. Apart from these undesirable impurities, the water exchange and the surface transport as a part of the three-dimensional circulation are crucial processes for the marine ecological system. With the SLM approach we address this transport with typical time scales of few days using a Lagrangian method, which is more direct and possibly more accurate than considering for example the residual flow derived as a temporal mean of Eulerian velocity fields [222].

The original work about SLM by Lipphardt et al. [107] was concerned with transport between the coast as a closed boundary and the ocean as an open boundary. However, since we are interested in the flow exchange in a domain with three entrance and exit sections, we focus here on the particles that enter and leave the domain through these open boundaries. Fig. 6.17 shows fields of initial particle positions classified by their origin and fate and coded with the color of the respective open section of the boundary (N, S, or I). In the first two rows steady wind conditions induce a directional flow along the main axis of the bay in southwest-northeast direction. In panel (a) we can observe a straight (green) plume of particles that entered the domain through the south mouth. A similar straight (red) area of particles in panel (b) marks the water body that flows towards the inner bay. In panels (c and d) the SLM reveal similar structures, but in reverse direction due to north-easterly winds. The third row shows a situation without a clear wind-induced directed flow. Fluid enters the domain through all three open boundary sections. In this case we can observe that the different water bodies mix and form the typical irregular mixing patterns with filaments.

Residence Time The examination of exit times of fluid particles is a common concept for chaotic advection in open flows [74, 131, 142, 143, 159] which has also been applied to oceanic flows [17, 170]. The exit time is the time a trajectory needs from its initial condition to a predefined boundary of the flow domain. In Fig. 6.17 the intensity of colors denotes the forward or backward exit time, T^+ and T^-, until a particle crosses the open boundary. The intersection of sets of particles with certain origins and fates defines a pathway through the domain from one open boundary section to another one. While trajectories cross the domain, we can measure their residence times (also called transit times) as the sum of the forward and backward exit time $T_R(\mathbf{x_0}) = T^+ + T^-$. In a chaotic flow the residence time sensitively depends on the initial condition of the trajectory. Fig. 6.18 shows an instantaneous map of the residence times of particles in the flow domain. Adjacent fluid patches exhibit drastically different residence times from less than one day up to about 8 days. This can be explained by the stable and unstable manifolds of hyperbolic points that separate fluid patches with different dynamic properties. Some fluid patches are quickly advected to the boundaries, while others stay in the domain for a long time.

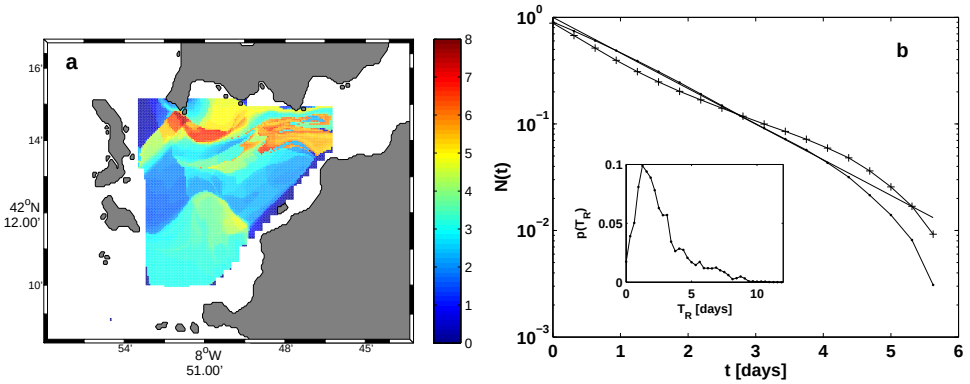

Figure 6.18: (a) Spatial distribution of the residence time of particles $T_R(\mathbf{x_0})$ [days] on 24 December 2011. (b) Number of particles remaining inside the domain vs. residence time. The curve follows an exponential with a constant exit rate of $\approx 1/2.1$ days (solid line). The inset shows the distribution of the residence time T_R.

If we assume that the fluid is well mixed in the flow domain and that a constant fluid volume per time escapes from the domain, the exit times T^+ and T^- have an exponential distribution [142]

$$p(T) \propto e^{-\kappa T} \tag{6.4}$$

where κ is the escape rate. For a given flow domain, $1/\kappa$ defines a time scale of the chaotic flow. The fraction of particles that have not escaped from the domain after a certain time t is given by

$$N(t)/N_0 = 1 - \int_0^t p(T)dT = \int_t^\infty p(T)dT = e^{-\kappa t}. \tag{6.5}$$

Fig. 6.18b shows the process of particles escaping the flow domain in terms of the fraction $N(t)/N_0$. The distribution is the average of month of flow data and is well approximated by an exponential function. Fluid particles escape with an average rate of $\kappa \approx 0.5\,\mathrm{d}^{-1}$ corresponding to a e-folding exit time of about 2 days. The inset shows the distribution of the residence times T_R over the same period of time. We observe that on average most particles transit the domain in less than 5 days, but for small fluid patches the residence time can be as high as 10 days. It is important to note that these distributions are only valid on average, while in single cases large deviations may occur. In particular, the escape of particles depends strongly on the character of the flow, and we have already noted that strong wind forcing can generate a directional rather than a chaotic flow in the Ria de Vigo. In order to demonstrate this dependence of the exit times on the flow character, we choose two different two-day periods with a directional flow in one case and an oscillating flow dominated by the tidal motion in the other case. For the directional flow we obtain an escape rate, which is about 5 times higher than for the oscillating flow (Fig. 6.19a). Hence, as expected, a directional wind induced surface flow rather than the pure oscillating tidal flow rapidly renews the

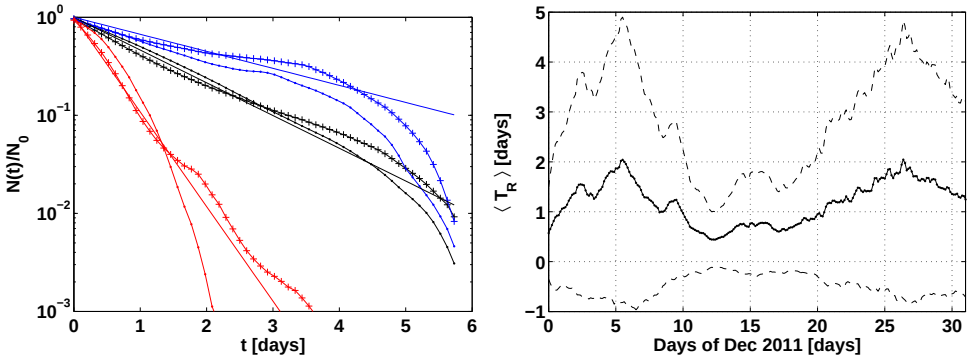

Figure 6.19: (a) The fraction of particles $N(t)/N_0$ inside the domain decreases exponentially with time. However, the escape rates κ vary significantly for two two-day periods with qualitatively different flow regimes: a directional wind-induced flow on 13 December 2011 (red), $\kappa \approx 2\,\mathrm{d}^{-1}$, and an oscillating tidal flow on 28 December 2011 (blue), $\kappa \approx 0.4\,\mathrm{d}^{-1}$. Points $(\cdot)$ denote forward-time escape statistics and crosses $(+)$ backward time. The black curve is the long time averaged data for the period of one month in December 2011. (b) Spatially averaged residence time $\langle T_R \rangle$ of particles during December 2011. Note the high standard deviation of values (dashed line) due to intermittent spatial patterns (see Fig. 6.18a).

water mass in the domain. The time series of the mean residence time (Fig. 6.19b) reveals important variations over time scales of several days that are most probably related to changes in the wind forcing. The very high standard deviation of the residence time values of different fluid particles is again a sign of the intermittent character of chaotic transport.

Comparison with Wind Data Here, we exemplarily relate the fluid transport through our domain more directly with the wind forcing that drives a significant part of the surface flow in the Ria de Vigo [167]. Therefore, we use the number of particles crossing the domain from one open boundary to another open boundary to quantify the through flow. Having three open boundaries (N,S,I), at each instant of time we count the trajectories making one of the possible transects through the domain N→S, S→N, N→I, I→N, S→I or I→S. In Fig. 6.20 we choose a period of 15 days in December 2011 and correlate the through flow with in-situ wind data measured at the *Cies* oceanographic buoy located at the south mouth (see Fig. 6.16). During the first five days, the through flow is totally dominated by the S→I direction, with a very small number of particles drifting from the south mouth to the north mouth (S→N). A strong southwesterly wind pushes the surface water through the south mouth into the Ria de Vigo where it continues towards the inner part. After five days, the wind weakens and changes to northeasterly directions. This reverses the surface flow such that particles transit the domain from the inner bay to the north mouth and south mouth, i.e., I→N and I→S flow directions dominate. This circulation pattern favors the positive estuary circulation, where fresher water drifts out of the bay on the surface, and denser saltier water flows in at the bottom.

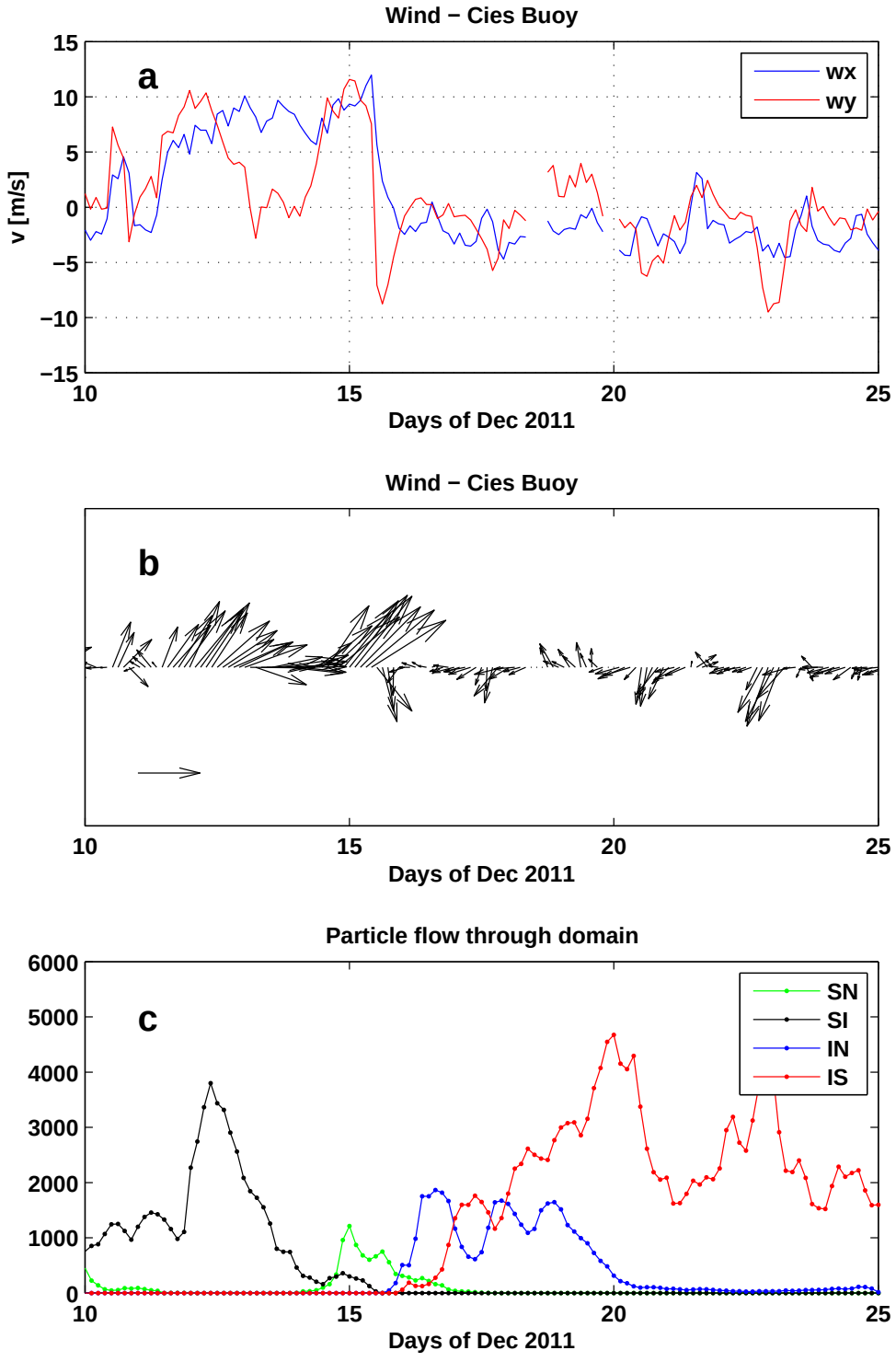

Figure 6.20: (a,b) Wind data measured at the *Cies* oceanographic buoy at the south mouth of the Ria de Vigo. The reference vector corresponds to $10\,\mathrm{m/s}$. (c) Number of trajectories that transit the domain from one open boundary to another, e.g., SI (S→I) denotes the transport from south mouth (S) into the inner bay (I).

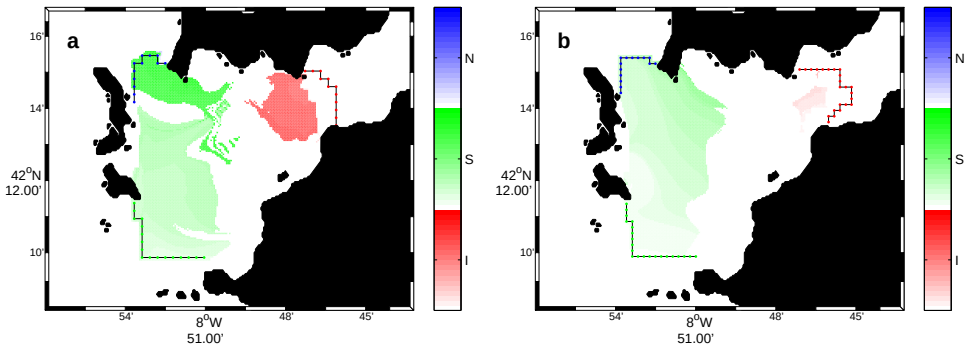

Figure 6.21: Forward SLMs on 16 July 2011, 12:00h, for particles escaping the domain. (a) Flow data from HF radar measurements. (b) Surface flow of the hydrodynamic model.

Comparison of Radar and Model Flow Data SLM are maps of transport from the interior of the flow domain to other regions outside the flow domain. The information about the fate or origin of trajectories is obtained by averaging the Eulerian flow field along trajectories, i.e., in a Lagrangian frame. In only slightly different flow data sets, single trajectories would typically diverge strongly from their counterpart in the other flow, even if the flow represents the same overall transport pattern. However, since the SLM approach does not consider the exact position of trajectories, but is instead concerned with the more general information whether or not a trajectory ends in a certain region, SLM are especially useful to compare the overall transport patterns in different flow data sets of the same domain. In Fig. 6.21 we show an example of a forward SLM based on flow data from HF radar measurements and a forward SLM on the same date based on the surface flow in the hydrodynamic model of the Ria de Vigo. Even though the predefined domains are not exactly the same, we observe a very similar flow pattern for both data sets. In both flows the particles in the left half of the flow domain escape through the south mouth (green), and a much smaller patch (red) escapes from the domain into the inner bay. Hence, if we consider the HF radar measurements as ground truth data, the SLM can be used as one method to validate the transport patterns in the model surface flow.

6.5 Conclusions and Outlook

In this chapter, we studied the surface transport at the submesoscale $(1 - 10\,\mathrm{km})$ in a tidal estuary. We compared trajectories of surface drifters to Lagrangian Coherent Structures (LCS) computed from the surface velocity fields of a coastal hydrodynamic model. We also used surface flow data from a HF radar system and Synoptic Lagrangian Maps (SLM) to visualize the flow exchange between different open boundaries of the flow domain. Regarding the three dimensionality of the flow at the coast, some limitations of the study of the horizontal surface flow have to be taken into account. Most often, vertical flow cannot be neglected

as upwelling and downwelling processes or the typical vertical estuary circulation imply. These vertical flows lead to divergence in the two-dimensional surface velocity fields, which modifies the FTLE field [87]. We also observe the occurrence of negative FTLE values (see Fig. 6.4a) corresponding to zones of convergence in the horizontal plane. Furthermore, Branicki and Malek-Madani [27] have suspected that a part of LCS extracted from estuary model flows can be artifacts due to coarse boundary conditions and imprecise forcings. In our case, the relatively accurate tidal forcing determines a large part of the flow dynamics, but coarse wind data and unresolved coastal topography, as well as the approximations for the hydrodynamic equations can certainly limit the reliability of the model output. Despite these limitations, the LCS and SLM represent a surface footprint of the complete 3-dimensional transport as given by the model, and we can draw the following conclusions:

- LCS, extracted from the surface flow in a hydrodynamic model, reveal the fundamental structure of Lagrangian transport in the Ria de Vigo imposed by the prominent coastal boundaries, as islands or capes. LCS connected to the Cies Islands and Cape 'Cabo Home' play a key role directing the in-and outflow of the estuary and controlling the water exchange with the shelf for the typical meteorological conditions of north wind and south wind.
- Water exchange in and out of the small bays Ria de Aldán and Ria de Baiona is prevented by LCS for both wind directions.
- SLM complete the picture of flow exchange and visualize the fluid patches that transit the flow domain from one open boundary to another. Wind forcing is found to correlate with the changing directions of surface transport as measured by HF radar.
- LCS computed from the model velocity fields are found to mark largely transport barriers for real drifters. This implies that the model output represents the general circulation in the estuary under different meteorological conditions and the surface transport has been validated with drifters.
- Similar to recently reported results [191], we find that drifter paths are better characterized by LCS than by single artificial tracers. Due to Lagrangian chaos, the trajectories of single artificial tracers in the model flow can significantly deviate from the drifter trajectories, although the main geometry of the circulation is captured correctly by the model.
- Based on the drifter experiments, we can estimate an uncertainty of the LCS positions of about $1\,\mathrm{km}$. This can partly be due to the tendency of the model to underestimate the dynamics.

Our results demonstrate the importance of the Lagrangian view on the output of coastal models and the power of the LCS method for the analysis of these flows. The LCS analysis applied to model data is especially interesting in coastal regions where direct high resolution measurements of the velocity field (e.g. HF Radar) are not available.

In relation with the intense fishery and seafood production in the Ria de Vigo, many biological and ecological studies are carried out in which the transport of nutrients, plankton, fish eggs, larvae, etc., plays a crucial role. Visualized surface transport patterns can be a useful hint for such studies. They can help to take horizontal transport processes into account as an explanation for biological observations [100, 165]. Future work could deal with a closer look at the position error of the LCS which can be determined by lines of drifters deployed across a predicted LCS. Moreover, the challenging task of 3-dimensional LCS in coastal models has been addressed by Branicki and Malek-Madani [27] and reliable results would be valuable for many ecological transport problems.

Chapter 7

Transport in a Quasi Two-dimensional Turbulent Flow with Application to a Chemical Reactive Front

Abstract

In this chapter we investigate the transport in a turbulent quasi two-dimensional laboratory flow induced by capillary Faraday waves on a thin fluid layer. In experiments with an excitable autocatalytic chemical reaction in this flow, propagating chemical waves with a highly wrinkled front have been observed. These observations demand for a detailed study of the underlying advective transport. We first characterize the vortex patterns in the flow in the Eulerian frame and relate them to the geometric pattern of the Faraday waves. In a second part, we compute Lagrangian coherent structures (LCS) that determine the spatiotemporal mixing patterns. Simultaneous experimental measurement of the velocity fields and the chemical concentration allow for a superposition of the LCS onto the concentration field. This reveals that the LCS shape the advancing reaction fronts.

7.1 Introduction

Mixing in time-dependent flows is generated by stretching and folding of fluid parcels. Especially in the last ten years, stretching rates experienced by the fluid parcels, e.g., quantified by Finite-time Lyapunov exponents (FTLE), have been used to measure the global mixing efficiency, but also to characterize local mixing processes in fluids. Many studies focus on the question how the spatial distribution of high stretching rates determines the patterns in the fields of passive tracers [99, 212, 221, 231]. It is now widely accepted that lines of high backward-in-time stretching act as transport barriers and align with the gradients of passive tracers [220]. These transport barriers have also been extracted from experimental turbulent flows [123]. In fields of reactive tracers, e.g., stirred chemical reactions,

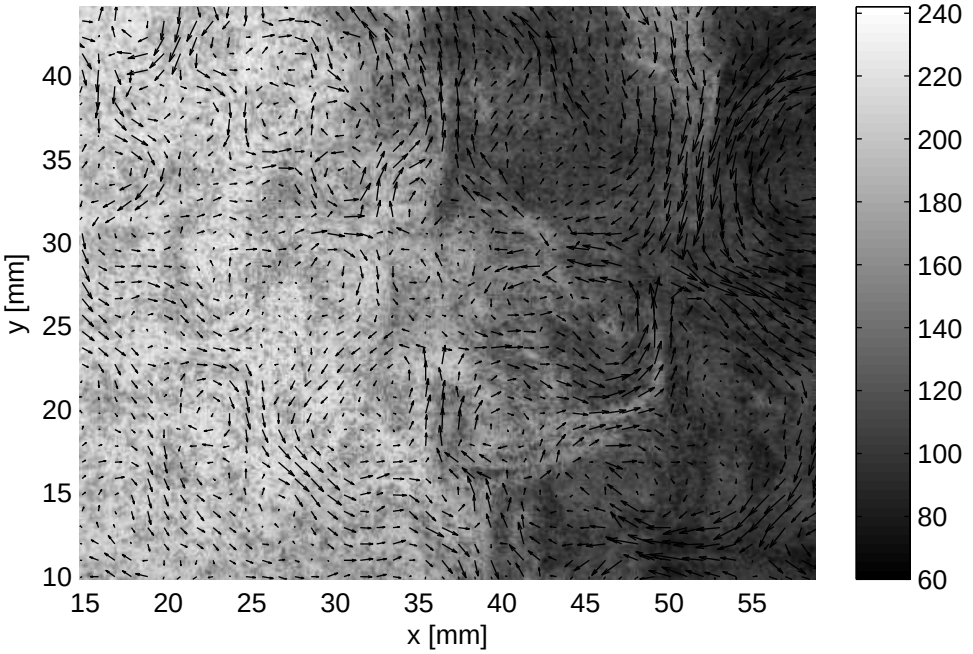

Figure 7.1: Detail of the chemical wave front that propagates from left to right. Grayscale values indicate light intensity which is a monotonically increasing function of ferrin concentration in the Belousov-Zhabotinsky reaction. The small-scale structures in the image are caused by the shadowing of floating particles for the PIV measurement. The velocity field extracted from subsequent images by PIV is overlayed (every 2nd vector plotted). The flow has a typical velocity of $v_{rms} = 21.9\,\mathrm{mm/s}$ and the Reynolds number based on the Faraday wavelength $\lambda_F \approx 9\,\mathrm{mm}$ is $Re \approx 140$.

the transport barriers separate the reactants from each other, or divide the fluid into regions with inhibited and excited chemicals. The stretching of the fluid increases the contact area of reactants, and therefore, the stretching rates of the fluid are closely linked to the spatial structure of chemical waves [164] and to the temporal evolution of chemical reactions [13, 95, 210]. In a similar approach, Mahoney et al. [114] propose active 'burning' invariant manifolds (BIMs) that mark the front of a chemical reaction in a laminar flow. BIMs can be seen as LCS of the extended dynamical system including advection and the reactive dynamics, where the latter is represented by a constant front velocity.

Motivation This study of local flow structures is motivated by experiments with an excitable chemical reaction (Belousov-Zhabotinsky reaction [96], BZ reaction hereafter) in a turbulent quasi-twodimensional flow induced by capillary Faraday waves (Sec. 3.3). A chemical wave with a propagating front can be observed in this experimental realization of a reaction-diffusion-advection system [216]. A closeup of the chemical wave front is shown in Fig. 7.1. The coherent global wave only exists for a certain range of parameters of the vertical vibration forcing, i.e., the advective transport in the flow is a key process for the chemical wave that can

favor or destroy it. In order to quantify the flow properties, we carried out detailed measurements of the horizontal surface velocity field of the flow via Particle Image Velocimetry (PIV), see Sec. 3.3.1. The obtained velocity data reveals typical characteristics of two-dimensional turbulence, forced at the wave length of the Faraday waves [217]. Moreover, based on the measured velocity data, we could demonstrate that the velocity of the chemical wave front depends on the intensity of asymptotic mixing induced by the fluid motion. Asymptotic mixing takes the statistical approach that turbulent fluid motion, on length scales comparable to or larger than the reaction front width, can be treated as a stochastic process. In particular, we found that when the asymptotic mixing is parametrized with a turbulent diffusion coefficient, the front velocity follows the Fisher-Kolmogorov-Petrovskii-Piskunov (FKPP) relation [218].

Here, instead of considering stochastic transport and the chemical wave as a global object, we focus on the local mixing of the leading edge of the wave by stretching and folding that shape the geometry on relatively small time and length scales. In the experiments we observe that the chemical wave front is not smooth, but exhibits a distinct filamentous structure (Fig. 7.1) which is indicative for advection-dominated transport. Indeed, the Peclét number is of the order of $Pe \sim 500$, i.e., diffusion is neglectable as a transport process. However, diffusion is certainly necessary to enable the chemical reaction. The Damköhler number, comparing advection and reaction time scales $Da = \tau_{advection}/\tau_{reaction}$, is of the order of unity. This indicates that both processes evolve on the same time scales, i.e., the chemical concentrations change while they are stirred by the flow. In the case of a large Da number, the spreading of the wrinkled front would be limited by advection and the chemical concentration could be treated as a passive tracer. This is not the case here. However, the filamentous structure of the front suggests that coherent structures in the flow, in particular Lagrangian coherent structures (LCS), must play an important role in shaping the chemically active front. The objective here is to extract and characterize these LCS in the experimental flow and to compare it with the concentration field at the front.

In the following, we analyze the experimentally measured turbulent velocity fields of the Faraday flow searching for coherent structures and examining their impact on the reaction front. First, in the Eulerian frame, the flow is characterized in terms of vorticity fields that are compared to the pattern of the capillary Faraday waves. In a second part, in the Lagrangian frame which is more relevant to transport, we discuss the distribution of finite-time Lyapunov exponents (FTLE) in the flow and relate the associated Lagrangian coherent structures to the geometry of the chemical wave front.

7.2 Results

7.2.1 Vortices and Faraday Waves

Since the capillary surface waves, which cause the Faraday flow, exhibit a transient regular rectangular pattern, it seems natural to assume that this wave pattern has an influence on the configuration of vortices in the flow. Persistent vortices can

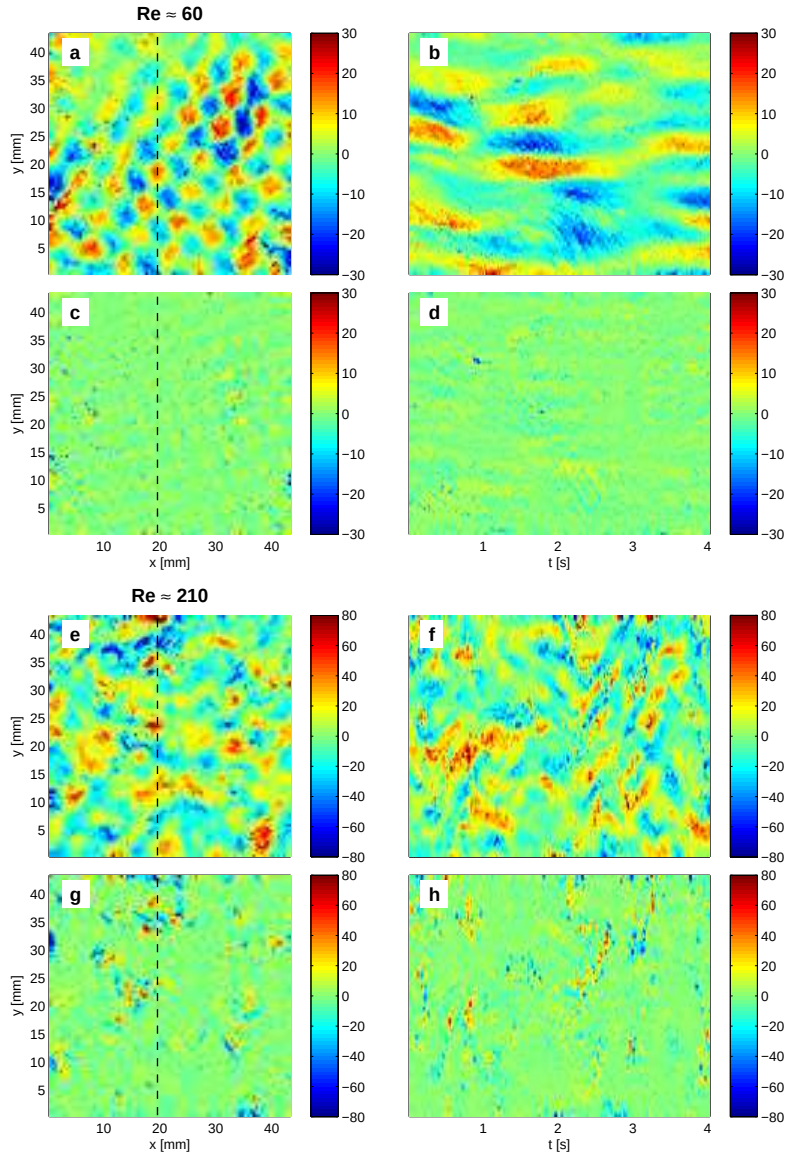

Figure 7.2: Vorticity and divergence fields [s^{-1}] of the Faraday flow at low forcing (top, $Re \approx 60$) and high forcing (bottom, $Re \approx 210$). (a,e) Vorticity fields. (b,f) Space-time plot of vorticity along the dashed line in (a,f). (c,g) Divergence fields. (d,h) Space-time plot of divergence along the dashed line in (c,g). Divergence in the Faraday flow is small and localized in space and time.

order the transport in fluids. When vortices in time-dependent velocity fields are diagnosed in the Eulerian frame, their role as coherent structures in transport cannot ultimately be ascertained, but their spatial distribution determines the overall geometry of Lagrangian coherent structures. Here, we therefore first analyze flow structures in the Eulerian velocity fields in terms of vorticity, estimate their persistence time and relate them to the widely regular pattern of the Faraday waves.

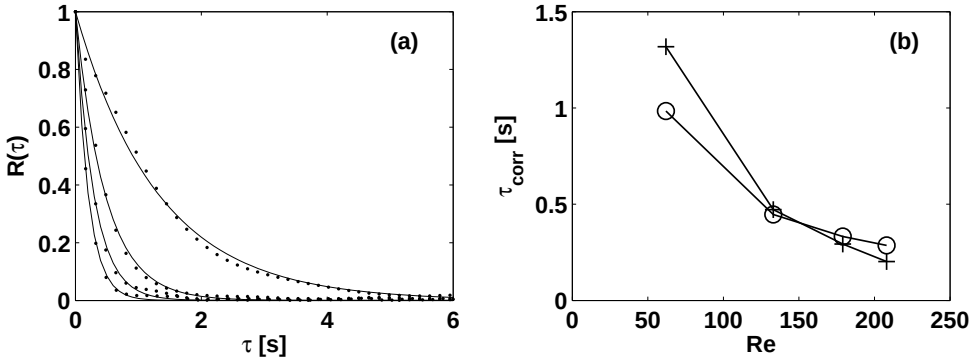

Figure 7.3: (a) Temporal autocorrelation function of the vorticity. (b) The correlation time τ_{corr} $(+)$, an estimate of the persistence time of vortices, decreases rapidly with increasing Reynolds number. For the fast flow the vortices still persist for about 10 periods of the Faraday waves. The eddy turnover time τ_ϵ $(\circ)$ is of the same magnitude as the correlation time, i.e., the vortices are persistent enough to affect the trajectories in the flow.

Vorticity Patterns The vorticity of the two-dimensional velocity field, defined as $\omega = \nabla \times \mathbf{v} = \partial_x v_y - \partial_y v_x$, is a local measure for the infinitesimal rotation of an infinitesimal fluid parcel, and it is useful to identify rotating structures in velocity fields. Vortices are characterized by high positive or negative vorticity depending on their orientation, i.e., in a right-handed coordinate system vortices with positive (negative) vorticity turn anti-clockwise (clockwise). Figure 7.2 shows exemplary vorticity fields of the Faraday flow at two different Reynolds numbers, $Re \approx 60$ and $Re \approx 210$. In two-dimensional flows a Reynolds number of the order of ~ 100 already indicates the onset of turbulence with a developed inverse energy cascade [217]. Generally, we observe that for the lower Reynolds number vortices are arranged on a grid (panel a) and persist for several seconds, as the space-time plot reveals (panel b). In contrast, for the higher Reynolds number, the grid-like vortex pattern is distorted (panel e) and vortices do not persist (panel f). Overall vorticity values are higher for the higher Reynolds number (note the different color bar).

We also show the divergence field for both flows. Theoretically, in a two-dimensional incompressible flow with zero vertical velocity, $\mathbf{v}_z = 0$, the continuity equation reduces to $\nabla \cdot \mathbf{v} = \partial_x v_x + \partial_y v_y = 0$. We expect small divergence in our quasi two-dimensional experimental Faraday flow since any non-zero divergence in the xy-plane would indicate a vertical flow. In the measured velocity fields, zones of non-zero divergence occur very locally in time and space (Fig. 7.2c and g). This is a typical characteristic of a stochastic signal, most probably pointing to measurement errors. Divergence values are higher and more frequent for the higher Reynolds number (panel g). Three possible effects can account for the measured non-zero divergence: (1) Since the Faraday flow is forced vertically by the capillary surface waves there is periodic vertical fluid motion inherent in the system. Although we take the images at the phase of the vertical oscillation when the water surface is as flat as possible, locally a divergence or convergence of

the surface is quite possible. (2) Persistent vertical flows might be a reason for divergence, but in this case, particles would cluster at zones of negative divergence and downward vertical flow, which is not observed. (3) The most probable cause for divergence in the measured velocity fields are uncertainties of the PIV method. Especially when the particle density is too high or too low in a small region, erroneous velocity vectors are the result and they cannot always be filtered out. With our measurement system we cannot separate the different effects contributing to divergence, but we assume the divergence to be neglectable for the analysis of Lagrangian transport below. In particular, the scalar vorticity fields serve to represent the entire flow while the divergent component of the flow does not pay a significant role.

We quantify the persistence time of the vortices in the Faraday flow by computing the autocorrelation time of the scalar vorticity field. The temporal autocorrelation functions $R(\tau) = \int_0^\infty \omega(t)\omega(t+\tau)dt$ for different Re numbers (Fig. 7.3a) are fit with an exponential function to obtain the correlation time τ_{corr}. With increasing forcing of the Faraday flow the correlation time decreases rapidly from $\tau_{corr} = 1.3\,\mathrm{s}$ for the slowest flow with $Re \approx 60$ to $\tau_{corr} = 0.2\,\mathrm{s}$ for the fastest measured flow with $Re \approx 210$ (cf. Fig. 7.2b and f). When we consider the vortices in the Faraday flow to persist during this correlation time of the vorticity field, this time scale has to be regarded with respect to a typical time scale in the flow, the eddy turnover time. We define it as

$$\tau_\epsilon = \frac{\lambda_F}{v_{rms}} \tag{7.1}$$

where a typical length scale in the flow is given by $\lambda_F = 9.1\,\mathrm{mm}$, the Faraday wavelength in our experiment for a forcing at $50\,\mathrm{Hz}$, and v_{rms} is the root-mean-square velocity of the flow. τ_ϵ is of the order of the time a particle needs to cross a vortex with diameter λ_F. Both time scales, τ_{corr} and τ_e, are similar, as is shown in Fig. 7.3b. This can be interpreted in the sense that vortices in the Faraday flow persist for times that are long enough to significantly affect the trajectories of particles in the vortex. A slight tendency is visible that with increasing Reynolds number the persistence time of vortices becomes smaller with respect to the eddy turnover time, i.e., for higher Reynolds numbers vortices in the Faraday flow deform and vanish faster compared to the time during which a trajectory stays in the vortex. The ratio $\tau_{corr}/\tau_\epsilon$ decreases. In the two limits, for $\tau_{corr}/\tau_\epsilon \to \infty$ the vortices would exist forever and would be completely isolated from each other in the time-independent flow, while trajectories would circle around one vortex many times. For $\tau_{corr}/\tau_\epsilon \to 0$, no coherent vortices could persist and the trajectories would move stochastically, as in a random walk. In our case, the ratio is of order one, $\tau_{corr}/\tau_\epsilon \sim 1$, and we expect the vortices to considerably direct the trajectories in the flow.

Patterns of Faraday waves The exact process of energy transfer from the vertical Faraday waves to the horizontal flow is still unclear. [58] showed for Faraday waves on liquid mercury that their statistics significantly change when a Lorentz-force induced horizontal vortex flow is present in the liquid. The energy transfer

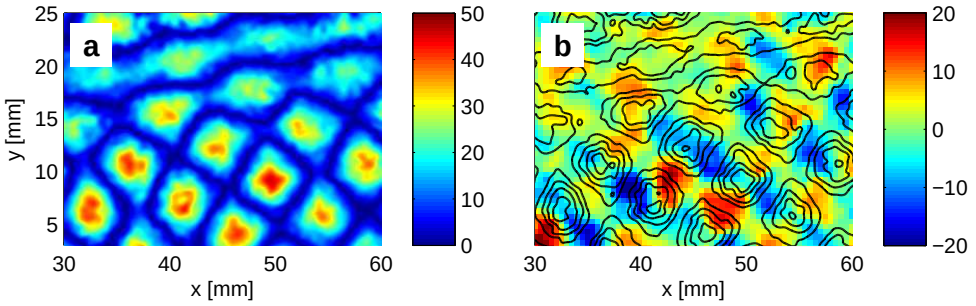

Figure 7.4: Coupling of Faraday waves and vortices in the horizontal flow for a flow with $Re \approx 60$. (a) Rectangular pattern in the Faraday waves, Eq. (7.2). Low values (blue) indicate nodes and high values (red) indicate antinodes. (b) Contours of the same wave pattern overlaid over the vorticity field. The grid of vortices aligns with the wave pattern such that vortices are located on nodes of the waves.

must be closely linked to these wave-vortex interactions. From the observational point of view, we see a direct coupling between the spatial pattern of the vortices and the spatial wave pattern. Fig. 7.4a shows the pattern of Faraday waves that force a flow of Reynolds number $Re \approx 90$. In experiments with the chemical BZ reaction in the inhibited state, the red ferroine dye allows for a simple detection of the surface elevation. The image appears brighter where the fluid layer is thinner, and darker where the fluid layer is thicker. If we substract the grayvalues of two images, I_1 and I_2, taken at the moment of maximal Faraday wave amplitude with a phase difference of π

$$I = |I_1(\varphi = 1/2\,\pi) - I_2(\varphi = 3/2\,\pi)| \tag{7.2}$$

we obtain the image I shown in Fig. 7.4a in grayvalue units. The nodes of the Faraday waves have the same surface elevation for both phases and the small difference appears in blue, while the anti-nodes have the highest difference in amplitude appearing in red. We observe this rectangular pattern of the Faraday waves in the entire flow region, but as time evolves the pattern deforms and imperfections travel through the grid, as can be seen at the top of Fig. 7.4a. In panel (b) of the same figure, we overlay the contours of the Faraday wave pattern onto the vorticity field. Especially in the lower part of the figure, where the wave pattern is most regular, vortices align with the wave pattern. Counter-rotating vortices (depicted by blue and red color) are located on the nodes of the wave pattern, while the hyperbolic regions in-between vortices coincide with the anti-nodes of the wave pattern. This coupled flow pattern is relatively unstable, as it exists only for transient times in parts of the flow field. It would be interesting to check if it was more stable in a steady rectangular Faraday wave field, e.g., in a square container. The congruence of the vortex pattern and the wave pattern is a clear hint that the position where a vortex is generated is at least partly determined by the pattern of the Faraday waves.

In order to estimate the time during which the Faraday wave pattern is stable without irregular translations and deformations, we analyze the time dependence

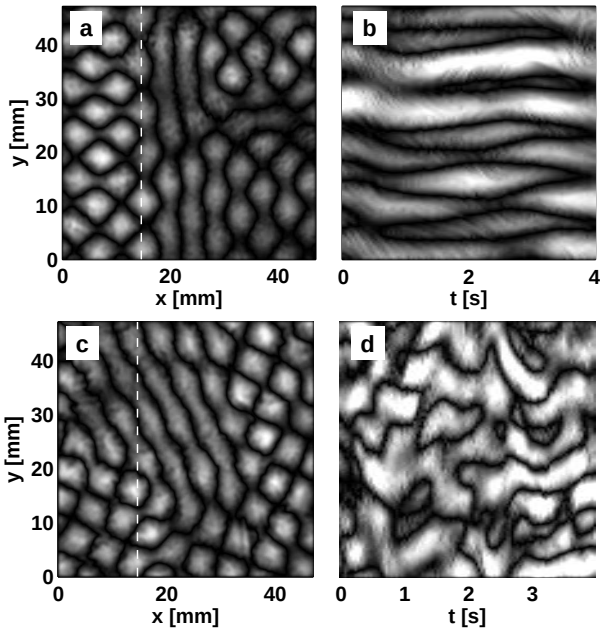

Figure 7.5: Patterns of Faraday waves in flows for Reynolds numbers (a) $Re \approx 60$ and (c) $Re \approx 210$. Nodes appear in dark tones and antinodes in bright tones. (b,d) Space-time plots of the wave pattern along the dashed line showing the stability of the wave pattern in time. Time scales of deformation and translation are estimated from the autocorrelation time to be (b) $\tau_{corr} \approx 0.7$ s and (d) $\tau_{corr} \approx 4.5$ s.

of the wave pattern for the fastest and slowest experimental flows with Reynolds numbers $Re \approx 60$ and $Re \approx 210$. Fig. 7.2.1 shows nodes and antinodes in the wave patterns of both flows (panel a and c) and the corresponding space-time plots (panel b and d). Nodes and antinodes deform and translate much faster for the intenser flow. The corresponding autocorrelation times for the wave patterns are $\tau_{corr} \approx 0.7$ s for the slow and $\tau_{corr} \approx 4.5$ s for the fast flow. When we assume that the vortices observed in the Faraday flow are coupled to the regular wave pattern as suggested in Fig. 7.4, the typical time during which the wave pattern stays stationary could be the limiting time for the vortices to exist. Hence, the instability in the wave pattern that itself might be due to wave-vortex interactions could be the limiting factor for stable rotating structures in the flow.

In this part, we analyzed vortices, or Eulerian coherent structures, in the Faraday flow from the observational point of view. The persistence time of the vortices is similar to the eddy turnover time and vortices should therefore considerably influence the trajectories of fluid parcels. With increasing Reynolds number the persistence time of vortices significantly decreases, as diagnosed by the autocorrelation time of the vorticity field. This decrease might be related to the increasing irregular movements of the Faraday wave pattern, as the position of vortices appears to be coupled to the rectangular pattern of the Faraday waves.

7.2.2 Lagrangian Coherent Structures

As we have seen in the previous section (7.2.1), the analysis of vortices, defined as small circular domains of high positive or negative vorticity, gives a first overview over the spatial structure and the time dependence of the velocity fields. However, transport is inherently Lagrangian and no final conclusion about the spatial structure of transport can be drawn from the Eulerian measures. Instead, the structures that are relevant for shaping the chemical front are of Lagrangian nature. In this section, we therefore characterize the transport in the Faraday flow with Lagrangian coherent structures (LCS) in fields of the finite-time Lyapunov exponent (FTLE), computed as described in Sec. 2.3. We focus on the FTLE fields resulting from a backward integration in time. Ridges of high values in these fields approximate unstable manifolds that are expected to align with lines of high tracer gradients of advected substances. We use velocity fields of experiments where the fluid is deionized water instead of the solution of the chemical reaction. This optimizes the contrast of tracer particles in the images such that the PIV analysis results in velocity fields with minimized uncertainties.

In Fig. 7.6 we examine the optimal finite integration time τ of particle trajectories to obtain a FTLE field that reveals most clearly the underlying transport structures. The three figures show the backward FTLE field for integration times $\tau = 1.5\,\tau_\epsilon$, $3\,\tau_\epsilon$ and $6\,\tau_\epsilon$, where τ_ϵ is the eddy turnover time, Eq. (7.1). For $\tau = 3\,\tau_\epsilon$ we obtain the best result, shown in panel (b). Elongated lines of high FTLE values trace the locations of unstable manifolds in a grid of counter-rotating vortices in the Faraday flow. The unstable manifolds have a perpendicular orientation to each other, since the vortices are collocated on a grid, given by the wave pattern of the Faraday waves. With increasing integration time, the trajectories pass different parts of the flow and the FTLE value represents a mean over stretching rates of variable magnitude. Therefore, the FTLE field in panel (c) becomes more uniform, while the fundamental Lagrangian structure can still be seen. In this case, the integration time is about six times the autocorrelation time of the vortices τ_{corr} (Fig. 7.3). Thus, the time-dependent velocity field totally changes its spatial structure during this time period leading to an efficient mixing and a similar value for a large part of the particles [99].

With the choice of $\tau = 3\,\tau_\epsilon$ we also obtain clearly defined LCS for Faraday flows with a higher forcing, shown in Fig. 7.7. The complexity of the structures is very similar to the complexity of previously reported LCS in a turbulent flow [123]. An important difference is that their quasi-twodimensional flow in a rotating tank, forced by 3D turbulence, is probably scale-free, such that the largest LCS are associated to vortices whose size is limited only by the system size [179]. In contrast, we have a sharply defined forcing wave length given by the Faraday waves that seems to determine the length scale of the largest LCS in our flow.

The probability distributions of the FTLE values are plotted in Fig. 7.8. For each flow, a narrowing of the pdf can be observed which corresponds to the effect that trajectories pass regions with different stretching rates and the Lyapunov exponent becomes similar for all trajectories (cf. Fig. 7.6). For the longest integration time $\tau = 6\,\tau_\epsilon$ (blue curves) the pdfs are biased, as the maximal attainable

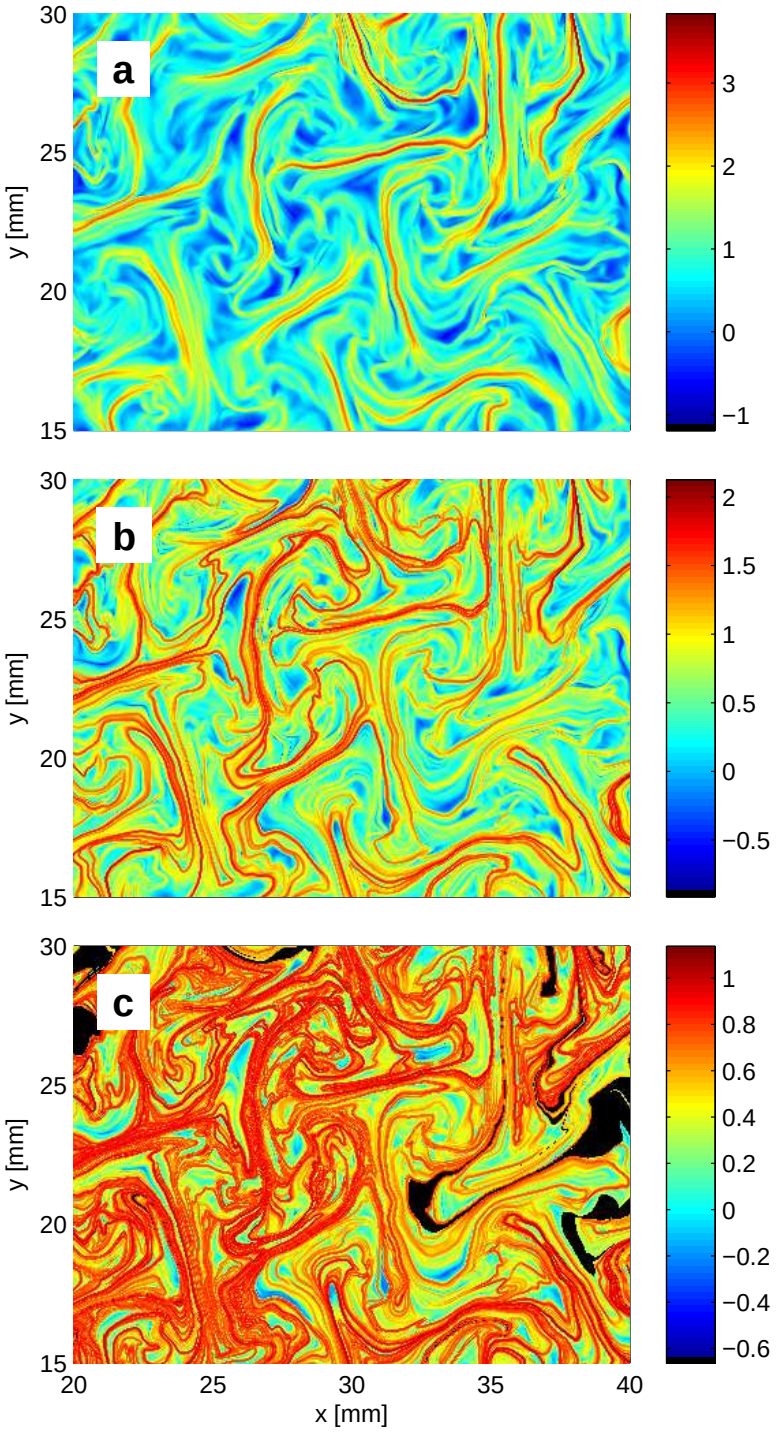

Figure 7.6: FTLE fields for an integration backward in time in a Faraday flow with $Re \approx 60$. Integration times τ are multiples of the eddy turnover time τ_ϵ, Eq. (7.1). (a) $\tau = 1.5\,\tau_\epsilon$. (b) $\tau = 3\,\tau_\epsilon$. (c) $\tau = 6\,\tau_\epsilon$. The transport is dominated by counter-rotating vortices arranged on a grid that is coupled to the regular pattern of the Faraday waves (cf. Fig. 7.4).

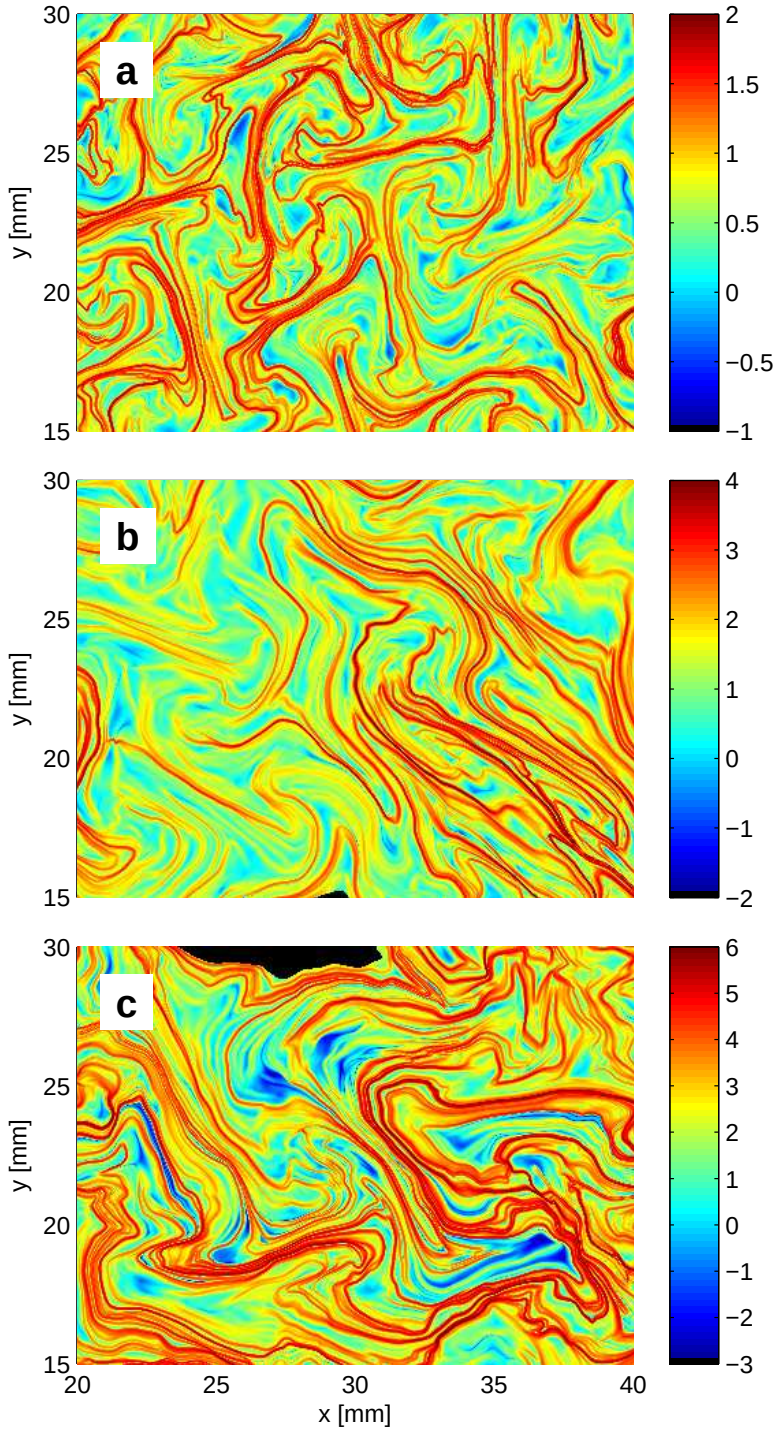

Figure 7.7: FTLE fields for three Faraday flows with increasing intensity: (a) $Re \approx 60$, (b) $Re \approx 130$, (c) $Re \approx 210$. The integration time is set according to the eddy turnover time in each flow as $\tau = 3\,\tau_\epsilon$. In all flows the length scale of the largest LCS seems to be dominated by the wave length of the Faraday waves $\lambda_F \sim 10\,\text{mm}$.

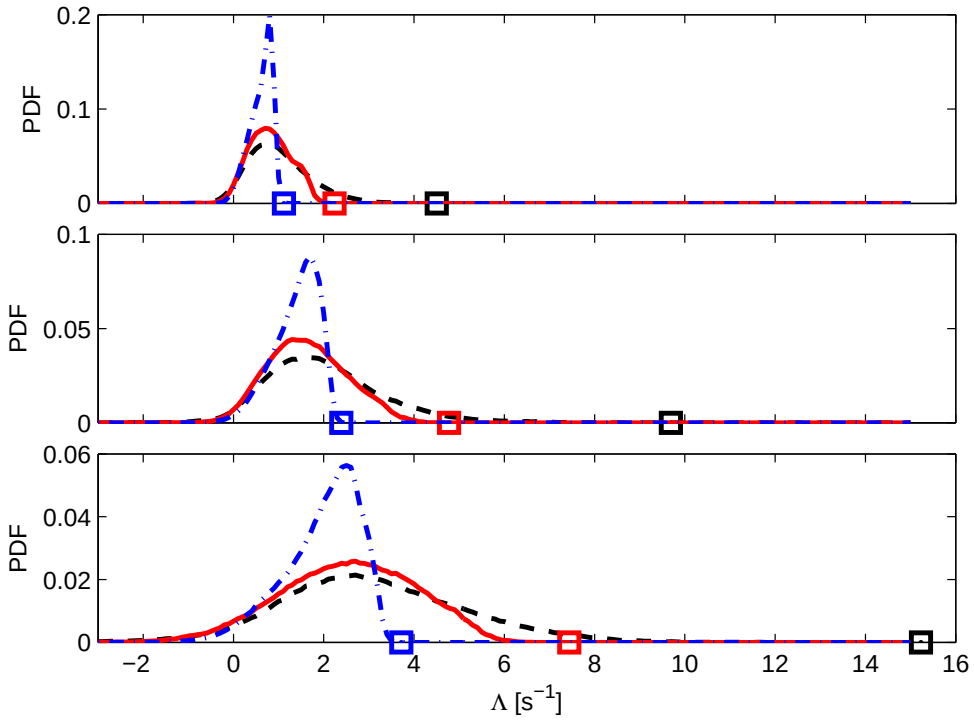

Figure 7.8: Probability density functions of FTLE values for three different flows. (a) $Re \approx 60$. (b) $Re \approx 130$. (c) $Re \approx 210$. Colors indicate the integration time of $1.5\,\tau_\epsilon$ (black, dashed), $3\,\tau_\epsilon$ (red, solid), and $6\,\tau_\epsilon$ (blue, dash-dotted). Squares indicate the maximal attainable FTLE value which is limited by the domain size.

Lyapunov exponent is limited by the domain size. The squares indicate this limit value. It is given by the fact that two initially close particles cannot separate further than the domain size during the integration time τ. Particles that separate faster automatically reach the boundary and are discarded for the computation of FTLE values.

The mean Lyapunov exponent is an important measure for the mixing intensity in fluids. Fig 7.9a shows the mean FTLE values averaged over the entire domain for the Faraday flows with different intensity. The values decrease rapidly with the integration time. However, they have not reached an asymptotic value when the domain size starts to limit an unbiased evaluation of the pdf. Generally, the mean FTLE value increases with the flow intensity. It is interesting to have a closer look at the pdfs of the FTLE values. In Fig. 7.9b we plot the pdf of the logarithmic stretching $p(\Lambda\tau)$. The curves for the different flow intensities collapse when τ is a multiple of the eddy turnover time representing a typical time scale in the flow. This basically means that in the Faraday flows with different Reynolds numbers (statistically) the same deformation of the fluid is reached if time is scaled with the eddy turnover time.

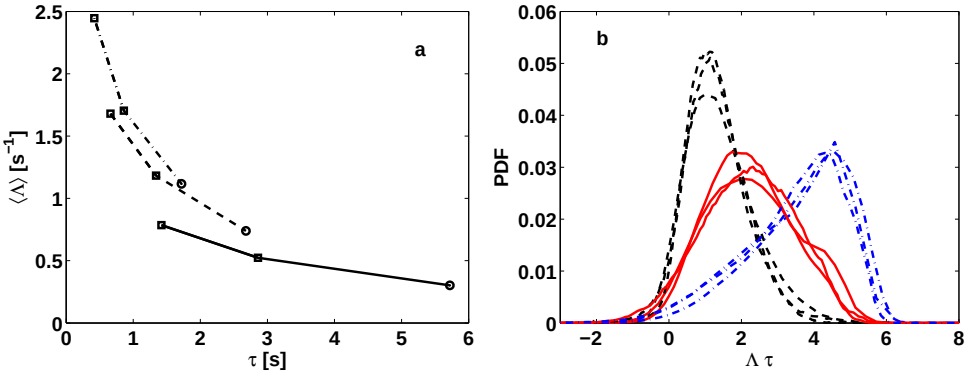

Figure 7.9: (a) Mean FTLE values for Faraday flows with $Re \approx 60$ (solid), $Re \approx 130$ (dashed), $Re \approx 210$ (dash-dot). Note that the round data points (○) are biased due to the limited size of the domain (cf. Fig. 7.8) (b) The pdfs of the logarithmic stretching $\Lambda\tau$ collapse for flows with different forcing intensity when τ is chosen as a multiple of the eddy turnover time $\tau_\epsilon = \lambda_F / v_{rms}$. Colors indicate the integration time of $1.5\,\tau_\epsilon$ (black, dashed), $3\,\tau_\epsilon$ (red, solid), and $6\,\tau_\epsilon$ (blue, dash-dotted).

7.2.3 Simultaneous LCS and Chemical Front

In the previous part, we examined LCS in velocity fields of the Faraday flow that were measured in deionized water. For this part, we use an aqueous solution of the BZ chemical reaction, such that a wrinkled chemical front propagates through the reactor. We simultaneously measure the flow by means of PIV and we determine qualitatively the concentration of the BZ reaction. The flow information is estimated from small PIV particles in the image and the concentration of the BZ reaction is given by the gray value in the image (Fig. 7.10a). The gray value in the images is a monotonically increasing function of the concentration of ferriin that represents the activator in the BZ reaction. Since the PIV particles are small compared to the structures in the concentration field, the flow information and the concentration field can be reasonably separated by smoothing. A spatial low-pass filter removes the particles, and a spatial high-pass filter removes the background concentration field. Certainly, this methods is not suitable to determine exact concentration fields and concentration gradient fields, but it is a relatively simple experiment without the need for two cameras that separately record the PIV particles and the chemical concentration.

The LCS were extracted from the backward FTLE field (Sec. B.1) based on the PIV measurements. Strictly, they are only valid for pure advection, while diffusion and especially the reaction also significantly contribute to the propagation of the chemical BZ front. However, as we argued above, the filamentous structure of the front suggests a strong influence of advection in shaping the front. Therefore, we compare the spatial structure of the front with LCS extracted from the PIV flow. Fig. 7.10b shows the smoothed image, where bright colors indicate a high activator concentration. The overlaid LCS are located along the boundaries of zones with a high activator concentration. Since they are estimates of the unstable

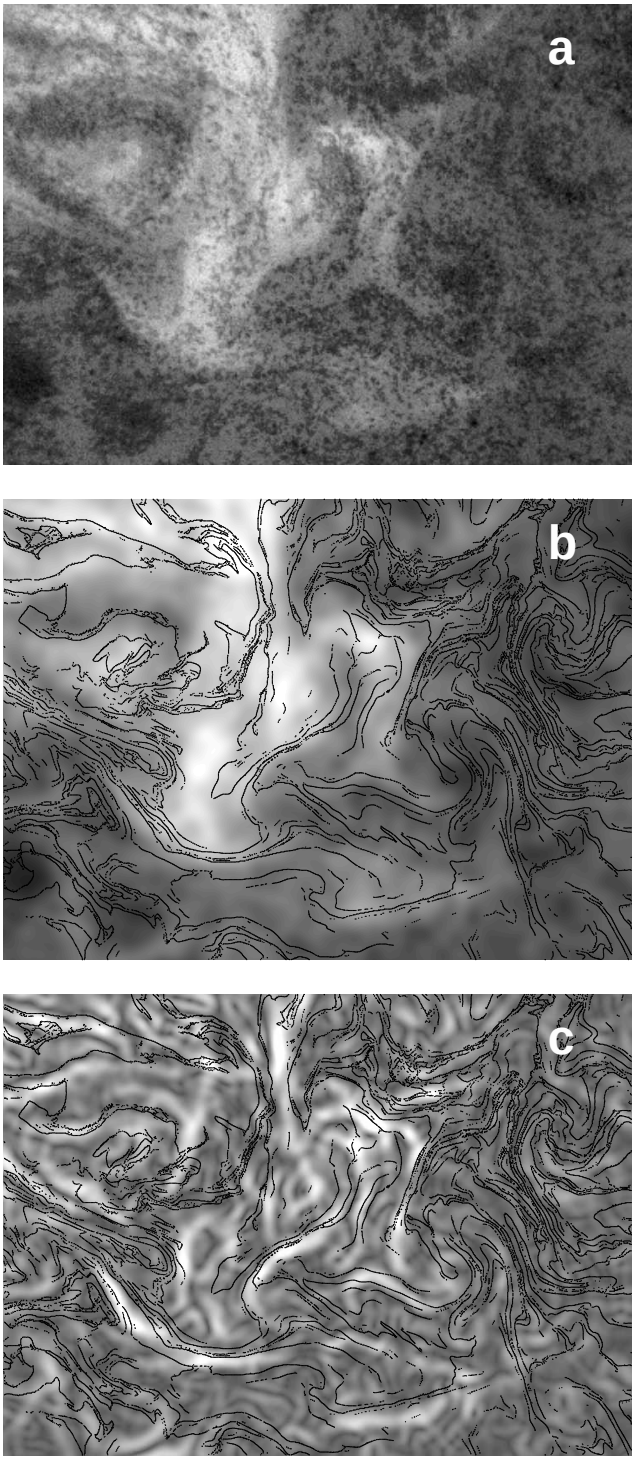

Figure 7.10: Propagating chemical front of the BZ reaction in the Faraday flow with $Re \approx 60$. (a) Original image in gray scale units. (b) Smoothed image and superimposed ridges of the backward FTLE field. (c) Gradient field of smoothed image with ridges of the backward FTLE field.

hyperbolic manifolds in the flow, they mark the lines where fluid patches merge. Consequently, high gradients occur along these lines. In Fig. 7.10c we show the gradient field of the smoothed image. High gradients at the boundary of the activated region align with the attracting LCS. The agreement of the concentration and gradient fields with the FTLE ridges is not perfect. This can mainly be attributed to the fact that the FTLE ridges are only estimates of transport barriers to advection, and the concentration field is only qualitatively measured here. Moreover, the LCS only take into account the advection, while the chemical concentration is not a passive tracer and diffusion and reaction make the front propagate as well. We also have to mention that the concentration fields show some indications for a vertical shear in the thin fluid layer, such that the chemical front has also a vertical structure.

7.3 Conclusions and Outlook

We studied transport in a quasi-twodimensional turbulent Faraday flow with the focus on a chemical wave front that propagates through the stirred fluid. From our Eulerian and Lagrangian analysis of the flow we can draw the following conclusions.

- Vorticity patterns in the moderately forced Faraday flow are directly correlated with the regular patterns of the Faraday capillary waves. In flow regions with a stable wave pattern, the vortices are ordered on a rectangular grid and persist for several seconds. For higher forcings, the vorticity pattern becomes less regular and less persistent.

- Lagrangian coherent structures (LCS) in the Faraday flow are most pronounced for integration times of about three eddy turnover times. For a weak forcing, LCS reflect the transport in the rectangular grid of eddies. For stronger forcings, this structure is observed less frequently, but still the wave length of the Faraday waves seem to be the dominate length scale in the transport patterns.

- Faraday flows with different Reynolds numbers reveal the same statistics of logarithmic stretching $\lambda\tau$, if the time τ is rescaled with the eddy turnover time, a typical time scale in the flow.

- In the moderately forced Faraday flow, attracting LCS from the backward FTLE fields align with the contours of the simultaneously measured concentration of the BZ chemical reaction. This demonstrates that the spreading of the reaction front is locally controlled by LCS. Chaotic advection generates the filamentous structure of the chemical wave wave front.

It would be very interesting to improve the experimental techniques towards a higher accuracy of a simultaneous flow and concentration measurement. Additionally, a reduction of the vertical shear would be desirable. This might possibly be achieved with a two-layer fluid, where the bottom layer consists of a dense immiscible fluid with a low viscosity (Fluorinert®). Test will have to show if a

horizontal Faraday flow is generated equally in such a two-layer fluid under similar forcings as for a single layer. Finally, the experiment could be a testbed for the promising approach of BIMs [114, 135] that until now have only been applied to laminar flows.

Chapter 8

Conclusions

In this thesis, we have studied fluid transport in several time-dependent two-dimensional flows given by discrete data sets of the velocity fields. The fluid flows exhibit chaotic advection, and consequently, the Lagrangian patterns of passive and reactive tracers have a highly irregular shape. We used the concept of Lagrangian coherent structures (LCS) that are computed from trajectories of fluid parcels in the chaotic flows. In the two-dimensional case, LCS are lines that separate fluid regions with dynamically different trajectories. They unveil the geometric structure of the stretching and folding process inherent to chaotic mixing. The LCS completely control and determine the chaotic advection in the flow. Therefore, they are extremely useful to analyze the spatial distribution of passive or reactive tracers subject to the flow.

In chapter 4, we studied the spreading of a single phytoplankton patch simulated with a simple NPZ model. The patch emerges from a localized nutrient source and is subject to advection in two different flow models, a random flow with Gaussian spatio-temporal correlation, and mesoscale oceanic flow. On average, over many realizations of the plankton patch, we find optimal Eulerian time and length scales that favor the plankton growth in the Gaussian correlated flow. When the advective flow changes on time scales similar to the typical time scale of the biological reaction, the growth of phytoplankton is maximal. On average, the Eulerian parameters of the flow can give a rough indication about the interaction of reaction and advection. However, to understand the shape of a plankton patch in a concrete case, we have to take into account the flow topology and the fluid trajectories, i.e., the Lagrangian view. Analyzing the flow topology in the vicinity of two eddies in the steady mesoscale flow, we can see that the positions of hyperbolic points control the pathways of the fluid motion.

In chapter 5, we examined the explosive spreading of the Madagascar plankton bloom and asked how advection by mesoscale ocean currents affects the bloom. It turns out that the recently discovered South Indian Ocean Countercurrent (SICC), a fast eastward jet, flows at the exact location where the bloom typically occurs. Here, LCS are an ideal method to compare the irregular patterns of the chlorophyll distribution with the mixing patterns hidden in the advective flow field. Using Lagrangian methods we found two basic mechanisms how the SICC can influence the Madagascar plankton bloom. First, it provides a fast and persistent eastward

transport that significantly contributes to the large extent of the plankton bloom. Second, zonal jet-like LCS associated with the SICC often represent a transport barrier in meridional direction, shaping the boundary of the bloom. Taking into account that we neglected the vertical circulation that may influence the plankton growth, e.g., by upwelling of nutrients, and also taking into account that we use only large scale ocean currents neglecting all subgrid motion, the agreement between the spatio-temporal patterns in the chlorophyll concentration and the advection patterns as revealed by LCS is notable. Moreover, our numerical experiments with a passive tracer concentration have shown that the tracer spreads to a similar final shape as the plankton bloom. This support the hypothesis that the main nutrient source of the Madagascar plankton bloom is located at the south tip of Madagascar. The results show that is it very important to address transport in the ocean with Lagrangian methods. Since the SICC is hidden in a field of counter-rotating eddies, we are only able to unveil the complex entangled structure of fluid transport in different directions, if we integrate the velocity field and analyze the trajectories.

In chapter 6, we analyzed the surface flow in the Ria de Vigo, an estuary in NW Spain. The main component of the flow is given by the tidal oscillating flow, which interacts with a longterm directional northward or southward flow on the shelf, and with the flow induced by high-frequency local winds. This leads to chaotic transport. Pronounced vortices are absent in the model flow that we use. Transport is rather directed by the complex coastal boundary. LCS are attached to capes or islands, where the flow separates or merges. As integrated and relatively stable structures, the LCS define coherent water masses and are ideal to compare transport in the model flow with the trajectories of real surface drifters. We find that the trajectories of surface drifters largely agree with the LCS dynamics in the model flow. In some cases the uncertainties of the position of the LCS lead to a crossing of the surface drifters over the LCS, where the fluid dynamics close to the coast is not sufficiently resolved in the model flow. Synoptic Lagrangian Maps (SLM) are a second method that we use to obtain transport patterns in the Ria de Vigo. In this case we also use velocity fields measured by a HF radar system. The SLM reveal the fluid transport through the outer part of the Ria de Vigo, from one open boundary to another. The transport is correlated with the wind direction. Residence times of single fluid patches in the flow domain vary largely from one day to up to ten days. Since, in the SLM, trajectories are classified by their origin and fate at one of the open boundaries, the resulting maps of global transport patterns are relatively independent of details of the flow field. SLM are therefore useful to validate the global transport patterns in the Ria de Vigo as given by the model flow with flow data from the HF radar system. For exemplary dates we find a good agreement between the SLM, while it would desirable to carry out a systematic analysis for a long period of flow data.

In chapter 7, we examined the advection in a turbulent quasi two-dimensional flow in the laboratory induced by capillary surface waves, Faraday waves, in a thin fluid layer. In a persistent rectangular pattern of Faraday waves the generated vortices are coupled to the locations of nodes and anti-nodes of the waves. For increased forcing, the Faraday waves become more and more disordered and

direct correlation of the pattern of vortices and the pattern of Faraday waves is less pronounced. The front of a chemical reaction propagating through the container exhibits a filamentous structure which is caused by the stirring of the fluid. We are able to simultaneously measure the velocity fields quantitatively and the concentration of the chemical reaction qualitatively. A superposition of the LCS extracted from the velocity fields onto the qualitative concentration field of the chemical reaction shows that the filaments at the front are shaped by advective stirring. As expected, high gradients appear along the attracting LCS where fluid with activated and inhibited chemical reaction merges.

In summary, we saw that the irregular fluid motion in time-dependent flows generates mixing patterns that affect passive and reactive fields in the flow. For many applications, we can extract the geometry of chaotic mixing from the flow thanks to the availability of complete spatio-temporal velocity data sets. Especially in the oceanic context, the access to such complete data sets was not possible until some years ago, and the data becomes increasingly accurate as the technology advances. HF radar systems and satellite altimetry provide measured velocity fields, while a vast amount of flow data is also produced by hydrodynamic numeric models on all length scales. In a controlled environment in the laboratory, velocity fields in scientific experiments can be obtained by PIV measurements. This completeness of the velocity data allows to obtain realistic trajectories of fluid parcels, so that we can examine transport with Lagrangian methods. For transport processes on finite times where persistent flow structures, such as vortices and jets, govern the transport, Lagrangian coherent structures reveal the decisive mixing patterns in the flow. It is a promising method to reduce the large velocity data sets to the transport information relevant for concrete applications. The improvement of the techniques to extract LCS even more accurately is an active field of research.

Bibliography

[1] October 2012. URL `http://www.mohid.com/Prestige/PrestigeSpill/Comparison/Comparison.htm`.

[2] October 2012. URL `https://www.me.bme.hu/~karolyi/results/active/activity.html`.

[3] A. Abascal, S. Castanedo, V. Fernández, and R. Medina. Backtracking drifting objects using surface currents from high-frequency (HF) radar technology. *Ocean Dynamics*, 62(7):1073–1089, 2012.

[4] A. J. Abascal, S. Castanedo, R. Medina, I. J. Losada, and E. Alvarez-Fanjul. Application of HF radar currents to oil spill modelling. *Marine Pollution Bulletin*, 58:238–248, 2009.

[5] E. Abraham. The generation of plankton patchiness by turbulent stirring. *Nature*, 391:577–580, 1998.

[6] E. R. Abraham and M. M. Bowen. Chaotic stirring by a mesoscale surface-ocean flow. *Chaos*, 12(2):373–381, 2002.

[7] R. Adrian. Twenty years of particle image velocimetry. *Exp. Fluids*, 39: 159–169, 2005.

[8] K. Alligood, T. Sauer, and J. Yorke. *Chaos - an introduction to dynamical systems*. Springer Verlag, New York, Berlin, Heidelberg, 1997.

[9] S. Alonso, F. Sagués, and J. Sancho. Excitability transitions and wave dynamics under spatiotemporal structured noise. *Phys. Rev. E*, 65:066107(1)–066107(11), 2002.

[10] H. Aref. Stirring by chaotic advection. *J. Fluid Mech.*, 143:1–21, 1984.

[11] H. Aref. Chaotic advection of fluid particles. *Phil. Trans. R. Soc. Lond. A*, 1333:273–288, 1990.

[12] H. Aref. The development of chaotic advection. *Phys. Fluids*, 14(4):1315–1325, 2002.

[13] P. Arratia and J. Gollub. Predicting the progress of diffusively limited chemical reactions in the presence of chaotic advection. *Phys. Rev. Lett.*, 96: 024501, 2006.

[14] V. Artale, G. Boffetta, A. Celani, M. Cencini, and A. Vulpiani. Dispersion of passive tracers in closed basins: Beyond the diffusion coefficient. *Phys. Fluids*, 9:11, 1997.

[15] R. Bainbridge. The size, shape and density of marine phytoplankton concentrations. *Biol. Rev.*, 32:91–115, 1957.

[16] G. L. Baker and J. P. Gollub. *Chaotic Dynamics - An Introduction*. Cambridge University Press, 1996.

[17] N. Banas and B. Hickey. Mapping exchange and residence time in a model of Willapa Bay, Washington, a branching, macrotidal estuary. *J. Geophys. Res.*, 110:C11011, 2005.

[18] D. Barrick, M. Evans, and B. Weber. Ocean surface currents mapped by radar. *Science*, 198(4313):138–144, 1977.

[19] E. Beltrami and T. Carroll. Modeling the role of viral desease in recurrent phytoplankton blooms. *J. Math. Biol.*, 32:857–863, 1994.

[20] F. Beron-Vera, M. Olascoaga, and G. Goni. Oceanic mesoscale eddies as revealed by Lagrangian Coherent Structures. *Geophys. Res. Lett.*, 35: L12603, 2008.

[21] F. J. Beron-Vera, M. Brown, M. Olascoaga, I. Rypina, H. Koak, and I. Udovydchenkov. Zonal jets as transport barriers in planetary atmospheres. *J. Atmos. Sci.*, 65:3316–3326, 2008.

[22] F. J. Beron-Vera, M. Olascoaga, and G. Goni. Surface ocean mixing inferred from different multisatellite altimetry measurements. *J. Phys. Oceanogr.*, 40:2466–2480, 2010.

[23] G. Boffetta, A. Celani, M. Cencini, G. Lacorata, and A. Vulpiani. Nonasymptotic properties of transport and mixing. *Chaos*, 10:1, 2000.

[24] G. Boffetta, G. Lacorata, G. Redaelli, and G. Vulpiani. Detecting barriers to transport: A review of different techniques. *Physica D*, 159:58–70, 2001.

[25] A. Bower. A simple kinematic mechanism for mixing fluid parcels across a meandering jet. *J. Phys. Ocean.*, 21:173–180, 1991.

[26] A. Bracco, S. Clayton, and C. Pasquero. Horizontal advection, diffusion, and plankton spectra at the sea surface. *J. Geophys. Res.*, 114:C02001, 2009. doi: $10.1029/2007\mathrm{JC}004671$.

[27] M. Branicki and R. Malek-Madani. Lagrangian structure of flows in the Chesapeake Bay: challenges and perspectives on the analysis of estuarine flows. *Nonlin. Processes Geophys.*, 17:149–168, 2010.

[28] M. Branicki and S. Wiggins. Finite-time Lagrangian transport analysis: stable and unstable manifolds of hyperbolic trajectories and finite-time Lyapunov exponents. *Nonlin. Processes Geophys.*, 17:1–36, 2010.

[29] M. Budyansky, M. Uleysky, and S. Prants. Detection of barriers to cross-jet Lagrangian transport and its destruction in a meandering flow. *Phys. Rev. E*, 79:056215, 2009.

[30] H. Burchard, K. Bolding, and M. Villarreal. GOTM, a General Ocean Turbulence Model: Theory, implementation and test cases, Report EUR 18745, 103, european commission, 1999.

[31] J. Campbell and H. Feng. The empirical chlorophyll algorithm for SeaWiFS: Testing the OC4.v4 algorithm using NOMAD data, 2005. URL `http://oceancolor.gsfc.nasa.gov/MEETINGS/OCBAM/docs/Evaluation_of_OC4.pdf`.

[32] P. Carracedo, S. Torres-López, M. Barreiro, P. Montero, C. F. Balseiro, E. Penabad, P. C. Leitao, and V. Pérez-Muñuzuri. Improvement of pollutant drift forecast system applied to the Prestige oil spills in Galicia coast (NW of Spain): Development of an operational system. *Marine Pollution Bulletin*, 53:350–360, 2006.

[33] M. Cerejo and J. M. Dias. Tidal transport and dispersal of marine toxic microalgae in a shallow, temperate coastal lagoon. *Marine Environmental Research*, 63:313–340, 2007.

[34] S. Chao and P. Shaw. Nonhydrostatic aspects of coastal upwelling meanders and filaments off eastern ocean boundaries. *Tellus A*, 54:63–75, 2002.

[35] R. Chapman, L. Shay, H. Graber, J. Edson, A. Karachintsev, C. Trump, and D. Ross. On the accuracy of HF radar surface current measurements: Intercomparisons with ship-based sensors. *J. Geophys. Res.*, 102(C8):18,737–18,748, 1997.

[36] D. Chelton, J. Ries, B. Hains, L. Fu, and P. Callahan. *Satellite Altimetry and Earth Science - A Handbook of Techniques and Applications*, chapter Satellite Altimetry, pages 1–132. Academic Press, 2001.

[37] D. Chelton, M. Schlax, R. Samelson, and R. de Szoeke. Global observations of large oceanic eddies. *Geophys. Res. Lett.*, 34:L15606, 2007.

[38] D. B. Chelton, P. Gaube, M. Schlax, J. Early, and R. Samelson. The influence of nonlinear mesoscale eddies on near-surface oceanic chlorophyll. *Science*, 334:328–332, 2011. doi: $10.1126/\mathrm{science}.1208897$.

[39] J. Christian, R. Murtugudde, J. Ballabrera-Poy, and C. McClain. A ribbon of dark water: phytoplankton blooms in the meanders of the Pacific North Equatorial Countercurrent. *Deep-Sea Res. II*, 51:209–258, 2004.

[40] H. Coelho, R. Neves, M. White, P. Leita, and A. Santos. A model for ocean circulation on the Iberian coast. *J. Mar. Syst.*, 32:153–179, 2002.

[41] C. Coulliette, F. Lekien, J. D. Paduan, G. Haller, and J. E. Marsden. Optimal Pollution Mitigation in Monterey Bay Based on Coastal Radar Data and Nonlinear Dynamics. *Environ. Sci. Technol.*, 41:6562–6572, 2007.

[42] R. K. Cowen, C. B. Paris, and A. Srinivasan. Scaling of Connectivity in Marine Populations. *Science*, 311(5760):522–527, 2006.

[43] G. Csanady. *Turbulent diffusion in the environment*. D. Reidel Publishing Company, Dordrecht, Holland, 1973.

[44] B. Cushman-Roisin and J.-M. Beckers. *Introduction to geophysical fluid dynamcis – Physical and numerical aspects*. Academic Press, 2009.

[45] W. de Ruijter, E. van Aken, H.M.and Beier, J. Lutjeharms, R. Mantano, and M. Schouten. Eddies and dipoles around South Madagascar: formation, pathways and large-scale impact. *Deep-Sea Res. I*, 51:383–400, 2004.

[46] M. deCastro, M. Gómez-Gesteira, R. Prego, J. J. Taboada, P. Montero, P. Herbello, and V. Pérez-Villar. Wind and Tidal Influence on Water Circulation in a Galician Ria (NW Spain). *Estuarine, Coastal and Shelf Science*, 51:161–176, 2000.

[47] M. deCastro, A. Dale, M. Gómez-Gesteira, R. Prego, and I. Alvarez. Hydrographic and atmospheric analysis of an autumnal upwelling event in the Ria of Vigo (NW Iberian Peninsula). *Estuarine, Coastal and Shelf Science*, 68:529–537, 2006.

[48] S. F. DiMarco, P. Chapman, and W. Nowlin Jr. Satellite observations of upwelling on the continental shelf south of Madagascar. *Geophys. Res. Lett.*, 27(24):3965–3968, 2000.

[49] K. Döös and A. Engqvist. Assessment of water exchange between a discharge region and the open sea - A comparison of different methodological concepts. *Estuarine, Coastal and Shelf Science*, 74:585–597, 2007.

[50] S. Douady. Experimental study of the Faraday instability. *J . Fluid Mech.*, 221:383–409, 1990.

[51] F. d'Ovidio, V. Fernández, E. Hernández-García, and C. López. Mixing structures in the Mediterranean Sea from finite-size Lyapunov exponents. *Geophys. Res. Lett.*, 31:L17203, 2004. doi: $10.1029/2004\mathrm{GL}020328$.

[52] F. d'Ovidio, V. Fernández, E. Hernández-García, and C. López. Comparison between Eulerian diagnostics and finite-size Lyapunov exponents computed from altimetry in the Algerian basin. *Deep-Sea Res. I*, 56:15–31, 2009.

[53] F. d'Ovidio, S. De Monte, S. Alvain, Y. Dandonneau, and M. Lévy. Fluid dynamical niches of phytoplankton types. *Proc. Natl. Acad. Sci. USA*, 107: 18,366–18,370, 2010. doi: $10.1073/\mathrm{pnas}.1004620107$.

[54] S. Dutkiewicz, A. Griffa, and D. Olson. Particle diffusion in a meandering jet. *J. Geophys. Res.*, 98(C9):16,487–16,500, 1993.

[55] C. Eckart. An analysis of stirring and mixing processes in incompressible fluids. *J. Mar. Res.*, 7:265–275, 1948.

[56] K. P. Edwards, F. E. Werner, and B. O. Blanton. Comparison of Observed and Modeled Drifter Trajectories in Coastal Regions: An Improvement through Adjustments for Observed Drifter Slip and Errors in Wind Fields. *J. Atmos. Ocean Tech.*, 23:1614–1620, 2006.

[57] P. Falco, A. Griffa, P. Poulain, and E. Zambianchi. Transport properties in the Adriatic Sea as deduced from drifter data. *J. Phys. Ocean.*, 30, 2000.

[58] C. Falcón and S. Fauve. Wave-vortex interaction. *Phys. Rev. E*, 80:056213, 2009.

[59] M. Faraday. On a peculiar class of acoustical figures. *Phil. Trans. R. Soc. Lond.*, 121:299–340, 1831.

[60] M. Fasham, H. Ducklow, and S. McKelvie. A nitrogen-based model of plankton dynamics in the oceanic mixed layer. *J. Mar. Res.*, 48:591–639, 1990.

[61] F. G. Figueiras, U. Labarta, and M. J. Fernández Reiriz. Coastal upwelling, primary production and mussel growth in the Rías Baixas of Galicia. *Hydrobiologia*, 484:121–131, 2002.

[62] F. Fraga. *Coastal Upwelling*, chapter Upwelling off the Galician Coast, Northwest Spain, pages 176–182. American Geophysical Union, Washington, 1981.

[63] S. Fraga. Ondas internas en la plataforma frente a la Ria de Vigo, y posibles consecuencias ecologicas. *Scientia Marina*, 60(4):543–547, 1996.

[64] S. Fraga, D. A. Anderson, I. Bravo, B. Reguera, K. A. Steidinger, and C. M. Yentsch. Influence of Upwelling Relaxation on Dinoflagellates and Shelfish Toxicity in Ria de Vigo, Spain. *Estuarine, Coastal and Shelf Science*, 27: 349–361, 1988.

[65] P. Franks. NPZ models of plankton dynamics: Their construction, coupling to physics, and application. *J. Oceanogr.*, 58:379–387, 2002.

[66] L. Fu and A. Cazenave, editors. *Satellite Altimetry and Earth Science - A Handbook of Techniques and Applications, International Geophysics Series, Vol. 69*. Academic Press, 2001.

[67] L. Fu and P.-Y. Le Traon. Satellite altimetry and ocean dynamics. *C. R. Geoscience*, 338, 2006.

[68] J. Furnans, J. Imberger, and B. R. Hodges. Including drag and inertia in drifter modelling. *Environ. Modell. Softw.*, 23:714–728, 2008.

[69] A. García-Olivares, J. Isern-Fontanet, and E. García-Ladona. Dispersion of passive tracers and finite-scale Lyapunov exponents in the Western Mediterranean Sea. *Deep-Sea Res. I*, 54:253–268, 2007.

[70] C. Garret. Turbulent dispersion in the ocean. *Progr. Oceanogr.*, 70:113–125, 2006.

[71] M. Gilcoto, P. C. Pardo, X. A. Álvarez Salgado, and F. F. Pérez. Exchange fluxes between the Ría de Vigo and the shelf: A bidirectional flow forced by remote wind. *J. Geophys. Res.*, 112:C06001, 2007. doi: $10.1029/2005\mathrm{JC}003140$.

[72] H. Gildor, E. Fredj, J. Steinbuck, and S. Monismith. Evidence for Submesoscale Barriers to Horizontal Mixing in the Ocean from Current Measurements and Aerial Photographs. *J. Phys. Ocean.*, 39:1975–1983, 2009. doi: $10.1175/2009\mathrm{JPO}4116.1$.

[73] M. Gómez-Gesteira, P. Montero, R. Prego, J. J. Taboada, P. Leitao, M. Ruiz-Villarreal, R. Neves, and V. Perez-Villar. A two-dimensional particle tracking model for pollution dispersion in A Coruña and Vigo Rías (NW Spain). *Oceanol. Acta*, 22(2):167–177, 1999.

[74] E. Gouillart, O. Dauchot, and J.-L. Thiffeault. Measures of mixing quality in open flows with chaotic advection. *Phys. Fluids*, 23:013604, 2011.

[75] A. Griffa, A. Kirwan, A. Mariano, T. Özgökmen, and T. Rossby, editors. *Lagrangian analysis and prediction of coastal and ocean dyamics*. Cambridge Univ. Press, 2007.

[76] B. Griffiths. Early references to water blooms in British lakes. *Procceedings of the Linnean Society of London*, 151:12–19, 1939.

[77] K.-W. Gurgel, G. Antonischki, H.-H. Essen, and T. Schlick. Wellen Radar (WERA): a new ground-wave HF radar for ocean remote sensing. *Coastal Engineering*, 37:219–234, 1999.

[78] G. Haller. Finding finite-time invariant manifolds in two-dimensional velocity fields. *Chaos*, 10(1):99–108, 2000.

[79] G. Haller. Lagrangian coherent structures from approximate velocity data. *Phys. Fluids*, 14(6):1851–1861, 2002.

[80] G. Haller. A variational theory of hyperbolic Lagrangian coherent structures. *Physica D*, 240:574–598, 2011.

[81] G. Haller and F. Beron-Vera. Geodesic theory of transport barriers in two-dimensional flows. *Physica D*, 241:1680–1702, 2012.

[82] G. Haller and F. Beron-Vera. Oral communication. 2012.

[83] G. Haller and G. Yuan. Lagrangian coherent structures and mixing in two-dimensional turbulence. *Physica D*, 147:352–370, 2000.

[84] T. Haszpra and T. Tél. Volcanic ash in the free atmosphere: a dynamical systems approach. *Journal of Physics: Conference Series*, 333(012008), 2011.

[85] A. Haza, T. Özgökmen, A. Griffa, Z. Garraffo, and L. Piterbarg. Parameterization of particle transport at submesoscales in the Gulf Stream region using Lagrangian subgridscale models. *Ocean Modelling*, 42:31–49, 2012.

[86] A. C. Haza, A. Griffa, P. Martin, A. Molcard, T. M. Özgökmen, A. C. Poje, R. Barbanti, J. W. Book, P. M. Poulain, M. Rixen, and P. Zanasca. Model-based directed drifter launches in the Adriatic Sea: Results from the DART experiment. *Geohphys. Res. Lett.*, 134:L10605, 2007. doi: 10.1029/2007GL029634.

[87] A. C. Haza, T. M. Özgökmen, A. Griffa, A. Molcard, P. M. Poulain, and G. Peggion. Transport properties in small-scale coastal flows: relative dispersion from VHF radar measurements in the Gulf of La Spezia. *Ocean Dynam.*, 60:861–882, 2010. doi: 10.1007/s10236-010-0301-7.

[88] I. Hernández-Carrasco, C. López, E. Hernández-García, and A. Turiel. How reliable are finite-size Lyapunov exponents for the assessment of ocean dynamics? *Ocean Modelling*, 36:208–218, 2011.

[89] C.-R. Ho, Q. Zheng, and N.-J. Kuo. SeaWiFS observations of upwelling south of Madagascar: Long-term variability and interaction with East Madagascar Current. *Deep Sea Res. II*, 51:59–67, 2004.

[90] F. Huhn, A. von Kameke, S. Allen-Perkins, P. Montero, A. Venancio, and V. Pérez-Muñuzuri. Horizontal Lagrangian transport in a tidal-driven estuary - transport barriers attached to prominent coastal boundaries. *Cont. Shelf Res.*, 39–40:1–13, 2012.

[91] F. Huhn, A. von Kameke, V. Pérez-Muñuzuri, M. Olascoaga, and F. Beron-Vera. The impact of advective transport by the South Indian Ocean Countercurrent on the Madagascar plankton bloom. *Geophys. Res. Lett.*, 39: L06602, 2012.

[92] H. Huntley, B. Lipphardt Jr., and A. Kirwan Jr. Lagrangian predictability assessed in the East China Sea. *Ocean. Modelling*, 36:163–178, 2011.

[93] K. Ide, D. Small, and S. Wiggins. Distinguished hyperbolic trajectories in time-dependent fluid flows: analytical and computational approach for velocity fields defined as data sets. *Nonlin. Process. Geophys.*, 9:237–263, 2002.

[94] D. Johnson and C. Pattiaratchi. Application, modelling and validation of surfzone drifters. *Coastal Engineering*, 51:455–471, 2004.

[95] G. Károlyi and T. Tél. Effective dimensions and chemical reactions in fluid flows. *Phys. Rev. E*, 76:046315, 2007.

[96] K. Kurin-Csörgei, A. Zhabotinsky, M. Orbán, and E. I.R. Bromate-1,4-cyclohexanedione-ferroin gas-free oscillating reaction. 1. Basic features and crossing wave patterns in a reaction-diffusion system without gel. *J. Phys. Chem.*, 100:5393–5397, 1996.

[97] J. H. LaCasce. Statistics from Lagrangian observations. *Progress in Oceanography*, 77:1–29, 2008.

[98] J. H. LaCasce and C. Ohlmann. Relative dispersion at the surface of the Gulf of Mexico. *Journal of Marine Research*, 61:285–312, 2003.

[99] G. Lapeyre. Characterization of finite-time Lyapunov exponents and vectors in two-dimensional turbulence. *Chaos*, 12(3):688–698, 2002.

[100] Y. Lehahn, F. d'Ovidio, M. Lévy, and E. Heifetz. Stirring of the northeast Atlantic spring bloom: A Lagrangian analysis based on multisatellite data. *J. Geophys. Res.*, 112:C08005, 2007. doi: $10.1029/2006\mathrm{JC}003927$.

[101] F. Lekien and N. Leonard. Dynamically Consistent Lagrangian Coherent Structures. *AIP Conf. Proc.*, 742:132–139, 2004.

[102] F. Lekien, C. Coulliette, R. Bank, and J. Marsden. Open-boundary modal analysis: Interpolation, extrapolation, and filtering. *J. Geophys. Res.*, 109: C12004, 2004.

[103] F. Lekien, C. Coulliette, A. J. Mariano, E. H. Ryan, L. K. Shay, G. Haller, and J. Marsden. Pollution release tied to invariant manifolds: A case study for the coast of Florida. *Physica D*, 210:1–20, 2005.

[104] M. Lévy. The modulation of biological production by oceanic measoscale turbulence. *Lect. Notes Phys.*, 744:219–261, 2008.

[105] M. Lévy and P. Klein. Does the low frequency variability of mesoscale dynamics explain a part of the phytoplankton and zooplankton spectral variability? *Proc. R. Soc. Lon. A*, 460:1637–1687, 2004.

[106] M. Lévy, D. Shankar, J.-M. André, S. Shenoi, F. Durand, and C. de Boyer Montégut. Basin-wide seasonal evolution of the Indian

Ocean's phytoplankton blooms. *J. Geophys. Res*, 112:C12014, 2007. doi: 10.1029/2007JC004090.

[107] B. Lipphardt, D. Small, A. Kirwan, S. Wiggins, K. Ide, C. Grosch, and J. Paduan. Synoptic Lagrangian maps: Application to surface transport in Monterey Bay. *J. Mar. Res.*, 64:221–247, 2006.

[108] A. Longhurst. A major seasonal phytoplankton bloom in the Madagascar Basin. *Deep Sea Res. I*, 48:2413–2422, 2001.

[109] M. Lorenzo, M. Santos, and V. Pérez-Muñuzuri. Spatiotemporal stochastic forcing effects in an ensemble consisting of arrays of diffusively coupled Lourenz cells. *Chaos*, 13:913–920, 2003.

[110] R. Lumpkin and S. Elipot. Surface drifter pair spreading in the North Atlantic. *J. Geophys. Res.*, 115:C12017, 2010.

[111] J. Lutjeharms. Remote sensing corroboration of retroflection of the East Madagascar Current. *Depp-Sea Res.*, 35(12):2045–2050, 1988.

[112] E. Machu, J. R. E. Lutjeharms, A. Webb, and H. Van Aken. First hydrographic evidence of the southeast Madagascar upwelling cell. *Geophys. Res. Lett.*, 29(21), 2002. doi: 10.1029/2002GL015381.

[113] A. Mahadevan and D. Archer. Modeling the impact of fronts and mecoscale circulations on the nutrient supply and biogeochemistry of the upper ocean. *J. Geophys. Res*, 105(C1):1209–1221, 2000.

[114] J. Mahoney, D. Bargteil, M. Kingsbury, K. Mitchell, and T. Solomon. Invariant barriers to reactive front propagation in fluid flows. *EPL*, 98:44005, 2012.

[115] A. M. Mancho, D. Small, and S. Wiggins. A tutorial on dynamical systems concepts applied to Lagrangian transport in oceanic flows defined as finite time data sets: Theoretical and computational issues. *Physics Reports*, 437: 55–124, 2006.

[116] A. M. Mancho, E. Hernández-García, D. Small, S. Wiggins, and V. Fernández. Lagrangian transport through an ocean front in the Northwestern Mediterranean Sea. *J. Phys. Ocean.*, 38:1222–1237, 2008.

[117] J. Marshall, C. Hill, L. Perelman, and A. Adcroft. Hydrostatic, quasi-hydrostatic, and nonhydrostatic ocean modelling. *J. Geophys. Res.*, 102(C3):5733–5752, 1997.

[118] A. Martin. On filament width in oceanic plankton distributions. *J. Plankton Res.*, 22:597–602, 2000.

[119] A. Martin. Phytoplankton patchiness: the role of lateral stirring and mixing. *Prog. Oceanogr.*, 57:125–174, 2003.

[120] A. Martin, K. Richards, and M. Fasham. Phytoplankton production and communtiy structure in an unstable frontal region. *J. Mar. Syst.*, 28:65–89, 2001.

[121] A. Martin, K. Richards, A. Bracco, and A. Provenzale. Patchy poroductivity in the open ocean. *Global Biochem Cycles*, 16, 2002.

[122] F. Martins, P. Leitao, A. Silva, and R. Neves. 3D modelling in the Sado estuary using a new generic vertical discretization approach. *Oceanologica Acta*, 24:S51–S62, 2001.

[123] M. Mathur, G. Haller, T. Peacock, J. Ruppert-Felsot, and H. Swinney. Uncovering the Lagrangian skeleton of turbulence. *Phys. Rev. Lett.*, 98: 144502, 2007.

[124] N. A. Maximenko, B. Bang, and H. Sasaki. Observational evidence of alternating zonal jets in the world ocean. *Geophys. Res. Lett.*, 32:L12607, 2005. doi: $10.1029/2005\mathrm{GL}022728$.

[125] W. McKiver, Z. Neufeld, and I. Scheuring. Plankton bloom controlled by horizontal stirring. *Nonlin. Process. Geophys.*, 16:623–630, 2009.

[126] P. McLeod, A. P. Martin, and K. Richards. Minimum length scale for growth-limited oceanic plankton distributions. *Ecol. Model.*, 158:111–120, 2002.

[127] A. Medvinsky, I. A. Tikhonova, R. Rubin, B. Li, Z. Lin, and H. Malchow. Patchy environment as a factor of complex plankton dynamics. *Phys. Rev. E.*, 64:021915, 2001.

[128] C. Mendoza and A. Mancho. Hidden geometry of ocean flows. *Phys. Rev. Lett.*, 105:038501, 2010.

[129] C. Mendoza, A. M. Mancho, and M. Rio. The turnstile mechanism across the Kuroshio current: analysis of dynamics in altimeter velocity fields. *Nonlin. Processes Geophys.*, 17:103–111, 2010.

[130] O. Mesquita, S. Kane, and J. Gollub. Transport by capillary waves: Fluctuating Stokes drift. *Phys. Rev. A*, 45(6), 1992.

[131] I. Mezić, S. Wiggins, and D. Betz. Residence-time distributions for chaotic flows in pipes. *CHAOS*, 9(1):171–182, 1999.

[132] I. Mezić, S. Loire, V. A. Fonoberov, and P. Hogan. A New Mixing Diagnostic and Gulf Oil Spill Movement. *Science*, 330(6003):486–489, 2010.

[133] B. M. Míguez, F. F. Pérez, C. Souto, and L. Fariña Busto. Flujos residuales de intercambio entre la Ría de Vigo y la plataforma continental. *Física de la Tierra*, 13:119–137, 2001.

[134] J. Miles and D. Henderson. Parametrically forced surface waves. *Annu. Rev. Fluid Mech.*, 22:143–165, 1990.

[135] K. Mitchell and J. Mahoney. Invariant manifolds and the geometry of front propagation in fluid flows. *arXiv*, arXiv:1205.1258v1, 2012.

[136] Mohid. MOHID Description, Maretec - Instituto Superior Técnico, Lisbon, Portugal, 2003. URL `http://www.maretec.mohid.com/portugueseestuaries/Reports/MOHID_Description.pdf`.

[137] A. Molcard, P. M. Poulain, P. Forget, A. Griffa, Y. Barbin, J. Gaggelli, J. C. De Maistre, and M. Rixen. Comparison between VHF radar observations and data from drifter clusters in the Gulf of La Spezia (Mediterranean Sea). *J. Mar. Syst.*, 78:S79–S89, 2009.

[138] P. Montero, M. Gómez-Gesteira, J. J. Taboada, M. Ruiz-Villarreal, A. P. Santos, R. R. Neves, R. Prego, and V. Pérez-Villar. On residual circulation of the Ría of Vigo, using a 3-D baroclinic model. *Bol. Inst. Esp. Oceanogr.*, 15(1-4):31–38, 1999.

[139] K.-A. Mori, N. Chang. Introduction to MPIV - PIV toolbox in Matlab [http://www.oceanwave.jp/softwares/mpiv/]. 2009.

[140] R. Morrow and Y.-P. Le Traon. 15 years of satelite altimetry and mesoscale ocean dynamics. 2012.

[141] J. J. Nauw, H. van Aken, A. Webb, J. R. E. Lutjeharms, and W. P. M. de Ruijter. Observations of the southern East Madagascar Current and undercurrent and countercurrent system. *J. Geophys. Res.*, 113:C08006, 2008.

[142] Z. Neufeld and E. Hernández-García. *Chemical and Biological Processes in Fluid Flows - A Dynamical Systems Approach*. Imperial College Press, 2010.

[143] Z. Neufeld and T. Tél. Advection in chaotically time-dependent open flows. *Phys. Rev. E*, 57(3):2832–2842, 1998.

[144] P. P. Niiler, A. S. Sybrandy, K. Bi, P. M. Poulain, and D. Bitterman. Measurements of the water-following capability of holey-sock and TRISTAR drifters. *Deep–Sea Res. I*, 42(11/12):1951–1964, 1995.

[145] E. Nogueira, F. F. Pérez, and A. F. Ríos. Seasonal Patterns and Long–term Trends in an Estuarine Upwelling Ecosystem (Ría de Vigo, NW Spain). *Estuar. Coast. Shelf Sci.*, 44:258–300, 1997.

[146] C. Ohlmann, P. F. White, A. L. Sybrandy, and P. P. Niiler. GPS-Cellular Drifter Technology for Coastal Ocean Observing Systems. *J. Atmos. Ocean. Tech.*, 22:1381–1388, 2005.

[147] C. Ohlmann, P. F. White, L. Washburn, E. Terrill, B. Emery, and M. Otero. Interpretation of Coastal HF Radar–Derived Surface Currents with High–Resolution Drifter Data. *J. Atmos. Ocean. Tech.*, 24:666–380, 2007.

[148] A. Okubo. Horizontal dispersion of floatable particles in the vicinity of velocity singularities such as convergences. *Deep-Sea Reas.*, 17:445, 1970.

[149] A. Okubo. Oceanic diffusion diagrams. *Deep-Sea Res.*, 18:789–802, 1971.

[150] M. Olascoaga and G. Haller. Forecasting sudden changes in environmental pollution patterns. *Proc. Natl. Acad. Sci. USA*, 109(13):4738–4743, 2012.

[151] M. J. Olascoaga. Isolation on the West Florida Shelf with implications for red tides and pollutant dispersal in the Gulf of Mexico. *Nonlin. Processes Geophys.*, 17:685–696, 2010.

[152] M. J. Olascoaga, I. I. Rypina, M. G. Brown, F. J. Beron-Vera, H. Koak, L. E. Brand, G. R. Halliwell, and L. K. Shay. Persistent transport barrier on the West Florida Shelf. *Geophys. Res. Lett.*, 33(22):L22603, 2006. doi: 10.1029/2006GL027800.

[153] M. J. Olascoaga, M. J., F. Beron-Vera, L. Brand, and H. Koak. Tracing the early development of harmful algal blooms on the West Florida shelf with the aid of Lagrangian coherent structures. *J Geophys Res.*, 113:C12014, 2008.

[154] J. O'Reilly, S. Maritorena, B. Mitchell, D. Siegel, K. Carder, S. Garver, M. Kahru, and C. McClain. Ocean color chlorophyll algorithms for SeaWiFS. *J. Geophys. Res.*, 103(C11):24,937–24,953, 1998.

[155] S. Orre, B. Gjevik, and J. H. LaCasce. Characterizing chaotic dispersion in a coastal tidal model. *Continental Shelf Res.*, 26:1360–1374, 2006.

[156] A. Oschlies and V. Garcon. Eddy-induced enhancement of primary production in a model of the North Atlantic Ocean. *Nature*, 394:266–269, 1998.

[157] A. Oschlies and V. Garcon. An eddy-permitting coupled physical-biological model of the North Atlantic: 1. sensitivity to advection numerics and mixed layer physics. *Global Biogeochem. Cycl.*, 13:135–160, 1999.

[158] E. Ott. *Chaos in dynamical systems*. Cambridge Univ. Press, 1993.

[159] J. Ottino. *The kinematics of mixing: stretching, chaos, and transport.* Cambridge Univ. Press, 1989.

[160] V. Palastanga, P. van Leeuwen, M. Schouten, and W. de Ruijter. Flow structure and variability in the subtropical Indian Ocean: Instability of the South Indian Ocean Countercurrent. *J. Geophys. Res.*, 112:C01001, 2007. doi: $10.1029/2005\mathrm{JC}003395$.

[161] A. Parks, L. Shay, W. Johns, J. Maritinez-Pedraja, and K.-W. Gurgel. HF radar observations of small-scale surface current variability in the Straits of Florida. *J. Geophys. Res.*, 114(C08002), 2009.

[162] C. Pasquero, A. Bracco, and A. Provenzale. Impact of the spatiotemporal variability of the nutrient flux on the primary productivity in the ocean. *J. Geohys. Res.*, 110:C07005, 2005. doi: $10.1029/2004\mathrm{JC}002738$.

[163] T. Peacock and J. Dabiri. Introduction to focus issue: Lagrangian coherent structures. *Chaos*, 20:017501, 2010. doi: $10.1063/1.3278173$.

[164] V. Pérez-Muñuzuri and G. Fernández-García. Mixing efficiency in an excitable medium with chaotic shear flow. *Phys. Rev. E*, 75:046209, 2008.

[165] V. Pérez-Muñuzuri and F. Huhn. The role of mesoscale eddies time and length scales on phytoplankton production. *Nonlin. Processes Geophys.*, 17:177–186, 2010.

[166] N. Périnet, D. Juric, and L. Tuckermann. Numerical simulation of Faraday waves. *J. Fluid Mech.*, 635:1–26, 2009.

[167] S. Piedracoba, X. Álvarez Salgado, G. Rosón, and J. Herrera. Short time scale thermohaline variability and residual circulation in the central segment of the coastal upwelling system of the Ría de Vigo (NW Spain) during four contrasting periods. *J. Geophys. Res.*, 110:C03018, 2005.

[168] R. Pierrehumbert. Tracer microstructure in the large-eddy dominated regime. *Chaos, Solitons & Fractals*, 4(6):1091–1110, 1994.

[169] A. Poje, A. Haza, T. Özgökmen, M. Magaldi, and Z. Garrafo. Resolution dependent relative dispersion statistics in a hierarchy of ocean models. *Ocean Modelling*, 31:36–50, 2010.

[170] S. Prants, M. Budyansky, and M. Uleysky. Lagrangian tools to monitor transport and mixing in the ocean. *arXiv*, arXiv:1205.4371v1, 2012.

[171] J. M. Price, M. Reed, M. K. Howard, W. R. Johnson, Z.-G. Jia, C. F. Marshall, N. J. J. Guinasso, and G. B. Rainey. Preliminary assessment of an oil-spill trajectory model using satellite-tracked, oil-spill-simulating drifters. *Environ. Modell. Softw.*, 21:258–270, 2006.

[172] G. D. Quartly, J. J. H. Buck, M. Srokosz, and A. Coward. Eddies around MadagascarThe retroflection re-considered. *J. Mar. Syst.*, 63:115–129, 2006.

[173] R. P. Raj, B. Peter, and D. Pushpadas. Oceanic and atmospheric influences on the variability of phytoplankton bloom in the southwestern Indian Ocean. *J. Mar. Syst.*, 82:217–229, 2010.

[174] K. J. Richards, N. Maximenko, F. Bryan, and H. Sasaki. Zonal jets in the Pacific Ocean. *Geophys. Res. Lett.*, 33:L03605, 2006. doi: $10.1029/2005\mathrm{GL}024645$.

[175] H. Ridderinkhof and J. T. F. Zimmerman. Chaotic Stirring in a Tidal System. *Science*, 258:1107–1111, 1992.

[176] M.-H. Rio, P. Schaeffer, J.-M. Lemoine, and F. Hernández. Estimation of the ocean Mean Dynamic Topography through the combination of altimetric data, in-situ measurements and GRACE geoid: From global to regional studies. *Paper presented at GOCINA International Workshop, Eur. Cent. for Geodyn. and Seismol., Luxembourg, 1315 April.*, 2005.

[177] M. Roughan, E. Terrill, J. Largier, and M. Otero. Observations of divergence and upwelling around Point Loma, California. *J. Geophys. Res.*, 110(C04011), 2005.

[178] V. Rupolo. *Lagrangian analysis and prediction of coastal and ocean dynamics*, chapter Observing turbulence regimes and Lagrangian dispersal properties in the oceans, pages 231–274. Cambridge Univ. Press, 2007.

[179] J. Ruppert-Felsot, O. Praud, E. Sharon, and H. Swinney. Extraction of coherent structures in a rotating turbulent flow experiment. *Phys. Rev. E*, 72:016311, 2005.

[180] I. Rypina, S. Scott, L. Pratt, and M. Brown. Investigating the connection between complexity of isolated trajectories and Lagrangian coherent structures. *Nonlin. Process. Geophys.*, 18:977–987, 2011.

[181] F. Sadlo and R. Peikert. Efficient Visualization of Lagrangian Coherent Structures by Filtered AMR Ridge Extraction. *IEEE T. Vis. Comput. Gr.*, 13(6):1456–1463, 2007.

[182] F. Sadlo and R. Peikert. *Visualizing Lagrangian Coherent Structures and Comparison to Vector Field Topology*, chapter 2, pages 15–30. Springer Verlag, 2009.

[183] F. Sagués, J. Sancho, and J. García-Ojalvo. Spatiotemporal order out of noise. *Rev. Mod. Phys*, 79:829–880, 2007.

[184] R. Samelson. Fluid exchange across a meandering jet. *J. Phys. Ocean.*, 22: 431–440, 1992.

[185] R. Samelson and S. Wiggins. *Lagrangian transport in geophysical jets and waves – The dynamical systems approach*. Springer, New York, 2006.

[186] M. Sandulescu, C. López, E. Hernández-García, and U. Feudel. Plankton blooms in vortices: the role of biological and hydrodynamic timescales. *Nonlin. Process. Geophys.*, 14:443–454, 2007.

[187] M. Sandulescu, C. López, E. Hernández-García, and U. Feudel. Biological activity in the wake of an island close to a coastal upwelling. *Ecol. Complex.*, 5:228–237, 2008.

[188] D. Sandwell and W. Smith. Marine gravity anomaly from Geosat and ERS 1 satellite altimetry. *J. Geophys. Res.*, 102(B5):10,039–10,054, 1997.

[189] S. C. Shadden. *A dynamical systems approach to unsteady systems*. PhD thesis, California Institute of Technology, Pasadena, California, 2006.

[190] S. C. Shadden, F. Lekien, and J. E. Marsden. Definition and properties of Langrangian Coherent Structures from finite-time Lyapunov exponents in two-dimensional aperiodic flows. *Physica D*, 212:271–304, 2005.

[191] S. C. Shadden, F. Lekien, J. D. Paduan, F. P. Chavez, and J. E. Marsden. The correlation between surface drifters and coherent structures basedon high-frequency radar data in Monterey Bay. *Deep-Sea Research II*, 56:161–172, 2009.

[192] P. Shaw and S. Chao. A nonhydrostatic primitive-equation model for studying small-scale processes: An object-oriented approach. *Cont. Shelf Res.*, 26:1416–1432, 2006.

[193] E. Shuckburgh, H. Jones, J. Marshall, and C. Hill. Understanding the regional variability of eddy diffusivity in the Pacific sector of the Southern Ocean. *J. Phys. Oceanogr.*, 39:2011–2023, 2009.

[194] G. Siedler, M. Rouault, and J. R. E. Lutjeharms. Structure and origin of the subtropical South Indian Ocean Countercurrent. *Geophys. Res. Lett.*, 33:L24609, 2006.

[195] J. Smith. *Models in Ecology*. Cambridge University Press, 1974.

[196] C. Souto, M. Gilcoto, L. Fariña Busto, and F. F. Pérez. Modeling the residual circulation of a coastal embayment affected by wind-driven upwelling: Circulation of the Ría de Vigo (NW Spain). *J. Geophys. Res.*, 108(C11): 3340, 2003. doi: $10.1029/2002\mathrm{JC}001512$.

[197] M. Spiegelmann and R. Katz. A semi-Lagrangian Crank-Nicholson algorithm for the numerical solution of advection-diffusion problems. *Geochem. Geophys. Geosyst.*, 7:Q04014, 2006.

[198] M. A. Srokosz, G. Quartly, and J. J. H. Buck. A possible plankton wave in the Indian Ocean. *Geophys. Res. Lett.*, 31:L13301, 2004. doi: 10.1029/2004GL019738.

[199] A. Staniforth and J. Cote. Semi-Lagrangian intergration schemes for atmospheric models – a review. *Mon. Weather Rev.*, 119:2206–2223, 1991.

[200] C. Stevens. Short-term dispersion and turbulence in a complex-shaped estuarine embayment. *Cont. Shelf Res.*, 30(5):393–402, 2009.

[201] R. Stewart. *Introduction to Physical Oceanography*. Department of Oceanography, Texas A & M University, 2003.

[202] J. R. Stirling. Transport and bifurcation in a non-area-preserving two-dimensional map with applications to the discharge of pollution in an estuarine flow. *Physica D*, 144:169–193, 2000.

[203] A. Subramaniam, P. Yager, E. Carpenter, C. Mahaffey, K. Björkman, S. Colley, A. Kustka, J. Montoya, S. Sañudo Wilhelmy, R. Shipe, and D. Capone. Amazon River enhances diazotrophy and carbon sequestration in the tropical North Atlantic Ocean. *Proc. Natl.Acad. Sci. USA*, 105:10460–10465, 2008.

[204] J. J. Taboada, R. Prego, M. Ruiz-Villarreal, M. Gómez-Gesteira, P. Montero, A. P. Santos, and P.-V. V. Evaluation of the Seasonal Variations in the Residual Circulation in the Ría of Vigo (NW Spain) by Means of a 3D Baroclinic Model. *Estuarine, Coastal and Shelf Sci.*, 47:661–670, 1998.

[205] G. Taylor. Diffusion by continuous movements. *Proc. Lond. Math. Soc.*, 20:196–212, 1921.

[206] G. H. Tilstone, F. H. Figueiras, and F. Fraga. Upwelling-downwelling sequences in the generation of red tides in a coastal upwelling system. *Mar. Ecol. Prog. Ser.*, 112:241–253, 1994.

[207] M. Toner, A. Kirwan Jr., L. Kantha, and J. Choi. Can general circulation models be assessed and their output enhanced with drifter data? *J. Geophys. Res.*, 106(C9):19563–19579, 2001.

[208] M. Toner, A. Kirwan Jr., A. Poje, L. Kantha, F. Müller-Karger, and C. Jones. Chlorophyll dispersal by eddy-eddy interactions in the Gulf of Mexico. *J. Geophys. Res.*, 108(C4):3105, 2003.

[209] S. Torres, R. A. Varela, and E. Delhez. Residual circulation and thermohaline distribution of the Ria de Vigo: a 3-D hydrodynamical model. *Scientia Marina*, 65:277–289, 2001.

[210] Y.-K. Tsang. Predicting the evolution of fast chemical reactions in chaotic flows. *Phys. Rev. E*, 80:026305, 2009.

[211] N. Tufillaro, R. Ramshankar, and J. Gollub. Order-disorder transition in capillary ripples. *Phys. Rev. Lett.*, 62(4):422–425, 1989.

[212] M. Twardos, P. Arratia, M. Rivera, G. Voth, J. Gollub, and R. Ecke. Stretching fields and mixing near the transition to nonperiodic two-dimensional flow. *Phys. Rev. E*, 77:056315, 2008.

[213] M. Uleysky, M. Budyansky, and S. Prants. Mechanism of destruction of transport barriers in geophysical jets with Rossby waves. *Phys. Rev. E*, 81: 017202, 2010.

[214] D. S. Ullman, J. O'Donnell, J. Kohut, T. Fake, and A. Allen. Trajectory prediction using HF radar surface currents: Monte Carlo simulations of prediction uncertainties. *J. Geophys. Res.*, 111:C12005, 2006. doi: 10.1029/2006JC003715.

[215] B. M. Uz. What causes the sporadic phytoplankton bloom southeast of Madagascar? *J. Geophys. Res.*, 112:C09010, 2007. doi: 10.1029/2006JC003685.

[216] A. von Kameke, F. Huhn, G. Fernández-García, A. Muñuzuri, and V. Pérez-Muñuzuri. Propagation of a chemical wave front in a quasi-two-dimensional superdiffusive flow. *Phys. Rev. E*, 81:066211, 2010.

[217] A. von Kameke, F. Huhn, G. Fernández-García, A. Muñuzuri, and V. Pérez-Muñuzuri. Double cascade turbulence and Richardson dispersion in a horizontal fluid flow induced by Faraday waves. *Phys. Rev. Lett.*, 107:074502, 2011.

[218] A. von Kameke, F. Huhn, A. Pérez-Muñuzuri, and V. Pérez-Muñuzuri. Large spiral and target waves: Turbulent diffusion boosts scales of pattern formation (submitted). 2012.

[219] A. von Kameke, F. Huhn, and V. Pérez-Muñuzuri. Asymptotic diffusion coefficients and anomalous diffusion in a meandering jet flow under environmental fluctuations. *Phys. Rev. E*, 85:017201, 2012.

[220] G. Voth, G. Haller, and J. Gollub. Experimental measurement of stretching fields in fluid mixing. *Phys. Rev. Lett.*, 88(25):254501, 2002.

[221] G. Voth, T. Saint, G. Dobler, and J. Gollub. Mixing rates and symmetry breaking in two-dimensional chaotic flow. *Phys. Fluids*, 15(9):2560–2566, 2003.

[222] H. Wei, D. Hainbucher, T. Pohlmann, S. Feng, and J. Suendermann. Tidal-induced Lagrangian and Eulerian mean circulation in the Bohai Sea. *J. Mar. Syst.*, 44:141–151, 2004.

[223] J. Weiss. The dynamics of enstrophy transfer in two-dimensional hydrodynamics. *Physica D*, 48:273, 1991.

[224] J. Weiss and A. E. Provenzale. *Transport and mixing in geophysical flows, Lect. Notes Phys. 744*. Springer-Verlag, Berlin Heidelberg, 2008.

[225] S. Wiggins. *Introduction to applied nonlin dynamical systems and chaos*. Springer Verlag, New York, Berlin, Heidelberg, 1990.

[226] S. Wiggins. *Chaotic transport in dynamical systems*. Springer Verlag, New York, 1992.

[227] S. Wiggins. The Dynamical Systems approach to Lagrangian transport in oceanic flows. *Annu. Rev. Fluid Mech.*, 37:295–328, 2005. doi: 10.1146/annurev.fluid.37.061903.175815.

[228] C. Wilson and X. Qiu. Global distribution of summer chlorophyll blooms in the oligotrophic gyres. *Prog. Oceanogr.*, 78:107–134, 2008.

[229] W. S. Wooster, A. Bakun, and D. R. Mclain. The seasonal upwelling cycle along the eastern boundary of the North Atlantic. *J. Mar. Res.*, 34:131–141, 1976.

[230] W. Young. Lectures on stirring and mixing from the 1999 Woods Hole program in Geophysical Fluid Dynamics, 1999.

[231] G.-C. Yuan, K. Nam, T. Antonsen, E. Ott, and P. Guzdar. Power spectrum of passive scalars in two dimensional chaotic flows. *Chaos*, 10(1):39–49, 2000.

Appendix A

Data

A.1 Ocean Color Remote Sensing - SeaWiFS

The chlorophyll data we used to analyze the Lagrangian patterns of the Madagascar plankton bloom are provided by the SeaWiFS project of the NASA Goddard Space Flight Center. The data have been downloaded from (`http://oceandata.sci.gsfc.nasa.gov/SeaWiFS/Mapped/8Day/9km/chlor/`). We present here some basic characteristics of the SeaWiFS sensor and its measurement principles based on the description on the webpage of the SeaWiFS project (`http://oceancolor.gsfc.nasa.gov/SeaWiFS/`).

Sensor description SeaWiFS (Sea-viewing Wide Field-of-view Sensor) is the name of the optical sensor on board of the SeaStar satellite that provides ocean color measurements. The satellite was launched on 1 August 1997 and flies on an orbit at a height of $705\,\text{km}$. One orbit has a period of $99\,\text{min}$ and the revisit time is $1\,\text{day}$, i.e., after one day the satellite passes again the same area on earth. In principle, daily data is available, but merged composite data of several days, in our case $8\,\text{days}$, have a better coverage, as data gaps exists, caused for example by cloud cover. The sensor measures optical radiation in the visible range on 8 bands with the corresponding central wavelength, see Tab. A.1. The relevant bands for the estimation of chlorophyll concentration are the blue and green bands $2-5$. The measurement principle is relatively simple. With an increasing concentration of phytoplankton in the ocean, chlorophyll *a*, the primary photosynthetic pigment, absorbs relatively more red and blue light, shifting the spectrum of backscattered sunlight from blue to green [154]. An ocean color chlorophyll algorithm is used to compute chlorophyll concentrations from the light intensities of different bands. The current SeaWiFS algorithm is *OC4v4* and the empirical parametrization reads [31, 154]

$$\log_{10}[Chl] = a_0 + a_1 X + a_2 X^2 + a_3 X^3 + a_4 X^4, \tag{A.1}$$

$$X = \log_{10}\left[\frac{\max(R_{rs}^{443}, R_{rs}^{490}, R_{rs}^{510})}{R_{rs}^{555}}\right]. \tag{A.2}$$

Band	Color	Central wavelength [nm]	Bandwidth [nm]
1	violet	412	402-422
2	blue	443	433-453
3	blue-green	490	480-500
4	blue-green	510	500-520
5	green	555	545-565
6	red	670	660-680
7	near IR	765	745-785
8	near IR	865	845-885

Table A.1: Bands of the Sea-viewing Wide Field-of-view Sensor (SeaWiFS).

R_{rs}^{λ} is the remote sensing reflectance at the optical wavelength λ. The variable X basically denotes the logarithmic ratio of the maximum green reflectance and the blue reflectance. In very simple words, the parametrization expresses the relation 'the greener the ocean- the more chlorophyll'. The coefficients a_i are determined by extensive calibration studies with in-situ chlorophyll measurements at the sea surface, see e.g. [31].

Appendix B

Numerical Schemes

B.1 Extraction and Filtering of FTLE Ridges

Ridges of the FTLE field $\lambda(\mathbf{x}_0, t_0, \tau)$ are estimates of stable and unstable manifolds of the time-dependent flow. They can easily be identified by eye in the FTLE fields, but a criterion is desirable to extract them as a line from the two-dimensional field. A ridge is a line of local maxima of the FTLE field and a criterion can be formulated using the Hessian matrix and the gradient of $\lambda(\mathbf{x}_0, t_0, \tau)$ [181, 182, 190]. A sharp ridge is characterized by a high negative curvature, i.e. high negative eigenvalues ϵ of the Hessian matrix. For points on the ridge, the gradient $\nabla\lambda(\mathbf{x}_0, t_0, \tau)$ is tangent to the ridge line and perpendicular to the eigenvector ϵ_{min} corresponding to the smallest eigenvalues ϵ_{min} of the Hessian, which leads to the condition

$$\Psi = \boldsymbol{\epsilon}_{min} \cdot \nabla\lambda(\mathbf{x}_0, t_0, \tau) = 0 \tag{B.1}$$

with a negative minimal eigenvector $\epsilon_{min} < 0$. Computing the gradient and Hessian for the FTLE field, ridges can be extracted as zero contour lines of the field Ψ. The use of differential properties of the FTLE field, like the gradient and the Hessian, demands for a smooth FTLE fields which can only be ensured for the cubic spline interpolation. Linear interpolation leads to discontinuities in the spatial derivatives and prevents an exact ridge extraction.

As a second step, filtering is preferable to extract only important Lagrangian structures. Two straight forward criteria are a lower threshold for the FTLE field $\lambda(\mathbf{x}) > \lambda_{min}$, to discard weak ridges in the background FTLE field, and a high negative curvature of the ridge $\epsilon_{min}(\mathbf{x}_0, t_0, \tau)$ to choose only sharp ridges. Using these criteria a spatial mask $M(\mathbf{x_0})$ is defined, and ridges outside of the mask are neglected.

B.2 Gradient of the Flow Map

In Sec. 2.3.3 we consider the growth of a small perturbation $\delta\mathbf{x_0}$ to a trajectory. In linear approximation, the gradient of the flow map determines the deformation

this perturbation under the flow

$$\delta\mathbf{x}(t_0+\tau) = F(\mathbf{x_0})\,\delta\mathbf{x_0}(t_0) \tag{B.2}$$

$$F(\mathbf{x_0}) = \nabla\Phi_{t_0}^{t_0+\tau}(\mathbf{x_0}) = \nabla\left[\mathbf{x}(t_0+\tau)\right] = \begin{bmatrix} \frac{\partial x}{\partial x_0} & \frac{\partial x}{\partial y_0} \\ \frac{\partial y}{\partial x_0} & \frac{\partial y}{\partial y_0} \end{bmatrix} \tag{B.3}$$

Numerically, the gradient of the flow map can be computed using central differencing [189]

$$F(\mathbf{x_0}) = \nabla\varphi_t^{t+\tau}(x_0(i,j), y_0(i,j)) = \begin{bmatrix} \frac{x(i+1,j)-x(i-1,j)}{x_0(i+1,j)-x_0(i-1,j)} & \frac{x(i,j+1)-x(i,j-1)}{y_0(i,j+1)-y_0(i,j-1)} \\ \frac{y(i+1,j)-y(i-1,j)}{x_0(i+1,j)-x_0(i-1,j)} & \frac{y(i,j+1)-y(i,j-1)}{y_0(i,j+1)-y_0(i,j-1)} \end{bmatrix} \tag{B.4}$$

where the indices i, j correspond to the direction x, y respectively. $x_0(i,j)$ is the initial position of the particle (i,j) and $x(i,j)$ is the position of particle (i,j) after time τ. For a regular grid of initial particle positions $\mathbf{x_0}$ with a distance between particles Δx this simplifies to

$$F(\mathbf{x_0}) = \frac{1}{2\Delta x}\begin{bmatrix} x(i+1,j)-x(i-1,j) & x(i,j+1)-x(i,j-1) \\ y(i+1,j)-y(i-1,j) & y(i,j+1)-y(i,j-1) \end{bmatrix} \tag{B.5}$$

Appendix C

List of Publications

Articles

- A. von Kameke, **F. Huhn**, A. P. Muñuzuri, and V. Pérez-Muñuzuri: Large spiral and target waves: Turbulent diffusion boosts scales of pattern formation (Phys. Rev. Lett., under revision), 2012.
- **F. Huhn**, A. von Kameke, V. Pérez-Muñuzuri, M.J. Olascoaga, and F.J. Beron-Vera: The impact of advective transport by the South Indian Ocean Countercurrent on the Madagascar plankton bloom, *Geophys. Res. Lett.* 39, L06602, 2012.
- A. von Kameke, **F. Huhn**, and V. Pérez-Muñuzuri: Asymptotic diffusion coefficients and anomalous diffusion in a meandering jet-flow under environmental fluctuations, *Phys. Rev. E* 85, 017201, 2012.
- **F. Huhn**, A. von Kameke, S. Allen-Perkins, P. Montero, A. Venancio, and V. Pérez-Muñuzuri: Horizontal Lagrangian transport in a tidal-driven estuary - transport barriers attached to prominent coastal boundaries, *Cont. Shelf Res.* 39-40, 1-13, 2012.
- A. von Kameke, **F. Huhn**, G. Fernández-García, A. P. Muñuzuri, and V. Pérez-Muñuzuri: Double Cascade Turbulence and Richardson Dispersion in a Horizontal Fluid Flow Induced by Faraday Waves, *Phys. Rev. Lett.* 107, 074502, 2011.
- V. Pérez-Muñuzuri, **F. Huhn**: The role of mesoscale eddies time and length scales on phytoplankton production, *Nonlin. Processes Geophys.* 17, 177–186, 2010.
- A. von Kameke, **F. Huhn**, G. Fernández-García, A. P. Muñuzuri, and V. Pérez-Muñuzuri: Propagation of a chemical wave front in a quasi-two-dimensional superdiffusive flow, *Phys. Rev. E* 81, 066211, 2010.